Variability and evolution of Active Galactic Nuclei

Author: Marzena Śniegowska

Advisor: Dr. hab. Michał Chodorowski, Prof. Bożena Czerny

CENTRUM ASTRONOMICZNE IM. MIKOŁAJA KOPERNIKA
POLSKIEJ AKADEMII NAUK

A thesis submitted in partial fulfillment of the requirements for the degree of
Doctor of Philosophy
in
Astronomy

May, 2022

Dedicated to
My family.

Abstract

The time-dependent phenomena in Active Galactic Nuclei are not yet well-understood. Those sources are massive, with a broad range of physical properties and available observations allow to explore their properties across the entire electromagnetic spectrum. The thesis presents a series of results on different timescales, from hours/days to the galaxy's chemical evolution over millions of years. Short-term variations are observed, for example, in the form of quasi-periodic eruptions (QPE) and Changing Look Active Galactic Nuclei (CL AGN), and none of the two have clear physical interpretation yet. I discuss the model of radiation pressure instability. Such a model basically predicts outbursts in timescales of hundreds of years. However, taking into account the narrow, unstable zone (in Paper I) or the reduced size of the accretion disk (in Paper II) gives a possibility of shrinking the timescales to those observed in CL AGN. In Paper III, I address the issue of whether large luminosity changes, in long timescales, couple with other AGN properties, and I show that highly accreting sources are more reach in metals.

Specifically, in Paper I, I explore the disc-instability outbursts at a relatively low Eddington ratio with the narrow radiation pressure instability zone, additionally limited by the inner hot flow. Our toy model gave the quantitative predictions for timescales and amplitudes for Changing Look AGN with multiple outbursts. We also discussed the possibility of modelling QPE using the radiation pressure instability model. However, such short timescales ($\approx$ hours) seem challenging to be reached using the model considered in this paper.

In Paper II we extended the model of radiation pressure instability from Paper I and using the time-evolution code GLADIS we explored the instability using a radially resolved, vertically averaged 1-D model. In this work, we focus on CL AGN phenomenon, and we explore different mass exchange scenarios between disk and corona, as well as the location of the outer radius of the accretion disk ($\approx$ 100 R_{schw}). The latter seems to be of the key importance in reducing the timescales of the outbursts. Such a small outer radius can imitate quantitatively event which causes the mass redistribution in the accretion disk, for example, a tidal disruption event. Similar effect of the disk radius reduction can be caused by the presence of the second black hole opening a gap in the disk.

Accretion disk instabilities can lead to large changes of luminosity also in long timescales, but it is not clear if they could consistently reproduce other luminosity-dependent AGN properties. Observations seem to shows the correlation between the observed accretion rate and the chemical composition. I address this issue by possibly accurately determining the metallicity of high accretion rate sources. In Paper III, we tested the physical properties of the broad line emitting gas for highly accreting quasars at redshift $\approx$ 2. This work highlights that those highly accreting sources seem to follow the same evolutionary trends and have similar values of ionization parameters and broad line region's density, as typical AGN. However, they show indication of strong outflows, and indeed high metal enrichment (above 10 times solar). This high metallicity may be explained by star forming events in those sources, particularly that we detect the enhancement of aluminium in comparison with carbon.

Streszczenie

(Abstract in Polish)

Zjawiska zależne od czasu w aktywnych jądrach galaktyk nie są jeszcze dobrze poznane. Źródła te są masywne, o szerokim zakresie właściwości fizycznych, a dostępne obserwacje pozwalają badać ich właściwości w całym widmie elektromagnetycznym. Praca przedstawia szereg wyników w różnych skalach czasowych - od godzin/dni po ewolucję chemiczną galaktyki na przestrzeni milionów lat. Obserwuje się krótkoterminowe zmiany, na przykład w postaci kwazi-okresowych erupcji (ang. quasi-periodic eruptions - QPE) i aktywnych jąder galaktycznych zmieniających swój typ morfologiczny (ang. Changing Look Active Galactic Nuclei - CL AGN). Żadne z nich nie ma jeszcze przejrzystej interpretacji fizycznej. Omawiam model niestabilnego dysku akrecyjnego ze względu na ciśnienie promieniowania. Taki model przewiduje wybuchy w skali czasowej setek lat. Jednak uwzględnienie wąskiej, niestabilnej strefy (w Pracy I) lub zredukowanego rozmiaru dysku akrecyjnego (w Pracy II) daje możliwość zmniejszenia skal czasowych do tych obserwowanych w CL AGN. W Pracy III badam związek pomiędzy dużymi zmianami jasności w długich skalach czasowych w aktywnych jądrach galaktyk a pozostałymi własnościami tych źródeł i pokazuję, że źródła silnie akreujące są bardziej bogate w metale.

W Pracy I skupiam się na badaniu zmian jasności spowodowanych rozbłyskami w wewnętrznych obszarach niestabilnego dysku akrecyjnego przy stosunkowo niskim współczynniku Eddingtona z wąską strefą niestabilności ciśnienia promieniowania. Dodatkowo strefa niestabilności jest ograniczona w części wewnętrznej przez gorący, optycznie cienki przepływ. Nasz model pozwolił na ilościowy opis skal czasowych i amplitud obiektów zmieniających typ morfologiczny z powtarzającymi się rozbłyskami. Omówiliśmy również możliwość modelowania kwazi-okresowych erupcji za pomocą tego modelu. Jednak tak krótkie skale czasowe (rzędu godzin) wydają się być trudne do osiągnięcia przy użyciu modelu rozważanego w tym artykule.

W Pracy II rozszerzyliśmy model niestabilności ciśnienia promieniowania z Pracy I i używając hydrodynamicznego kodu GLADIS, zbadaliśmy niestabilność za pomocą uśrednionego w kierunku wertykalnym jednowymiarowego modelu. W tej pracy koncentrujemy się na zjawisku CL AGN i badamy różne scenariusze wymiany masy między dyskiem a koroną, a także położenie zewnętrznego promienia dysku akrecyjnego ($\approx$ 100 promieni Schwarzschilda). Położenie zewnętrznego promienia dysku akrecyjnego wydaje się mieć kluczowe znaczenie w skracaniu skal czasowych wybuchów. Tak mały promień zewnętrzny może imitować ilościowo zdarzenie, które powoduje redystrybucję masy w dysku akrecyjnym, na przykład rozerwania pływowego gwiazdy. Podobny efekt zmniejszenia promienia dysku może być spowodowany przez obecnością drugiej czarnej dziury, która może utworzyć szczelinę w dysku akrecyjnym. Niestabilności dysku akrecyjnego mogą prowadzić do dużych zmian jasności również w długich skalach czasowych. Nie jest natomiast jasne, czy mogą one odtwarzać inne właściwości aktywnych glaktyk zależne od jasności. Obserwacje sugerują korelację między obserwowanym tempem akrecji a składem chemicznym. Odnoszę się do tego zagadnienia poprzez określanie metaliczności źródeł o wysokim współczynniku akrecji.

W Pracy III badaliśmy własności gazu emitującego szerokie linie widmowe dla silnie akreujących kwazarów przy przesunięciu ku czerwieni $\approx$ 2. Praca ta podkreśla, że silnie akreujące źródła wydają się podążać za trendami ewolucyjnymi typowej aktywnej galaktyki. Mają też podobne wartości parametrów jonizacji i gęstości obszaru emitującego szerokie linie co typowa aktywna galaktyka. Silnie akreujące źródła wykazują jednak oznaki silnych wypływów a nawet wysokiego wzbogacenia metalami

(ponad 10-krotność metaliczności słonecznej). Wspomnianą wysoką metaliczność można wytłumaczyć procesami gwiazdotwórczymi w tych źródłach, zwłaszcza że wykrywamy nadwyżkę glinu w porównaniu z węglem.

Declarations

I hereby declare that the content of this thesis was undertaken between October 2018 and January 2022 under the supervision of Dr. hab. Michał Chodorowski from Nicolaus Copernicus Astronomical Center, Polish Academy of Sciences, and Prof. Bożena Czerny from the Center for Theoretical Physics, Polish Academy of Sciences, after my registration for the degree of PhD at Nicolaus Copernicus Astronomical Center, Polish Academy of Sciences.

Wherever the contributions of others are involved, I indicate this clearly, with due to reference to the literature, acknowledgment in manuscripts, and statements of contribution from coauthors, which I include in the Appendix.

This thesis includes content which have appeared in the following works:

- *Chapter 2:* **Śniegowska, M.**, Czerny, B., Bon, E., Bon, N., 2020 *Possible mechanism for multiple changing-look phenomena in active galactic nuclei*, Astronomy and Astrophysics, 641, A167
- *Chapter 3:* **Śniegowska, M.**, Grzedzielski, M., Czerny, B., Janiuk, A., 2022 *Modeling changing-look active galactic nuclei phenomenon in 1D using accretion disk instabilities*, Astronomische Nachrichten, 343, e210065
- *Chapter 4:* **Śniegowska, M.**, Marziani, P., Czerny, B., Panda, S., Martınez-Aldama M.L., del Olmo , A., D'Onofrio, M., 2021 *High Metal Content of Highly Accreting Quasars*, The Astrophysical Journal, 910, 115

Apart from manuscripts included in this thesis, I have been involved in the following work:

- Panda, S. et al. **7th author** (2018), *Modeling of the Quasar Main Sequence in the Optical Plane*, The Astrophysical Journal, 866, 115
- Czerny, B. et al. **8th author** (2019), *Interpretation of Departure from the Broad-line Region Scaling in Active Galactic Nuclei*, The Astrophysical Journal, 870, 84
- Czerny, B. et al. **19th author** (2019), *Time Delay Measurement of Mg II Line in CTS C30.10 with SALT*, The Astrophysical Journal, 880, 46
- Wyrzykowski, Ł. et al. **158th author** (2020), *Full orbital solution for the binary system in the northern Galactic disc microlensing event Gaia16aye*, Astronomy and Astrophysics, 633, A98
- Zajaček, M. et al. **8th author** (2020), *Time-delay Measurement of Mg II Broad-line Response for the Highly Accreting Quasar HE 0413-4031: Implications for the Mg II-based Radius-Luminosity Relation*, The Astrophysical Journal, 896, 146
- **Śniegowska, M.** et al. **1st author** (2020), *Quasar Main Sequence in the UV Plane*, The Astrophysical Journal, 900, 64
- Czerny, B. et al. **12th author** (2021), *Dark Energy Constraints from Quasar Observations*, Acta Physica Polonica A, 139, 389
- Zajaček, M. et al. **9th author** (2021), *Time Delay of Mg II Emission Response for the Luminous Quasar HE 0435-4312: toward Application of the High-accretor Radius-Luminosity Relation in Cosmology*, The Astrophysical Journal, 912, 10

- Jiang, B.-W. et al. **11th author** (2021), *Linear spectropolarimetric analysis of fairall 9 with VLT/FORS2*, Monthly Notices of the Royal Astronomical Society, 508, 79

- Marziani, P. et al. **6th author** (2022), *The main sequence of quasars: The taming of the extremes*, Astronomische Nachrichten, 343, e210082

Moreover, I have contributed to the following manuscripts submitted to the refereed journals:

- **Śniegowska, M.** et al. **1st author** (2022), *Modified models of radiation pressure instability in application to 10, 10^5, and 10^7 $M_\odot$ accreting black holes*, sumbitted to Astronomy and Astrophysics, arXiv e-prints, arXiv:2204.10067

- **Śniegowska, M.** et al. **1st author** (2022), *Spectropolarimetry and spectral decomposition of high-accreting Narrow Line Seyfert 1 galaxies*, sumbitted to Astronomy and Astrophysics, arXiv e-prints, arXiv:2202.13839

- Prince R. et al. **11th author** (2022), *Wavelength-resolved Reverberation Mapping of quasar CTSC30.10: Dissecting MgII and FeII emission regions*, sumbitted to Astronomy and Astrophysics, arXiv e-prints, arXiv:2201.11062

Acknowledgements

I am greatly indebted to my PhD advisors, Professor Bożena Czerny and Dr. hab. Michał Chodorowski. Thanks to the infinite patience and the constant support of Professor Bożena Czerny, without which this thesis would not have been possible. I have no words to express my gratitude.

I want to thank all my collaborators, I owe them my deepest gratitude for their guidance and support. Firstly, I would like to thank Professor Paola Marziani for her great help, support, and enthusiasm. I am grateful to Professor Paola Marziani and Professor Mauro D'Onofrio for their warm hospitality and for hosting me in Padova. I would like to thank Professor Agnieszka Janiuk for her support throughout my journey in the numerical world, it seems a bit less dangerous now.

I thank Dr. Swayamtrupta Panda, your never-ending enthusiasm is truly inspiring, and I was fortunate to have your help throughout my PhD studies. I would like to thank Dr. Mary Loli Martínez-Aldama, Mohammad-Hassan Naddaf, Dr. Michal Zajaček, Dr. Raj Prince. Thank you for all the brilliant discussions during group meetings.

I am also grateful to Dr. Krzysztof Hryniewicz for his engaging questions, patient explanation, and discussions. I would like to thank Professor Agata Różańska and Dr. Alex Markowitz for organizing weekly group meetings. I would like to thank all students attending those meetings for many fruitful discussions.

I would like to express gratitude to my previous supervisors, Professor Łukasz Wyrzykowski (bachelor thesis) and Dr. Szymon Kozłowski (master thesis). Thank you for your support during my first steps in science. Both of you helped me to start my career.

I would like to express my thanks to my family for their unconditional support throughout all these years. From the bottom of my heart, I would like to thank Giovanni Librizzi for his unflinching support and for believing in my abilities. My special thanks to Dr. Marta Dziełak, Jacek Krajczok, Aleksandra Łopion, Kacper Oreszczuk, Mateusz Mazelanik, Wojciech Górski, Karol Czyżkowski, Veronika Shalamova for all discussions and all the memorable moments we shared.

I would like to acknowledge Nicolaus Copernicus Astronomical Center and Center for Theoretical Physics for assistance during my PhD studies. Finally, I would like to thank the Polish grant agency, NCN, for the grants that funded research activities during my PhD studies. [1]

[1] The work in this thesis was supported by the Polish National Science Centre grants no. 2021/41/N/ST9/02280 (PRELUDIUM 20) and 2017/26/A/ST9/-00756 (MAESTRO 9).

Contents

Part I

Introduction

Chapter 1

Introduction

The Active Galactic Nuclei (AGN) phenomenon is a fascinating episode in the evolution of galaxies. Processes taking place in the accreting matter close to the black hole are not yet well understood, and recent observations challenge the simplest models built over the years. There is also more to that. Most galaxies are not strongly active at any given moment, but the relatively short activity period is a crucial stage in galaxy evolution. Star forming activity in the host galaxy and the nuclear activity are coupled through the so-called feedback process, so some of the AGN properties can be tied to its surrounding.

My Thesis consists of three published papers which address those issues. They are included as Chapters 2, 3, and 4. But in order to set a stage for my results, in this Chapter, I will briefly introduce the Active Galactic Nuclei, their physical properties and the timescales in which we observe these sources to notice changes in their physical properties, and the timescales we expect them to perform secular evolution. Later on, I focus on topics which serve as a background for the presentation of the publications which form the PhD Thesis. I introduce the phenomenon of the Quasi-Periodic Ejections and Changing-Look AGN since the aim of Paper I and Paper II was to address this issue. Later I focus on the longer timescale evolution of AGN, with particular stress on high Eddington rate sources, and the methods to determine metal content in such high accretors since, as I conclude in Paper III, these two properties are somehow evolutionary connected. At the end of this section, I overview the results obtained in Papers I-III in more detail. In Chapter 5, I summarize my presented work and briefly describe the forthcoming results, which are connected to results from this Thesis.

1.1 AGN in the period of data-driven science

We are approaching the era of big data and new discoveries. We are already facing the increasing inflow of data from the ground-based large-area astronomical surveys, e.g. The Sloan Digital Sky Survey (SDSS; York et al. 2000) which has been collecting data since the year 2000, and from space missions, e.g. Gaia (Gaia Collaboration et al., 2016) launched in 2013. We expect even more data to come soon in the optical and the IR band. The James Webb Space Telescope (JWST; Gardner et al. 2006) was successfully launched on 25 December 2021 to L2 orbit, and we already had an opportunity to admire the first calibrated photo. SDSS (York et al., 2000) improved over the years, expanded the field of view, and became an all-sky multi-epoch spectroscopic survey (see an overview about the newest SDSS V by Kollmeier et al. 2017). The Zwicky Transient Facility (ZTF), using an extremely wide field of view camera, scans the entire Northern sky every two days (Bellm et al., 2019). The

ten-year Rubin Observatory Legacy Survey of Space and Time (LSST) (Ivezić et al., 2019) is planned to be operational in 2024 and will provide us with photometric monitoring, which will be of great use in the transient searching. Not to mention instruments at different wavelengths, the amount of available data is overwhelming. Thus, we have to exploit the data to the limit and do it wisely. Let us focus on Active Galactic Nuclei. The number of known quasars - the brightest Active Galactic Nuclei - has already crossed one million [1] and over 850 000 of those are from the SDSS-DR17 (Abdurro'uf et al., 2022) and LAMOST DR7 (Yan et al., 2022). Such vast statistics, supplemented with variability studies, will allow unprecedented insight into a more complete picture of the time evolution of AGN in various timescales, from the shortest rare episodes of fast changes to global evolutionary trends.

Active Galactic Nuclei (AGN) are powered by accretion onto supermassive black holes (SMBHs) $> 10^5 M_\odot$ (Netzer, 2015). Supermassive black holes are found in all regular galaxies, although very active nuclei are only observed in 10% of the currently known galaxies, and highest luminosities reach even up to $L_{BOL} \sim 10^{48}$ erg s^{-1} (Wu et al., 2010). The term 'active' refers to processes besides the nuclear reactions inside the stars that produce a significant amount of energy in the galaxy. This nuclear emission is mainly due to the accretion process.

Accretion onto black holes is a basic astrophysical process, which is an energy source both in the Active Galactic Nuclei and X-ray binaries. An accreting black hole system has a complex structure and emits radiation in a broad spectral band, from radio and infrared (IR) through optical/ultraviolet (UV) up to X-ray and gamma-ray. AGN activity is a significant phase of galaxy evolution, regulating the rate of star formation around it and thus impacting the overall galaxy evolution, which is one of the essential topics in modern astrophysics.

1.2 Brief historical overview

From a historical point of view, the first observed AGN (now known as NGC 1068) and its strong emission lines were noticed in the spectrum obtained by Fath (1909). Eighteen years later, Slipher (1917) reobserved this source and noticed broad emission lines in the obtained spectrum. Seyfert (1943) systematically studied selected galaxies with unusually bright nuclei and noticed the similarity of those sources to NGC 1068. Seyfert pointed out also different total widths of emission lines between objects (Table 5 in Seyfert, 1943).

During the 1960s, objects were discovered in the radio band and first classified as a new class of stars due to their point-like optical appearance. However, their spectra differed significantly from the known stellar spectra (e.g. by multiple strong emission lines not coinciding with known elements), so they were called 'star-like' or quasars. The problem was solved when Schmidt (1963) noticed that the strange lines in the optical spectrum of the source 3C 273 were shifted Balmer lines! He assumed that this is the result of the cosmological Doppler effect. He calculated the redshift of 3C 273 to be z = 0.158. This distance was comparable to the distances to the farthest known galaxies at the time. This discovery was so exciting that TIME magazine dedicated its cover story to Maarten Schmidt.

Years later, it was understood that 'star-like' objects - quasars - can be described by a unification model of Active Galactic Nuclei (AGN), thus forming a single family with sources like NGC 1068. Currently, the observations of active nuclei cover the whole range of electromagnetic radiation from radio, IR, UV, X-ray and gamma-rays since most AGN are seen in many bands. The resolution of

[1] https://heasarc.gsfc.nasa.gov/W3Browse/all/milliquas.html

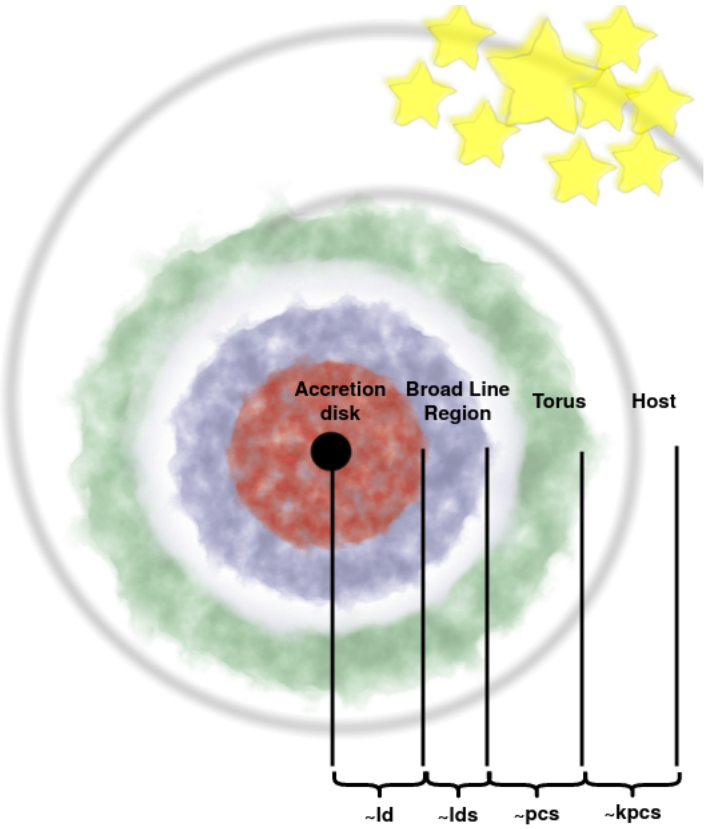

Figure 1.1: The distance scales of different parts of AGN. From the inside out: a supermassive black hole (marked as a black circle); an accretion disk (marked as a red ring); a broad line region (marked as a blue ring); a dusty torus (marked as a green ring); and a host galaxy region (marked as yellow stars). As grey spiral, we marked schematic spiral arm. The sizes do not represent the accurate scale.

observations also improves, with the highest resolution achieved by interferometry. However, the image of the central black hole was seen so far only for two objects: M87 - a weakly active, nearby massive elliptical galaxy containing a very massive black hole and Sagittarius A* - even less active massive black hole located at the Galactic Center of the Milky Way. Those images were achieved by the Event Horizon Telescope (Akiyama et al., 2022; Event Horizon Telescope Collaboration et al., 2019). In other AGN, we do not have direct access to the black hole vicinity due to too low spatial resolution of the images. However, we improve our knowledge considerably by using the variability of AGN and light echo studies.

1.3 Basic properties of AGN

1.3.1 Structure of AGN

The key element of an active nucleus is the central supermassive black hole and the medium surrounding it in its direct vicinity (see Figure 1.1). The inflow of the material is responsible for the generation of the energy powering the emitted radiation, and gravitational energy is the underlying energy source. The inflow is accompanied by some outflow in the form of a collimated jet and/or uncollimated wind.

Black hole

A black hole (BH) is an area in space-time that cannot be abandoned by particles or electromagnetic radiation. The astrophysical black hole is fully described by two parameters: its mass and angular momentum. The charge of the black hole is usually assumed to be small, although it may have some importance in the case of very low activity, like in the Milky Way (Zajaček et al., 2018). It is impossible to observe black holes directly, but we can study the phenomena occurring around them and thus infer the properties of black holes. Even if we do not observe them directly, we can estimate their masses (using various methods (Czerny & Nikolajuk, 2010), i.e. direct ones, which use the motion of orbiting stars or gas around a black hole or indirect ones, which use correlations between black hole mass and properties of the galaxy which was found using bigger samples based on empirical relations (e.g. Ferrarese & Merritt, 2000). We can categorise BHs by their masses into classes, starting from stellar mass black holes (3-100$M_\odot$), through intermediate mass black holes (100-$10^5 M_\odot$) (Farrell et al., 2009), to supermassive black holes ($> 10^5 M_\odot$). One of the basic parameters to describe a black hole is the Schwarzschild radius R_{schw} (for a non-rotating black hole).

$$R_{schw} = \frac{2GM}{c^2}, \tag{1.1}$$

Here M is the object's mass, c is the speed of light in a vacuum, and G is the gravitational constant. This formula is the mathematical description of the size at which the collapsing body becomes a black hole. In Newtonian theory, all circular orbits are stable, and their angular momentum increases monotonically outward. In the pseudo-Newtonian potential that has been introduced by Paczyński and Wiita (1980) and 'imitates' the effects of the general theory of relativity there is a marginally stable orbit, or the innermost stable circular orbit (ISCO). ISCO is the natural limit for a stable circular orbit. The slightest disturbance will change the movement of the matter at ISCO (fall onto a black hole). This orbit is at the distance of $r_{ISCO} = 3R_{schw}$ for a non-rotating black hole. The same value is obtained if the proper general relativistic solution of Schwarzschild (1916) is used for a non-rotating black hole. If the angular momentum is a non-zero, a more general solution for the gravitational field has to be used, which was derived much later by Kerr (1963). The motion of test particles is then more complicated. For particles moving in the symmetry plane perpendicular to the rotation axis, the ISCO also exist but depends on the angular momentum of a black hole and the direction of the motion of a particle (co-rotating or counter-rotating).

Accretion disk

The accretion process appears to be an efficient source of X-ray to optical emission in AGN (Rees, 1984). The character of the flow depends on the amount of angular momentum in the matter reservoir and the inflow rate. In weakly active galaxies, the Bondi flow (spherically symmetric hot inflow, with negligible angular momentum) is frequently considered, but close to the black hole, even the small amount of angular momentum becomes important. When the amount of material is more prominent, a much denser and cooler disk can form. The simplest model of the accretion disk is a stationary, optically thick and geometrically thin Keplerian accretion disk (Shakura & Sunyaev, 1973). The matter falls onto the BH, the angular momentum is transported outwards, and energy dissipates. The size of the accretion disk is estimated at 10^{-2} pc or 10 light days (Hawkins, 2007).

The accretion process leads to the emission of a significant amount of thermal radiation (Shakura

& Sunyaev, 1973), which dominates the optical/UV bands (Sun & Malkan, 1989).

The radiation flux from a disk at the radius r from a unit area is given by the formula (Novikov & Thorne, 1973; Shakura & Sunyaev, 1973):

$$F(r) = \frac{3GM\dot{M}}{8\pi r^3} I(r), \tag{1.2}$$

where M is the mass of the central black hole, $\dot{M}$ is the mass accretion rate. I(r) is the factor whose value depends on the adopted boundary condition and the description of the gravitational field of the black hole (e.g. non-rotating black hole model, no torque due to strong magnetic field). The radiation spectrum of such a disk can be approximated locally as a black body

$$\sigma T_{eff}(r)^4 = F(r), \tag{1.3}$$

and in this case, the disk spectrum does not depend on the assumptions about the viscous forces transporting the angular momentum and providing dissipation. The efficiency of the accretion process is determined by the function I(r).

For accretion disk with a lower accretion rate, we observe the departure from Shakura and Sunyaev (1973), with the inner disk changing into less luminous and less efficient geometrically thick and optically thin advection-dominated accretion flow (ADAF) (Ichimaru, 1977; Narayan & Yi, 1994). ADAF spectra are in the shape of power-law, with a Compton component; they do not emit black body radiation.

It is worth stressing in the context of this thesis that the stationary solution of Shakura and Sunyaev (1973) accretion disk does not depend on viscosity and opacity. In contrast, the time-dependent solution depends in those parameters (see e.g. Frank et al., 2002).

In Shakura and Sunyaev (1973) the viscous forces are parameterized by the viscosity parameter α and scale with the pressure. Later it was shown that the underlying physical process behind the accretion disk viscosity is the magneto-rotational instability (Balbus & Hawley, 1991). 3D models of the accretion disk evolution, which properly include this mechanism as well as the radiative cooling and general relativity effects, are numerically extremely demanding and were possible to perform only recently (e.g. Liska et al., 2022). However, creating this type of models is time-consuming, and the computation were not done for a broad range of radii.

Broad and Narrow Line Regions

AGN were discovered and understood due to studies of their strong emission lines, including Balmer lines (e.g. Schmidt, 1963). The natural width of the emission lines is small, but they can become broader due to the thermal movement of atoms. However, in AGN, the line kinematic widths are far greater than possible due to thermal motion, and they must reflect the dispersion in the dynamical velocities of the emitting medium, as already realized by Seyfert (1943). The lines originate in the medium surrounding SMBH and contain partially ionized species that produce emission lines primarily through photoionization processes (e.g. Osterbrock & Ferland, 2006).

The photoionization mechanism explains the formation of emission lines, particularly those which respond to the variable continuum radiation. Atoms are ionized or excited by absorption of the incident radiation. Later an atom can emit a photon during the spontaneous transition of an electron from an excited state to a lower energy level. When an atom collides with another atom before emission, the

excitation energy can be converted to energy of colliding particles, thus increasing the thermal energy of the medium instead of the emitting photon, so de-excitation is not always a radiative process. The lines' widths are Doppler-broadened, and in AGN, we distinguish two basic types of emission lines: broad and narrow ones. Those two types are produced in two separated regions called Broad and Narrow Line Regions (BLR/NLR), with the distance from light-days (BLR) to parsecs (NLR) from the SMBH. The material velocity in the BLR roughly corresponds to the local Keplerian velocity, in the NLR it mostly reveals the outflow.

The density of the material in the BLR is so high, the order of $n_e \sim 10^{11}$ cm^{-3}, that forbidden lines are not observed. BLR is closer to the SMBH than NLR, and the Doppler broadening is much stronger in this region. Narrow lines are formed further away, in low density region (significantly lower than in BLR $n_e \sim 10^{3-4}$ cm^{-3}) and due to low density and lower temperature (T $\sim 10^3$ K), also forbidden lines can be emitted there, i.e. [OIII] 4959Å, 5007Å doublet.

In some active Galactic Nuclei, the broad lines were not visible (such sources are classified as Type 2 AGN), and the physical reason was initially unclear. This problem was solved in 1985, when observations of one of the active galaxies (NGC 1068) were performed in polarized light (Antonucci & Miller, 1985). Authors have shown that the lack of the observed broad lines is related to the obscuration of the central areas by the dusty torus, as the broad lines were clearly seen in the scattered polarized light.

Torus

The dusty torus is cold circumnuclear gas (mainly carbon or silicon-rich) surrounding the SMBH at a distance of tens of pc (Hönig, 2019). By cold, I mean the temperature lower than the dust sublimation temperature. The maximum temperature of the torus is estimated at 1000 - 1500K. The torus absorbs part of the radiation from the accretion disk and then re-emits as infrared radiation. The exact structure of the torus is still under debate. Several models propose a homogeneous matter (e.g. Fritz et al., 2006), a clumpy distribution (Nenkova et al., 2008), a combination of both (Stalevski et al., 2012), or a conical type of dusty outflow (Hönig, 2019).

Host galaxy

Kauffmann et al. (2003) found that AGN are preferentially located in massive galaxies with a young stellar population. The host galaxies of low-luminosity AGN have stellar populations similar to typical early types. In contrast, the hosts of high-luminosity AGN have much younger mean stellar ages, and many of them experienced a burst of star formation in the recent past. However, there is no tight correlation between the properties of AGN hosts' structure and AGN power (Masoura et al., 2021).

The dusty interstellar medium in the hosts is preferentially located at distances in the order of kpc (e.g. Trakhtenbrot et al., 2017). This is the cold dust, with temperatures ~ 100 K, observed in the far-IR. Hot dust is present closer in, both in the equatorial plane, i.e. in the dusty torus, but also the polar directions, as implied by interferometric studies in the IR (e.g. Hönig et al., 2013; Leftley et al., 2018), as well as by polarization studies (e.g. Lira et al., 2021; Śniegowska et al., 2022c), and can be rather outflowing from the nuclear regions.

AGN show some level of starburst activity. Brighter AGN usually ride in hosts more vigorously forming stars (Kauffmann et al., 2003), but most recent research found a connection of star formation rate with the host mass, and not current activity level (Masoura et al., 2021; Rosario et al., 2013).

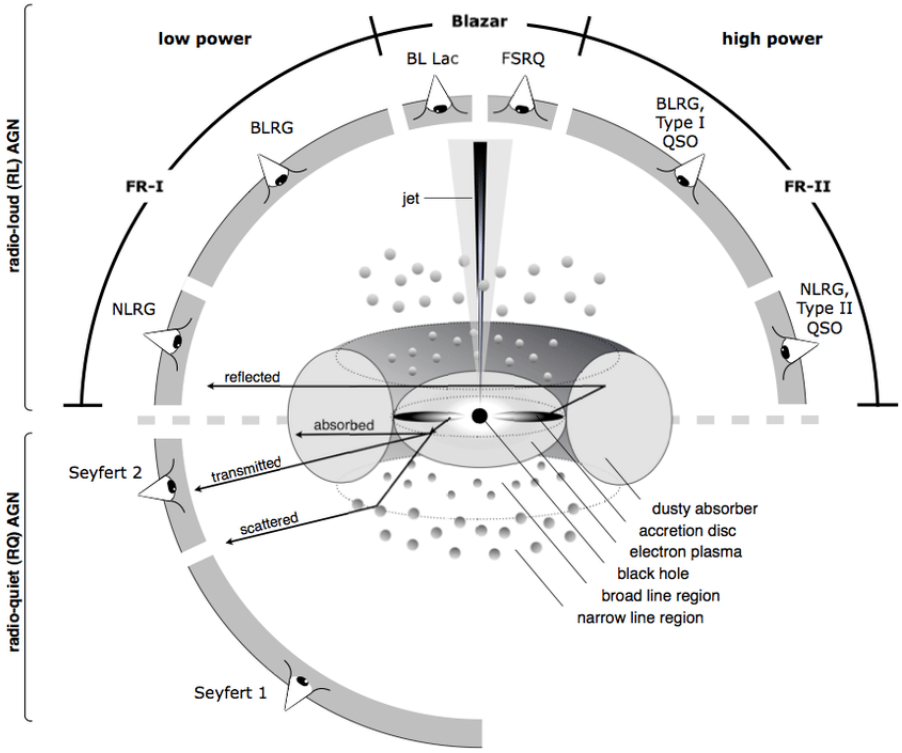

Figure 1.2: A schematic representation of the unified model of AGN adapted from Beckmann and Shrader (2012) Black signed lines mark the main components of the model. Black signed arrows indicate possible physical processes. Drawing is not in scale.

Starburst is frequently located far from the nucleus, at a distance of $\sim$ 1 kpc, forming a ring-like structure (e.g. Levenson et al., 2005, for Seyfert 1.9 galaxy NGC 7130). However, even in the same galaxy, there may be a much more compact nuclear starburst at a distance of $\sim$100 pc, which can be resolved only for nearby sources with the use of HST imaging (e.g. González Delgado et al., 1998).

Stars formation even closer to the nucleus, for example, in the outer self-gravitating accretion disk, is postulated by theoretical models, (Collin & Zahn, 2008; Collin & Zahn, 1999; Thompson et al., 2005). These regions are too compact to be resolved, and thus the evidence of this process can be only circumstantial.

The structure of the host is also directly related to the presence of the AGN. The momentum of the wind/jest outflow and the energy from black-hole accretion are powerful enough to affect even the outer parts of the galaxy. Even weakly active galaxies reveal the presence of the Extended Narrow Line Region, reaching up to a few kpc (see e.g. Husemann et al., 2022, and the references therein).

The outflow can also impact star formation. The host and the nucleus affect each other. However, this effect is very complex, and (Kormendy & Ho, 2013) suggests several characteristic stages of this interaction, dependent also on the basic structure of the host, being a bulge or bulgeless galaxy. The feedback (i.e. the influence of the AGN on the host) and the feeding are ultimately related. The issue of the host-AGN coevolution is further discussed in Section 1.4. The host galaxy is also a source of obscuration (Bianchi et al., 2012).

1.3.2 AGN unification

The observational discovery of the variety of properties like BLR and NLR objects posed the question initially of whether the underlying mechanism in all AGN is identical. However, with the progress of understanding the AGN structure, a clearer picture appeared.

The first important aspect responsible for apparent spectral variety is purely geometrical. AGN are not spherically symmetric, as we assume in the case of single stars. The type of an active galaxy depends on the viewing angle, and in a fraction of objects, we are not able to observe the centre of an active galaxy (e.g. because of the dusty torus) (Antonucci & Miller, 1985). As mentioned before, AGN were categorized based on the width of their optical emission lines. AGN Type 1 show broad, of order a few thousand km s^{-1}, and narrow, few hundred km s^{-1}, lines. In Type 2, we observe only narrow lines. Two kinds of lines are produced in regions (Broad and Narrow Line Regions (BLR/NLR)), as I point out in Section 1.3.1. The presence of the obscuring torus fully explains this phenomenon. Since the obscuration is not always complete, besides this basic Type 1/Type 2 classification, we also have the intermediate classes (1.2, 1.5, 1.8, 1.9) (Osterbrock, 1981). Those intermediate classes are based on relative strengths of the broad components of Hα and Hβ lines.

However, two other important parameters determine the specific view of a given AGN. The first one is the presence or absence of a strong collimated jet. Physically, the formation of this component depends either on the black hole spin, the large scale magnetic field, or both, as the issue of the radio-loud/radio-quiet dichotomy and the origin is still a topic of discussion (e.g. Keenan et al., 2021; Sikora, 2009). This relativistic well collimated stream changes the appearance of an active nucleus also in a strongly viewing-angle dependent way (Padovani et al., 2017). Strong jet viewed face-on leads to the blazar phenomenon, and relativistically boosted emission can dominate the entire spectrum and lead to very rapid variations.

Based on the schematic provided by the unified AGN model, we can describe the various types of active galaxies (Antonucci, 1993; Urry & Padovani, 1995). The scheme of this model is shown in Fig. 1.2. It assumes the location of a supermassive black hole in the centre of AGN, and most of the radiation is emitted due to the accretion onto BH. When matter falls into the black hole, it flattens and creates an accretion disk. The basic idea behind the unified model is that the same engine powers different classes of AGN, and the main differences can then be explained by the viewing angle or differences in the AGN intrinsic radio loudness.

However, there is also a second important parameter related to the intrinsic properties of an active nucleus, namely an accretion rate, as it is clear that not all galaxies have the same activity level. This parameter can affect the internal structure of the accretion disk, as already mentioned in Section 1.3.1, and therefore the appearance of an AGN, in addition to the viewing angle effects.

The level of AGN activity is conveniently measured using the concept of the Eddington ratio - the quantity used for linking the information about the BH mass and its accretion rate.

Before defining the Eddington ratio, I will define the quantities (bolometric and Eddington luminosities) from which we obtain the Eddington ratio. Bolometric luminosity is the luminosity of the source integrated across the whole electromagnetic spectrum. Eddington luminosity is the luminosity of an object with spherical symmetry for which the force of gravity balances the force of radiation pressure emitted by the object and acting on fully ionized hydrogen gas. The (spherically symmetric !) object emitting at the Eddington rate is still in hydrostatic equilibrium and can accrete. However, if the luminosity of the object exceeds L_{EDD}, there is an intense outflow of matter in the form of wind.

Eddington luminosity is given by the formula:

$$L_{EDD} = 1.3 \cdot 10^{38} \frac{M}{M_\odot} [erg/s], \tag{1.4}$$

where M is the mass of the object and $M_\odot$ is the mass of the Sun. Eddington luminosity is independent of the source's radius and depends only on the object's mass. However, the accretion disk is not spherically symmetric, so this definition is only approximate; nevertheless, this quantity is used to characterize the luminosity of active galaxies.

The Eddington ratio is then defined as the ratio λ_{EDD} between bolometric and Eddington luminosities:

$$\lambda_{EDD} = (L_{BOL}/L_{EDD}). \tag{1.5}$$

Using this concept we can also define the Eddington accretion rate, but this concept is less simple since it includes the accretion flow energetic efficiency, $\dot{M}_{EDD} = L_{EDD}/(c^2\eta)$, and the corresponding dimensionless accretion rate as $\dot{m} = \dot{M}/\dot{M}_{EDD}$.

As mentioned in Section 1.3.1, the inner disk in low λ_{EDD} sources is replaced by the hot inner ADAF flow. Thus the hot inner parts of the disk are absent, and the disk emits less UV than the standard disk extending to ISCO, but the source must be brighter in X-rays coming from the hot part of the flow. There is still a discussion about whether pure Seyfert 2 galaxies exist, i.e. there is no BLR in low luminosity sources where the very large inner ADAF prevents its formation (e.g. Cao, 2010; Czerny et al., 2004; Elitzur & Ho, 2009; Pons & Watson, 2016).

At the high λ_{EDD} end, since the accretion disk geometry is not spherical, the accretion can exceed the Eddington rate, but for $\dot{m} > 0.3$, the disk structure starts to be modified, turning into a slim disk model (Abramowicz et al., 1988). The luminosity predicted by the model rises more slowly with the accretion rate than in the standard Shakura and Sunyaev (1973) disk.

The connection between the host properties and the level of nuclear activity was always an important but challenging topic of the studies. Kauffmann et al. (2003) show that AGN are hosted mostly in massive but otherwise somewhat normal early-type galaxies: single spheroidal/amorphous galaxies but with blue colors ($\approx$ 40% of the sample), disk galaxies ($\approx$ 30% of the sample), and interacting galaxies ($\approx$ 30% of the sample). For very vigorously accreting AGN, classified as Narrow line Seyfert 1 (NLSy1s) host galaxies are spiral (Zhou et al., 2007) or gas-rich disk galaxies with gas enrichment caused by merger (Yuan et al., 2008), whereas lower Eddington ratio accretors like blazars and radio galaxies are located in elliptical host galaxies (Urry & Padovani, 1995).

1.3.3 Spectral Energy Distributions of AGN

Active galaxies emit radiation in all possible wavelength ranges, which makes the continuum emission of Active Galactic Nuclei very complex, as presented in Figure 1.3, adopted from Harrison (2014). The black curve represents the total emission of the source. Starting from the lowest wave frequencies, we observe radio, IR, optical/UV, X-ray, and gamma emission.

AGN radio emission (orange curve in Figure 1.3) is dominated by the synchrotron emission, which is non-thermal and originates from relativistic particles accelerated by the magnetic field. The AGN radio emission component does not contribute significantly to the total radiation flux for radio-loud AGN, and it is even less prominent for radio-quiet AGN. In radio-loud AGN, this radiation mostly comes from a relativistic well collimated jet which is resolved in radio images and can extend far

beyond the host galaxy. The observed effect of the jet presence on the broadband spectrum, however, may depend on the source orientation - strong relativistically Doppler-boosted strong jet radiation can dominate the entire spectrum if the jet is oriented directly towards the observed, as indicated in Figure 1.2. In radio-quiet AGN, the origin of the radio emission is less clear. It may come from the inner hot corona or a very short/non-relativistic jet. Such jets are marginally resolved in some Seyfert galaxies (e.g. Yao et al., 2021).

The major part of the accretion radiation generated by the central engine is absorbed and reprocessed by dust grains and gas in the surrounding medium (emission peaking in the NIR and presented as a red dashed line in Figure 1.3). The near-IR emission originates from reprocessing of emission by the inner dusty/molecular torus, with eventually some contribution from the outer the accretion disk. The mid-IR comes from outer parts of the torus but also the dust located in the polar direction, as seen from the mid-IR interferometric maps (Hönig et al., 2013). Far-IR emission comes from the host galaxy dust, not directly related to AGN activity, and it is particularly strong if the starburst activity of the host (grey line).

The first attempt to explain the shape of the optical and UV cosmological mission (blue dot-dashed curve in Figure 1.3) from the BBB (Big Blue Bump) continuum was the comparison of the thermal emission of accretion disk (Shakura & Sunyaev, 1973) to the optical/UV data (Laor & Netzer, 1989; Shields, 1978). In Figure 1.3) this component is marked with a blue dashed/dotted line. The magenta dashed/dotted line marks the soft X-ray excess seen in many AGN (Done et al., 2012). In Figure 1.3 it is marked as a separate component, but in more advanced models, including the disk and the warm corona, such a single spectral BBB component could even directly extend to soft X-rays (Czerny & Elvis, 1987). The origin of this component is not yet fully set. However, most likely, it is either the warm dissipative corona with the temperature $\sim$ 1 keV (Gierliński & Done, 2004; Petrucci et al., 2020; Różańska et al., 2015), or a result of reprocessing of hard X-rays by the surface of the disk (e.g. Ding et al., 2021). In Figure 1.3 the black continuum line has a gap between the far-UV and the soft X-ray band. This part of the spectrum is unobservable due to our Galaxy's absorption, mostly by hydrogen. The data gap can be shortened by combining the spectra from low and high redshift objects (Laor et al., 1997) to form a composite broadband spectrum. Another way to address the issue was the comparison of photoionization models under assumed SED shape with observed emission lines (Mathews & Ferland, 1987).

The hard X-ray emission is produced by inverse Compton processes (IC) in hot corona (temperature $\sim$ 100 keV) located in the innermost region of the AGN (cyan dotted power-law component in Figure 1.3). Hot corona exact location and its geometry is still under discussion (e.g. Haardt & Maraschi, 1993; Kubota & Done, 2018; Matt et al., 1991) The green dashed line represents the reflection component which includes the scattered component affected by absorption and the cross-section decrease by the Klein-Nishina effect (so-called Compton Hump) and the Kα line peaking at 6.4 keV, which results from photon absorption and reemission.

Various emission processes can be understood by studying the shape of the various components of the continuous spectrum. However, due to different timescales of variability at different wavelengths (i.e. hours/minutes in the X-ray band and days in the optical band), it is challenging to construct the broadband SED for a given source from the data obtained at different epochs or even compare spectra of the same AGN obtained at different times.

The general picture outlined above concentrated on Type 1 sources, unobscured by the dusty torus, and the obscuration modifies the overall SED considerably. Most notably, in Type 2 sources, the BBB

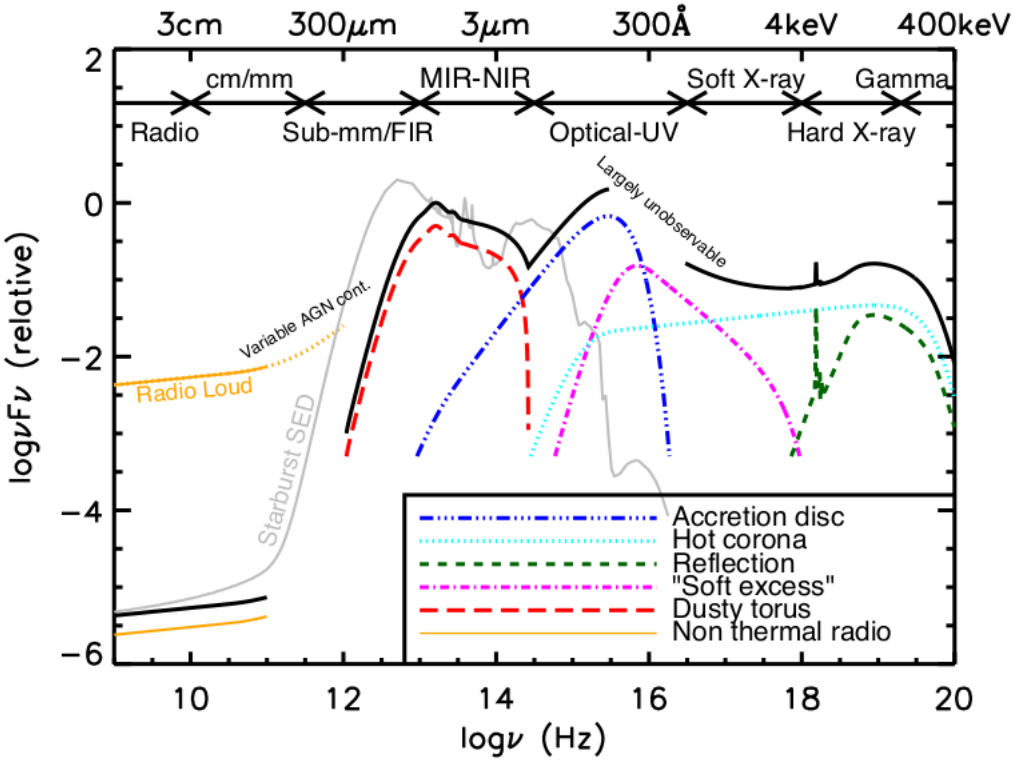

Figure 1.3: A schematic representation of an AGN broadband continuum spectral energy distribution in the different types of AGN. Adopted from Harrison (2014). The main features I describe in Section 1.3.3.

component mostly disappears. Also, the range of Eddington rate contributes to the fact that in source samples, actual SED of sources show considerable dispersion even if only Type 1 sources are selected (e.g. Richards et al., 2006).

1.4 Supermassive black holes connection to the host galaxies

The quasar phenomenon was originally only of particular interest to specialists studying the processes close to the black hole. The size of the black hole is small in comparison with the host galaxy, the mass is also small in comparison with the stellar mass of the host, and the sphere of the dynamical influence onto the host is limited to the host's innermost nuclear parts. Therefore, the phenomenon of AGN was initially not recognized as of importance for the host. Observations, however, have changed this view.

Masses of supermassive black holes correlate with the properties of the host galaxy: black hole mass was found to correlate well with the stellar mass of the bulge (Magorrian et al., 1998), and later statistical correlations were studied between the black hole mass and stellar mass (e.g. Reines & Volonteri, 2015), the bulge luminosity (e.g. Bentz et al., 2009), and stellar velocity dispersion (σ), (e.g. Ferrarese & Merritt, 2000; Ho & Kim, 2014). This relation was initially very surprising since the size of the black hole is nine orders of magnitudes smaller than the size of the bulge, the mass of the black hole is a fraction of a per cent of the bulge mass (Magorrian et al., 1998; Schutte et al., 2019). Thus the dynamical influence of the central black hole does not reach as far as the bulge.

Instead, this may indicate the co-evolution of SMBH with its host galaxy. The physical interaction

between the active nucleus and the host is rather complex (e.g. see Eckert et al., 2021; Kormendy & Ho, 2013). However, all numerical codes of the evolution of the large scale structure contain such a term (see, for example, the EAGLE software (Crain et al., 2015; Schaye et al., 2015) [2]).

The level of galaxy activity varies between objects: from very weak activity (i.e. Sgr A *, Low Luminosity AGN) to quasars, which are the brightest sources currently known and are observed even at distances of $z \gtrsim 6.5$ (Bañados et al., 2018; Mazzucchelli et al., 2017; Wang et al., 2021). The activity of the galaxy itself evolves. During periods of activity, a black hole is fed by an accretion disk. Thus, studying active galaxies is important for studying the evolution of all galaxies. With the coverage of the entire spectrum range in AGN observation, we can understand the physics behind the multiband properties (Padovani et al., 2017).

1.5 AGN important timescales and the character of variability

1.5.1 Theoretical timescales

There are a few kinds of timescales that are important in different galaxy/AGN evolution stages. In this section I summarize them assuming a Keplerian, geometrically-thin and optically-thick disk for the timescales related to the disk accretion. I also describe here the robust estimation of the timescale of the chemical evolution of the host galaxy.

- **Light travel time,** $t_{\rm light} = \mathbf{R/c}$,

  is the most basic timescale, and it is used to express the distance R to the given part of the extended source from its central parts (e.g. in light days) or to find the size of an object.

- **Dynamical timescale,** $t_{\rm dyn} \sim 1/\Omega_K$,

  is the inverse of the angular frequency for gas on an approximately Keplerian orbit around the SMBH. It is also a timescale of the propagation of the sound waves in the vertical direction to restore the hydrostatic equilibrium.

- **Thermal timescale,** $t_{\rm th} \sim \alpha^{-1} t_{\rm dyn}$,

  is the timescale needed to restore the thermal equilibrium, and it depends on the viscous parameter α, i.e. the assumption about the viscous forces.

- **Viscous timescale,** $t_{\rm visc} \sim \alpha^{-1}(H/R)^{-2} t_{\rm dyn}$,

  is the timescale of an inflow of the material in the Keplerian disk.

- **Chemical evolution timescale,** $t_{\rm chem} \sim M_{gas}/SFR$,

  which can be defined as the timescale of gas conversion to stars using the star formation rate (SFR). This can be evaluated assuming that a starburst at the nucleus outskirt is finally responsible for the nuclear activity, $M_{gas} \sim 10^8 M_\odot$, and assuming SFR $10 M_\odot$ yr^{-1} (Combes, 2001), we get $\sim 10^7$ years. However, the star formation can also take place in the outer part of an accretion disk, which becomes self-gravitating, particularly for larger black hole masses, and these can lead to rapid star formation and chemical enrichment, as already proposed by Collin and Zahn (1999).

[2] https://eagle.strw.leidenuniv.nl/

As an example, we estimated different timescales for an exemplary AGN. We assume the black hole mass $\log M = 7$, $\alpha = 0.01$ (the viscosity parameter introduced by Shakura and Sunyaev (1973)), H/R = 0.1 for the accretion disk, H/R = 1/3 for the BLR (the ratio of the thickness of the region to its radius). As distances, we adopt the following values: for accretion disk 1 ld, for BLR 10 ld, for torus 0.1 pc, and the host galaxy 1 pc. This last quantity comes from the general assumption that the inflow of the material from the host takes place where the central black hole stops dominating the galaxy's gravitational field. The approximate expression is GM/V_∞^2 (Combes, 2001), where V_∞ is the typical stellar velocity dispersion ≈ 200km s^{-1}.

Table 1.1: The timescales for an exemplary AGN.

	AD	BLR	torus	host
$t_{\rm light}$ [days]	1	10	119	1191
$t_{\rm dyn}$ [years]	0.11	3.63	149	4716
$t_{\rm th}$ [years]	11	...	...	...
$t_{\rm vis}$ [years]	1147	...	...	...
$t_{\rm chem}$ [years]	...	...	...	$\sim 10^7$

The light travel time we can calculate for all 4 components from Table 1.1: accretion disk, BLR, dusty torus and host galaxy, since this value is used to measure the distance from SMBH. This timescale (in the form of time delay in the emissions at two different wavelengths - i.e. between Hβ luminosity and continuum luminosity at 5100Å) is used to measure the size of the Broad Line Region. To characterize the accretion flow in the accretion disk, we use three timescales: dynamical, thermal and viscous. To characterize the timescale of changes in the inner part of the host galaxy, directly feeding the black hole, we can refer to two timescales. The inflow of the new material can be in the dynamical timescale (see Combes, 2001, for a review), if the dynamical instabilities in the stellar material sets in. The second timescale is the timescale of the chemical evolution of the material available for feeding the black hole.

1.5.2 AGN stochastic variability

AGN are variable in all energy bands, although the fastest variability is seen in the X-ray and gamma-ray bands. The basic variability mode is aperiodic (stochastic) (e.g. Krishnan et al., 2021, and the references therein). It is best studied in the X-ray band (McHardy et al., 2006; Mushotzky et al., 1993) and in the optical band (e.g. Giallongo et al., 1991; Stone et al., 2022). The power spectrum of a light curve is generally of a power-law shape but with (eventually) some breaks pointing towards a possible connection with the theoretical timescales. However, this connection is not yet well understood. The frequency break in the hard X-ray band corresponds to the timescale of the order of a day (e.g. McHardy et al., 2006), while in the optical band, it is generally of the order of 300 days (Kozlowski, 2016). Optical variability is generally believed to be linked to the thermal timescales (Kelly et al., 2009; Ruan et al., 2014; Siemiginowska & Czerny, 1989).

There are systematic searches for periodic signals since any sign of periodicity convolved with the stochastic signal could indicate a presence of a binary supermassive black hole, as shown by recent searches (Bartos et al., 2017; Charisi et al., 2016; Foord et al., 2022). Apart from the stochastic variations, other, more regular variations were detected in AGN.

1.5.3 Microquasars

X-ray binaries contain a compact object which accretes matter from a companion star. Microquasars are the subclass of X-ray binaries in our Galaxy. The name 'microquasar' comes from the similarities to quasars (Mirabel, 2010). Due to microquasars-quasars similarities, microquasars are important objects to examine.

The basic physical mechanism of the energy dissipation and emission of radiation in microquasars is the same as in quasars, but due to the black hole mass being smaller by many orders of magnitude, the timescale of luminosity changes, thermal/viscous timescales are much shorter than for AGN. For AGN with the black hole of $10^7 M_\odot$ the evolutionary timescales are rather hundreds/thousands of years (see Table 1.1), whereas for microquasar with the black hole mass of $10 M_\odot$ it is minutes (e.g. GRS 1915+105 Janiuk and Czerny (2011).) Because of a much shorter timescale, we can observe the whole evolution of the outburst and scale this behaviour onto sources with higher black hole masses. This is important in the context of this thesis, as a model of accretion disk instabilities can be conveniently tested across the whole mass scale.

1.5.4 Quasi-Periodic Oscillations

Several classes of the quasi-periodic oscillations are frequently observed in Galactic X-ray sources, but on rare occasions, such a quasi-periodic oscillation (QPO) is seen in AGN, with the best example seen in RE J1034+396 (Gierlinski et al., 2008; Hu et al., 2014). This source shows regular, almost sinusoidal changes of the X-ray luminosity in the timescale of hours. The nature of these variations is not clear, but the most likely model is the precession of the inner ADAF flow, dominated by the strong magnetic field (Ingram et al., 2009).

1.5.5 Quasi-Periodic Eruptions

Quasi-Periodic Eruptions (QPEs) are high-amplitude outbursts with peculiar short timescale, symmetric flares, and flare separation about 10 times longer than the flare duration. The first object of this type (GSN 069) was found by Miniutti et al. (2019) in 2MASX J01190869-3411305 with the nine hours period. Later, more sources of this type were found, like RX J1301.9+2747 (Giustini et al., 2020) and 2MASXJ0249 (Chakraborty et al., 2021) (both by using archival data) or eRO-QPE1 and eRO-QPE by Arcodia et al. (2021). The origin of this phenomenon is not yet well understood. The phenomenon that lasts in a similar timescale ($\approx$ hours) is QPO. However, the shape of the outburst is different, as shown in Figure 1.4. QPOs show the sinusoidal shape of the luminosity changes, whereas QPEs are characterised by the short flare duration and gaps between outbursts.

Various models have been proposed, mostly focusing on two main scenarios: the orbital phenomenon or intrinsic changes of the accretion flow. As orbital phenomena, gravitational lensing was proposed (Ingram et al., 2021), nearly missed tidal disruption event (TDE) of orbiting star (King, 2020) or star which orbits and impacts the accretion disk (Suková et al., 2021; Xian et al., 2021). As intrinsic phenomena, changes involving accretion instabilities are taken into account. For example, radiation pressure instabilities with area of occurrence nearby black hole (Pan et al., 2022; Sniegowska et al., 2020; Śniegowska et al., 2022a; Śniegowska et al., 2022b), dynamical instabilities due to disk tearing (Raj & Nixon, 2021) or magnetic instabilities (Ripperda et al., 2022). The characteristic properties of host galaxies in which QPEs were observed are the rather lower mass of supermassive black

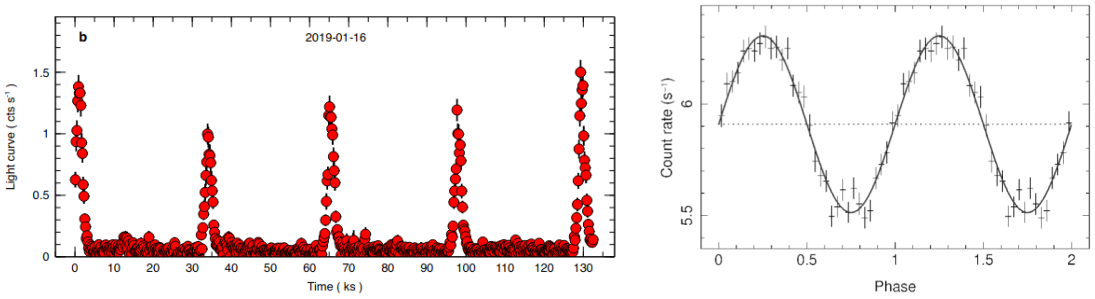

Figure 1.4: Left panel: the Chandra background-subtracted 0.4-2 keV light curve of QPE phenomenon (time binned of 500s) adapted from Miniutti et al. (2019). Right panel: the XMM-Newton light curve of QPO phenomenon present in RE J1034+396 adapted from Gierlinski et al. (2008).

hole ($\sim 10^{5-7} M_{\odot}$) and the lack of broad emission lines in the optical part of the spectrum.

This phenomenon is addressed in two of the papers constituting my PhD Thesis (Paper I and II) where we consider the possibility of explaining this phenomenon by radiation pressure instability.

1.5.6 Changing Look AGN

Introducing the term Changing Look AGN

The name 'Changing Look AGN' was originally used to identify a subset of the phenomena measured in X-rays (Bianchi et al., 2005; Matt et al., 2003). Those objects show the transition between the transmission and the reflection-dominated spectral state, i.e., passing from a typical obscured Seyfert 2 state to a Seyfert 1 state or in the opposite direction. It seemed like, at least in X-rays, the dusty torus disappeared or reappeared. Nowadays, this term refers also to quasars in which, on relatively short time scales (order of a few years), we observe the disappearance or the appearance of broad emission lines in the optical band.

Development of the field

LaMassa et al. (2015) found in SDSS J015957.6+003310 the disappearance of the broad emission lines and decreased luminosity in the g-band between SDSS spectra from 2001 and 2010. The X-ray observations (Chandra and XMM-Newton) for this source showed no significant change in the spectral shape (the source just dimmed (see Figure 5 in LaMassa et al., 2015)). It is one of the arguments to rule out the obscuration scenario for this source (another one is, for example, too long crossing-time timescale (see LaMassa et al., 2015)).

The variations of the broad emission lines were noticed in the past, for example, in NGC 7603 (Tohline & Osterbrock, 1976) or in NGC 1566 (Alloin et al., 1986). Recently, bigger samples of those objects are being collected (Graham et al., 2020; Green et al., 2022; López-Navas et al., 2022; MacLeod et al., 2019; Ruan et al., 2016; Yang et al., 2018). It shows that the CL AGN phenomenon is not that extraordinary, and the lack of larger samples results from a limited ability to reobserve AGN. Selection by multiple observations of the sources and the dense follow-up observation of sudden brightening/dimming events are of key importance to get insight into physical processes which can be responsible for flux and spectral changes in CL AGN. Trakhtenbrot et al. (2019) and Ricci et al. (2021) using data from X-ray monitoring by SWIFT/XRT, NICER, and XMM-Newton as well as optical and UV photometry and spectroscopy, obtained with ATLAS, ASAS-SN, and SWIFT/UVOT, have shown

in the example of 1ES 1927+654 how much information we can obtain by using the broadband and follow-up observations for this kind of objects. 1ES 1927+654 was observed with very dense follow-up optical spectroscopy, and $\approx$ 2 months after the increase of UV flux, the broad components of Hα and Hβ appeared. In the X-ray band, Ricci et al. (2021) noticed peculiar behaviour: decreasing of flux and after a few hundred days rebrighrening, to stage with higher flux than before the event. What is even more interesting, recent studies by Laha et al. (2022) show that this source came back to its pre-event stage in optical, UV, and X-ray bands.

We cannot explain CL AGN episodes by changing the viewing angle (i.e., the orientation of the AGN to the observer) - we, as observers, remain in the same place, and the precession of the BLR would require a longer timescale, so most likely the transition is due to some intrinsic change close to the black hole. Moreover, CL AGN are also characterised by no radio detection, and this excludes jet-related variability in them (e.g. MacLeod et al., 2019). In the literature, objects are examined in the optical, ultraviolet, or X-ray range, among others. However, few objects were tested in more than one of these ranges, for example, 1ES 1927+654 (Ricci et al., 2021; Trakhtenbrot et al., 2019). To understand the nature of changes in AGN, this problem needs to be studied in different wavelength bands.

The phenomenon of CL AGN challenges the current theory of standard disk accretion flow. On the one hand, the standard theory does not predict any significant changes in the accretion process in timescales shorter than hundreds of years. On the other hand, the observed phenomenon implies such changes, affecting the energy output from the nucleus regulating the host evolution. From pilot population studies (e.g. MacLeod et al., 2019), we know that this extreme variability of AGN on short timescales is a property of AGN with a low Eddington ratio. This topic is discussed in two of the papers being part of the presented Thesis (Paper I and Paper II).

Proposed models

Several mechanisms related to black hole accretion have been proposed that could possibly explain such phenomena (Noda and Done (2018) - the temporary disappearance of the warm corona; Sniegowska et al. (2020) and Śniegowska et al. (2022a) - radiation pressure instability; Ross et al. (2018) - shocks caused by magnetic fields threading the inner disk; Dexter and Begelman (2019) and Scepi et al. (2021) - reversing magnetic field or supermassive black hole binaries interaction suggested in Wang and Bon (2020)). As we have presented in Figure 1.5, proposed mechanisms differ from each other. On the left side, we present components in Type 1 state for each model, whereas on the right, in Type 1.9 state, in which broad lines almost disappear. We show the most extreme possible changes for CL AGN. However, not all CL AGN show this extreme kind of transition; for example, HE 1136-2304 (Parker et al., 2016) source has shown a transition from a Type 1.9 to Type 1.5. From the top in Figure 1.5: the first panel shows the model by Noda and Done (2018), in which authors suggest the explanation for the CL behaviour in the source Mrk 1018 caused by the hydrogen ionization disk instability. Warm corona produces soft excess that possibly evaporates into ADAF (advection-dominated accretion flow) or ADAF condensates. Soft excess component changes the most (see Figure 1 therein) compared to other components, and it may indicate that soft excess may be responsible for the disappearance of the broad emission lines. However, not all observed CL AGN sources can be explained by this scenario. For example, the source NGC 1566, notable for numerous CL outbursts, does not show the presence of the warm corona component before the outburst (Parker et al., 2019) and this source cannot be

explained by the same mechanism as Mrk 1018 (Noda & Done, 2018).

The next panel represents a model by Sniegowska et al. (2020), in which we propose the explanation for the repeated CL behaviour in well-monitored sources: NGC 1566, NGC 4151, and NGC 5548 and suggest that the unstable part of the disk, which is responsible for changes, due to instabilities in radiation pressure increases or decreases vertically. In this model, we consider a narrow, unstable disk surrounded by an outer stable disk and constrained by inner ADAF and reproduce the time scales and the amplitudes of the outbursts. This work is shown in Chapter 2. Recently, we explored a more complex model based on the same physical mechanism, using GLADIS code (Janiuk, 2020). In comparison to the previous model, we added the mass exchange between the accretion disk and corona and took different mass evaporation mechanisms into account and the short outer radius of the disk. This work is shown in Chapter 3.

The third panel in Figure 1.5 shows a model proposed by Ross et al. (2018), in which authors report four spectra for one object - SDSS J110057.70-005304. This source changed its spectral type (with the dramatic change of the UV continuum, see Figure 2 therein) and returned to the previous state in 20 years. The authors suggest that the change may be caused by stochastic variation in the mass supply or a shift in the local magnetic field configuration.

The last panel shows the model proposed by Scepi et al. (2021) for 1ES 1927+654 (Fig. 1 therein), which explains changes in X-ray and UV/optical part with a magnetic flux inversion in a magnetically arrested disk. The inversion of polarity is driven by accretion. It causes the disappearance of the corona (which is seen as dimming in the X-ray band), and the increase of the UV flux may be due to the higher efficiency of the disk accretion. Once the polarity is inverted, a magnetically arrested disk and corona are recreated, which causes an increase of flux in the X-ray band and a decrease in UV. This model reproduces the behaviour of 1ES 1927+654 from observations.

Vertical arrows represent the sign and strength of the magnetic field. The geometrically thick disk represents radiatively inefficient accretion flow with the presence of corona (left panel of Fig. 1 in Scepi et al. (2021)), whereas the geometrically thin disk represents radiatively efficient accretion flow (right panel of Fig. 1 in Scepi et al. (2021)).

The models we present in this figure are just part of the proposed mechanisms. The problem with testing models is generally hindered by the fact that there is likely more than one mechanism that can lead to the observed changes (i.e., NGC 1566 does not show the presence of the warm corona before the outburst, so we cannot explain this changes by the model proposed by Noda and Done (2018)). It is assumed that in some objects, the changes may occur spontaneously in the flow close to the black hole. In some objects, those changes may be the result of a stellar rupture in the vicinity of black hole tidal disruption events (TDEs; Chan et al., 2019; Merloni et al., 2015), and in other objects, the change may be apparent, caused by the temporary absorption of gas by clouds in the host galaxy, possibly in the area of the dusty torus (Kokubo & Minezaki, 2020). By now, for some objects, we have already noticed numerous outbursts in the optical band (like in NGC 1566 (e.g. Alloin et al., 1986; Oknyansky et al., 2019), NGC 4151 (Guo et al., 2014), or the most detailed examined one - NGC 5548 (e.g. Di Gesu et al., 2015; Kriss et al., 2019, and refs. therein). The open issue is still how common are objects with repetitive outbursts. Another open issue is that changes in CL AGN may be caused not by just one mechanism. This opens possibilities to model and explore different scenarios, which may provide new insights into AGN physics.

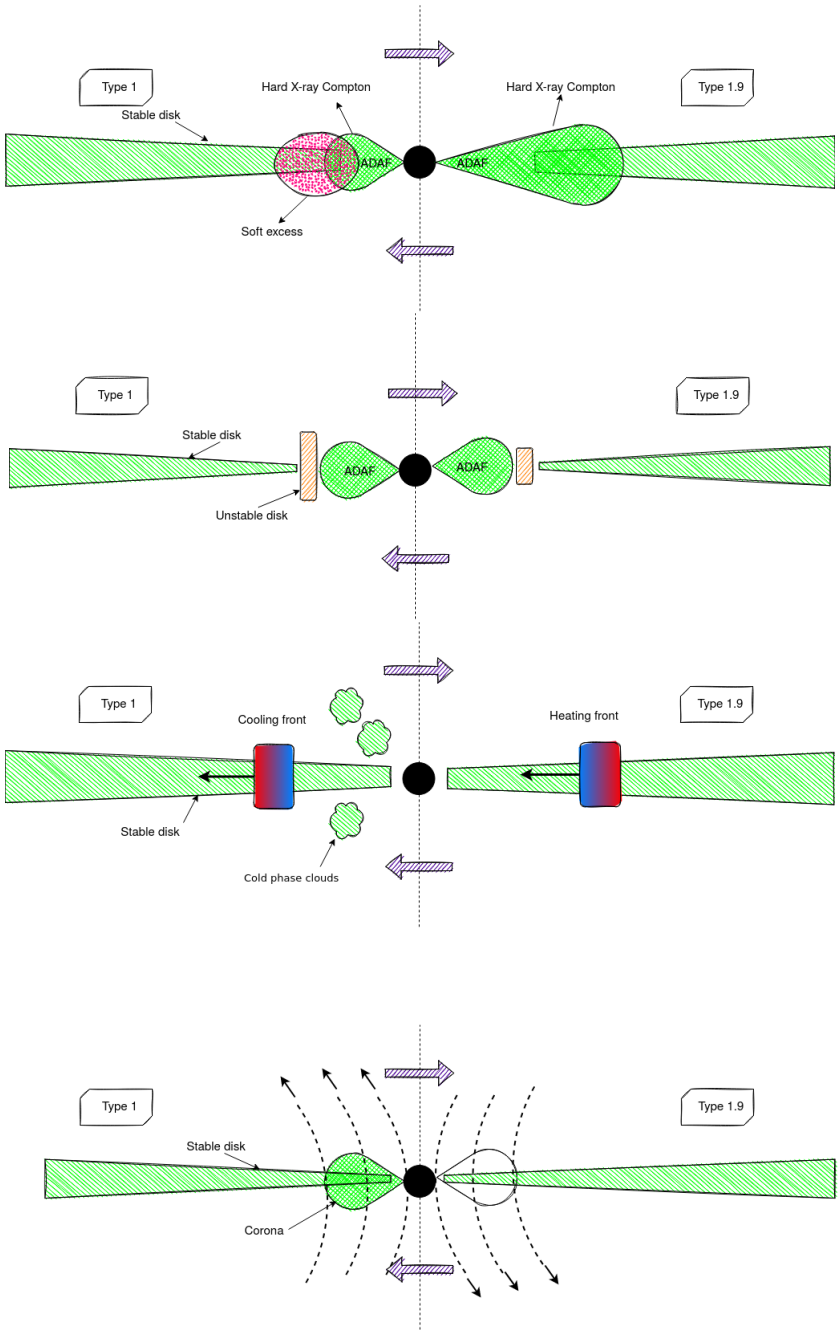

Figure 1.5: The schematic representation of time evolution of chosen models. On the left, we present components in Type 1 state for each model, whereas on the right, in Type 1.9. Violet arrows represent the possibility of transition between both states. From the top: representation of model readapted from Noda and Done (2018) based the temporary (dis)appearance of the warm corona, representation of model readapted from Sniegowska et al. (2020) based on radiation pressure instabilities, representation of model readapted from Ross et al. (2018) based on magnetic field shocks, which causes threading the inner disk, and representation of model readapted from Scepi et al. (2021), which is based on reversing magnetic field.

1.6 The global evolution of the host galaxy

The evolution of galaxies involves gravitational interaction and merging, leading to gas accumulation in the galaxy central regions and a burst of star formation. The central black hole's mass during this process grows, and the galaxy is active for part of the time. Since only a small fraction of galaxies are highly active, the activity period (the AGN duty cycle) is relatively short, $\sim 10^7$ yr, corresponding to the current fraction of active sources 10^{-3}(e.g. Wang et al., 2006).

However, AGN space density is not constant over time. The number density of quasars was much higher in the past, at redshifts close to 2, as seen in Fig. 1.6 (red stripe and the blue line). The corresponding duty cycle is much higher at that epoch, around 10^{-2} (Shankar et al., 2010; Wang et al., 2006) so the usually adopted timescale for the active quasar stage is 10^8 yr.

The same strong redshift-dependent distribution is observed for starforming galaxies, as presented in Fig. 1.6. AGN (marked in red) and star formation (marked in cyan) distribution peak at similar epoch z $\sim$ 2-3 and then decreases. Moreover, the shape of both distributions look similar and suggest that BH and galaxy growth are connected. The rise of the number of quasars with redshift was known for a long time, but it was a surprising result when the plot of the starburst rate was presented for the first time by Madau et al. (1998). The consequences of this trend for the metallicity evolution of the galaxy content were immediately recognized in the original paper. It fits well the global image. The star formation episode, at least in the quasar stage, must come first since the stellar winds provide the ultimate source of the material which fuels the black hole at the galaxy center. Numerous supernova explosions must have happened before we see an active quasar since even high redshift quasars are rich in heavy elements like C, N, O, and Fe. The clear correlation of the AGN distribution with redshift with the SFR, as well as the relation between the black hole mass and the starlight mass discussed in Section 1.4. show the tight connection between the central black hole and its host.

In the galaxy-black hole co-evolution scenario, the galaxy affects the growth of the black hole by controlling the amount of gas that falls onto the black hole. The black hole affects the host galaxy by controlling the amount of gas available for stars to form. Simulations (e.g. Barai, 2020) show that star formation is quenched when the black holes grow massive and this phenomenon is very likely accompanied by powerful outflows. Cosmological simulations require growing supermassive black holes (AGN) to regulate star formation (e.g. Crain et al., 2015; Ruthven Ward et al., 2022; Schaye et al., 2015).

1.7 High Eddington sources

High Eddington sources are of particular interest for the galaxy evolution since, during such a phase, the central black hole grows fast. The nearby sources called attention since their properties differed from the typical Seyfert 1 properties. First, a particular class of sources was identified in the optical band, where strong low ionization lines with a Lorenzian-like relatively narrow profiles were seen, together with not very prominent [OIII]$\lambda\lambda$4959,5007 (in comparison to Hβ) doublet and strong contribution of the Fe II. These sources were not Seyfert 2, so a new name of Narrow Line Seyfert 1 (NLSy1) was introduced by Osterbrock and Pogge (1985). It was later established that also X-ray properties of NLSy1 differ systematically from Seyfert 1 galaxies in the X-ray band since they show much more prominent soft X-ray excess and overall steeper (redder) X-ray slope (Brandt et al., 1997). More systematic statistical studies of nearby AGN were done with the use of the Principal Compo-

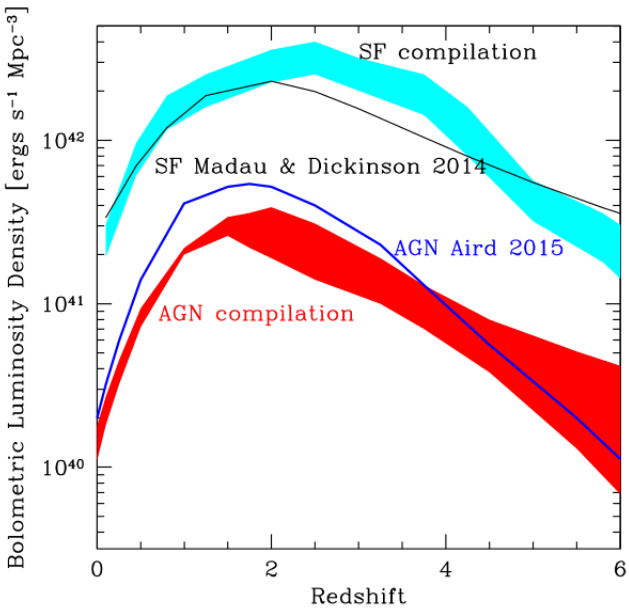

Figure 1.6: Adapted from Fiore et al. (2017). On red the evolution of the AGN bolometric luminosity density marked, with overplotted in dark-blue similar determination done by Aird et al. (2015). As cyan, star formation luminosity density estimated from Santini et al. (2009), Bouwens et al. (2011), Gruppioni et al. (2015), and Bouwens et al. (2015), with overplotted determination of average SF luminosity density done by Madau and Dickinson (2014).

nent Analysis (PCA), and they showed the overall spectral properties are categorised via Eigenvector 1 (Boroson & Green, 1992), with the Eddington ration being the most likely driver.

In quasars, in the high ionization lines (like CIV or SiIV), we frequently notice an indication of outflows because of asymmetries on the blue part of emission lines (e.g. Brotherton et al., 1994). These sources also contain the strong contribution of Fe II and Fe III. PCA technique was also advantageous for broader sample studies, including quasars (Panda et al., 2017; Shen & Ho, 2014; Sulentic et al., 2000). An observational division between low and high Eddington ratio sources seems to depend on mass, which the line width limit set at 2000 km s^{-1} for NLSy1 (Osterbrock & Pogge, 1985) and 4000 km s^{-1} (Sulentic et al., 2000) for quasars, with systematically higher black hole masses than Seyfert 1 galaxies.

1.7.1 Eddington ratio measurements

The basic and most appropriate method to estimate the Eddington ratio is to measure the bolometric luminosity of the source by direct integration of the broadband SED, to measure the black hole mass, and to use Equation 1.5. If the full SED is not available, L_{BOL} is frequently estimated from monochromatic luminosity by using the color-correction (Netzer, 2019). The significant source of uncertainty in this procedure comes from the measurement of the black hole mass. In general, estimation of the black hole mass of the source is more complex than the computation of its bolometric luminosity.

To determine the black hole mass, we can use the virial relation for the BLR, which is the relation between the black hole mass, the distance, and the velocity as in Keplerian motion. The velocity is represented in observations by the line width, the distance by the delay of the line with respect to the continuum. If the line delay is not measured, we use the statistical relation between the

BLR radius and the luminosity of the source (e.g. Bentz et al., 2013). All uncertainties connected with the underlying assumptions in this procedure are contained in the so-called virial factor. This virial factor f is the factor that depends on the geometry, kinematic, and the viewing angle of the BLR to the observer. Mostly, black hole masses are calculated under assumption $f \approx 1$ since we do not have direct information about the structure of the BLR. However, this assumption may cause under/overestimation by a factor of 2-3, as Mejía-Restrepo et al. (2018) pointed out.

The small viewing angle can cause considerable underestimation of the black hole mass. An independent estimate of the viewing angle or the mass measurement with the viewing-angle independent method can be particularly useful. One of such methods is the use of spectropolarimetry to Type 1 sources; since then the comparison of the emission lines in natural light and the polarized light. For example, in the paper by Śniegowska et al. (2022c) using the observations performed with VLT/FORS2, we were able to confirm the high Eddington accretion in three sources selected as super-Eddington for monitoring at the basis of standard mass measurement.

1.7.2 Eddington ratio and the metallicity

A very surprising property of the AGN is the apparent strong relation between the metallicity of the gas constituting the BLR and the Eddington ratio. Observationally, it is clearly seen in the PCA analysis (see Section 1.7) where the Eigenvector one is mainly driven by the Fe II/Hβ ratio of the equivalent widths. As I discussed in Section 1.5, AGN change their luminosity continuously, in different timescales, and it is a priori unclear why the change of the luminosity should couple to the chemical evolution of the inflowing gas and consequently enhance metal content. It is easy to imagine that a strong circumnuclear outburst enriches the material and later causes an epoch of the vigorous inflow towards the black hole. However, after that period, when the accretion rate drops, there is no obvious reason why the metal content would drop as well. Thus, the correlation between the metallicity and the Eddington ratio must be carefully studied, and that requires reliable metallicity measurements.

1.7.3 Metallicity determination

The line ratios by themselves, like Fe II pseudo-continuum in the optical band to the broad component of Hβ, do not necessarily determine the luminosity directly since they measure the number of ions at a given energy state, which in turn depends not only on the number of atoms but also on the ionization state of the material, which is a function of the radiation field, and local density. Therefore, computations involving the modelling of the ionization state of the material are necessary to conclude the actual metallicity of the plasma.

The studies of the metallicity are broadly performed in the context of galaxy evolution since the relative chemical abundances, their spatial distribution, and their relation to the galaxy properties change with time and are of key importance for modelling the galaxy evolution (Maiolino & Mannucci, 2019). Metallicity determination is based on complex line ratio diagnostics, frequently used in the parametric form, and different methods are applied to stellar spectra and the gaseous phase of the medium.

In the context of AGN, the computations of the predicted line intensities for a given plasma and incident radiation parameters are usually performed with complex codes, like CLOUDY (Ferland et al., 2017). Such a code solves the ionization balance (Saha equation), the thermal equilibrium for the plasma, and finally, the radiative transfer. The code parameters usually adopted are the local

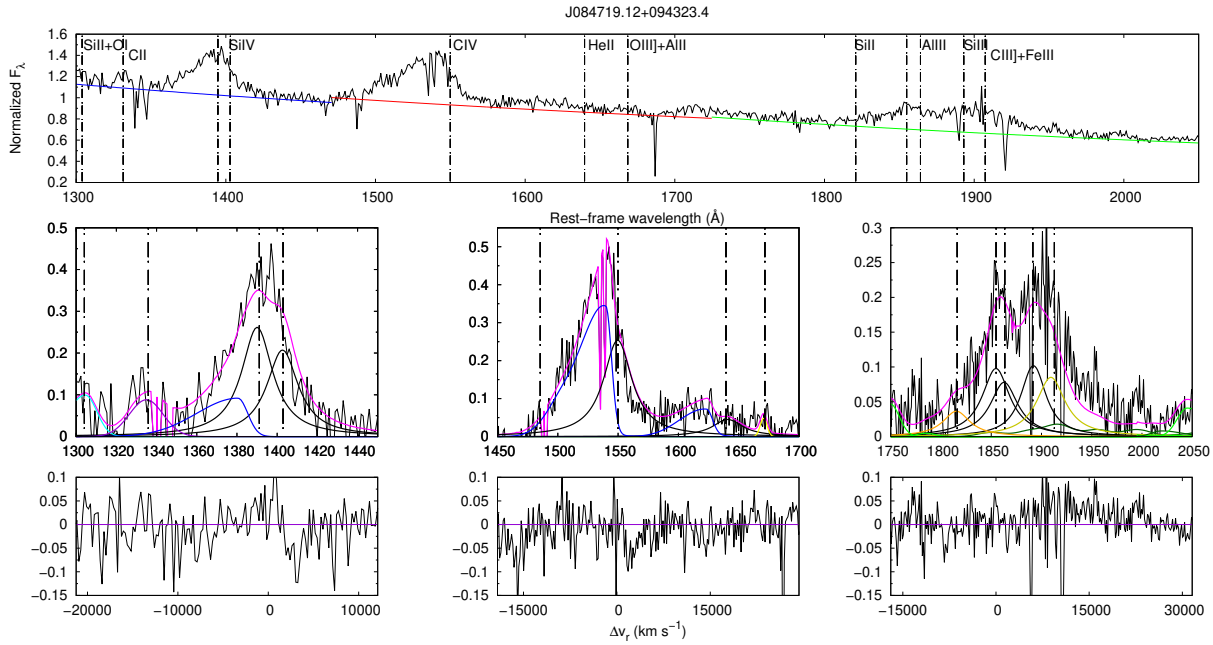

Figure 1.7: The exemplary spectrum (of SDSS J084719.12+094323.4) adapted from (Śniegowska et al., 2021). Top panel: Rest-framed spectrum with local continuum colored lines (blue, red and green) and dashed vertical lines marking emission lines along the wavelength. Bottom panel: the fits after continuum subtraction for the three ranges: SiIVλ1397, CIVλ1549, and CIII]. The magenta line marks the fit of the whole spectrum including all components. The continuous black line marks the broad component: SiIVλ1397, CIVλ1549 and AlIIIλ1860, whereas blue one marks the blueshifted components. In the left bottom panel, the light blue line marks the contribution of OI + SIIλ1304, and the violet line corresponds to the CIIλ1335 emission line. In the middle panel, which is CIVλ1549 region, NIV]λ1486 is marked by a light blue line, while the gold line corresponf to the OIII]λ1663 + AlIIλ1670 blend. In the right panel, which is λ1900 blend range, Fe III and Fe II pseudo-continua are shown as dark and light green lines respectively. Violet lines mark the NIII]λ1750, the orange one corresponds to the SIIIλ1816 and the gold one to the CIII]λ1909 line. In the lower panels the residuals are shown, in radial velocity units km s^{-1}.

density, the metallicity, the shape and intensity of the incident flux. Code CLOUDY was used to show that indeed the quasars, corresponding to the extreme population along the Eigenvalue 1, with the strongest relative Fe II emission and the highest accretion rate, require supersolar metallicity (Panda et al., 2018).

Fe II emission, however, is not the most sensitive metallicity determinant. Other line ratios, particularly in the UV band easily accessible for distant quasars, are much more reliable in disentangling the BLR parameters: the BLR gas density ($n_{\rm H}$), the ionization parameter (U) or metallicity Z (e.g. Marziani et al., 2020; Negrete et al., 2012; Śniegowska et al., 2021). I discuss this issue in more detail since this is tightly related to Paper III of my Thesis.

1.7.4 Diagnostic ratios

Selection of the lines most suitable for plasma diagnostics, including the metallicity, is done by theoretical modelling of the line ratios under different conditions. Such modelling requires complex modelling of the plasma, done with the use of the codes like CLOUDY (mentioned already in Sect. 1.7.3 since the ionization state of the material depends on all atomic transitions, not just a single ion of interest,

and the density, incident radiation, etc. Metallicity or density indicators are never perfect, and the full modelling is always needed.

I present the typical UV spectrum of high accreting AGN in Figure 1.7. The advantage of using the UV range to diagnose the physical condition is the variety of emission lines compared to, for example, the optical range (with the prospect of using the Fe II/Hβ ratio.)

In the UV range, three groups of extremely useful diagnostic ratios are defined in the literature (e.g. Martínez-Aldama et al., 2018; Negrete et al., 2012).

- The ratios including CIV, like CIV/SiIV+OIV] or CIV/HeII are used as metallicity indicators (Shin et al., 2013; Śniegowska et al., 2021). In Śniegowska et al. (2021), we show with CLOUDY photoionization code (Ferland et al., 2017) simulations that CIV/SiIV+OIV] increases monotonically with the metallicity range and CIV/HeII monotonically decreases between $\approx$ 1-100$Z_{\odot}$ (see Figure 3 in Śniegowska et al., 2021).

- The ratios AlIII/SiIII] and SiIII]/CIII] are sensitive to density, since AlIII and CIII] are intercombination lines with a well defined critical density (Hamann et al., 2002).

- The ratios SiIII]/SiIV, SiIIλ1814/SiIII], and SiIIλ1814/SiIV are sensitive to the ionization level, since the same element with different ionic species is involved in those ratios.

Other intensity ratios show more complex dependence. They depend on metallicity Z, but the dependence is affected by ionization parameter U or density $n_{\rm H}$ (Marziani et al., 2020), which causes degeneracy. Thus, to estimate Z, we have to consider more than one intensity ratio.

Some dependence on the other parameters is still present, so careful studies must be based on line ratio computations. In Śniegowska et al. (2021) (Paper III in this Thesis), we saw that the selected line ratios still had some dependence on the other two parameters, U and $n_{\rm H}$, so the conversion from the line ratios measured in a sample of objects to metallicity parameter Z is not unique, and therefore final errors on metallicity determination are significant. Nevertheless, for a sample of 13 high Eddington ratio high redshift quasars with good UV spectra, we obtained a significantly supersolar metallicity, Z up to $\approx 20-50Z_{\odot}$.

1.7.5 Implications for quasar structure evolution

The relation between the Eddington rate and the metallicity does not have a clear explanation yet. The evolutionary timescale for the host may be longer than the epoch of the high Eddington rate phase, particularly for nearby AGN. Therefore, suggested explanations look for a mechanism closer to the black hole.

Gaskell et al. (2022) suggested that the enhanced amount of heavy elements come from the simple fact that the dust present in the direct vicinity of an active nucleus is efficiently evaporated by the enhanced radiation during the brightening phase, particularly due to the presence of copious UV photons from the soft X-ray excess.

The other mechanism could be the efficient star formation in the direct vicinity, perhaps in the outer part of the accretion disk itself (e.g. Collin & Zahn, 1999). Repeated supernova explosions in the inner AGN disks were already suggested by Lin (1997). Jermyn et al. (2021) found in their stellar evolution models that stars in an AGN environment may rapidly become massive (M > 100M$_{\odot}$) and

affect the evolution of AGN metallicities. Those massive stars, after a short evolution, explode as core-collapse supernovae and enrich the disk with metals (Cantiello et al., 2021). The tentative selective enhancement of Al to C found in Śniegowska et al. (2021) is consistent with the supernovae scenario where such excess can be produced.

The active phase in the galaxy lasts $\approx 10^5$ years (Husemann et al., 2022; King & Nixon, 2015; Schawinski et al., 2015). The timescale estimate by Schawinski et al. (2015) is based on the light travel time across massive galaxies and the observed fraction of X-ray-selected AGN without AGN-photoionized narrow lines. Similarly, the timescale estimate of a single AGN event by Husemann et al. (2022) is based on the resolved size of the Extended Narrow Line Region, and from their sample they get a similar mean value, and in addition, an interesting scaling with the black hole mass. This timescale is much shorter than discussed in Section 1.6, and it is much too short for the black hole mass to grow. It implies that the full activity cycle consists of many shorter activity periods separated by the quiet state of the nucleus. As argued by Schawinski et al. (2015), this is the basic reason why the observed correlation between the host properties and the AGN is not strong, as discussed by Hickox et al. (2014).

Radiation pressure instability discussed in Paper I and II in the context of fast variations is capable of explaining timescales of the order of 10^5 yr if the whole disk is considered, that is, the R_{out} is set at value large enough to allow the instability to develop freely. Such timescales were derived in several papers (e.g. Czerny et al., 2009; Grzędzielski et al., 2017). Long ago, it was noticed that another instability - ionization instability - can also give similar timescales if the viscosity parameters are well adjusted, and such a model can reproduce the quasar luminosity function (Siemiginowska & Elvis, 1997).

However, now such short $\approx 10^5$ yr timescales of the AGN event should be reconciled with the enhanced metallicity during the active period. In Paper III (Śniegowska et al., 2021) I showed that the metallicity values determined for the BLR of selected high Eddington ratio quasars are extraordinarily high, even in comparison to the highest Z value detected in the molecular cloud in their host galaxies, $\approx$ 5 solar (Maiolino & Mannucci, 2019). Similar results has been derived from different diagnostic ratios, like NV/CIV (Hamann & Ferland, 1999) or HeII/CIV and CIV/SiIV+OIV] (Martínez-Aldama et al., 2018). Therefore the conclusion of Paper III seems reliable: there is a connection between high metal content and high Eddington ratio.

It is probably difficult to modify the metal content in BLR in such a short timescale as 10^5 yr. It is not clear that stars, even very massive, can evolve that fast. Removal of the metal-rich gas is simpler, and this can be done by outflow.

Wang et al. (2012) found a correlation between metallicity and the energetic outflow in quasars. Shin et al. (2017) analysed the presence of the blue component in the line shapes and its indication for outflow. In Śniegowska et al. (2021) we also noticed an indication of strong outflow in the line shape (blue asymmetry) in our high Eddington sources. However, if outflow is able to modify the BLR metal content in a short timescale, this would be in contradiction with the results of Du et al. (2014) who show significant correlation between NLR and BLR metallicities using [N II]/Hα as NLR metallicity indicator and NV/CIV as BLR metalicity indicator. Outflow from BLR can enrich NLR but in much longer timescales.

Another explanation may be that not all sources ever go through the very high Eddington rate stage, and they thus follow a different evolutionary pattern. The amplitude of variability in AGN may be connected with large-scale magnetic fields, as suggested by Śniegowska et al. (2022b). Some objects

may have a stronger magnetic field which may keep the Eddington rate relatively low, and therefore it may affect the evolution track of the source. Whereas the high Eddington sources may have a lower magnetic field and different conditions to enrich the material in metals. Then vigorous star formation would be present in some epochs of some sources, not all the sources.

Metallicity and the prominence of outflows in quasars were found to be highly correlated (Shin et al., 2017; Wang et al., 2012). The implication of these results is that high Eddington ratio sources, which show the highest blueshifts (Martínez-Aldama et al., 2018; Martínez-Aldama et al., 2018; Sulentic et al., 2017; Vietri et al., 2018), should also be the most metal-rich. Our results from Śniegowska et al. (2021) strongly support such claims, giving the metallicity in the range $10-50Z_{\odot}$ for our sample.

1.8 Thesis overview

Here I provide a summary of each chapter of this dissertation in connection to the concepts I reviewed earlier. In Chapters 2 and 3, I focus on variability in shorter timescales: (thermal/viscous), whereas in Chapter 4, I focus on high-metallicity sources around redshift 2, which may help to explore chemical evolution of AGN. In Chapter 5, I present a summary of my work, as well as a description of forthcoming works.

Paper I:

In this paper, we address the observed phenomenon of fast and multiple events of the brightening and dimming of galaxies known as QPE and CL AGN. We propose that the outburst may be caused by the radiation pressure instability in the accretion disk with a very narrow instability zone, limited by the outer stable disk and the inner ADAF flow. This model is appropriate for sources at relatively low Eddington ratio, as observed in CL AGN phenomena. We model the time-dependent outburst approximating the whole unstable disk by a single, relatively narrow zone. Our toy model gives quantitative predictions for the timescale and the amplitude of outbursts. We claim that an accretion disk around the black hole, with the unstable narrow radial zone changing its vertical height and luminosity, can be responsible for luminosity and spectral changes of active galaxies. We compared our model results with the observational data for the most known multiple outbursts changing look objects and QPE like NGC 1566, NGC 4151, NGC 5548, and GSN 069. In the case of CL AGN, we obtain characteristic timescales of the order of 10 years. However, for QPE, we need much shorter timescales ($\approx$ hours). Thus, we decided to explore effects that can decrease the timescale of the outbursts in the radiation pressure instability mechanism. Furthermore, we present our pilot studies for CL AGN in the next Chapter.

Paper II:

In this manuscript, we extended our work from Chapter 2 and investigated the accretion disk instabilities with more complex time-dependent code. For this work, we use the publicly available code GLADIS (Global Accretion Disk Instability Simulation), developed by Agnieszka Janiuk and her group (Janiuk, 2020). This code computes the time-dependent evolution of a black hole accretion disk, assuming vertically averaged (but time-dependent) accretion disk structure. The code allows for the second vertical layer - the accreting corona - also vertically averaged and time-dependent, but exchanging mass with the disk also in a time-dependent way. The preliminary results for the black hole

mass of 10^7 solar masses are contained in Paper II. The timescales of outbursts are longer than those obtained in Paper I. However, I was able to shorten the timescales by the assumption of a smaller size of the outer radius of the accretion disk ($R_{out} = 100R_{schw}$). Such timescales are much shorter than expected from the computation of the full size of the accretion disk. This shorter timescale (which in this work is still too long to match the timescale from observations) could be further shortened

Recently, we explored all the effects which may shrink the timescales of outbursts in a systematic way. We also included a new effect that a large-scale magnetic field can have on the vertical disk structure. We show that the model, under the condition of a strong field and small outer radius corresponding to the TDE effect or a binary black hole scenario (which may cause a gap in the accretion disk), can eventually bring the model to the agreement with CL AGN or even QPE phenomenon. This work is submitted, and I summarize this part in Chapter 5.

Paper III:

In this paper, we aim to establish that in high Eddington ratio sources, the metallicity is higher, as claimed before, at the basis of the Fe II/Hβ ratio. We selected a sample of high redshift quasars (~ 2) with extreme Eddington ratio and with good quality spectra in the UV band where several broad emission lines may be more reliable metallicity indicators than Fe II/Hβ. The simulations done with the code CLOUDY show that diagnostic line ratios CIV/HeII, AlIII/HeII, and SiIV+OIV]/HeII are monotonically increasing with metallicity for a wide range of ionization parameter values, under the assumption of fixed spectral energy distribution.

We compared the simulated and observed line ratios and then estimated the metallicity in the sample, and the determined metallicity was high, of the order of $Z \sim 20 - 50 Z_{\odot}$. We also detect two emission line components (broad component and blue component), which are produced in different physical conditions: the broad component is associated with a virialized low-ionization BLR, whereas the blue component is associated with a high-ionization outflowing material. We report a relatively large range of uncertainty for the U and $n_{\rm H}$, especially for the blue component, those parameters are poorly constrained. However, the metallicity seems to be well-defined and converges toward high values. The high metallicity values suggest a complex process that involves star formation and impacts the evolution of those high Eddington ratio sources. Moreover, we also detected the overabundance of aluminium to carbon, which likely implies that extended high Eddington accretion is coupled to supernovae outbursts enriching the BLR and may suggest possible selective enrichment.

Part II

Variability in AGN: modelling of repetitive outbursts using radiation pressure mechanism

Chapter 2

Paper I: Possible mechanism for multiple changing-look phenomena in active galactic nuclei

A&A 641, A167 (2020)
https://doi.org/10.1051/0004-6361/202038575

Astronomy & Astrophysics

Possible mechanism for multiple changing-look phenomena in active galactic nuclei

M. Sniegowska[1,2], B. Czerny[2], E. Bon[3], and N. Bon[3]

[1] Nicolaus Copernicus Astronomical Center (PAN), ul. Bartycka 18, 00-716 Warsaw, Poland
e-mail: msniegowska@camk.edu.pl
[2] Center for Theoretical Physics, Polish Academy of Sciences, Al. Lotników 32/46, 02-668 Warsaw, Poland
e-mail: bcz@cft.edu.pl
[3] Astronomical Observatory Belgrade, Volgina 7, 11060 Belgrade, Serbia

Received 3 June 2020 / Accepted 3 July 2020

ABSTRACT

Context. The changing-look phenomenon observed in a growing number of active galaxies challenges our understanding of the accretion process close to a black hole.
Aims. We propose a simple explanation for the sources where multiple semi-periodic outbursts are observed, and the sources are operating close to the Eddington limit.
Methods. The outburst are caused by the radiation pressure instability operating in the narrow ring between the standard gas-dominated outer disk and the hot optically thin inner advection-dominated accretion flow. The corresponding limit cycle is responsible for periodic outbursts, and the timescales are much shorter than the standard viscous timescale due to the narrowness of the unstable radial zone.
Results. Our toy model gives quantitative predictions and works well for multiple outbursts like those observed in NGC 1566, NGC 4151, NGC 5548, and GSN 069, although the shapes of the outbursts are not yet well modeled, and further development of the model is necessary.

Key words. accretion, accretion disks – galaxies: active

1. Introduction

Active galactic nuclei have been always known as strongly variable sources in most of their broadband spectra (e.g., IR: Edelson & Malkan 1987; Kozłowski et al. 2016; optical: Ulrich et al. 1997; Kawaguchi et al. 1998; Sesar et al. 2007; X-ray: Ulrich et al. 1997; Lawrence & Papadakis 1993). Most of the variability can be attributed to variations in the red noise, both in the optical and in the X-ray band (McHardy & Czerny 1987; Lehto et al. 1993; Czerny et al. 1999; Gaskell & Klimek 2003). However, some of the observed changes lead to far more dramatic changes than expected from the red noise trend. These changes are sometimes revealed in the temporary change of the source classification, and these sources are known as changing-look AGN (CL AGN; Matt et al. 2003). There is no well-established definition of what can or cannot be classified as a CL AGN, and we adopted the view that the name can be used for the broad class of objects, not necessarily showing confirmed changes in the optical flux. With progressing understanding of the mechanisms, proper classification will be certainly introduced.

The CL AGN phenomenon was once considered rather rare. The changes corresponded either to a drastic change in X-ray spectrum or in the optical/UV emission lines and continuum, depending on the studied wavelength range (Bianchi et al. 2005; Denney et al. 2014; Shappee et al. 2014). On the other hand, historical light curves of nearby sources, including well-studied AGN (e.g., Cohen et al. 1986; Iijima et al. 1992; Storchi-Bergmann et al. 1993; Bon et al. 2016; Oknyanskij et al. 2016; Shapovalova et al. 2019) indicated that such episodes do happen. With ever more optical and X-ray surveys, the number of CL AGN is rapidly growing (Ruan et al. 2016; Ross et al. 2018; Yang et al. 2018; Stern et al. 2018; Trakhtenbrot et al. 2019; MacLeod et al. 2019), and the question regarding the mechanism of the phenomenon must be addressed. The most extreme case of this phenomenon in the form of quasi-periodic eruptions (QPEs) has recently been discovered by Miniutti et al. (2019) and Giustini et al. (2020).

There is an ongoing discussion whether the phenomenon is intrinsic to the central engine of the active galaxy or just a result of a temporary obscuration or disappearance of such obscuration. While for some CL AGN phenomena the obscuration mechanism can work, for most of the sources there are strong arguments in favor of the intrinsic changes:

– complex multi-band recovery, inconsistent with obscuration (e.g., Mathur et al. 2018);

– strong changes seen in the IR where the obscuration should not play a role (Sheng et al. 2017; Stern et al. 2018);

– low level of polarization in CL AGN which argues against the scattering (and obscuration) scenario (Hutsemékers et al. 2019);

– different variability behaviors of the observed emission lines in spectra of CL AGN (e.g., Kynoch et al. 2019);

– regular QPE behavior cannot be due obscuration because of the characteristic spectral evolution during outbursts (Miniutti et al. 2019; Giustini et al. 2020).

Thus, in most sources the intrinsic change in the bolometric luminosity later affects the X-ray spectra and the appearance of the broad-line regions (BLR). These intrinsic changes can either be related to tidal disruption events (TDEs) or can be a

result of the spontaneous unforced behavior of the accretion flow close to a black hole. In some cases perhaps TDEs provide the answer, but in sources with repeated events a TDE is statistically unlikely.

In the present paper we concentrate on the discussion of the plausible mechanism that can lead to regular or semi-regular repeating outbursts intrinsic to the nucleus. In such cases the source behavior might be related to some instabilities in the accretion flow. However, the radiation pressure instability expected to be operational in the innermost part of an AGN accretion disk does not provide the proper timescales (e.g., Gezari et al. 2017). Convenient formulae for the duration of such outbursts given in Grzędzielski et al. (2017) give timescales of hundreds of years for a black hole mass of $10^7\,M_\odot$. Dexter & Begelman (2019) suggest that strong magnetization can shorten the estimated timescales. On the other hand, we can look for another mechanism related to the complexity of the innermost part of the flow, and Noda & Done (2018) propose that the CL behavior in the source Mrk 1018 is related to the temporary disappearance of the warm corona. The source NGC 1566 notable for numerous CL outbursts (e.g., Alloin et al. 1986; Baribaud et al. 1992; Oknyansky et al. 2019) does not show the presence of the warm corona component before the outburst (Parker et al. 2019). The present observations cannot resolve directly any of these issues since they show at best the presence of the gas reservoir at a distance of 60 pc from the black hole (Mkn 590; Raimundo et al. 2019). They only show that the phenomenon is complex; for example, the reappearance of broad lines in Mkn 590 is not accompanied by the full recovery of the continuum (Raimundo et al. 2019).

In this paper we propose a new mechanism that is suitable for explaining regular outbursts in sources that are not very close to the Eddington ratio. Using a highly simplified toy model we discuss whether the mechanism is likely to reproduce the observed timescales, and thus deserves the effort of more detailed description in the future.

2. Analytical estimates and the model geometry

The character of the accretion flow in AGN strongly depends on the Eddington ratio of the source. In sources where the Eddington ratio is above a few percent, the optically thick geometrically thin disk extends down to the innermost stable circular orbit (ISCO). Modeling of the optical/UV emission of quasars supports this view (e.g., Capellupo et al. 2015), although warm corona need to be invoked to explain the soft X-ray excess. However, low-luminosity AGN, showing low-ionization nuclear emission-line regions (LINERS) do not show this component in the optical/UV spectra, and it is generally accepted that in these sources the innermost part of the accretion flow proceeds in the form of an optically thin advection-dominated accretion flow (ADAF).

For simplicity, we introduce here a definition of the Eddington accretion rate based on Newtonian physics:

$$\dot{M}_{\rm Edd} = \frac{48\pi G M_{\rm BH} m_{\rm p}}{\sigma_T c}. \tag{1}$$

Here $M_{\rm BH}$ is the black hole mass, $m_{\rm p}$ is the proton mass, and σ_T is the Thomson cross-section. We thus measure the ratio of the accretion rate to the Eddington accretion rate using $\dot{m} = \dot{M}/\dot{M}_{\rm Edd}$.

In these units, the transition between an inner ADAF flow and an outer standard accretion disk (Abramowicz et al. 1995; Czerny et al. 2019) takes place at

$$R_{\rm ADAF} = 2\alpha_{0.1}^4 \dot{m}^{-2} R_{\rm Schw}, \tag{2}$$

where $\alpha_{0.1}$ is the viscosity parameter introduced by Shakura & Sunyaev (1973) in units of 0.1, and $R_{\rm Schw} = 2GM_{\rm BH}/c^2$ is the Schwarzschild radius of the black hole.

A standard accretion disk is unstable in the innermost part when the radiation pressure dominates (Lightman & Eardley 1974; Pringle et al. 1973; Shakura & Sunyaev 1976), and the transition from the outer stable to the inner unstable radius takes place at

$$R_{\rm tr} = 1522(\alpha_{0.1} m_7)^{2/21} \dot{m}^{16/21} R_{\rm Schw} \tag{3}$$

(Shakura & Sunyaev 1973). Here m is the black hole mass expressed in units of $10^7\,M_\odot$. The two lines cross at the specific accretion rate, $\dot{m}_{\rm st}$,

$$\dot{m}_{\rm st} = 0.0905 \alpha_{0.1}^{41/29} m_7^{-1/29}, \tag{4}$$

where the dependence on the black hole mass is negligible, but the dependence on the viscosity coefficient is stronger than linear. The radius where it happens is given by

$$R_{\rm st} = 244 \alpha_{0.1}^{43/29} m_7^{2/29} R_{\rm Schw}. \tag{5}$$

If the accretion rate of the flow is lower than this limiting value, $\dot{m}_{\rm st}$, the whole flow is stable since both the gas-dominated cold outer disk and the inner ADAF flow are stable solutions. On the other hand, if the accretion rate is higher that $\dot{m}_{\rm st}$ the disk range is dominated by the radiation pressure, which is unstable and could lead to a limit cycle behavior.

The timescale for these oscillations is generally set by the viscous timescale of the Shakura-Sunyaev disk,

$$\tau_{\rm visc,SS} = \frac{1}{\alpha}\left(\frac{R}{H}\right)^2 \left(\frac{R^3}{GM_{\rm BH}}\right)^{1/2} \tag{6}$$

(Shakura & Sunyaev 1973; see, e.g., a review by Czerny 2006), which is hundreds of years for the case of AGN. However, if $\dot{m}$ is just above the threshold defined by Eq. (4), then the radial extension of the unstable zone, δR, is much smaller than the radius R itself. We illustrate schematically this geometry in Fig. 1. In this case, the time needed to empty the zone is reduced, and the viscous evolution will happen on the following timescale:

$$\tau_{\rm visc} = \tau_{\rm visc,SS} \frac{\Delta R}{R}. \tag{7}$$

Thus, for sources at low Eddington accretion rates the radiation pressure instability, operating in a very narrow zone at the border between the outer standard disk and an inner ADAF flow, can provide a viable mechanism that explains repeating outbursts in some CL AGN on timescales of a few years. The schematic view of our new model of CL AGN is shown in Fig. 1.

The small radial extension of the instability zone reduces also the amount of variable radiation flux by the same factor. On the other hand, the zone regulates the accretion flow in the inner ADAF, and most of the radiation is actually produced there in the form of X-rays. The efficiency of the inner ADAF flow is not well known, but significant part of the energy goes directly to electrons, and subsequently to radiation (e.g., Bisnovatyi-Kogan & Lovelace 1997; Yuan & Narayan 2014; Marcel et al. 2018). The outburst should thus be clearly seen in X-rays; in addition, X-ray irradiation of the cold disk will lead to enhancement of the disk emission in optical/UV band.

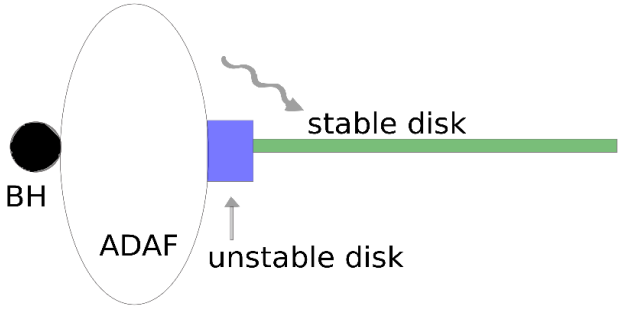

Fig. 1. Schematic view of the innermost part of the flow: outer cold stable disk (green), intermediate zone (disk part unstable due to radiation pressure instability), and inner hot ADAF which illuminates the outer disk.

3. One-zone time-dependent toy model

We construct a simple toy model in order to check whether the mechanism may indeed give repeated outbursts of the observationally required properties. We basically follow the 1D model of time evolution of accretion disk under radiation pressure instability Janiuk et al. (2002), but we simplify it further by concentrating on a single-zone approximation, thus reducing the numerical problem to ordinary differential equation in time. Instead of solving for vertically averaged disk structure as functions of both time and disk radius, we follow the time-dependent evolution of a single zone, representing the radiation pressure dominated region. It is a good approximation if the radial extension of the zone is small, i.e., if the zone is narrow and comparable to the disk thickness.

The evolution of the zone on thermal timescale is very similar to the one in the multi-radius approach as the thermal evolution results from the net effect of the heating, radiative cooling, and advection cooling. We assume that the disk is in hydrostatic equilibrium. However, the viscous evolution is now set simply by the boundary conditions: (i) between the zone and outer stationary disk and (ii) between the zone and inner ADAF:

– at the border between the zone and the outer disk, we assume a constant inflow rate of the material provided by the stable outer disk, $\dot{M}_0$;

– at the border between the zone and the inner ADAF, the material is removed from the disk at a rate $\dot{M}$ by evaporation due to the electron conduction.

Since this is a simple toy model, we do not use any advanced description of this process which would require the knowledge of the ADAF density or ion and electron temperature (e.g., Różańska & Czerny 2000; Liu et al. 2007; Qiao & Liu 2020). Instead, we postulate that the efficiency of the process should be proportional to the zone height since the hot inner ADAF is geometrically thick so the interacting surface is set by the cold disk state. We additionally assume that evaporation is more efficient when there is more mass in the unstable zone. If the zone and ADAF happen to be in equilibrium, then the outflow rate from the zone should be equal to the inflow rate. So introducing the equilibrium zone thickness, H_0, and equilibrium surface density in the disk, Σ_0, our approach allows us to specify the evaporation rate in general as

$$\dot{M} = \dot{M}_0 \frac{H}{H_0} \frac{\Sigma}{\Sigma_0}, \tag{8}$$

where the quantities H and Σ describe the height and surface density of the evolving zone. We always start our time-dependent evolution from an equilibrium model, but if the solution corresponds to an unstable one, the disk will perform the limit cycle.

From the two assumptions above, we obtain the time evolution of the surface density in the zone

$$\frac{\mathrm{d}\Sigma}{\mathrm{d}t} = \frac{\dot{M}_0 - \dot{M}}{2\pi R \Delta R}, \tag{9}$$

meaning that it is given by the imbalance between a constant inflow rate into the zone, $\dot{M}_0$, and variable outflow rate, $\dot{M}$, from the zone to inner ADAF flow.

The evolution of the zone in the thermal timescale, given by Eq. (33) in Janiuk et al. (2002), under our assumptions, for a narrow zone, reduces to the following equation for the equatorial disk temperature, T:

$$\frac{\mathrm{d}\log T}{\mathrm{d}t} = \frac{(Q^+ - Q^- - Q_{\rm adv})(1+\beta)}{PH[(12-10.5\beta)(1+\beta)+(4-3\beta)^2]} + 2\frac{\mathrm{d}\log\Sigma}{\mathrm{d}t}\frac{4-3\beta}{(12-10.5\beta)(1+\beta)+(4-3\beta)^2}. \tag{10}$$

Here the calculation of the derivatives of the disk thickness H are already included in the expression. The values of the disk thickness; total pressure, P; gas-to-total pressure ratio, β; viscous heating, Q^+; and radiative cooling, Q^-, are determined from the standard equations of the vertically averaged disk structure in hydrostatic equilibrium as in Janiuk et al. (2002), but here we do not introduce any additional correction coefficients related to the disk vertical structure (e.g., C_1, C_2) since the current model is very simple. The advection cooling term, $Q_{\rm adv}$, is determined as

$$Q_{\rm adv} = \frac{\dot{M}PH}{2\pi R\Delta R\Sigma}, \tag{11}$$

so we include only an advection term related to the inflow from the zone to inner ADAF, and we neglect the energy carried into the zone from the outer disk, which should be negligible. Thus, time-dependent partial differential equations (26) and (33) from Janiuk et al. (2002) reduce to ordinary differential equation for the time evolution of a surface density and temperature in the equatorial plane of a single zone.

The geometrically narrow instability zone evolves quickly, but the amount of energy dissipated in this zone is also correspondingly small. Therefore, the changes in the zone luminosity by itself do not change significantly the system luminosity. However, the zone acts as a regulator of the accretion flow in the innermost ADAF.

ADAF flow was frequently considered inefficient, but most estimates of the ion-electron coupling and of the Ohmic heating imply that actually ADAF flow is energetically quite efficient, at least when the accretion rate is not many orders of magnitude below the Eddington accretion rate. (e.g., Bisnovatyi-Kogan & Lovelace 1997; Ferreira & Petrucci 2011; Hirotani 2018). Therefore, the inner part of the flow generates more energy than the outer part of the disk and the transition zone (the exact number would depend on the black hole spin). This energy is emitted in X-rays, but part of the produced X-ray radiation will illuminate the disk and enhance the disk emission.

We thus assume the typical flow efficiency of 10% in ADAF and calculate the result of the disk irradiation. ADAF is an extended medium so in principle this is a complex 2D issue, but in our simple model we represent the ADAF emission by emission localized along the symmetry axes since that allows us to calculate the effect in a simple way: we used the method and the code developed in Loska et al. (2004). This irradiation is

very important, strong illumination is observed in reverberation-studied sources like NGC 5548 (Edelson et al. 2015, 2017; De Rosa et al. 2015; Goad et al. 2016; Fausnaugh et al. 2016; Starkey et al. 2017; McHardy et al. 2018; Kriss et al. 2019) where the variable X-ray emission drives the accretion disk continuum variability, although the correlation is not always perfect.

In our toy model we assume, for simplicity, that the inner region luminosity is equal to the total (time-dependent) bolometric luminosity

$$L_{\rm ADAF} = \eta \dot{M} c^2, \tag{12}$$

with the flow efficiency η equal to 0.1, as in radiatively efficient flow. The illumination of the outer disk is calculated semi-analytically, as in Loska et al. (2004), assuming that the emission is localized along the symmetry axis, otherwise 3D computations would be necessary. The emissivity is adopted as a power law with index $\beta = 2.0$, the maximum distance is equal to the transition radius $R_{\rm tr}$, and the minimum distance along the axis is set at 1/3 of this value. We assume complete local thermalization of the incident flux by the cold disk.

In principle, the free parameters in our models are the black hole mass, the accretion rate, and the viscosity since the location of the transition and the extension of the unstable zone should results from the computations of the disk structure. However, our toy model does not have all the ingredients (such as proper description of the vertical structure, opacity, convection, irradiation; see, e.g., Różańska et al. 1999). So we additionally treat the radius and the zone width as independent parameters.

4. Results

We now use our toy model of radiation pressure instability in a narrow zone between the outer cold disk and an inner hot flow to model the repeating outbursts observed in some AGN. The model parameters are the external accretion rate, $\dot{M}_0$; the radius, R; the width of the unstable zone, ΔR; and the viscosity parameter, α, in the zone. The two remaining parameters, Σ_0 and H_0, are determined self-consistently from the equilibrium (unstable) solution located at the stability curve.

4.1. Stability curve

The stability curve is built of solutions to Eqs. (9) and (10), assuming that all time derivatives are equal to 0. They are conveniently plotted as a function of the external accretion rate, $\dot{M}$. We express it in dimensionless units. In the case of the stationary solution, the accretion rate inside the zone is coupled to the zone properties

$$\dot{M} = 4\pi\alpha P H/\Omega_K, \tag{13}$$

as in the standard stationary disk of Shakura & Sunyaev (1973).

The result is shown in Fig. 2 (blue line). Here we adopt parameters appropriate for NGC 1566. For black hole mass we assume $\log M = 6.92$ after Woo & Urry (2002), we adopt the viscosity paramater $\alpha_{0.1} = 0.2$ (i.e., $\alpha = 0.02$) after Grzędzielski et al. (2017), and we take $30R_{\rm Schw}$ for the radius. The zone width is assumed to be very narrow, $0.003R$, comparable to the disk thickness.

Our stability curves in their high accretion rate parts depend on the adopted width of the zone since the advection term in our model explicitly contains it (see Eq. (11)). When the zone is narrow, the advection works very efficiently.

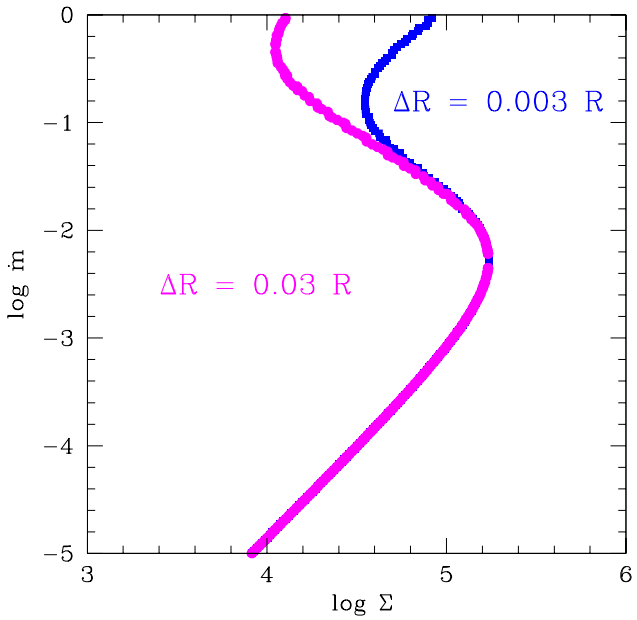

Fig. 2. Accretion rate vs. surface density in the transition zone between the cold SS outer disk and the inner ADAF in a stationary model in two cases $\Delta R = 0.003R$ (blue points), and $\Delta R = 0.03R$ (magenta points). Other parameters: $\log M = 6.92$, $R = 30R_{\rm Schw}$, $\alpha = 0.02$.

The negative slope of the stability curve implies that the solution is unstable. For the assumed radius and the black hole mass, the flow with accretion rate higher than $\dot{m} \sim 0.01$ is unstable. The upper stable branch starts quite early for a narrow zone, so the instability is expected to operate for $\dot{m}$ between 0.01 and 0.1 in this case. If the zone width increases, the branch stabilized by advection starts at higher accretion rates, and for ΔR on the order of R the stabilization would happen above the Eddington accretion rate, as in a standard slim disk (Abramowicz et al. 1988). However, our toy model is not expected to work for a geometrically broad zone.

4.2. Time evolution of the accretion rate through the zone

We compute the time evolution of the zone by assuming the value of the black hole mass, the radius, the radial width of the zone, and the viscosity parameter. We then choose the external accretion rate from the range corresponding to the unstable branch. The disk irradiation parameters are fixed, as described in Sect. 3.

Exemplary time evolution of the accretion rate regulated by the unstable zone is given in Fig. 3. We fixed the black hole mass there at the value corresponding to NGC 1566, but we varied the accretion rate, the viscosity parameters, and the radial size of the unstable zone. We see there that the timescales of outbursts and the outburst amplitudes are very sensitive to these parameters. The shape of the outbursts varies less, and in our model the duration of the bright phase (outburst) is always longer then the outburst separation because the accumulation phase is longer than the evaporation rate and the transfer through ADAF. Outbursts are regular since our toy model is very simple. More advanced models of disk instabilities, which include the wind, irradiation, magnetic field, or tidal interaction with a companion in a binary system frequently lead to much more complex outbursts (see, e.g., Hameury 2019, and the references therein). These models, however, do not consider the inner ADAF and

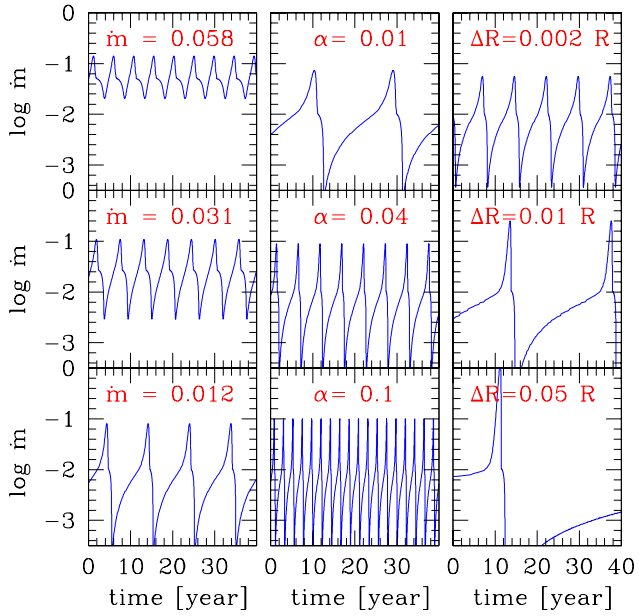

Fig. 3. Dependence of the time-dependent accretion rate on the external steady accretion rate, $\dot{m}_0$; viscosity parameter, α; and the geometrical thickness of the unstable zone, ΔR. The parameters are labeled in each panel. The default parameters are $\dot{m} = 0.0122$, $\alpha = 0.02$, $\Delta R = 0.003R$. The fixed parameters are black hole mass $\log M = 6.92$, inner radius of the disk $R = 30R_{\rm Schw}$.

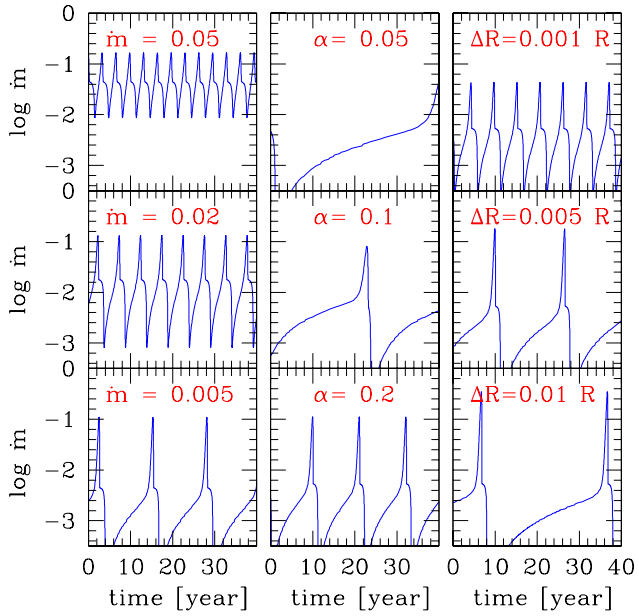

Fig. 4. Dependence of the time-dependent accretion rate on the external steady accretion rate, $\dot{m}_0$; viscosity parameter, α; and the geometrical thickness of the unstable zone, ΔR. The parameters are labeled in each panel. The default parameters are $\dot{m} = 0.006$, $\alpha = 0.2$, $\Delta R = 0.003R$. The fixed parameters are black hole mass $\log M = 7.94$, inner radius of the disk $R = 20R_{\rm Schw}$.

narrow instability zone, so our toy model gives interesting estimates of the timescales, and further development may easily lead to more complex light curve shapes.

The evolution is significantly slower for more massive black holes. Therefore, in Fig. 4 we show a set of light curves for a black hole mass more appropriate for sources like NGC 5548. In order to model frequent outbursts we have to request values of the higher viscosity parameter.

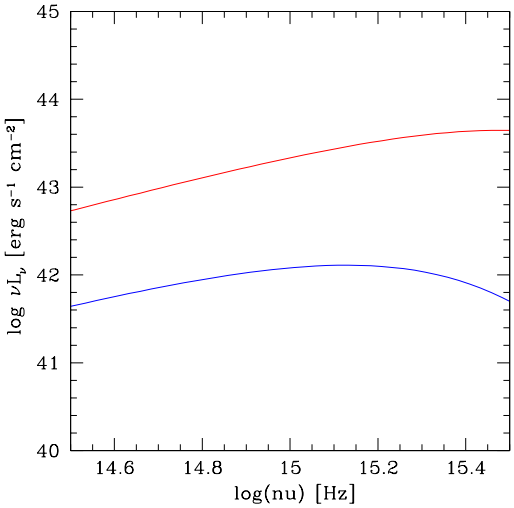

Fig. 5. Two extreme states of the accretion disk in the source: between outbursts (blue line) and during outburst (red line). Here we neglect the contribution from the starlight.

4.3. Irradiation of the cold outer disk

As discussed in Sect. 3, the variable accretion rate in the unstable zone and in the innermost part of the flow strongly affects the outer disk. Thus, the variable accretion rate as shown in Fig. 3 must be used to receive the time evolution of the monochromatic flux and the line luminosity.

In Fig. 5 we show two extreme examples of the spectra from an illuminated disk: between the outburst and at the peak of the outburst. For the chosen parameters, given in the figure caption, the flux at V band changes by an order of magnitude and the spectrum becomes much bluer in the far UV. Parameters that were used in this case are $\dot{m} = 0.012$ and $\log M = 6.92$, appropriate for NGC 1566.

We thus compare the bolometric light curve resulting from the instability to the corresponding monochromatic light curve. As explained in Sect. 3, we derive the monochromatic light curve taking into account the disk plus transition zone flux at V band for all the time steps of the evolution, always using the current value of $\dot{M}$ to calculate the disk illumination. The shape of the curve is similar, but not identical, to the shape of the accretion rate variability. An example is shown in Fig. 6. This light curve can be directly compared to the continuum light curve of a given source, but the observed light curve should be corrected for the starlight contamination.

If the line luminosity light curve is available, in principle we should compute the structure of the BLR, but in our toy model we can assume that the line follows the bolometric luminosity of the source, which is well represented by the varying accretion rate.

4.4. Comparison with the observational data

Our toy model is not yet ready for detailed fitting of the observed light curves. What is more, such a comparison would always be inherently difficult since the observed variability in AGN is never strictly periodic. Thus, our aim is to test if the model can roughly cover the characteristic variability timescales in the few exemplary sources. The physical parameters that we obtained for each object are shown in Table 2.

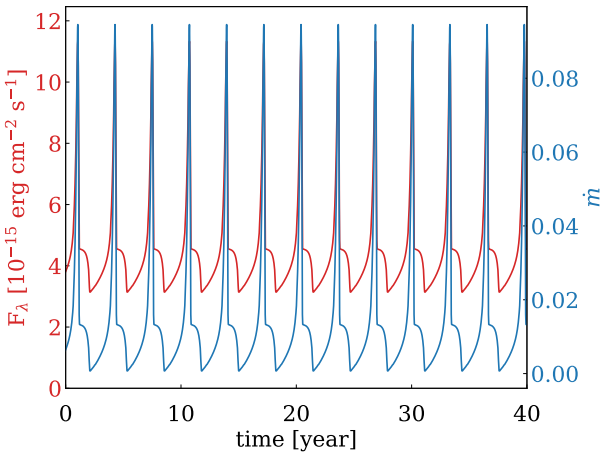

Fig. 6. Comparison of the modeled variations of the bolometric luminosity measured as the Eddington ration (blue line) with the modeled variations of the monochromatic disk luminosity in V band (red line), with irradiation included.

4.4.1. NGC 1566

This source, usually classified as a Seyfert 1.5 galaxy (z = 0.005017 after NED[1]) is a well-known CL AGN. Its semi-regular outbursts were already observed by Alloin et al. (1986). Later, in September 2017, the source started a spectacular brightening in optical band (Dai et al. 2018), and in X-rays Parker et al. (2019). The bolometric luminosity of the source thus strongly varies from $\log L_{\rm bol}$ = 41.4 (Combes et al. 2019) to $\log L_{\rm bol}$ = 44.45 (Woo & Urry 2002). Parker et al. (2019) reported an Eddington ratio of 0.05 during the outburst and 0.002 between the outbursts.

Mostly concentrating on the old data showing multiple outbursts (see Fig. 7) we assume that the characteristic timescale in this source is 5 years. For the black hole mass we assume the value $\log M$ = 6.92 from Woo & Urry (2002) (which is consistent with the value 6.8 ± 0.3 derived from molecular gas dynamics by Combes et al. 2019). We assume the mean accretion rate of $\dot{m}$ = 0.012 in Eddington units, corresponding to the mean value.

We can find an example of the unstable solution for these input parameters assuming the value of $25R_{\rm Schw}$ for the radius. The zone width is assumed to be very narrow ($0.002R$, which is comparable to the disk thickness). The required value, α = 0.04, is a factor of 2 larger than the value of α = 0.02 used by Grzędzielski et al. (2017). The solution roughly corresponds to the middle panel of Fig. 3

The source behavior, however, is not regular; the last outburst appeared earlier than expected and had higher amplitude than the remaining three. The optical V-band light curve reported by Dai et al. (2018) shows a small outburst lasting about one year, at around 2014, thus shorter by a factor of a few than the outbursts observed by Alloin et al. (1986).

The duration of the outburst seems too short in comparison to the time separation. This is a characteristic property of the current version of the model, particularly for lower accretion rates, and large outburst amplitudes.

[1] https://ned.ipac.caltech.edu/classic/

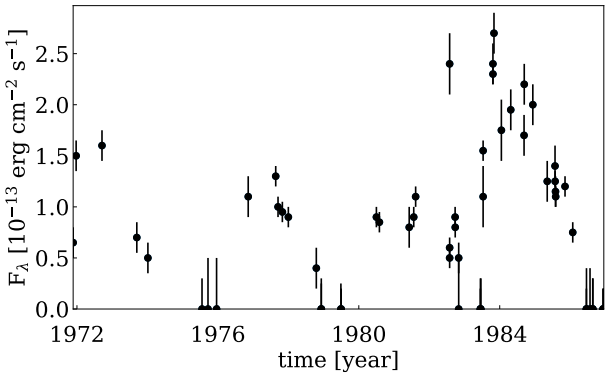

Fig. 7. Hβ line flux evolution in NGC 1566 from Alloin et al. (1986).

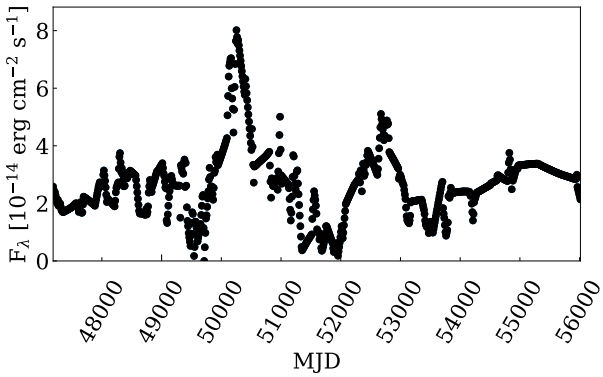

Fig. 8. Continuum flux evolution in NGC 4151 points.

4.4.2. NGC 4151

For this source we assume mass from Woo & Urry (2002) ($\log(M_{\rm BH}/M_\odot) = 7.12$) and bolometric luminosity 43.73 from Kaspi et al. (2005), z = 0.003262 after NED. We estimate $\dot{m}$ as 0.027. Guo et al. (2014) suggest three possible periodicities for that source ($P_1 = 4 \pm 0.1$, $P_2 = 7.5 \pm 0.3$, and $P_3 = 15.9 \pm 0.3$ yr). Bon et al. (2012) also derive P = 15.9 yr for that source. The same periodicity is also found in radial velocity curves of Hα broad line. Similar values were suggested by Kovačević et al. (2018) (~5 and ~8 years). Oknyanskij & Lyuty (2007) suggest a period of about 15.6 years obtained using power spectrum. However, as Czerny et al. (2003a) shows, changes are not strictly periodic, and the possible characteristic timescale is of order of 10 years.

The photometry continuum flux data set includes data from Bentz et al. (2006), Shapovalova et al. (2008), AGN Watch provided by Kaspi et al. (1996), and Malkov et al. (1997). To reduce the influence of the longest timescale systematic trend (which is probably due to various mechanisms), we rebin the data. The result is shown in Fig. 8.

If we adopt the value of 10 years for a characteristic timescale in this source, we require values of the remaining parameters similar to those in the case of NGC 1566. For these parameters outbursts amplitudes are large, and outbursts rather short lasting.

4.4.3. NGC 5548

NGC 5548 is an object with long-term and dense data coverage in various wavelengths (Chiang & Blaes 2003; Mehdipour et al. 2015; Mathur et al. 2017). Optical reverberation campaigns

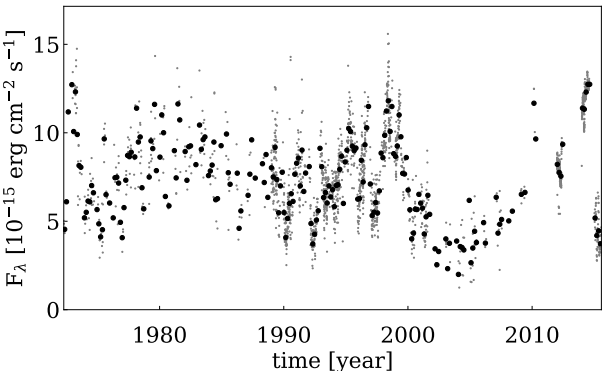

Fig. 9. Continuum flux evolution in NGC 5548. Gray points represent observational data, black points represent data rebinned to 300 bins in total.

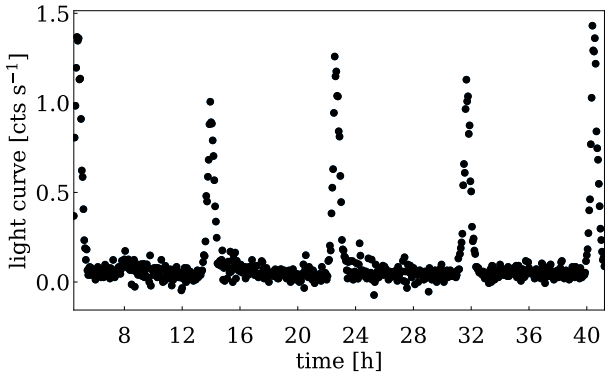

Fig. 10. GSN 069 disk contribution in 0.2–2 keV from Miniutti et al. (2019).

determined the mass of its black hole (Peterson et al. 2004; Bentz & Katz 2015). This complex source is known by the changes of the BLR, which may not be linked with only one physical origin. NGC 5548 showed the obscuration in X-ray and UV range (Kriss et al. 2019), both the intrinsic continuum and the obscurer are variable (Di Gesu et al. 2015). Dehghanian et al. (2019a) and references therein suggest that cloud shadowing should be considered as an appropriate explanation for variability in observation.

We assume the physical parameters for this source as follows: $L_{\rm BOL} = 44.45$ from Ebrero et al. (2016) and $M = 8.71^{+3.21}_{-2.61} \times 10^7\,M_\odot$ from Lu et al. (2016); Kovačević et al. (2018) suggest for that source period 13.3 ± 2.26 yr, accretion rate 0.01 from Papadakis et al. (2019); Bon et al. (2016) suggested slightly longer period of ~5700 days. The continuum flux data set for NGC 5548 includes data from Bon et al. (2016) is shown in Fig. 9.

We decided to model outbursts with a period of around 13 years. In that case, for the adopted mass and accretion rate as described above we can find the proper representation of the outbursts assuming much higher viscosity and somewhat smaller radius since the timescale is similar to that in the two previous sources, while the black hole mass is an order of magnitude higher.

It is interesting to note that the location of the unstable zone in this source, at a distance of 0.23 light days from the center is nicely consistent with the location of the obscurer (below 0.5 light days) discussed by Dehghanian et al. (2019b).

4.4.4. GSN 069

This relatively low-mass Seyfert galaxy ($M_{\rm BH} = 4.5 \times 10^5\,M_\odot$, Miniutti et al. 2019) was inactive when measured by ROSAT. In 2010 it showed a spectacular rise in the nuclear luminosity, followed by a slow decay. During the late decay phase, in December 2018, the source showed spectacularly rapid large amplitude oscillations with a period of roughly 9 hours (Miniutti et al. 2019). The behavior was still observed in February 2019. The nature of these quasi-periodic eruptions (QPE) is not clear, but the spectral changes strongly suggest the coupling with the corona formation and likely the coronal inflow. The outbursts are shown in Fig. 10.

We represented the variations in the disk luminosity using our toy model. We assumed the black hole mass of $4.5 \times 10^5\,M_\odot$, after Miniutti et al. (2019), and we adjusted the remaining parameters to reproduce the timescale. QPE time separation can indeed be reproduced, although it requires a small radius and large value of the viscosity coefficient. The external accretion rate favored by our model (0.013 in Eddington units) is much lower than the bolometric luminosity 0.46 estimated by Miniutti et al. (2019). The low accretion rate was implied by the instability zone present very close to the black hole. Clearly the current toy model does not describe yet the source behavior, and most likely the source performed just disk–corona pulsations, as suggested by Miniutti et al. (2019). If so, more complex model with two-phase disk–corona medium is needed to accurately represent this source.

5. Discussion

The changing-look behavior, rapid large amplitude changes in active galaxies, is reported now with increasing frequency, but the mechanism is still unknown. Some of the phenomena can actually be related to tidal disruptions, particularly in the case of a single, long-lasting large-amplitude event. On the other hand, if multiple events takes place in a single source, particularly in a semi-regular form, the TDE mechanism is ruled out. There is at least one source where we observe a combination of the two phenomena: a galaxy GSN 069. Classified as a Seyfert 2 galaxy, GSN 069 was undetected in ROSAT All Sky Survey, but in 2010 the source showed a spectacular brightening, and when the dimming continued, the source showed very regular outbursts (Miniutti et al. 2019).

In this paper we concentrate of modeling the repeating semi-regular outbursts observed in the sources radiating at a few percent of the Eddington ratio. We propose that the radiation pressure instability operating in the narrow zone between the outer gas-dominated stable accretion disk and an inner hot ADAF flow may be responsible for repeating outbursts in some CL AGN, such as NGC 1566. We show that the proposed mechanism can lead to outbursts on a timescale much shorter than the usual viscous timescale in a cold disk.

For this mechanism to operate we require that the mean accretion rate in the source be relatively low so the inner ADAF flow extends to a radius that is not much smaller than the radius where the radiation pressure in a standard Keplerian disk dominates. The amplitudes of the outbursts in the optical band are large, due to the irradiation of the outer disk by the enhanced inner hot flow.

The generic prediction of the model is that the spectrum of the nucleus should become much bluer during outburst, and the outbursts in X-ray band should have comparable or larger amplitude. On the other hand, the current model does not give

Table 1. Information about sources.

Name	Redshift	$d_L(z)$	$\log(M_{\rm BH})$	$L_{\rm BOL}$	Data coverage	σ exp	σ obs Hβ	σ obs cont
NGC 1566	0.005017	22.5	6.92	2.5×10^{42}	1972–1987	0.18	0.73	–
NGC 4151	0.003319	14.9	7.12	7×10^{43}	1988–2012	0.27	–	0.36
NGC 5548	0.017175	77.8	7.94	2.8×10^{44}	1972–2015	0.20	0.40	0.33
GSN 069	0.018	81.6	5.65	2.7×10^{43}	January 16/17, 2019 (130 [ks])	0.21	–	1.85

Notes. Culmns are: name of the source, redshift, luminosity distance [Mpc], assuming the cosmology: $H_O = 67\,{\rm km\,s^{-1}}$, $\Omega_m = 0.32$, $\Omega_L = 0.68$ (Planck Collaboration I 2014), black hole mass, bolometric luminosity, time span for the optical data coverage, the amplitude expected from the stochastic behavior of AGN, the observed amplitude from line or continuum.

Table 2. Summary of the results for each object.

Name	$R_{\rm in}$	Δ_R	α	$\dot{m}$	Period	Amplitude
NGC 1566	25	0.002	0.04	0.015	5 yr	62.05
NGC 4151	26	0.006	0.05	0.027	10 yr	341.3
NGC 5548	20	0.003	0.20	0.0055	13 yr	4892.36
GSN 069	5	0.03	0.25	0.013	0.387 day	3.95

Notes. Columns show name of the source, inner radius in $R_{\rm Schw}$, thickness of the unstable zone, viscosity parameter, period in years (except of the last object), and amplitude. The black hole mass used in the model was taken from Table 1.

an outburst shape consistent with the observational data. Our toy model relies only on the viscous timescale in the unstable ring close to ADAF, without addressing the full complexity of the standard disk–ADAF transition.

The model predicts strong semi-periodic variations in the emitted flux for sources at a few percent of the Eddington ratio but these changes may, or may not be revealed in the properties of the BLR. If the variability timescale is long in comparison to the time required for the adjustment of the BLR structure to the change of the nuclear emission, then the BLR will follow the changes in the nucleus in a quasi-stationary way, and we should see the classical CL AGN phenomenon. On the other hand, if the nuclear changes do not last long enough, then the BLR may not fully adjust. For example, in sources like GSN 069 the eruption lasts about an hour, while the distance to the BLR is likely a few hours, like in another low-mass Seyfert galaxy NGC 4395 (Peterson et al. 2005). What is more, the light travel time describes just a change in irradiation, while the BLR structure adjusts more slowly (see, e.g., Hryniewicz et al. 2010).

Ross et al. (2018) considered a possibility that the behavior of the quasar J1100-0053 is related to instability in a cold disk–ADAF transition zone, but argues against it since in other objects (e.g., NGC 1097) the transition zone is stable. The position of the transition radius determined by balancing the cold disk evaporation rate and the inner hot flow depends on the global accretion rate (e.g., Różańska & Czerny 2000; Spruit & Deufel 2002; Taam et al. 2012) and seems rather stable. Our solution to the problem comes from introducing the radiation pressure instability. It also implies that for lower Eddington ratio objects the instability would not operate, while for higher Eddington ratio objects this mechanism would lead to outbursts of a much larger part of the disk and it would operate on a timescale of thousands of years, as typically predicted for the radiation pressure instability (Janiuk et al. 2002; Czerny et al. 2009; Wu et al. 2016; Grzędzielski et al. 2017). However, if the evolution includes the time-dependent coronal flow (e.g., Janiuk & Czerny 2007) or time-dependent vertical stratification of the disk into cold standard disk and the warm corona (e.g., Czerny et al. 2003b; Gronkiewicz & Różańska 2020; Petrucci et al. 2020), the timescales will be strongly affected by quadratic dependence of the viscous timescale on the ratio of the local medium geometrical thickness to the local radius.

In most cases the outbursts we model are not clearly quasi-periodic (the behavior of the source GSN 069 discovered by Miniutti et al. 2019 is a nice exception) so there is a danger that we try to model the source behavior using a dedicated mechanism, while in reality all AGN show a stochastic variability, and this stochastic variability may lead sometimes, with certain statistical probability, to a behavior that looks quasi-periodic (Vaughan et al. 2016). However, stochastic variability has a well-defined power spectrum shape and normalization, both in X-rays (McHardy et al. 2004) and in the optical band (e.g., Czerny et al. 1999, 2003a). Thus, the amplitude for a given time span is limited. For the studied sources we thus report the observed variability amplitude for a given time period and we compare it to the amplitude expected from the stochastic behavior of AGN. For NGC 1566, NGC 4151, and NGC 5548 this stochastic amplitude was predicted assuming the power spectrum from the recent work of Breedt et al. (2010), including the scaling by a factor of 100 between the optical and the X-ray power spectrum, and the break in the X-ray spectrum for each source was estimated following McHardy et al. (2006). Knowing the optical power spectrum we could predict the source variance expected from the standard stochastic variability. For GSN 069 we estimated the expected X-ray variability from the typical X-ray variability level of AGN Uttley et al. (2002) by averaging the provided σ values for four sources on timescales on the order of 10^6 s. The dispersion in those values was small, and we took the timescales longer than the length of the used GSN 069 light curve since the level of X-ray variability at a given timescale scales with the black hole mass (e.g., Nikolajuk et al. 2004). All values are reported in Table 1. We see that the observed dispersion is much larger than expected from the stochastic variations. Therefore, invoking a separate mechanism to explain this phenomenon is justified.

The presented toy model is still too simplistic to account quantitatively for the observed outbursts. The comparison shows that the duration of the outburst in some models is far too short in comparison with the rising phase, while is some cases (e.g., GSN 069) they are too long. This is partially because the model does not account properly for the evaporation mechanism of the zone. In a realistic model Eq. (8) should be replaced with the physically motivated equation containing the additional timescale for the process. However, this is not simple. The spectral changes observed in GSN 069 during outbursts (Miniutti et al. 2019) suggest that a Comptonizing corona forms above the disk, and it may be that the real mechanism is actually a two-step mechanism, with corona formation as a stage one, and then the corona inflow as a stage two, finishing outbursts. Thus the future model should have both radial and vertical stratification, perhaps actually a full 2D since the height of the zone is comparable to its radial extension, and it should include full time-dependence of the outer disk since the irradiation would couple to the stability properties. However, such a model is far beyond the aim of the current project.

The second equally important aspect is the time delay in the signal propagation. The current model assumes that the change in the irradiation patters happens without any time delay, while actually the outer parts of the disk react with significant time delay of days, as is well known from reverberation studies of AGN continua (e.g., Collier et al. 1998; Sergeev et al. 2005; Cackett et al. 2007, 2020; Edelson et al. 2015, and the references therein). The response of the emission lines is delayed even more strongly as shown by numerous campaigns (e.g., Liutyi 1977; Collier et al. 1998; Kaspi et al. 2000; Peterson et al. 2004; Grier et al. 2017; Du et al. 2018), thus the final model has to include these effects, particularly in the case of relatively fast variations in the source.

Acknowledgements. We thank Alex Markowitz for helpful discussion and Giovanni Miniutti for providing the data for the source GSN 069 and very helpful comments to the manuscript. The project was partially supported by National Science Centre, Poland, Grant No. 2017/26/A/ST9/00756 (Maestro 9), and by the MNiSW grant DIR/WK/2018/12. Part of the work was done when BC was supported by a Durham Senior Research Fellowship COFUNDed between Durham University and the European Union under Grant agreement number 609412. E.B. and N.B. acknowledge the support of Serbian Ministry of Education, Science and Technological Development, contract number 451-03-68/2020/14/20002. The binned values were generated for this paper was generated using R Core Team (2019).

References

Abramowicz, M. A., Czerny, B., Lasota, J. P., & Szuszkiewicz, E. 1988, ApJ, 332, 646
Abramowicz, M. A., Chen, X., Kato, S., Lasota, J.-P., & Regev, O. 1995, ApJ, 438, L37
Alloin, D., Pelat, D., Phillips, M. M., Fosbury, R. A. E., & Freeman, K. 1986, ApJ, 308, 23
Baribaud, T., Alloin, D., Glass, I., & Pelat, D. 1992, A&A, 256, 375
Bentz, M. C., & Katz, S. 2015, PASP, 127, 67
Bentz, M. C., Denney, K. D., Cackett, E. M., et al. 2006, ApJ, 651, 775
Bianchi, S., Guainazzi, M., Matt, G., et al. 2005, A&A, 442, 185
Bisnovatyi-Kogan, G. S., & Lovelace, R. V. E. 1997, ApJ, 486, L43
Bon, E., Jovanović, P., Marziani, P., et al. 2012, ApJ, 759, 118
Bon, E., Zucker, S., Netzer, H., et al. 2016, ApJS, 225, 29
Breedt, E., McHardy, I. M., Arévalo, P., et al. 2010, MNRAS, 403, 605
Cackett, E. M., Horne, K., & Winkler, H. 2007, MNRAS, 380, 669
Cackett, E. M., Gelbord, J., Li, Y.-R., et al. 2020, ApJ, 896, 1
Capellupo, D. M., Netzer, H., Lira, P., Trakhtenbrot, B., & Mejía-Restrepo, J. 2015, MNRAS, 446, 3427
Chiang, J., & Blaes, O. 2003, ApJ, 586, 97
Cohen, R. D., Rudy, R. J., Puetter, R. C., Ake, T. B., & Foltz, C. B. 1986, ApJ, 311, 135
Collier, S. J., Horne, K., Kaspi, S., et al. 1998, ApJ, 500, 162
Combes, F., García-Burillo, S., Audibert, A., et al. 2019, A&A, 623, A79
Czerny, B. 2006, in AGN Variability from X-Rays to Radio Waves, IAU Symp., 360
Czerny, B., Schwarzenberg-Czerny, A., & Loska, Z. 1999, MNRAS, 303, 148
Czerny, B., Doroshenko, V. T., Nikołajuk, M., et al. 2003a, MNRAS, 342, 1222
Czerny, B., Nikołajuk, M., Różańska, A., et al. 2003b, A&A, 412, 317
Czerny, B., Siemiginowska, A., Janiuk, A., Nikiel-Wroczyński, B., & Stawarz, Ł. 2009, ApJ, 698, 840
Czerny, B., Wang, J.-M., Du, P., et al. 2019, ApJ, 870, 84
Dai, X., Stanek, K. Z., Kochanek, C. S., Shappee, B. J., & ASAS-SN Collaboration 2018, ATel, 11893, 1
De Rosa, G., Peterson, B. M., Ely, J., et al. 2015, ApJ, 806, 128
Dehghanian, M., Ferland, G. J., Kriss, G. A., et al. 2019a, ApJ, 877, 119
Dehghanian, M., Ferland, G. J., Peterson, B. M., et al. 2019b, ApJ, 882, L30
Denney, K. D., De Rosa, G., Croxall, K., et al. 2014, ApJ, 796, 134
Dexter, J., & Begelman, M. C. 2019, MNRAS, 483, L17
Di Gesu, L., Costantini, E., Ebrero, J., et al. 2015, A&A, 579, A42
Du, P., Zhang, Z.-X., Wang, K., et al. 2018, ApJ, 856, 6
Ebrero, J., Kaastra, J. S., Kriss, G. A., et al. 2016, A&A, 587, A129
Edelson, R. A., & Malkan, M. A. 1987, ApJ, 323, 516
Edelson, R., Gelbord, J. M., Horne, K., et al. 2015, ApJ, 806, 129
Edelson, R., Gelbord, J., Cackett, E., et al. 2017, ApJ, 840, 41
Fausnaugh, M. M., Denney, K. D., Barth, A. J., et al. 2016, ApJ, 821, 56
Ferreira, J., & Petrucci, P. O. 2011, in Jets at All Scales, eds. G. E. Romero, R. A. Sunyaev, & T. Belloni, IAU Symp., 275, 260
Gaskell, C. M., & Klimek, E. S. 2003, Astron. Astrophys. Trans., 22, 661
Gezari, S., Hung, T., Cenko, S. B., et al. 2017, ApJ, 835, 144
Giustini, M., Miniutti, G., & Saxton, R. D. 2020, A&A, 636, L2
Goad, M. R., Korista, K. T., De Rosa, G., et al. 2016, ApJ, 824, 11
Grier, C. J., Trump, J. R., Shen, Y., et al. 2017, ApJ, 851, 21
Gronkiewicz, D., & Różańska, A. 2020, A&A, 633, A35
Grzędzielski, M., Janiuk, A., Czerny, B., & Wu, Q. 2017, A&A, 603, A110
Guo, D. F., Hu, S. M., Tao, J., et al. 2014, Res. Astron. Astrophys., 14, 923
Hameury, J. M. 2019, Adv. Space Res., 66, 1004
Hirotani, K. 2018, Galaxies, 6, 122
Hryniewicz, K., Czerny, B., Nikołajuk, M., & Kuraszkiewicz, J. 2010, MNRAS, 404, 2028
Hutsemékers, D., González, B. A., Marin, F., et al. 2019, A&A, 625, A54
Iijima, T., Rafanelli, P., & Bianchini, A. 1992, A&A, 265, L25
Janiuk, A., & Czerny, B. 2007, A&A, 466, 793
Janiuk, A., Czerny, B., & Siemiginowska, A. 2002, ApJ, 576, 908
Kaspi, S., Maoz, D., Netzer, H., et al. 1996, ApJ, 470, 336
Kaspi, S., Smith, P. S., Netzer, H., et al. 2000, ApJ, 533, 631
Kaspi, S., Maoz, D., Netzer, H., et al. 2005, ApJ, 629, 61
Kawaguchi, T., Mineshige, S., Umemura, M., & Turner, E. L. 1998, ApJ, 504, 671
Kovačević, A. B., Pérez-Hernández, E., Popović, L. Č., et al. 2018, MNRAS, 475, 2051
Kozłowski, S., Kochanek, C. S., Ashby, M. L. N., et al. 2016, ApJ, 817, 119
Kriss, G. A., De Rosa, G., Ely, J., et al. 2019, ApJ, 881, 153
Kynoch, D., Ward, M. J., Lawrence, A., et al. 2019, MNRAS, 485, 2573
Lawrence, A., & Papadakis, I. 1993, ApJ, 414, L85
Lehto, H. J., Czerny, B., & McHardy, I. M. 1993, MNRAS, 261, 125
Lightman, A. P., & Eardley, D. M. 1974, ApJ, 187, L1
Liu, B. F., Taam, R. E., Meyer-Hofmeister, E., & Meyer, F. 2007, ApJ, 671, 695
Liutyi, V. M. 1977, Sov. Astron., 21, 655
Loska, Z., Czerny, B., & Szczerba, R. 2004, MNRAS, 355, 1080
Lu, K.-X., Du, P., Hu, C., et al. 2016, ApJ, 827, 118
MacLeod, C. L., Green, P. J., Anderson, S. F., et al. 2019, ApJ, 874, 8
Malkov, Y. F., Pronik, V. I., & Sergeev, S. G. 1997, A&A, 324, 904
Marcel, G., Ferreira, J., Petrucci, P. O., et al. 2018, A&A, 617, A46
Mathur, S., Gupta, A., Page, K., et al. 2017, ApJ, 846, 55
Mathur, S., Denney, K. D., Gupta, A., et al. 2018, ApJ, 866, 123
Matt, G., Guainazzi, M., & Maiolino, R. 2003, MNRAS, 342, 422
McHardy, I., & Czerny, B. 1987, Nature, 325, 696
McHardy, I. M., Papadakis, I. E., Uttley, P., Page, M. J., & Mason, K. O. 2004, MNRAS, 348, 783
McHardy, I. M., Koerding, E., Knigge, C., Uttley, P., & Fender, R. P. 2006, Nature, 444, 730
McHardy, I. M., Connolly, S. D., Horne, K., et al. 2018, MNRAS, 480, 2881
Mehdipour, M., Kaastra, J. S., Kriss, G. A., et al. 2015, A&A, 575, A22
Miniutti, G., Saxton, R. D., Giustini, M., et al. 2019, Nature, 573, 381

Nikolajuk, M., Papadakis, I. E., & Czerny, B. 2004, MNRAS, 350, L26
Noda, H., & Done, C. 2018, MNRAS, 480, 3898
Oknyanskij, V., & Lyuty, V. 2007, Peremennye Zvezdy Prilozhenie, 7, 28
Oknyanskij, V. L., Metlova, N. V., Huseynov, N. A., Guo, D.-F., & Lyuty, V. M. 2016, Odessa Astron. Publ., 29, 95
Oknyansky, V. L., Winkler, H., Tsygankov, S. S., et al. 2019, MNRAS, 483, 558
Papadakis, I., Kammoun, E., & Dovciak, M. 2019, Proceedings, 17, 12
Parker, M. L., Schartel, N., Grupe, D., et al. 2019, MNRAS, 483, L88
Peterson, B. M., Ferrarese, L., Gilbert, K. M., et al. 2004, ApJ, 613, 682
Peterson, B. M., Bentz, M. C., Desroches, L.-B., et al. 2005, ApJ, 632, 799
Petrucci, P. O., Gronkiewicz, D., Rozanska, A., et al. 2020, A&A, 634, A85
Planck Collaboration I. 2014, A&A, 571, A1
Pringle, J. E., Rees, M. J., & Pacholczyk, A. G. 1973, A&A, 29, 179
Qiao, E., & Liu, B. F. 2020, MNRAS, 492, 615
R Core Team 2019, R: A Language and Environment for Statistical Computing, R Foundation for Statistical Computing, Vienna, Austria
Raimundo, S. I., Vestergaard, M., Koay, J. Y., et al. 2019, MNRAS, 486, 123
Ross, N. P., Ford, K. E. S., Graham, M., et al. 2018, MNRAS, 480, 4468
Różańska, A., & Czerny, B. 2000, MNRAS, 316, 473
Różańska, A., Czerny, B., Życki, P. T., & Pojmański, G. 1999, MNRAS, 305, 481
Ruan, J. J., Anderson, S. F., Cales, S. L., et al. 2016, ApJ, 826, 188
Sergeev, S. G., Doroshenko, V. T., Golubinskiy, Y. V., Merkulova, N. I., & Sergeeva, E. A. 2005, ApJ, 622, 129
Sesar, B., Ivezić, Ž., Lupton, R. H., et al. 2007, AJ, 134, 2236
Shakura, N. I., & Sunyaev, R. A. 1973, A&A, 24, 337
Shakura, N. I., & Sunyaev, R. A. 1976, MNRAS, 175, 613
Shapovalova, A. I., Popović, L. Č., Collin, S., et al. 2008, A&A, 486, 99
Shapovalova, A. I., Popović, L. Č., et al. 2019, MNRAS, 485, 4790
Shappee, B. J., Prieto, J. L., Grupe, D., et al. 2014, ApJ, 788, 48
Sheng, Z., Wang, T., Jiang, N., et al. 2017, ApJ, 846, L7
Spruit, H. C., & Deufel, B. 2002, A&A, 387, 918
Starkey, D., Horne, K., Fausnaugh, M. M., et al. 2017, ApJ, 835, 65
Stern, D., McKernan, B., Graham, M. J., et al. 2018, ApJ, 864, 27
Storchi-Bergmann, T., Baldwin, J. A., & Wilson, A. S. 1993, ApJ, 410, L11
Taam, R. E., Liu, B. F., Yuan, W., & Qiao, E. 2012, ApJ, 759, 65
Trakhtenbrot, B., Arcavi, I., MacLeod, C. L., et al. 2019, ApJ, 883, 94
Ulrich, M.-H., Maraschi, L., & Urry, C. M. 1997, ARA&A, 35, 445
Uttley, P., McHardy, I. M., & Papadakis, I. E. 2002, MNRAS, 332, 231
Vaughan, S., Uttley, P., Markowitz, A. G., et al. 2016, MNRAS, 461, 3145
Woo, J.-H., & Urry, C. M. 2002, ApJ, 579, 530
Wu, Q., Czerny, B., Grzedzielski, M., et al. 2016, ApJ, 833, 79
Yang, Q., Wu, X.-B., Fan, X., et al. 2018, ApJ, 862, 109
Yuan, F., & Narayan, R. 2014, ARA&A, 52, 529

Chapter 3

Paper II: Modeling changing-look active galactic nuclei phenomenon in 1D using accretion disk instabilities

Received: 24 October 2021 | Accepted: 25 October 2021 | Published on: 11 November 2021

DOI: 10.1002/asna.20210065

Astronomische Nachrichten

PROCEEDING

Modeling changing-look active galactic nuclei phenomenon in 1D using accretion disk instabilities

Marzena Śniegowska[1,2] | **Mikołaj Grzędzielski**[2] | **Bożena Czerny**[2] | **Agnieszka Janiuk**[2]

[1]Nicolaus Copernicus Astronomical Center (PAN), Warsaw, Poland

[2]Center for Theoretical Physics, Polish Academy of Sciences, Warsaw, Poland

Correspondence
Marzena Śniegowska, Nicolaus Copernicus Astronomical Center (PAN), ul. Bartycka 18, 00-716 Warsaw, Poland.
Email: msniegowska@camk.edu.pl

Funding information
MNiSW, Grant/Award Number: DIR/WK/2018/12; Polish Funding Agency National Science Centre, Grant/Award Number: 2017/26/A/ST9/-00756 (MAESTRO 9)

Abstract

Apart from regular, low-level stochastic variability, some active galactic nuclei (AGN) occasionally show exceptionally large changes in the luminosity, spectral shape, and/or X-ray absorption. The most notable are the changes of the spectral type when the source classified as a Seyfert 1 becomes a Seyfert 2 galaxy or vice versa. Thus, a name was coined of "changing-look AGN" (CL AGN). The origin of this phenomenon is still unknown, but for most of the sources, there are strong arguments in favor of the intrinsic changes. Understanding the nature of such rapid changes is a challenge to the models of black hole accretion flows since the timescales of the changes are much shorter than the standard disk viscous timescales. We aim to model the CL AGN phenomenon assuming that the underlying mechanism is the time-dependent evolution of a black hole accretion disk unstable due to the dominant radiation pressure. We use a one-dimensional, vertically integrated disk model, but we allow for the presence of the hot coronal layer above the disk and the presence of the inner purely hot flow. We focus on the variability timescales and amplitudes, which can be regulated by the action of large-scale magnetic fields, the description of the disk-corona coupling and the presence of an inner optically thin flow, like advection-dominated accretion flow. We compare model predictions for the accretion disk around black hole mass $10^7\ M_\odot$.

KEYWORDS

accretion, accretion disks, viscosity

1 | INTRODUCTION

In the simplest theoretical framework, active galactic nuclei (AGN) are sources in which a supermassive black hole is surrounded by a geometrically thin, optically thick accretion disk Shakura & Sunyaev (1973). For some objects, though, modifications to accretion disk, like advection-dominated accretion flow (ADAF) or slim accretion disks (for review see Czerny 2019), are needed to better represent the observed spectra. AGN also show variability in different timescale, pattern and wavelengths like X-ray (Lawrence & Papadakis 1993), optical (Sesar et al. 2007), and infrared (Kozłowski et al. 2016) bands.

Generally, in accretion disk, heating processes are mediated by the turbulent magnetic field. Thus, the stochastic variability observed in light curves of AGN is not surprising. However, objects with significant changes in the luminosity and the noticeable (dis)appearance of broad emission lines are less likely to be explained by stochastic variability. They are called changing-look (CL) AGN and

the discussion about their physical nature is coming under scrutiny in recent years.

In this paper, we focus on accretion disk around supermassive black holes ($10^7\ M_\odot$). The variations in global accretion rate in this kind of accretion disks are one of the candidates for CL AGN physical explanation. However, it seems that those objects may be explained by different scenarios and just one explanation for them is not likely. CL AGN differ between each other in the shape of the light curve, timescale of changes, and its amplitude. For example, changes in some objects (like Mrk 590 Kokubo & Minezaki 2020) can be explained by the extrinsic matter, which causes the dimming of the flux and spectral changes. Whereas, for others (like in sources investigated by Hutsemékers et al. 2019), the obscuration is ruled out because of no changes in polarization degree, which should appear if we assume dusty matter is temporary obscuring the source. Thus, intrinsic changes are in favor to explain it in most cases. Intrinsic changes in accretion disks are rather a broad concept and may include scenarios with tidal disruption events (i.e SDSS J224113-012108 investigated by Zhang 2021), tidal interaction between disks in supermassive black hole binaries (Wang & Bon 2020), the presence and disappearance of the warm corona (Noda & Done 2018), changes in the magnetization of accretion disk Scepi et al. (2021), or magnetic accretion disk-outflows (Feng et al. 2021). The rapidly increasing number of observations of CL AGN (Graham et al. 2020; MacLeod et al. 2016; Sánchez-Sáez et al. 2021) and variety of possible scenarios of changes motivates us to explore this field.

To model CL AGN phenomenon (especially for objects with repetitive outbursts), we assume the radiation pressure instability mechanism. In the current work, we use time-evolution code GLADIS (Global Accretion Disk Instability Simulation) developed by Janiuk et al. (2002) (recently publicly available version is presented in Janiuk 2020), which allows performing a time-dependent simulation of accreting matter onto massive objects. This code was already used to model the "heartbeat" outbursts in microquasars (e.g. for IGR J17091-3624 by Janiuk et al. 2015) as caused by radiation pressure instabilities. The idea of explaining the changes in CL AGN with the radiation pressure instability was used in Sniegowska et al. (2020); however, the concept of the geometry of the system was very simplistic, reducing the unstable region to a single zone both in radial and vertical direction. In this work, we explore the instability using 1-D radially resolved model. In Figure 1, we present the scheme of the model, which we use. This model contains the advection-dominated accretion flow (ADAF) in which hot coronal matter is freely advected inwards, the unstable standard cold disk zone radially resolved, the stable outer

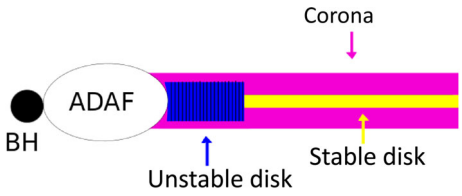

FIGURE 1 The schematic view of the model sliced through the disk plane: from the left black hole marked as a black circle, and inner hot ADAF, disk part, which is unstable due to radiation pressure instability marked in blue, with black stripes to emphasize radial grid, and outer cold stable disk represented as a yellow area. The corona, which is covering the disk is shown in magenta

disk and the geometrically thick, optically thin corona above the disk. Therefore, in comparison to Sniegowska et al. (2020), this model is extended by two important aspects: (i) the presence of the disk corona, and (ii) radially resolved unstable cold disk. The grid in the unstable zone is improving the model, because the ring in which instabilities are present is not artificially limited in its size. Disk instabilities in system disk-corona interacting were investigated for the microquasar GRS 1915 + 105 by Janiuk & Czerny (2005), with the disk/corona mass exchange model developed later on Janiuk & Czerny (2007) for variability in X-ray binaries in their soft state and AGN. The presence of the inner ADAF was not included in these papers. The structure of the paper is as follows: In Section 2, we introduce the physical assumptions, which we use throughout this work for three computed models. In Section 3, we show and describe the preliminary cycle-behavior time-dependent model results. Finally, in Section 4, we conclude on the current results and comment on the plans for future work.

2 | THEORY

In the standard accretion disk theory, (Shakura & Sunyaev 1973) the assumption of the radiation pressure dominance leads to the accretion disk instability (thermal and viscous), which was shown by Pringle et al. (1973) and Lightman & Eardley (1974). Those instabilities may appear in the broad range of black hole masses' objects.

Outbursts that may appear due to radiation pressure instabilities in microquasars (masses $\approx 10\ M_\odot$) were explored by Janiuk et al. (2002). This kind of instabilities in objects with central black hole mass up to $10^8\ M_\odot$ was further described by Grzędzielski et al. (2017). The latter work gives also the quantitative prescriptions for estimating periods and amplitudes of outbursts. We use those prescriptions to discuss the predicted limits of the minimum period for black hole mass of $10^7\ M_\odot$.

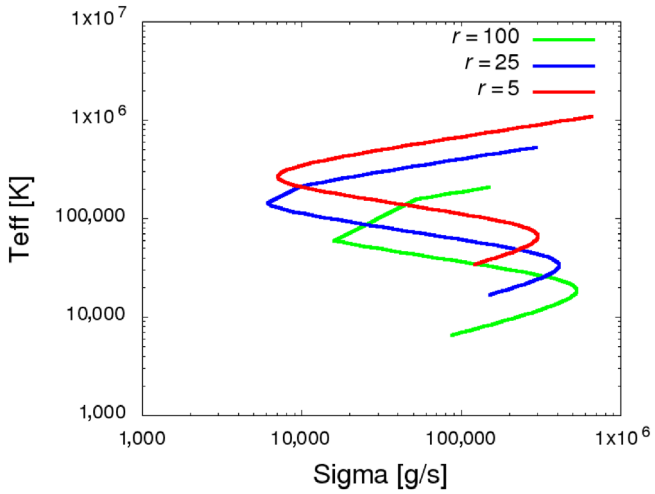

FIGURE 2 Local stability curves for black hole mass $10^7 M_\odot$, $\alpha = 0.02$ and different radii from the top: $5R_{\rm Schw}$ marked as red curve, $25R_{\rm Schw}$ marked as blue curve and $100R_{\rm Schw}$ marked as green curve

2.1 | S-curve as the signpost for the initial conditions

A stability curve, in general, is a sequence of stationary solutions to equations of disk structure equations, solved locally for surface density and temperature. Before we perform the time-dependent simulation with the GLADIS code, we compute the stability S-curves in an effective temperature—surface density plane to get an overall picture (see Figure 2). From the shape of the S-curve and specifically the range of its unstable branch (i.e., the negative slope of $T - \Sigma$ dependence), we infer the information about the amplitudes and timescales of outbursts. Along the unstable branch, the higher accretion rates correspond to smaller surface densities. The position of the curve depends on the radius. Hence, by changing the distance from the central source at a fixed temperature, we switch between the stable and unstable branch. Note, however, that the local effective temperature scales with the radius and the local accretion rate; hence at a fixed accretion rate, the (sufficiently large) outer disk is always located at a stable branch. By investigating S-curves behavior before running the time evolution code, we predict proper initial conditions and model parameters, which allow us to obtain instability of a desired range.

2.2 | Set-up of the model

The two time-dependent equations adopted by GLADIS code are equations of hydrodynamics for surface density and temperature evolution under assumptions of energy conservation, viscous diffusion, and radiation pressure dominance (see eqs 3.1 and 3.2 in Janiuk (2020)).

In this work, we investigate three possible scenarios of mass exchange and evaporation:

- Mass exchange between disk and corona is on, and disk evaporation is due to the flux generated in the disk and the corona—case A (see Janiuk & Czerny 2005, their eq. 17, with coefficients $B_1 = 0.5$, $B_2 = 0.5$). This description represents the disk evaporation due to the electron conduction between the disk and the corona.
- Mass exchange between disk and corona is on, and disk evaporation is due to magnetic field—case B (see Janiuk & Czerny 2007, their eq. 10, their case B). This description represents the corona heated by the magnetic buoyancy.
- Mass exchange between disk and corona is off, which implies no disk evaporation—case C.

For all calculated models in this work, we assume that the heating term is proportional to the total pressure, as was assumed by Shakura & Sunyaev (1973).

We fix the following physical parameters throughout all the computed models: the black hole mass $10^7\ M_\odot$, viscosity coefficient $\alpha = 0.02$ for disk and corona after Grzędzielski et al. (2017), global accretion rate as 0.007 solar masses per year, the inner radius of the disk 20 $R_{\rm Schw}$, and the outer radius of the disk 100 $R_{\rm Schw}$. We discuss this issue later. Corona temperature is fixed at the virial temperature, whereas the temperature of the disk evolves in time. The total duration of each simulation is 274 years in the source time.

3 | RESULTS

In this section, we compare the properties of time-dependent models for different underlying assumptions. We calculate three solutions based on different assumptions about the disk/corona mass exchange (see Section 2.2).

3.1 | The outburst cycle

The example of outburst for the object with the black hole mass $10^7\ M_\odot$ is shown in Figure 3. The luminosities (for disk and for corona) presented in this work are the integrated radiation flux between inner and outer radius.

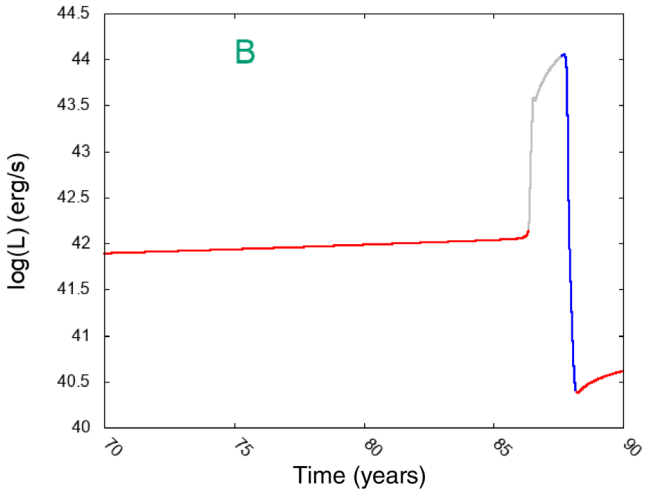

FIGURE 3 The exemplary fragment of the disk lightcurve with cycle-steps marked for black hole mass $10^7 M_\odot$, $R_{\rm in} = 20R_{shw}$ and $R_{\rm out} = 100R_{\rm shw}$ for case B. The gray part of the light curve represents heating phase, the blue one advective phase and the red one diffusive phase. Note that we present in this plot just part of the diffusive phase, not the full cycle

Each outburst has three characteristic phases[1]:

1. Viscous phase (red part of the lightcurve), in which the approximate thermal equilibrium holds, and the surface density increases till the system meets the loss of equilibrium (lower branch in the S-curve).
2. Heating phase and hot viscous phase (the gray part of the lightcurve), when the temperature in the inner regions of the disk increases rapidly, and the accretion rate is enhanced, the system then evolves along the upper S-curve branch till the turning point of the S-curve is met.
3. Cooling phase (blue part of the lightcurve), where the temperature and accretion rate drop-down till the lower branch of the S-curve is achieved.

Outbursts can be then characterized by the amplitude, the period, and the relative duration of the outburst in comparison with the total period, as discussed by Grzędzielski et al. (2017) for their set of models.

3.2 | Time-dependent solutions

In Figure 4, we show the modeled lightcurves of the disk (marked in gray) and the corona (marked as red dotted line). This calculation is representative for objects with observed repetitive outbursts (like NGC 1566, with $\log(M) = 6.92\ M_\odot$ (Woo & Urry 2002)). We fixed the viscosity coefficient in the disk and corona $\alpha = 0.02$ for both, as we stress out in Section 2.2. We concentrate on the comparison of the three physical scenarios included in the model. The lightcurve for corona is shown only in cases when disk-corona mass exchange was used in computations. In the first model (left panel of Figure 4—case A), for assumed physical parameters disk and corona are stabilized. No outbursts are seen, and the system simply evolves from the initial conditions to the equilibrium solution. For two other investigated scenarios, outbursts are present. The characteristic three phases of the outbursts are thus visible both when the disk/corona coupling is described by magnetic buoyancy (middle panel of Figure 4—case B) as well as for model with no corona included (right panel of Figure 4—case C). The diffusive phase is the longest of the three phases.

The outbursts in both cases are very strong, with the amplitude (the ratio of the maximum to the minimum flux in the disk $\frac{L_{max}}{L_{min}}$) $\approx 10^4$. The period of the outburst for case B is 156 years. Flare duration to period ratio is 0.006.

For corona in case B (see Figure 5 for the expanded illustration of both disk and corona outburst), the luminosity starts to increase ≈0.5 year before the disk's outburst and gets to the lowest luminosity level ≈0.5 year before the disk's dimming, so the period of the outburst is the same for corona and accretion disk. The relative amplitude, in this case, is 50, and the flare duration to period ratio is 0.009. Thus for these specific model parameters, the outbursts should be seen predominantly in the UV band, with more moderate outbursts in X-ray. In case C, the relative amplitude of the outburst is 5000, by a factor 2 smaller than for case B, with the period of 147 years, which is shorter than in case B. Flare duration to period ratio is 0.007.

4 | DISCUSSION

We performed simulations of the disk/corona/inner ADAF system (see Figure 1) under the radiation pressure instability in order to check if this mechanism can explain the CL behavior, as proposed by Sniegowska et al. (2020). In the preliminary one-zone model of Sniegowska et al. (2020), the expected timescales were much shorter than the local viscous timescale due to the narrowness of the instability zone. In the present computations, the outer radius is set at 100 R_{Schw}, and the extension of the instability zone is determined numerically. During the outburst, the larger part of the disk becomes a subject of instability than just the narrow unstable zone as described by the stationary S-curves (see e.g. Grzędzielski et al. 2017). Therefore, the timescales cannot be arbitrarily shortened by selecting the

[1]Due to limitations in computing time, we decided to keep outer radius in this position, however, unstable zones are more extended (see Janiuk & Czerny (2011)).

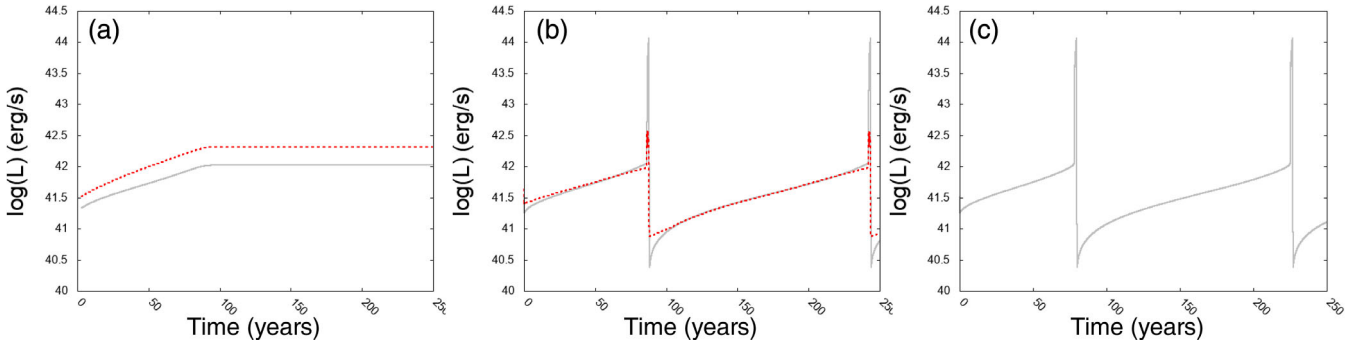

FIGURE 4 Comparison of the modeled variations, for disc (gray line) and corona (red dotted line) luminosity time evolution for $10^7\ M_\odot$ for three scenarios: case A—mass exchange between disk and corona is on and mass evaporation is due to the electron conduction (left panel), case B—mass exchange between disk and corona is on and mass evaporation is due to magnetic buoyancy (middle panel), and case C—mass exchange between disk and corona is off (right panel)

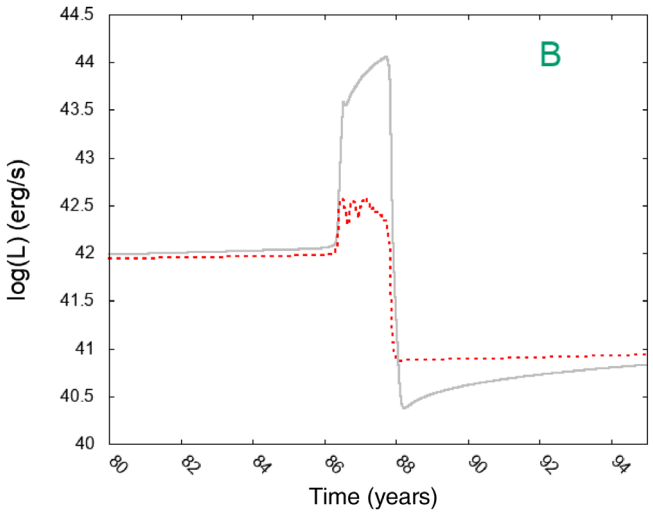

FIGURE 5 The exemplary fragment of the disk (marked in gray) and corona (marked as dotted red line) lightcurve for case B

specific accretion rate and the transition radius between the disk/corona part and the inner ADAF. Here, we show only one example for the global parameter values (black hole mass $10^7 M_\odot$, $\dot{m} = 0.007$) but the same holds for other values of the black hole and accretion rates (Sniegowska et al., in preparation).[2]

We show that the model is actually sensitive to various assumptions about the role of the electron conduction and/or magnetic field inside the disk, and the description of the mass exchange between the disk and the corona. The disk is stabilized in model A. The outbursts are slightly shorter if the mass exchange between the disk and the corona is turned off (see Figure 4). The duration of the outburst in the presented model is very short in comparison with the separation of outbursts.

The timescales derived in Section 3.2 are the order of 150 years, shorter than the outbursts timescales obtained by Grzedzielski et al. (2017) in case of modified viscosity (using the maximum to the minimum luminosity in the outburst from Figure 4 and using with eq. 31 of Grzedzielski et al. (2017), we obtain 7,000 years). This effect is not related to the presence of the corona, which also transports a fraction of the accreting material, but most of the effect is due to the small outer disk radius used in current computations. Radiation pressure instabilities mechanism would lead to outbursts of the much larger part of the disk than $100R_{\rm Schw}$ (which we consider in this work as the outer radius of simulated accretion disk). We checked that by computing one more model for case B, adopting the outer radius at 80 $R_{\rm Schw}$, and those computations gave a total period of 85 years, and apparently, the outer radius is the most critical parameter of the current model.

This is a very interesting aspect of the model, but we currently cannot address properly it without considerable modification of the GLADIS code. Currently, we assume that the outer disk is stationary. If the disk outer radius is indeed very small since the event is related to tidal disruption event, we would need to model the whole disk as initially a ring, with a freely expanding outer radius due to the viscous evolution. We will address this in the future.

Those results are not yet ready for detailed comparison with the lightcurve for observed AGN, because the calculated zone is not extended enough to do so. In the incoming paper (Sniegowska et al., in preparation), we will study a much broader parameter range. However, they show the critical role of the outer disk radius, and, on the other hand, a moderate dependence of the modifications of the description of the disk structure. This second aspect is very promising for the future, since the disk structure,

[2]As a flare duration, we assume the time between $(L_{\rm max} + L_{\rm min})/2$ approached during the rise of the outburst, and $(L_{\rm max} + L_{\rm min})/2$ approached during the dimming, following parametrization from Grzędzielski et al. (2017).

corona formation, and the transition to ADAF are still subject to vigorous modeling, both numerical and analytical or semi-analytical.

Summarizing, we see from the simulations presented in this paper that the timescales of the order of years can be recovered from the model, after proper adjustment of the parameters. However, rapid oscillations discovered recently in two sources and named the quasi-periodic ejections seem to be beyond the reach of the radiation pressure instability model. Below we include a short discussion of these observed phenomena.

4.1 | Case study—timescales in NGC 1566

NGC 1566 is one of the sources in which outbursts seem to appear semi-repetitively, in the timescales of years, it is thus a source, which may be modeled by radiation pressure instability, as postulated by Sniegowska et al. (2020). First observations of the source, which report optical variability are obtained by Quintana et al. (1975). Later, changes in $H\beta$ and $H\alpha$ lines were detected, as well as the change in spectral continuum Alloin et al. (1985). Monitoring of those changes was continued by Alloin et al. (1986).

New changes (hard X-ray emission) in this source were detected by Ducci et al. (2018) with INTEGRAL (Winkler et al. 2003) mission and then followed up with using SWIFT observatory data by Ferrigno et al. (2018). Those observations were complemented by photometry and spectroscopy later on. Oknyansky et al. (2019) report the increase in the luminosity by 25–30 times in June 2018, which was followed by smaller outbursts and makes this source even more interesting.

Jana et al. (2021) analyze *XMM-Newton* (Jansen et al. 2001), *NuSTAR* (Harrison et al. 2013) and *Swift* (Evans et al. 2009) X-ray band archival observations of NGC 1566 from the period between 2015 and 2019.

Amplitudes in the X-ray band change by the factor of 70, whereas bolometric luminosity by the factor of 25. Our models shown in Figure 4 imply higher amplitude in the UV band, but by searching the parameter space, we can possibly find more suitable solutions. The timescales of the order of a few years are also longer than what we show in Figure 4, but allowing for higher viscosity parameter, adjusting the parameters in such a way as to get lower outburst amplitude, and (more importantly) for still lower outer radius, we could shortened the period. Using the timescale for radiation pressure dominated outburst from Grzędzielski et al. (2017) for the 10^7 solar masses and change in luminosity factor as 25 for this source we get 135 years as the minimal timescale of outburst. However, in this paper, modified viscosity was used (which in general shortened the period) but the outer radius was large allowing for unconstrained radial development of the outburst. A smaller outer radius in these models also could easily shorten the period to the requested few years timescale.

4.2 | Case study—timescales in RX J1301.9 + 2747

The regular quasi-periodic eruptions were discovered so far in two sources (Giustini et al. 2020; Miniutti et al. 2019). The second of these two papers brings the discovery of regular X-ray outbursts in the timescales of the order of 5 h. The black hole mass in this source ($\sim 10^6 M_\odot$) is lower than the value used in our simulations ($\sim 10^7 M_\odot$), so the timescales from the model should be scaled down by (at least) the mass ratio. However, such short timescales cannot be reached within the frame of the radiation pressure instability model considered in this paper. As discussed by Giustini et al. (2020), the underlying mechanism requires a large height to radius ratio, that is, the instability must happen not in the cold disk zone but (most likely) in the warm corona. In our model, we have only hot corona at local virial temperature, which is stable, and the warm corona is not present. Hints for thermal instabilities come from the problems to derive stationary warm corona solutions for some parameter range (see Gronkiewicz & Różańska 2020) but no time-dependent models are available so far.

5 | SUMMARY

In this work:

- We perform the full computations of time-dependent evolution of the accretion disk induced by the radiation pressure using GLADIS code.
- We confirm that it is possible to obtain limit-cycle oscillations for the black hole mass 10^7 $M_\odot$ using this model.
- Inclusion of the inner ADAF and coronal flow does not shorten the outburst.
- The timescales from the model are not very sensitive to the disk/corona coupling if outbursts are present, but the amplitudes do change.
- The outburst timescales shorten strongly with the decrease of the outer disk radius.
- The phenomenon of CL AGN seems to be complex and challenging to model, since observed objects show different behaviors. The radiation pressure model may describe (after further modifications) the yearly variability in the sources like NGC 1566, but most probably,

a different mechanism must account for quasi-periodic ejections.

However, these results require confirmation, with testing the different resolution. The code is grid-based, and such hydrodynamical codes are known to have resolution-dependent convergence.

ACKNOWLEDGMENTS

MS acknowledges the organizers and participants of 13th Serbian Conference on Spectral Line Shapes in Astrophysics for the fruitful discussion and comments, which help to improve this work. BC and MS acknowledge the financial support from the Polish Funding Agency National Science Centre, project 2017/26/A/ST9/-00756 (MAESTRO 9) and MNiSW grant DIR/WK/2018/12.

The package (tar.gz) with the source code GLADIS is available at http://www.cft.edu.pl/astrofizyka/ under tab numerics.

ORCID

Marzena Śniegowska https://orcid.org/0000-0003-2656-6726

REFERENCES

Alloin, D., Pelat, D., Phillips, M., & Whittle, M. 1985, *ApJ*, *288*, 205.

Alloin, D., Pelat, D., Phillips, M. M., Fosbury, R. A. E., & Freeman, K. 1986, *ApJ*, *308*, 23.

Czerny, B. 2019, *Universe*, *5*(5), 131.

Ducci, L., Siegert, T., Diehl, R., Sanchez-Fernandez, C., Ferrigno, C., Savchenko, V., & Bozzo, E. 2018, June. *The Astronomer's Telegram*, 11754, 1.

Evans, P. A., Beardmore, A. P., Page, K. L., et al. 2009, *Mon. Not. R. Astron. Soc.*, *397*(3), 1177. https://doi.org/10.1111/j.1365-2966.2009.14913.x.

Feng, J., Cao, X., Li, J.-W., & Gu, W.-M. 2021, *ApJ*, *916*(2), 61.

Ferrigno, C., Siegert, T., Sanchez-Fernandez, C., Kuulkers, E., Ducci, L., Savchenko, V., & Bozzo, E. 2018, June, *The Astronomer's Telegram*, 11783, 1.

Giustini, M., Miniutti, G., & Saxton, R. D. 2020, *A&A*, *636*, L2.

Graham, M. J., Ross, N. P., Stern, D., et al. 2020, *MNRAS*, *491*(4), 4925.

Gronkiewicz, D., & Różańska, A. 2020, *A&A*, *633*, A35.

Grzędzielski, M., Janiuk, A., Czerny, B., & Wu, Q. 2017, *A&A*, *603*, A110.

Harrison, F. A., Craig, W. W., Christensen, F. E., et al. 2013, *ApJ*, *770*(2), 103.

Hutsemékers, D., Agís González, B., Marin, F., Sluse, D., Ramos Almeida, C., & Acosta Pulido, J. A. 2019, *A&A*, *625*, A54.

Jana, A., Kumari, N., Nandi, P., et al. 2021, *MNRAS*, *507*(1), 687.

Janiuk, A. 2020, December. GLADIS: GLobal Accretion Disk Instability Simulation. Multifrequency Behaviour of High Energy Cosmic Sources—XIII. June 3–8, 2019. Palermo p. 48.

Janiuk, A., & Czerny, B. 2005, *MNRAS*, *356*(1), 205.

Janiuk, A., & Czerny, B. 2007, *A&A*, *466*(3), 793.

Janiuk, A., & Czerny, B. 2011, *MNRAS*, *414*(3), 2186.

Janiuk, A., Czerny, B., & Siemiginowska, A. 2002, *ApJ*, *576*, 908.

Janiuk, A., Grzedzielski, M., Capitanio, F., & Bianchi, S. 2015, *A&A*, *574*, A92.

Jansen, F., Lumb, D., Altieri, B., et al. 2001, *A&A*, *365*, L1.

Kokubo, M., & Minezaki, T. 2020, *MNRAS*, *491*(4), 4615.

Kozłowski, S., Kochanek, C. S., Ashby, M. L. N., et al. 2016, *ApJ*, *817*, 119.

Lawrence, A., & Papadakis, I. 1993, *ApJ*, *414*, L85.

Lightman, A. P., & Eardley, D. M. 1974, *ApJ*, *187*, L1.

MacLeod, C. L., Ross, N. P., Lawrence, A., et al. 2016, *MNRAS*, *457*(1), 389.

Miniutti, G., Saxton, R. D., Giustini, M., et al. 2019, *Nature*, *573*(7774), 381.

Noda, H., & Done, C. 2018, *MNRAS*, *480*, 3898.

Oknyansky, V. L., Winkler, H., Tsygankov, S. S., et al. 2019, *MNRAS*, *483*(1), 558.

Pringle, J. E., Rees, M. J., & Pacholczyk, A. G. 1973, *A&A*, *29*, 179.

Quintana, H., Kaufmann, P., & Sasic, J. L. 1975, *MNRAS*, *173*, 57P.

Sánchez-Sáez, P., Lira, H., Martí, L. et al. 2021, *arXiv e-prints*, arXiv:2106.07660.

Scepi, N., Begelman, M. C., & Dexter, J. 2021, *MNRAS*, *502*(1), L50.

Sesar, B., Ivezi¢, Z., Lupton, R. H., et al. 2007, *AJ*, *134*, 2236.

Shakura, N. I., & Sunyaev, R. A. 1973, *A&A*, *24*, 337.

Sniegowska, M., Czerny, B., Bon, E., & Bon, N. 2020, *A&A*, *641*, A167.

Wang, J.-M., & Bon, E. 2020, *A&A*, *643*, L9.

Winkler, C., Courvoisier, T. J. L., Di Cocco, G., et al. 2003, *A&A*, *411*, L1.

Woo, J.-H., & Urry, C. M. 2002, *ApJ*, *579*, 530.

Zhang, X.-G. 2021, *MNRAS*, *500*(1), L57.

AUTHOR BIOGRAPHY

Marzena Śniegowska is a Current PhD student at Nicolaus Copernicus Astronomical Center Polish Academy of Sciences. Her main field of research are spectroscopy of Active Galactic Nuclei, and modeling the variability of an accreting disk around a black hole (stellar or supermassive).

How to cite this article: Śniegowska, M., Grzędzielski, M., Czerny, B., & Janiuk, A. 2022, *Astron. Nachr.*, *343*, e210065. https://doi.org/10.1002/asna.20210065

Part III

Chemical evolution in highly accreting quasars: metal enrichment on galactic and supergalactic scales?

Chapter 4

Paper III: High Metal Content of Highly Accreting Quasars

The Astrophysical Journal, 910:115 (33pp), 2021 April 1 https://doi.org/10.3847/1538-4357/abe1c8

High Metal Content of Highly Accreting Quasars

Marzena Śniegowska[1,2], Paola Marziani[3], Bożena Czerny[2], Swayamtrupta Panda[1,2], Mary Loli Martínez-Aldama[2], Ascensión del Olmo[4], and Mauro D'Onofrio[5]
[1] Nicolaus Copernicus Astronomical Center, Polish Academy of Sciences, Bartycka 18, 00-716 Warsaw, Poland; msniegowska@camk.edu.pl
[2] Center for Theoretical Physics, Polish Academy of Sciences, Al. Lotników 32/46, 02-668 Warsaw, Poland
[3] Istituto Nazionale di Astrofisica (INAF), Osservatorio Astronomico di Padova, I-35122 Padova, Italy
[4] Instituto de Astrofísica de Andalucía (IAA- CSIC), Glorieta de Astronomía, E-18080 Granada, Spain
[5] Dipartmento di Fisica & Astronomia, Università di Padova, Padova, Italy
Received 2020 September 28; revised 2021 January 13; accepted 2021 January 26; published 2021 April 2

Abstract

We present an analysis of UV spectra of 13 quasars believed to belong to extreme Population A (xA) quasars, aimed at the estimation of the chemical abundances of the broad-line-emitting gas. Metallicity estimates for the broad-line-emitting gas of quasars are subject to a number of caveats; xA sources with the strongest Fe II emission offer several advantages with respect to the quasar general population, as their optical and UV emission lines can be interpreted as the sum of a low-ionization component roughly at quasar rest frame (from virialized gas), plus a blueshifted excess (a disk wind), in different physical conditions. Capitalizing on these results, we analyze the component at rest frame and the blueshifted one, exploiting the dependence of several intensity line ratios on metallicity Z. We find that the validity of intensity line ratios as metallicity indicators depends on the physical conditions. We apply the measured diagnostic ratios to estimate the physical properties of sources such as density, ionization, and metallicity of the gas. Our results confirm that the two regions (the low-ionization component and the blueshifted excess) of different dynamical conditions also show different physical conditions and suggest metallicity values that are high, and probably the highest along the quasar main sequence, with $Z \sim 20-50\ Z_{\odot}$, if the solar abundance ratios can be assumed constant. We found some evidence of an overabundance of aluminum with respect to carbon, possibly due to selective enrichment of the broad-line-emitting gas by supernova ejecta.

Unified Astronomy Thesaurus concepts: Quasars (1319); Active galactic nuclei (16); Radio quiet quasars (1354)

1. Introduction

Thanks to large public databases such as the Sloan Digital Sky Survey (SDSS), we have unrestricted access to a large wealth of astronomical data (e.g., several editions of quasar catalogs, Schneider et al. 2010; Pâris et al. 2017; and of value-added measurements by Shen et al. 2011). SDSS spectra of high-redshift quasars ($z \gtrsim 2$) cover the rest-frame UV spectral range. It has been known since the 1970s that measurements of UV emission lines can be used to explore the physical and chemical properties of active galactic nuclei (AGNs). Landmark papers provided the basic understanding of line formation processes due to photoionization (e.g., Davidson & Netzer 1979; Wills & Netzer 1979; Baldwin et al. 2003).

The chemical composition of the line-emitting gas is an especially intriguing problem from the point of view of the evolution of cosmic structures, but also from the technical side. Nagao et al. (2006b) investigated BLR metallicities using various emission-line flux ratios and claimed that the typical metallicity of the gas in that region is at least supersolar, with typical $Z \sim 5\ Z_{\odot}$. Moreover, studies of metallicity−redshift dependence (Nagao et al. 2006b; Juarez et al. 2009) show a lack of metallicity evolution up to $z \approx 5$. Similar results are obtained for Nagao et al. (2006a). The highest-redshift quasars ($z \gtrsim 5$; e.g., Bañados et al. 2016; Nardini et al. 2019) are known to show UV spectra remarkably similar to the ones observed at low redshift, especially the ones accreting at a high rate and radiating at high Eddington ratio (Diamond-Stanic et al. 2009; Plotkin et al. 2015; Sulentic et al. 2017).[6] Perhaps surprisingly, these sources are suspected to have high metal content in their line-emitting gas, due to the consistent values of several diagnostic ratios measured in quasars with similar spectral properties at low and high z (Martínez-Aldama et al. 2018a), and indicating highly supersolar metal content.

Several techniques are applied to estimate the chemical composition in Galactic nebulae (see, e.g., Feibelman & Aller 1987 for planetary nebulae). Classical techniques used for H II and other nebulae (including the narrow-line regions (NLRs)) are unfortunately not applicable to the broad-line regions of quasars. Permitted and intercombination lines are too broad to resolve fine-structure components of doublets; line profiles are composites and may originate in regions that are spatially unresolved, and unresolved or only partially resolved in radial velocity as well.

However, quasar emission-line profiles still offer important clues in the radial velocity domain. The shape of the profile is strongly dependent on the ionization potential of the ionic species from which the line is emitted: it is expedient to subdivide the broad lines in low- and high-ionization lines (LILs and HILs). The LIL group in the spectral range under analysis (1200–2000 Å) includes the following lines: Si II λ1263, Si II λ1814, Al II λ1671, Al III λ1860, Si III] λ1892, and C III] λ1909. High-ionization lines are N IV] λ1486, O IV] λ1402, C IV λ1549, Si IV λ1397, O III] λ1663, and He II λ1640 (for detailed discussion see Collin-Souffrin & Lasota 1988; Collin-Souffrin et al. 1988; Gaskell 2000). The Al III, Si III], and C III] lines are sometimes referred to as "intermediate-ionization lines": even if they are mainly produced within the fully ionized region of the emitting gas clouds (Negrete et al. 2012), the ionization potential of their

[6] The effect is most likely due to a bias: for a flux-limited sample, the highest radiators at a given black hole mass are the ones that remain detectable at highest z (Sulentic et al. 2014).

ionic species is closer to the ones of the LILs, and typically $\lesssim$20 eV.

Not only do the two groups of lines (HILs and LILs) show different kinematic properties (Sulentic et al. 1995), but their emission is also likely to occur in fundamentally different physical conditions (Marziani et al. 2010). The HILs are characterized also by the evidence of strong blueshifted emission, very evident in C IV (e.g., Sulentic et al. 2007; Richards et al. 2011; Coatman et al. 2016). Therefore, a careful line comparison/decomposition is necessary, lest inferences may be associated with a nonexistent region with inexplicable properties.

The interpretation of two line components involves a virialized region, of relatively low ionization (hereafter referred to as the virialized, low-ionization BLR associated with a symmetric broad component (BC)), possibly including emission from the accretion disk, and a region of higher ionization, associated with a disk wind or a clumpy outflow, a scenario first proposed by Collin-Souffrin et al. (1988) and further developed by Elvis (2000), and observationally supported by reverberation mapping (e.g., Peterson & Wandel 1999) and the apparent lack of correlation between HILs and LILs in luminous quasars (e.g., Mejía-Restrepo et al. 2016; Sulentic et al. 2017). Even if all lines were emitted by a wind (Murray et al. 1995; Murray & Chiang 1997; Proga 2007a), the conditions at the base of the wind may strongly differ from the ones downstream in the outflow.

While each UV metal line contains information related to composition (Hamann & Ferland 1992), not all of the lines listed above can be used in practice. For instance, the N V and Si II λ1263 lines are strongly affected by blending with Lyα; other lines, such as Si II λ1814 and N IV] λ1486, are usually weak and require high signal-to-noise ratio (S/N) to be properly measured. The choice of diagnostic ratios used for metallicity estimates will be a compromise between S/N, easiness of deblending, and straightforwardness of physical interpretation. In practice, apart from Lyα, only the strongest broad features will be considered as potential metallicity estimators in this work (Section 3). The ratio (Si IV + O IV])/C IV has been widely used in past studies (Hamann & Ferland 1999 and references therein); this ratio is relatively easy to measure and seems to be the most stable ratio against distribution of gas densities and ionization parameter in the BLR (Nagao et al. 2006b). The ratios involving N V λ1240, like N V/C IV, are sensitive to ionization parameter and to nitrogen abundance (e.g., Dietrich et al. 2003; Wang et al. 2012a). We will rediscuss the use of these ratios in the context of the xA quasar spectral properties (Section 5.8).

Both physical conditions and chemical abundances vary along the quasar main sequence (see, e.g., Sulentic et al. 2000b; Kuraszkiewicz et al. 2009; Shen & Ho 2014; Wildy et al. 2019; Panda et al. 2020b). Solar and even slightly subsolar values are possible toward the extreme Population B, where Fe II emission is often undetectable above noise (e.g., Hamann et al. 2002; Punsly et al. 2018). At the other extreme, where Fe II is most prominent, estimates suggest $Z \gtrsim 10\ Z_{\odot}$ (Panda et al. 2018, 2019). Baldwin et al. (2003) derived $Z \approx 15\ Z_{\odot}$, although in the particular case of "nitrogen-loud" quasars. Apart from the extremes, it is not obvious whether there is a continuous systematic trend along the sequence. Previous estimates consistently suggest supersolar metallicity up to $Z \lesssim 10\ Z_{\odot}$ (Warner et al. 2004). Other landmark studies consistently found supersolar metallicity: Hamann & Ferland (1992) derived Z up to $\lesssim 15\ Z_{\odot}$; Nagao et al. (2006b) found typical values $Z \approx 5\ Z_{\odot}$, with $Z \sim 10\ Z_{\odot}$ for the most luminous quasars from the (Si IV + O IV])/C IV ratio. Sulentic et al. (2014) inferred a large dispersion with the largest value in excess of 10 $Z_{\odot}$. Similar results were reached by Shin et al. (2013), whose Si IV + O IV]/C IV ratio measurements suggested $Z \gtrsim 10\ Z_{\odot}$.

Most interesting along the quasar main sequence are the high accretors. They are selected according to empirical criteria (e.g., Wang et al. 2013, 2014; Marziani & Sulentic 2014; Du et al. 2016b) and defined by having $R_{\rm Fe\,II} > 1$, that is, with the Fe II λ4570 blend on the blue side of Hβ (as defined by Boroson & Green 1992) flux exceeding the flux of Hβ. In the optical diagram of the quasar main sequence (Sulentic et al. 2000b; Shen & Ho 2014) they are at the extreme tip in terms of Fe II prominence and identified as extreme Population A (hereafter xA), following Sulentic et al. (2002). Depending on redshift, we look for high accretors using different criteria. In the case of $z \gtrsim 1$, it is expedient to use a criterion based on two UV line intensity ratios:

1. Al III/Si III] > 0.5,
2. C III]/Si III] < 1.0,

following Marziani & Sulentic (2014). These criteria are met by the sources identified as the xA population by Sulentic and collaborators. xA quasars are radiating at the highest luminosity per unit mass, and at low z they are characterized by relatively low black hole masses for their luminosities and high Eddington ratios (Mathur 2000; Sulentic et al. 2000a). There is evidence that xA sources tend to have high metallicity (Shemmer et al. 2004; Martínez-Aldama et al. 2018a). Similar properties have been identified as characteristic of narrow-line Seyfert 1 galaxies (NLSy1s) with strong Fe II emission. NLS1s also have unusually high metallicities for their luminosities. Shemmer & Netzer (2002) have shown that NLSy1s deviate significantly from the nominal relationship between metallicity and luminosity in AGNs. As several studies distinguish between NLSy1s and "broader-lined" AGNs, we remark here that all Fe II-strong NLSy1s meeting the selection criterion $R_{\rm Fe\,II} > 1$ are extreme Population A sources.[7]

The aim of this work is to investigate the metallicity-sensitive diagnostic ratios of the UV spectral range for extreme Population A quasars, i.e., for highly accreting quasars. Section 2 defines our sample and provides some basic information. In Section 3 we define the diagnostic ratios and describe the basic observational results. In Section 4 we compare measured diagnostic ratios and compare them with the ones obtained from photoionization simulations. In Section 5 we discuss our results in terms of method caveats, metal enrichment, accretion parameters, and their implications on the nature of xA sources. We show the UV spectra in Appendix A (Figure 16), along with the multicomponent fit analysis of the emission blends, and in Appendix B we show the trend of Z-sensitive ratios as a function of ionization parameter, density, and metallicity.

[7] NLSy1s are identified by the line width of the Hβ BC being FWHM(H$\beta_{\rm BC}$) $\leqslant$ 2000 km s^{-1} (Osterbrock & Pogge 1985), Population A sources are identified by FWHM(H$\beta_{\rm BC}$) $\leqslant$ 4000 km s^{-1} (Sulentic et al. 2000a). Imposing a fixed limit on line FWHM, although very convenient observationally, has no direct physical meaning, and its interpretation might be sample dependent. See Marziani et al. (2018) for a discussion of the issue.

2. Sample

2.1. Sample Definition

Qualitatively, extreme Population A objects show prominent Al III and weak or absent C III] emission lines. In general, they show low emission-line equivalent widths ($\approx\frac{1}{2}$ of them meet the W(C IV) $\lesssim 10$ Å and qualify as weak-lined quasars following Diamond-Stanic et al. 2009)[8] and a spectrum that is easily recognizable even by a visual inspection, also because of the "trapezoidal" shape of the C IV profile and the intensity of the λ1400 blend, comparable to the one of C IV (Martinez-Aldama et al. 2018b).

xA sources were selected according to the criteria given in Section 1, using line measurements automatically obtained by the `splot` task with a cursor script within the IRAF data reduction package. We focus on the spectral range from ≈1200 to 2100 Å, where (1) UV lines used for xA identification are present and (2) the strongest emission features helpful for metallicity diagnostics are also located. The Lyα + N V blend is usually too heavily compromised by absorptions, which make it impossible to reconstruct the emission components especially for Lyα. We will make some consideration on the mean strength of the N V with respect to C IV and He II λ1640 (Section 5.3), but we will not consider N V as a diagnostic. We selected SDSS DR12[9] spectra in the redshift range $2.15 < z < 2.40$, relatively bright ($r < 19$) to ensure moderate to high S/N in the continua (in all cases S/N $\gtrsim 5$ in the continuum, and the wide majority with S/N $\gtrsim 10$), and of low decl. $\delta < 10$. The redshift range was chosen to allow for the possibility of Hβ coverage in the H band by eventual near-IR spectroscopic observations. The DR12 sample selected with these criteria is ≈500 sources strong. xA sources were selected out of this sample with an automated procedure, inspected to avoid broad absorption lines, and further vetted for obtaining a small pilot sample of ∼10 sources. A larger sample of xA sources will be considered in a subsequent work (K. Garnica et al. 2021, in preparation). The final selection includes 13 sources. With the adopted selection criteria in flux and redshift, we expect a small dispersion in the accretion parameters (especially luminosity; Section 5.2). Indeed, the selected sources are rather homogeneous in terms of spectral appearance, with a few sources included in our sample that, however, show borderline criteria. They will be considered in Section 4.1.1 in terms of their individual U, $n_{\rm H}$.

2.2. Sample Properties

Table 1 provides basic information for the 13 sources of our sample: SDSS name, redshift from the SDSS, the difference between our redshift estimation using Al III (described in 3.1) and the SDSS redshift $\delta z = z - z_{\rm SDSS}$, the g-band magnitude provided by Adelman-McCarthy et al. (2008), the $g - r$ color index, the rest-frame-specific continuum flux at 1700 and 1350 Å measured on the rest frame, and the S/N at 1450 Å. All other sources were covered by FIRST (Becker et al. 1995) but undetected. Considering that the typical rms scatter of FIRST radio maps is ≈0.15 Jy, as well as the typical fluxes in the g band, we have upper limits $\lesssim 5$ in the radio-to-optical ratio, qualifying the sample sources as radio-quiet. Distances were computed using the formula provided by Sulentic et al. (2006, their Equation (B.5)), and ΛCDM cosmology ($\Omega_\Lambda = 0.7$, $\Omega_{\rm M} = 0.3$, $H_0 = 70$ km s^{-1} Mpc^{-1}). The bolometric luminosity is $\sim 10^{47}$ erg s^{-1}, assuming a bolometric correction B.C.$_{1350} = 3.5$ (Richards et al. 2006). The sample rms is just ≈0.2 dex: all sources are in a narrow range of distances and have observed fluxes within a factor of ≈2 from their average. This is, in principle, an advantage for the estimation of the physical parameters such as $L/L_{\rm Edd}$, considering the large uncertainty and serious biases associated with the estimation of $M_{\rm BH}$ from UV high-ionization lines. Accretion parameters will be discussed in Section 5.2.

3. Methods

3.1. Redshift Determination

The estimate of the quasar systemic redshift in the UV is not trivial, as there are no low-ionization narrow lines available in the spectral range (Vanden Berk et al. 2001). In practice, one can resort to the broad LIL. Negrete et al. (2014) and Martínez-Aldama et al. (2018a) consider the Si II λ1263 and O I λ1302 lines to obtain a first estimate. A readjustment is then made from the wavelength of the Al III doublet, which is found, in almost all cases, to have a consistent redshift. To determine the Al III shift, those authors used multicomponent fits with all the lines in the region of the blend λ1900 included. The peak of Al III is clearly visible in the spectra of our sample, since in high accretors emission of Al III is strong with respect to the other lines in the blend at 1900 Å. We decided to use only this method for redshift estimation (in Table 1), and to measure the peak, we use single Gaussian fitting from the `splot` task of the Al III doublet and/or of the Si III] line, depending on which feature is sharper. The obtained values are usually $\geqslant z_{\rm SDSS}$ (Table 1). This is not a surprise, as $z_{\rm SDSS}$ is based on lines that are mainly blueshifted in xA sources and hence is a systematic underestimation of the unbiased redshift.

3.2. Diagnostic Ratios Sensitive to U, Density, Z

Line ratios are sensitive to different parameters. In the UV range, four groups of diagnostic ratios are defined in the literature (e.g., Negrete et al. 2012; Martinez-Aldama et al. 2018b):

1. C IV/Si IV + O IV] and C IV/He II have been widely applied as metallicity indicators (e.g., Shin et al. 2013). In principle, C IV/He II and Si IV/He II should be sensitive to C and Si abundance because the He abundance relative to hydrogen can be considered constant. The ionization potentials of C^{2+} and He^{+} are similar. The main difference is that the He II line is a recombination line, equivalent to H I Hα, and the regions where they are formed are not coincident (see Figure 4).
2. Ratios involving N V, N V/C IV, and N V/He II have been also widely used in past work, after it was noted that the N V line was stronger than expected in a photoionization scenario (e.g., Osmer & Smith 1976). A selective enhancement of nitrogen (Shields 1976) is expected owing to secondary production of N by massive and intermediate-mass stars, yielding [N/H] $\propto Z^2$ (Vila-Costas & Edmunds 1993; Izotov & Thuan 1999).

[8] Weak-lined quasars are mostly xA sources, judging from their location along the main sequence (Marziani et al. 2016a) and that the limit at $W \approx 10$ Å separates the low-W side of a continuous distribution of the xA C IV equivalent width peaked right at around 10 Å (Martínez-Aldama et al. 2018a).

[9] https://www.sdss.org/dr12/

Table 1
Source Identification and Basic Properties

SDSS NAME (1)	z_{SDSS} (2)	δz (3)	g (4)	$g-r$ (5)	f_λ(1700 Å) (6)	f_λ(1350 Å) (7)	S/N (8)
J010657.94−085500.1	2.355	0.006	18.18	0.095	662	951	20
J082936.30+080140.6	2.189	0.008	18.366	0.302	672	939	11
J084525.84+072222.3	2.269	0.017	18.204	0.331	668	989	13
J084719.12+094323.4	2.295	0.004	18.940	0.234	368	511	17
J085856.00+015219.4	2.160	0.002	17.916	0.255	709	1204	21
J092641.41+013506.6	2.181	0.004	18.591	0.337	377	670	21
J094637.83−012411.5	2.212	0.002	18.561	0.178	385	595	18
J102421.32+024520.2	2.319	0.008	18.49	0.177	478	694	23
J102606.67+011459.0	2.253	0.003	18.982	0.206	428	525	13
J114557.84+080029.0	2.338	0.009	18.545	0.369	243	360	5
J150959.16+074450.1	2.255	0.008	18.938	0.278	223	346	9
J151929.45+072328.7	2.394	0.008	18.662	0.171	405	507	19
J211651.48+044123.7	2.352	0.000	18.825	0.220	404	573	32

Note. Column (1): SDSS coordinate name. Column (2): SDSS redshift. Column (3): correction to redshift estimated in the present work ($\delta z = z - z_{SDSS}$). Column (4): g-band magnitude from Adelman-McCarthy et al. (2008). Column (5): color index $g-r$. Column (6): continuum flux measured at 1700 Å in units of 10^{-17} erg s^{-1} cm^{-2} Å^{-1}. Column (7): continuum flux measured at 1350 Å in the same units. Column (8): S/N measured at continuum level at 1450 Å.

This process might be especially important at the high metallicities inferred for the quasar BLR. Therefore, estimates based on N V may differ in a systematic way from estimates based on other metal lines (e.g., Matsuoka et al. 2011). In the present sample of quasars, contamination by narrow and semibroad absorption is severe, and even if we model precisely the high-ionization lines, it might be impossible to reconstruct the unabsorbed profile of the red wing of Lyα. In addition, S/N is not sufficient to allow for a careful measurement of N IV] λ1486 and N III] λ1750 lines. We defer the systematic analysis of nitrogen lines to a subsequent work, while discussing the consistency of the N V measures in a high-Z scenario (Section 5.3).

3. The ratios Al III/Si III] and Si III]/C III] are sensitive to density, as the ratios involve intercombination lines with a well-defined critical density ($n_c \sim 10^{10}$ cm^{-3} for C III], Hamann et al. 2002; $n_c \sim 10^{11}$ cm^{-3} for Si III], Negrete et al. 2010).
4. Si III]/Si IV, Si II λ1814/Si III], and Si II λ1814/Si IV are sensitive to the ionization parameters and insensitive to Z, as they are different ionic species of the same element.

Other intensity ratios entail a dependence on metallicity Z, but also on ionization parameter U and density n_H (Marziani et al. 2020).

3.3. Line Interpretation and Diagnostic Ratios

The comparison between LILs and HILs has provided insightful information over a broad range of redshift and luminosity (Corbin & Boroson 1996; Marziani et al. 1996, 2010; Shen 2016; Bisogni et al. 2017; Sulentic et al. 2017; Vietri et al. 2018). An LIL BLR appears to remain basically virialized (Marziani et al. 2009; Sulentic et al. 2017), as the Hβ profile remains (almost) symmetric and unshifted with respect to rest frame even if C IV blueshifts can reach several thousands of kilometers per second. In Population A, the lines have been decomposed into two components:

1. The BC, also known as the intermediate component, the core component, or the central BC following various authors (e.g., Brotherton et al. 1994; Popović et al. 2002; Kovačević-Dojčinović et al. 2015; Adhikari et al. 2016). The BC is modeled by a symmetric and unshifted profile (Lorentzian for Population A; Véron-Cetty et al. 2001; Sulentic et al. 2002; Zhou et al. 2006) and is believed to be associated with a virialized BLR subsystem.
2. The blueshifted component (BLUE). A strong blue excess in Population A C IV profiles is obvious, as in some C IV profiles—like the one of the xA prototype I Zw 1 or high-luminosity quasars—BLUE dominates the total emission-line flux (Marziani et al. 1996; Leighly & Moore 2004; Sulentic et al. 2017). For BLUE, there is no evidence of a regular profile, and the fit attempts to empirically reproduce the observed excess emission. BLUE is detected in an LIL such as Hβ at a very low level and is not strongly affecting FWHM measurements (Negrete et al. 2018).

3.3.1. Broad Component

Diagnostic ratios are not equally well measurable for the BC and the BLUE. For the BC, the following constraints and caveats apply:

C IV/, Si IV/, Al III/ over He II.—He II is weak but measurable in most of the objects. Ratios such as C IV/He II λ1640, Si IV/He II λ1640, and Al III/He II λ1640 (U dependent) offer Z indicators. Especially for the low-ionization conditions of the BC emitting gas, these ratios are well behaved (Sections 3.5 and 3.6) and will form the basis of the Z estimates presented in this paper.

Si IV/C IV.—There are problems in estimating the Si IV line intensity: an overestimation might be possible because of difficult continuum placement (see, e.g., the case of SDSS J085856.00+015219.4 in Appendix A). The relative contribution of Si IV to the blend at 1400 Å is unclear (Wills & Netzer 1979). A strong BC contribution of O IV] is unlikely, as this line has a critical density $n_c \sim 10^{10}$ cm^{-3} (Zheng 1988; see also the isophotal contour of Si IV/O IV] in Appendix B). Our measurements are nonetheless compared to Si IV + total O IV] CLOUDY prediction.

Al III/Si III].—This ratio is sensitive to density in the low-ionization BLR domain (Negrete et al. 2012). Values Al III/Si III] > 1 are possible if density is higher than 10^{11} cm^{-3}, the critical density of Si III]. We will not use this parameter as a metallicity estimator, although, in principle, for fixed physical conditions (setting $n_{\rm H}$ and U) the Al III/Si III] and Si III]/C III] ratios may become dependent mainly on electron temperature and so on metallicity (Section 3.5). The ratio of the total emission in the λ1900 blend Al III+Si III]+C III] over C IV has been used as a metallicity estimator (Sulentic et al. 2014). Considering the uncertain contribution of Fe III emission and especially of the Fe III λ1914 line in the xA spectra, we will not use the total intensity of the λ1900 blend as a diagnostic.

C IV/Al III.—Biases might be associated with the estimate of the C IV $\lambda1549_{\rm BC}$, especially when BLUE is so prominent that C IV $\lambda1549_{\rm BC}$ contributes to a minority fraction.

3.3.2. BLUE Component

C IV/He II λ1640.—The He II λ1640 BLUE is well visible merging smoothly with the red wing of C IV. The ratio C IV/He II λ1640 might be affected by the decomposition of the blend, leading to an overestimate of the He II emission. This ratio is in principle sensitive to metallicity. However, the increase is not monotonic at relatively high U (see the panel for C IV/He II λ1640 in Figure 2). The resulting effect is that the C IV/He II λ1640 ratio within the uncertainties leaves the Z unconstrained between 0.1 and 100 solar.

C IV/(O IV] + Si IV).—The blueshifted excess at 1400 Å is ascribed to O IV + Si IV emission. A significant contribution can be associated with O IV], and several transitions of O IV that are computed by CLOUDY (see, e.g., Keenan et al. 2002) are especially relevant at high U values and moderately low $n_{\rm H}$ ($\sim10^8$ cm^{-3}). The blue side of the line is relatively straightforward to measure for computing C IV/λ1400 with a multicomponent fit, although difficult continuum placement, narrow absorption lines, and blending on the blue side make it difficult to obtain a very precise measurement. A total λ1400 BLUE emission exceeding C IV is possible if, assuming $\log U \gtrsim 0$, $\log\ n_{\rm H} \gtrsim 9$ [cm^{-3}], the metallicity value is very high, $20\ Z_\odot \lesssim Z \lesssim 100\ Z_\odot$ (Section 3.6).

(O IV]+Si IV)/He II λ1640.—By the same token, the He II λ1640 overestimation may lead to a lower (O IV]+Si IV)/He II λ1640 ratio.

3.4. Analysis via Multicomponent Fits

We analyze 13 objects using the `specfit` task from IRAF (Kriss 1994). The use of the χ^2 minimization is aimed at providing a heuristic separation between the BC and the blue component (BLUE) of the emission lines. After redshift correction following the method described in Section 3.1, for each source of our sample we perform a detailed modeling using various components as described below, including computation of asymmetric errors (Section 3.4.1). As mentioned in Section 3.2, in our analysis we consider five diagnostic ratios for the BC, C IV/λ1400, C IV/He II λ1640, Al III/He II λ1640, λ1400/He II λ1640, and λ1400/Al III, and three for the BLUE, C IV/λ1400, C IV/He II λ1640, and λ1400/He II λ1640. The C IV/He II λ1640 is used with care, as it may yield poor constraints. In addition, it is important to stress that, of the five ratios measured on the BC, only three (the ones dividing by the intensity of He II λ1640 BC) are independent. We compare the fit results with arrays of CLOUDY (Ferland et al. 2013) simulations for various metallicities and physical conditions (Section 3.5).

For each source we perform the multicomponent fitting in three ranges described below. The best fit is identified by the model with the lowest χ^2, i.e., with a minimized difference between the observed and the model spectrum. Following the data analysis by Negrete et al. (2012), we use the following components:

The continuum.—This was modeled as a power law, and we use the line-free windows around 1300 and 1700 Å (two small ranges where there are no strong emission lines) to scale it. If needed, we divide the continuum into three parts (corresponding to the three regions mentioned below). Assumed continua are shown in the figures of Appendix A.

Fe II *emission.*—This usually does not contribute significantly in the studied spectral ranges. We consider the Fe II template that is based on CLOUDY simulations of Brühweiler & Verner (2008) when necessary. In practice, the contamination by the blended Fe II emission yielding a pseudo-continuum is negligible. Some Fe II emission lines were detectable in only a few objects and around ≈1715 Å, at 1785 Å, and at 2020 Å. In these cases, we model them using single Gaussians.

Fe III *emission.*—This affects more the λ1900 region and seems to be strong when Al III λ1860 is strong as well (Hartig & Baldwin 1986). To model these lines, we use the template of Vestergaard & Wilkes (2001).

Region 1300–1450 Å.—This is dominated by the Si IV + O IV] high-ionization blend with strong blueshifted component. Fainter lines such as Si II λ1306, O I λ1304, and C II λ1335 are also detectable. For the broad and blueshifted components we use the same model as in the case of C IV and He II λ1640. This spectral range is often strongly affected by absorption.

Region 1450–1700 Å.—This is dominated by the C IV emission line, which we model as fixed in the rest-frame wavelength Lorentzian profile representing the BC, and two blueshifted asymmetric Gaussian profiles vary freely. The same model is used for He II λ1640.

Region 1700–2200 Å is dominated by Al III, Si III], and Fe III intermediate-ionization lines. We model Al III and Si III] using Lorentzian profiles, following Negrete et al. (2012). C III] emission is also included in the fit, although the dominant contribution around 1900 Å is to be ascribed to Fe III (Martínez-Aldama et al. 2018a and references therein). We use the template of Vestergaard & Wilkes (2001) to model Fe III emission. No BLUE is ascribed to these intermediate-ionization lines.

Absorption lines.—These are modeled by Gaussians and included whenever necessary to obtain a good fit.

The fits to the observed spectral ranges are shown in the figures of Appendix A.

3.4.1. Error Estimation on Line Fluxes

The choice of the continuum placement is the main source of uncertainty in the measurement of the emission-line intensities. The fits in Appendix A show that, in the majority of cases, the FWHMs of the Al III and Si III] lines (assumed equal) satisfy the condition FWHM(Al III) ∼ FWHM(C IV$_{\rm BC}$ ∼ FWHM(Si IV$_{\rm BC}$). Figure 1 shows the best-fit, maximum, and minimum placement of the continuum, which we choose empirically. With this approach the continua of Figure 1 should provide the continuum uncertainty at a $\pm3\sigma$ confidence.

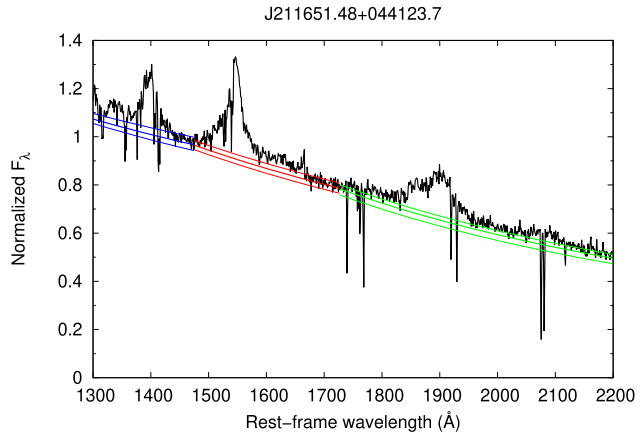

Figure 1. Continuum estimation for J211651.48+044123.7 from our sample. Range 1300–1450 Å is shown in blue, 1450–1700 Å in red, and 1750–2200 Å in green. The continuum lines in each range represent from the top: the maximum, the best-fit, and the minimum continuum placement.

The continuum placement strongly affects the measurement of an extended feature such as the Fe III blends and the He II λ1640 emission. Figure 1 makes it evident that errors on fluxes are asymmetric. The thick line shows the continuum best fit and the thinner minimum and maximum plausible continua. Even if the minimum and maximum are displaced by the same difference in the intensity with respect to the best-fit continuum, assuming the minimum continuum would yield an increase in line flux larger than the flux decrease assuming the maximum continuum level. In other words, a symmetric uncertainty in the continuum-specific flux translates into an asymmetric uncertainty in the line fluxes. To manage asymmetric uncertainties, we assume that the distribution of errors follows the triangular distribution (D' Agostini 2003). This method assumes linear decreasing on either side of maximum of the distribution (which is the best fit in our case) to the values obtained for maximum and minimum contributions of the continuum. We motivate using the triangular error distribution as a relatively easy analytical method to deal with asymmetric errors. For each line measurement we calculate the variance using the following formula for the triangular distribution:

$$\sigma^2(X) = \frac{\Delta^2 x_+ + \Delta^2 x_- + \Delta x_+ + \Delta x_-}{18}, \quad (1)$$

where Δx_+ and Δx_- are differences between measurement with maximum and best continuum and measurement with best and minimum continuum, respectively. To analyze the error of diagnostic ratios, we propagate uncertainties using standard formulas of error propagation.

3.5. Photoionization Modeling

To interpret our fitting results, we compare the line intensity ratio for BC and BLUE with the ones predicted by CLOUDY 13.05 and 17.02 simulations (Ferland et al. 2013, 2017).[10] An array of simulations is used as reference for comparison with the observed line intensity ratios. It was computed under the assumption that (1) column density is $N_c = 10^{23}\,\mathrm{cm}^{-2}$; (2) the continuum is represented by the model continuum of Mathews & Ferland (1987), which is believed to be appropriate for Population A quasars; and (3) microturbulence is negligible. The simulation arrays cover the hydrogen density range $7.00 \leqslant \log(n_H) \leqslant 14.00$ and the ionization parameter $-4.5 \leqslant \log(U) \leqslant 1.00$, in intervals of 0.25 dex. They are repeated for values of metallicities in a range encompassing five orders of magnitude: 0.01, 0.1, 1, 2, 5, 10, 20, 50, 100, 200, 500, and 1000 $Z_\odot$. Extremely high metallicity $Z \gtrsim 100\ Z_\odot$ is considered physically unrealistic ($Z \approx 100\ Z_\odot$ implies that more than half of the gas mass is made up by metals!), unless the enrichment is provided in situ within the disk (Cantiello et al. 2020). The behavior of diagnostic line ratios as a function of U and n_H for selected values of Z is shown in Figure 17 of Appendix B.

3.5.1. Basic Interpretation

The line emissivity $\epsilon_{\rm coll}$ (ergs cm^{-3} s^{-1}) of a collisionally excited line emitted from an element X in its ith ionization stage has a strong temperature dependence. In the high-density limit

$$\epsilon_{\mathrm{X}^i,\mathrm{coll}} = n_{\mathrm{X}^i,\mathrm{l}} \beta A_{\mathrm{X}^i,\mathrm{ul}} h\nu_0 \frac{g_{\mathrm{X}^i,\mathrm{l}}}{g_{\mathrm{X}^i,\mathrm{u}}} \exp\left(-\frac{h\nu_0}{kT_e}\right) \propto n_{\mathrm{X}^i,\mathrm{l}} \exp\left(-\frac{h\nu_0}{kT_e}\right) \quad (2)$$

the line is said to be "thermalized," as its strength depends only on the atomic level population and not on the transition strength (Hamann & Ferland 1999). β is the photon escape probability, and $A_{\mathrm{X}^i,\mathrm{ul}}$ is the spontaneous decay coefficient. At low densities we have

$$\epsilon_{\mathrm{X}^i,\mathrm{coll}} = n_{\mathrm{X}^i,\mathrm{l}} n_e q_{\mathrm{X}^i,\mathrm{lu}} h\nu_0 \propto n_{\mathrm{X}^i}^2 T_e^{-1/2} \exp\left(-\frac{h\nu_0}{kT_e}\right). \quad (3)$$

The recombination lines considered in our analysis are Hβ and He II λ1640, for which the emissivity (with an approximate dependence of radiative recombination coefficient α on electron temperature; Osterbrock & Ferland 2006) becomes

$$\epsilon_{\mathrm{Y}^j,\mathrm{rec}} = n_{\mathrm{Y}^j}\, n_e\, \alpha\, h\nu_0 \propto n_{\mathrm{Y}^j}^2 T_e^{-1}, \quad (4)$$

and n_{Y^j} is the number density of the parent ion.

Under these simplifying, illustrative assumptions we can write

$$\frac{\epsilon_{\mathrm{X}^i,\mathrm{coll}}}{\epsilon_{\mathrm{Y}^j,\mathrm{rec}}} \propto \left(\frac{n_{\mathrm{X}^i}}{n_{\mathrm{Y}^j}}\right)^2 T_e^{\frac{1}{2}} \exp\left(-\frac{h\nu_0}{kT_e}\right) \quad (5)$$

for the low-density case and

$$\frac{\epsilon_{\mathrm{X}^i,\mathrm{coll}}}{\epsilon_{\mathrm{Y}^j,\mathrm{rec}}} \propto \frac{n_{\mathrm{X}^i}}{n_{\mathrm{Y}^j}^2} T_e \exp\left(-\frac{h\nu_0}{kT_e}\right) \quad (6)$$

for the high-density case.

Similarly, for the ratio of two collisionally excited lines at frequencies ν_0 and ν_1,

$$\frac{\epsilon_{\mathrm{X}^i,\mathrm{coll}}}{\epsilon_{\mathrm{Y}^j,\mathrm{coll}}} \propto \left(\frac{n_{\mathrm{X}^i}}{n_{\mathrm{Y}^j}}\right)^\kappa \exp\left(-\frac{h(\nu_0 - \nu_1)}{kT_e}\right), \quad (7)$$

[10] The arrays were computed over several years with CLOUDY 13.05, in large part before CLOUDY 17.02 became available. The computations with the two versions of the code are in agreement as far as the trends with U, n_H, and Z are concerned, although the derived Z values are a factor of $\approx$2 systematically lower with the 17.02 release of CLOUDY. In this paper we present the CLOUDY 17.02 for all estimates of metallicity and physical parameters U and n_H.

where $\kappa = 1$ and 2 in the high- and low-density case, respectively.

Connecting the relative chemical abundance to the line emissivity ratios in the previous equation requires the reconstruction of the ionic stage distribution for each element, i.e., the computation of the ionic equilibrium, as well as the consideration of the extension of the emitting region within the gas clouds, i.e., that the line emission is not cospatial, and possible differences in optical depth effects. This is achieved by the CLOUDY simulations. However, we can see that the main variable parameter for a given relative emissivity is T_e. In other words, electron temperature is the main parameter connected to metallicity. This is especially true for a fixed physical condition (U, n_H, $N_c = 10^{23}$, spectral energy distribution (SED) given). This is most likely the case for xA sources: the spectral similarity implies that the scatter in physical properties is modest. We further investigate this issue in Section 4.3.

The electron temperature is also the dominating factor affecting the strength of the He II λ1640 line, for a given density. The He II Lyα line at 304 Å ionizes hydrogen atoms and other ionic species with ionization potential up to 3 ryd. Being absorbed by different ionic species, He II λ1640 Lyα cannot sustain a population of excited electrons at the level $n = 2$ of He II λ1640. This is markedly different from hydrogen Lyα, which in case B is assumed to scatter many times and to sustain a population of hydrogen atoms at level $n = 2$. The He II line is therefore produced almost only by recombination, and no collisional excitation from level $n = 2$ or radiative transfer effects are expected, unlike the case of the hydrogen Balmer lines (Marziani et al. 2020). The prediction of the He II line is relatively simple once the electron temperature and the density are known by assumption or computation. The additional advantage in the use of He II is that there is no significant enhancement of the He abundance over the entire lifetime of the universe (Peimbert et al. 2001; Peimbert 2008). The normalization to the He II line flux of the flux of metal lines should yield robust Z estimates. This is shown by the isophotal contours of Appendix B (Figure 17), tracing the behavior of the diagnostic ratios as a function of Z and U: the (Si IV + O IV])/He II and Al III/He II ratios monotonically increase with Z over a large range of U; for C IV/He II λ1640 the behavior is monotonic at low U, but more complex at $\log U \sim -1 - 0$. Ratios involving pairs of metal lines yield more complex trends in the plane Z–U. At low n_H, the C IV/Al III ratio is a good Z estimator, although of limited usefulness since Al III is weak; at high n_H, its sensitivity is greatly reduced (Appendix B, Figure 17). The C IV/(Si IV + O IV]) does not appear to be especially sensitive to Z. The diagnostic ratios change as a function of Z, although the behavior as a function of n_H and U is roughly preserved (Appendix B, Figure 18).

3.6. Explorative Analysis of Photoionization Trends at Fixed Ionization Parameter and Density

One of the main results of previous investigations is the systematic differences in ionization between BLUE and BC (Marziani et al. 2010; Negrete et al. 2012; Sulentic et al. 2017). Previous inferences suggest very low ionization ($U \sim 10^{-2.5}$), also because of the relatively low C IV/Hβ ratio for the BC emitting part of the BLR, and high density. A robust lower limit to density $n_H \sim 10^{11.5}$ cm^{-3} has been obtained from the analysis of the Ca II triplet emission (Matsuoka et al. 2007; Panda et al. 2020a). Less constrained are the physical conditions for BLUE emission. Apart from C IV/H$\beta \gg 1$ and Lyα/Hβ and C IV/C III] also $\gg$1, few constraints exist on density and column density. This result hardly comes as a surprise considering the difference in dynamical status associated with the two components. It is expected that the BC is emitted in a region of high column density $\log N_c \gtrsim 23$ [cm^{-2}], not last because radiation forces are proportional to the inverse of N_c (Netzer & Marziani 2010, see also Ferland et al. 2009). More explicitly, the equation of motion for a gas cloud under the combined effect of gravitation and radiation forces contains an acceleration term due to radiation that is inversely proportional to N_c. The high-N_c region is expected to be relatively stable (at rest frame, with no sign of systematic, large shifts in Population A) and presumably devoid of low-density gas (considering the weakness of C III]; Negrete et al. 2012). The same cannot be assumed for BLUE. BLUE is associated with a high radial velocity outflow, probably with the outflowing streams creating BAL features when intercepted by the line of sight (e.g., Elvis 2000).

Here we consider $\log U = -2.5$, $\log n_H = 12$ (−2.5, 12), and $\log U = 0$, $\log n_H = 9$ (0, 9) as representative of the low- and high-ionization emitting gas. Figure 2 illustrates the behavior of the C IV/Hβ, He II λ1640/Hβ, and C IV/He II λ1640 in the high- and low-ionization cases as a function of metallicity. The C IV intensity with respect to Hβ has a steep drop around $Z \gtrsim 1\ Z_\odot$, after a steady increase for subsolar Z. The He II λ1640/Hβ ratio decreases steadily, with a steepening at around solar value. Physically, this behavior is due to the high value of the ionization parameter (assumed constant), while the electron temperature decreases with metallicity, implying a much lower collisional excitation rate for C IV production. The dominant effect for the He II λ1640 decrease is likely the "ionization competition" between C IV and He II λ1640 parent ionic species (Hamann & Ferland 1999). As a consequence, the ratio C IV/He II λ1640 has a nonmonotonic behavior with a local maximum around solar metallicity. At low ionization and high density, the behavior is more regular, as the steady increase in C IV/Hβ is followed by a saturation to a maximum C IV/Hβ. The He II λ1640/Hβ ratio is constant up to solar and steadily decreases above solar, where the ionization competition with triply ionized carbon sets on. The result is a smooth, steady increase in the C IV/He II λ1640 ratio.

Figure 3 shows the behavior of the other intensity ratios used as metallicity diagnostics, for BLUE and BC. Si IV + O IV]/C IV and Si IV + O IV]/He II λ1640 saturate above 100 $Z_\odot$. Only around $Z \sim 10\ Z_\odot$ are values C IV/Si IV + O IV] $\lesssim 1$ possible, but the behavior is not monotonic and the ratio rises again at $Z \gtrsim 30\ Z_\odot$, with the unpleasant consequence that a ratio C IV/Si IV + O IV] ≈ 1.6 might imply 10 $Z_\odot$ as well as 1000 $Z_\odot$. The ratios usable for the BC also show regular behavior. The C IV/Al III ratio remains almost constant up $Z \sim 0.1\ Z_\odot$, and then starts a regular decrease with increasing Z, due to the decrease of T_e with Z (C IV is affected more strongly than Al III). Interestingly, Al III/He II λ1640 shows the opposite trend, due to the steady decrease of the He II λ1640 prominence with Z. Especially of interest is, however, the behavior of ratio Al III/He II λ1640 that shows a monotonic, very linear behavior in the log-log diagram. As for the high-ionization case, values (Si IV + O IV])/C IV $\gtrsim 1$ are possible only at very high metallicity, although the nonmonotonic

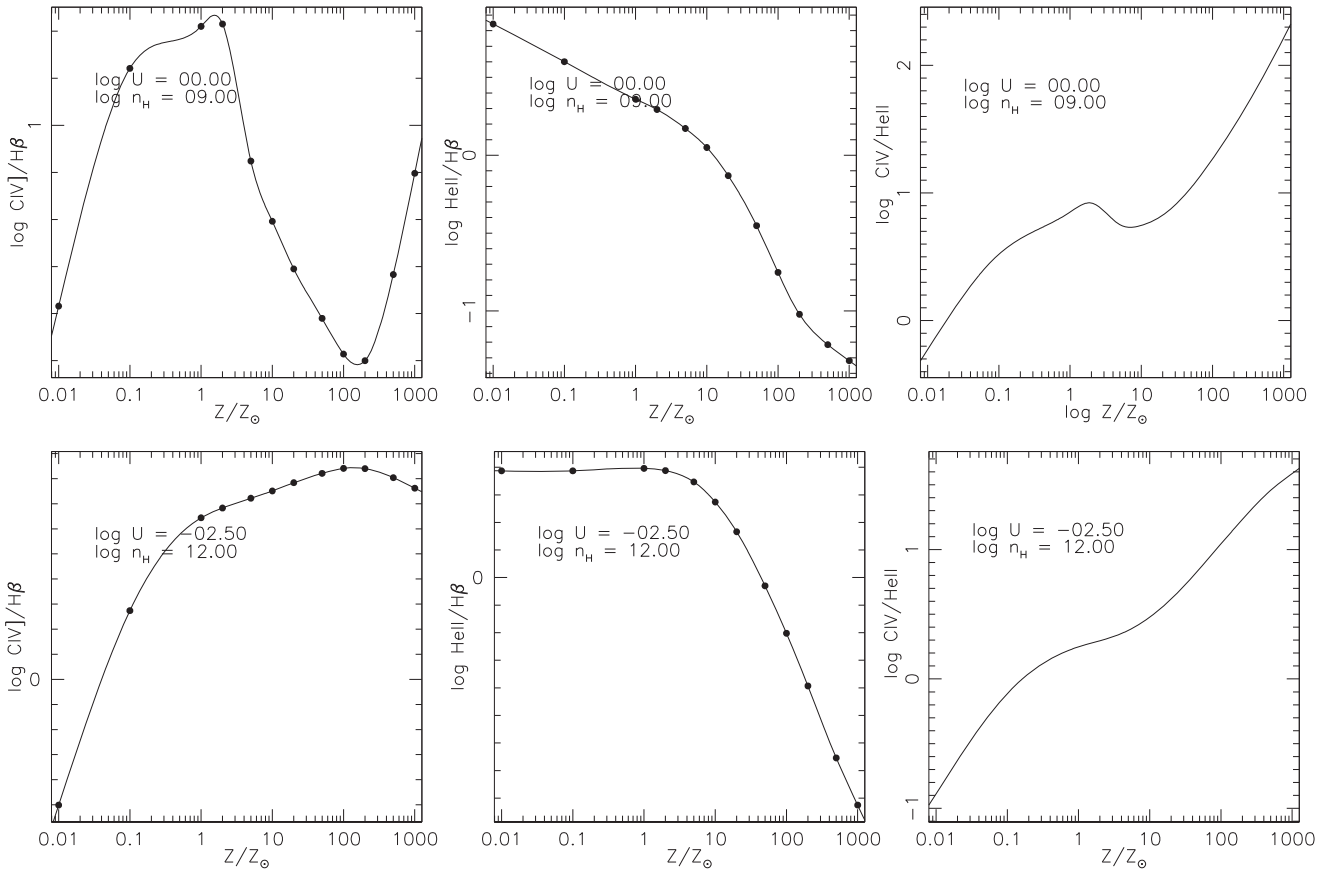

Figure 2. Computed intensity ratios involving C IV and He II λ1640 as a function of metallicity, for physical parameters U and $n_{\rm H}$ fixed: ($\log U$, $\log\ n_{\rm H}$) = (−1, 9) (top) and ($\log U$, $\log\ n_{\rm H}$) = (−2.5, 12) (bottom). Columns from left to right show C IV/Hβ, He II λ1640/Hβ, and C IV/He II λ1640.

behavior (around the minimum at $Z \approx 200\ Z_{\odot}$) complicates the interpretation of the observed emission-line ratios.

The ionization structure within the slab remains self-similar over a wide metallicity range, with the same systematic differences between the high- and low-ionization case (Figure 4), consistent with the assumption of a constant ionization parameter. As expected, the electron temperature decreases with metallicity, and the transition between the fully and partially ionized zone (FIZ and PIZ) occurs at smaller depth. In addition, close to the illuminated side of the cloud the electron temperature remains almost constant; the gas starts becoming colder before the transition from FIZ to PIZ. The depth at which $T_{\rm e}$ starts decreasing is well defined, and its value becomes lower with increasing Z (Figure 4). The effect is present for both the low- and high-ionization case, although it is more pronounced for the high-ionization case. Figure 5 shows how an increase in metallicity is affecting the $T_{\rm e}$ in the line-emitting cloud. Figure 5 reports the behavior of $T_{\rm e}$ at the illuminated face of the cloud ($\tau \sim 0$) and at maximum τ (corresponding to $N_{\rm c} = 10^{23}$ cm^{-2}, the side facing the observer) for the high- and low-ionization case. The $T_{\rm e}$ monotonically decreases as a function of metallicity. The difference between the two cloud faces is almost constant for the low-ionization case, with $\delta \log T_{\rm e} \approx 0.5$ dex, while it increases for the high-ionization case, reaching $\delta \log T_{\rm e} \approx 0.75$ dex at the highest Z value considered, $10^3\ Z_{\odot}$.

4. Results

4.1. Immediate Results

The observational results of our analysis involve the measurements of the intensity of the line BC and BLUE component separately. The rest-frame spectra with the continuum placements and the fits to the blends of the spectra are shown in Appendix A. Table 2 reports the measurement for the λ1900 blend. The columns list the SDSS identification code, the FWHM (in units of km s^{-1}) and equivalent width and flux of Al III (the sum of the doublet lines, in units of Å and 10^{-14} erg s^{-1} cm^{-2}, respectively), FWHM and flux of C III], and flux of Si III] (its FWHM is assumed equal to the one of the single Al III lines). Similarly, Table 3 reports the parameter of the C IV blend: equivalent width, FWHM and flux of the C IV BC, the flux of the C IV blueshifted component, and the fluxes of the BC and BLUE of He II λ1640. FWHM values are reported, but especially values $\gtrsim$5000 km s^{-1} should be considered as highly uncertain. There is the concrete possibility of an additional broadening ($\sim$10% of the observed FWHM) associated with nonvirial motions for the Al III line (A. del Olmo et al. 2021, in preparation). The fluxes of the BC and of BLUE of Si IV and O IV] are reported in Table 4. Intensity ratios with uncertainties are reported in Table 5. The last row lists the median values of the ratios with their semi-interquartile ranges (SIQR).

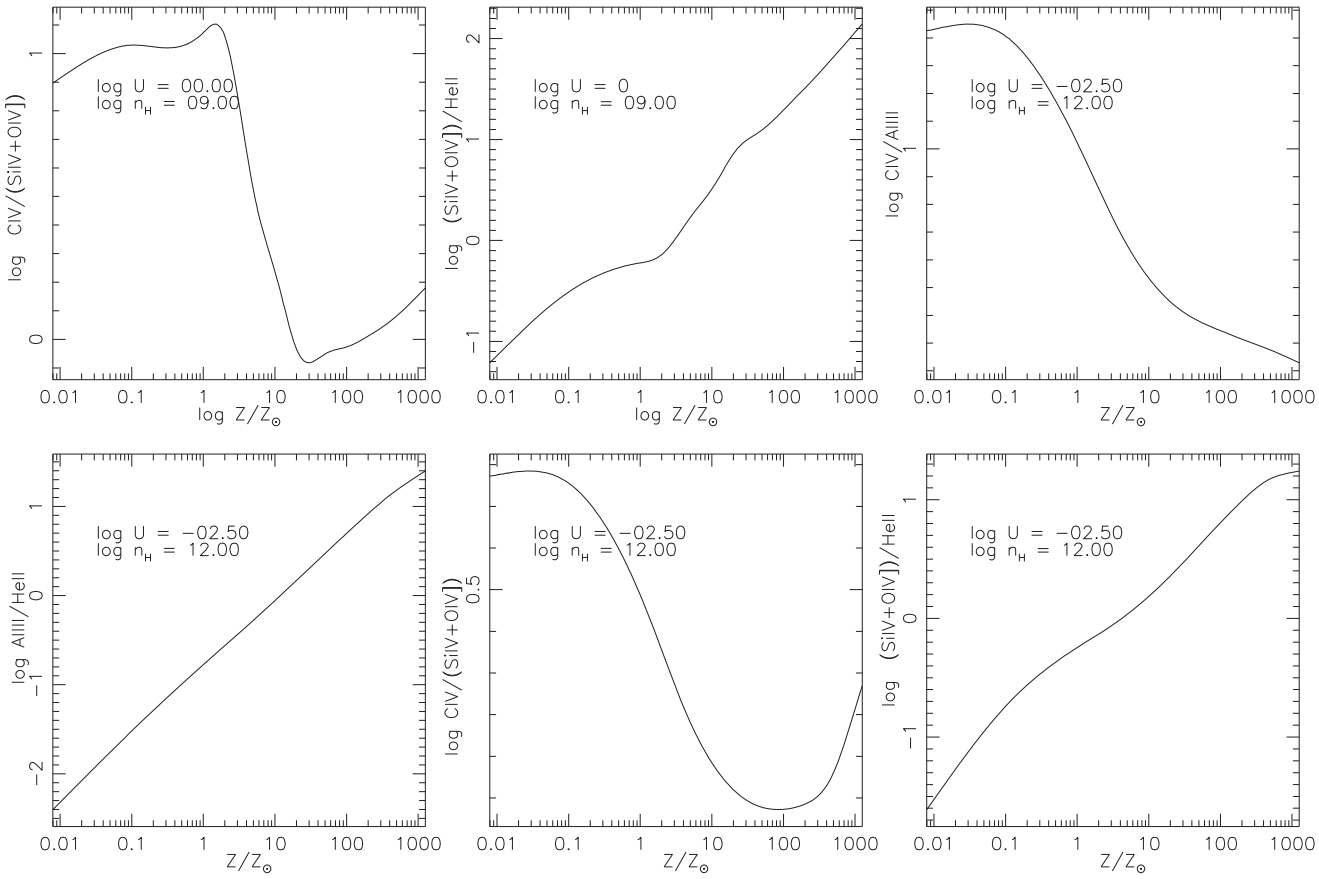

Figure 3. Behavior of the intensity ratios employed in this work (with the exception of C IV/He II λ1640 shown in the previous figure), as a function of metallicity, for physical parameters U and $n_{\rm H}$ fixed: ($\log U$, $\log n_{\rm H}$) = (−1, 9) and ($\log U$, $\log n_{\rm H}$) = (−2.5, 12). Top panels, from left to right: C IV/Si IV + O IV], (Si IV + O IV])/He II λ1640, C IV/Al III. Bottom panels, from left to right: Al III/He II λ1640, C IV/(Si IV + O IV]), (Si IV + O IV])/He II λ1640.

4.1.1. Identification of xA Sources and of "Intruders"

Figure 6 shows that the majority of sources meet both UV selection criteria and should be considered xA quasars. The median value of the Al III/Si III] (last row of Table 5) implies that the Al III is strong relative to Si III]. Also, Si III] is stronger than C III]. Both selection criteria are satisfied by the median ratios. Only one source (SDSS J084525.84+072222.3) shows C III]/Si III] significantly larger than 1. This quasar is, however, confirmed as an xA by the very large Al III/Si III], by the blueshift of C IV, and by the prominent λ1400 blend comparable to the C IV emission. The lines in the spectrum of SDSS J084525.84+072222.3 are broad, and any C III] emission is heavily blended with Fe III emission. The C III] value should be considered an upper limit. Three outlying/borderline data points (in orange) in Figure 6 have ratio C III]/Si III] $\sim$ 1, and Al III/Si III] consistent with the selection criteria within the uncertainties, but other criteria support their classification as xA. The borderline sources will be further discussed in Section 4.3. In conclusion, all 13 sources of the present sample save one should be considered bona fide xA sources.

It is intriguing that the intensity ratios C III]/Si III] and Al III/Si III] are apparently anticorrelated in Figure 6, if we exclude the two outlying points. Excluding the two outlying data points, the Spearman rank correlation coefficient is $\rho \approx 0.8$, which implies a 4σ significance for a correlation, but the correlation coefficient between the two ratios for the full sample is much lower. Given the small number of sources, a larger sample is needed to confirm the trend.

4.1.2. BC Intensity Ratios

Figure 7 shows the distribution of diagnostic intensity ratios C IV/He II λ1640, Si IV/He II λ1640, and Al III/He II λ1640 for the BC. The bottom panels of Figure 7 show the results for individual sources.

The vertical lines identify the median values, $\mu_{\frac{1}{2}}$(C IV/He II λ1640) $\approx$ 4.03, $\mu_{\frac{1}{2}}$(Al III/He II λ1640) $\approx$ 4.31, $\mu_{\frac{1}{2}}$(Si IV/He II λ1640) $\approx$ 6.39. The higher value for Si IV/He II λ1640 than for C IV/He II λ1640 implies $\mu_{\frac{1}{2}}$(C IV/Si IV) $\approx$ 0.69, a value that is predicted by CLOUDY for very low values of the ionization parameter (Appendix B). The C IV/Al III ratio is also constraining: the CLOUDY simulations indicate high Z and low ionization.

The distribution of the data points is relatively well behaved, with individual ratios showing small scatter around their median values. In the histogram, we see a tail made by three to five objects, suggesting systematically higher values. In particular, at least two objects (SDSS J102606.67+011459.0 and SDSS J085856.00+015219.4) show systematically higher ratios, with C IV/He II λ1640 $\approx$ 10, and Al III/He II λ1640 $\approx$ 4. Both of them show extreme C IV blueshifts, and SDSS J102606.67+011459.0 shows the highest Al III/Si III] ratio in the sample.

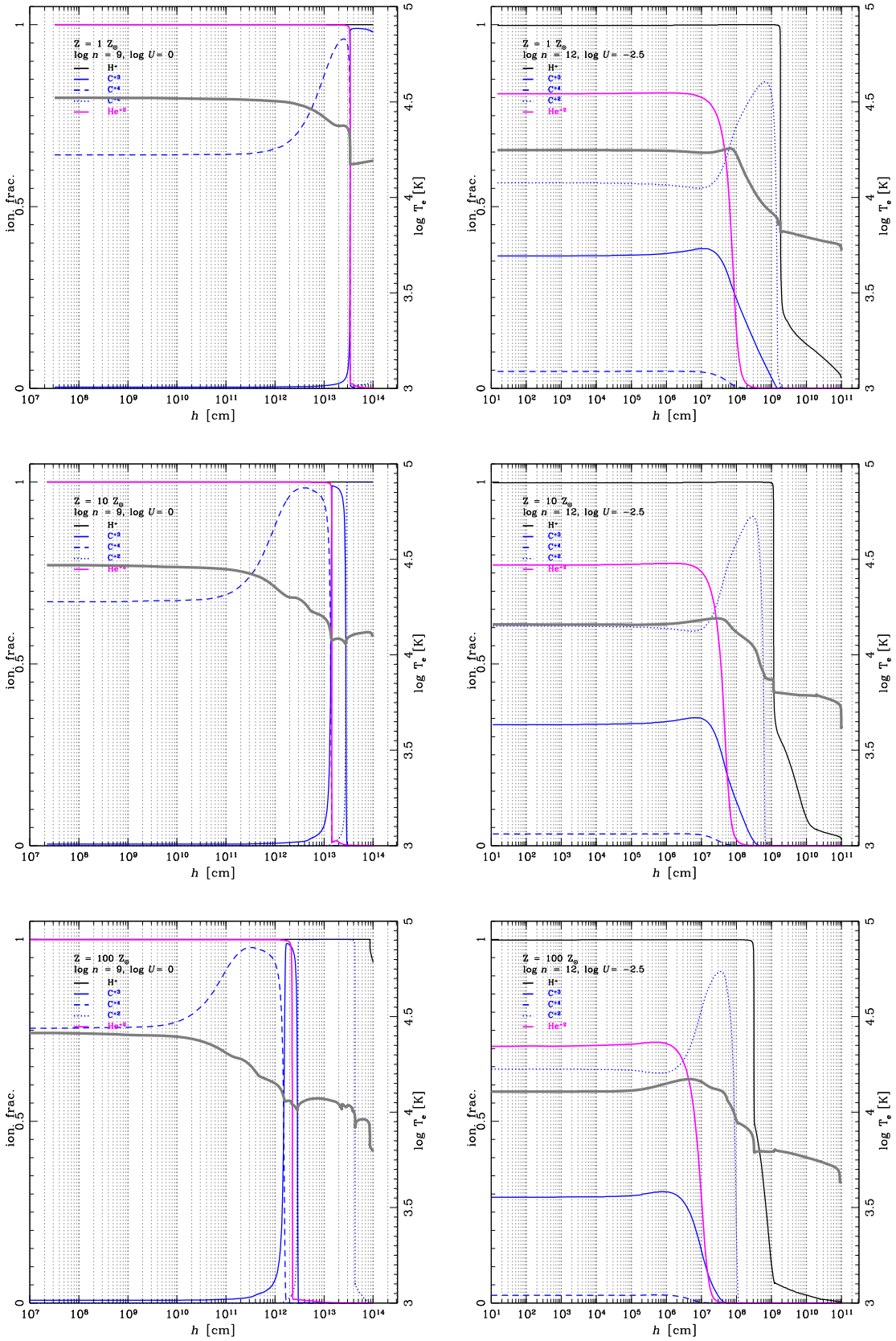

Figure 4. Ionization fraction and electron temperature (thick gray line) as a function of depth within the emitting gas slab, for physical parameters U and $n_{\rm H}$ fixed, computed with CLOUDY 13.05: ($\log U$, $\log n_{\rm H}$) = (−1, 9) (representative of BLUE and high-ionization case; left) and ($\log U$, $\log n_{\rm H}$) = (−2.5, 12) (representative of the low-ionization BLR; right), in order of increasing metallicity from top to bottom.

Table 2
Measurements in the λ1900 Blend Region

SDSS JCODE	Al III *W*	Al III FWHM	Al III Flux	C III] FWHM	C III] Flux	Si III] Flux
(1)	(2)	(3)	(4)	(5)	(6)	(7)
J010657.94−085500.1	7.9	5560	5.41 ± 0.38	6050	2.88 ± 0.14	7.2 ± 0.93
J082936.30+080140.6	10.2	5710	7.43 ± 0.42	5950	2.39 ± 0.21	4.85 ± 0.66
J084525.84+072222.3	13.1	5510	6.04 ± 0.52	5570	4.25 ± 0.53	3.13 ± 0.08
J084719.12+094323.4	9.9	5410	9.24 ± 0.24	5630	4.63 ± 0.36	5.61 ± 0.73
J085856.00+015219.4	7.7	5520	4.57 ± 0.37	5660	3.98 ± 0.12	4.39 ± 0.58
J092641.41+013506.6	8.0	5550	4.82 ± 0.3	5720	6.53 ± 0.23	5.48 ± 0.96
J094637.83−012411.5	5.0	2730	3.54 ± 0.24	2090	6.38 ± 0.22	5.1 ± 0.67
J102421.32+024520.2	10.1	5520	6.15 ± 0.31	6080	3.31 ± 0.2	5.1 ± 0.39
J102606.67+011459.0	9.5	5590	7.7 ± 0.35	5470	1.83 ± 0.33	3.64 ± 0.3
J114557.84+080029.0	11.4	5520	8.74 ± 0.38	6060	5.91 ± 0.83	6.3 ± 0.81
J150959.16+074450.1	11.8	5530	6.44 ± 0.53	6090	7.62 ± 0.25	7.58 ± 1.32
J151929.45+072328.7	10.5	5320	7.37 ± 0.51	5310	5.6 ± 0.62	7.16 ± 1.12
J211651.48+044123.7	6.1	5550	4.21 ± 0.4	5620	5.29 ± 0.2	5.35 ± 0.7

Note. Column (1): SDSS name. Columns (2) and (3): FWHM of Al III and C III] in km s^{-1}. Columns (4), (5), and (6): fluxes in units of 10^{-14} erg s^{-1} cm^{-2} for Al III, C III], and Si III].

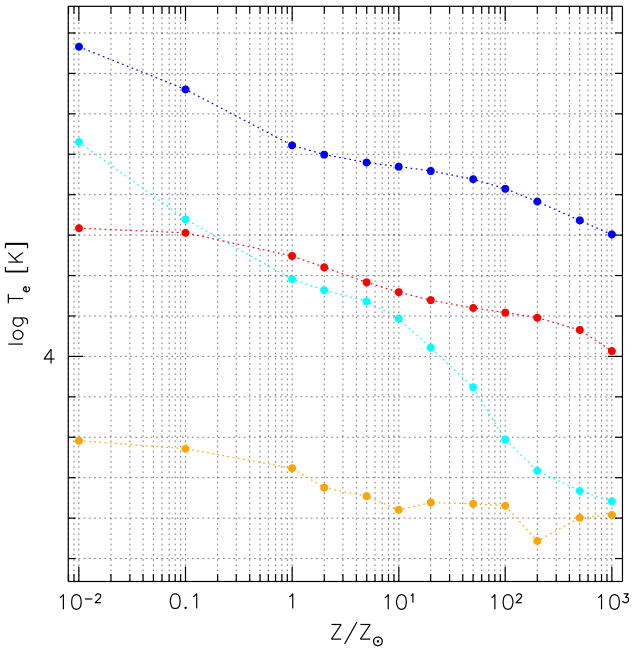

Figure 5. Electron temperature T_e as a function of metallicity Z, for physical parameters U and n_H fixed: ($\log U$, $\log n_H$) = (−1, 9) (representative of BLUE and high-ionization case; blue and cyan) and ($\log U$, $\log n_H$) = (−2.5,12) (representative of the low-ionization BLR; red and orange), from CLOUDY 13.05 computations. Blue and red refer to the first zone of the CLOUDY computation, i.e., to the illuminated surface of the clouds; cyan and orange, to the side of the cloud farther from the continuum sources, i.e., facing the observer.

Since the three ratios are, for fixed physical conditions, proportional to metallicity, we expect an overall consistency in their behavior, i.e., if one ratio is higher than the median for one object, also the other intensity ratios should be also higher. The lower diagrams are helpful to identify sources for which only one intensity ratio deviates significantly from the rest of the sample. A case in point is SDSS J082936.30+080140.6, whose ratio Al III/He II λ1640 ≈ 8 is one of the highest values, but whose C IV/He II λ1640 and Si IV/He II λ1640 are slightly below the median values. The fits of Appendix A show that this object is indeed extreme in Al III emission. The C IV and λ1400 blends are dominated by the BLUE excess, and an estimate of the C IV and Si IV BC is very difficult, as it accounts for a small fraction of the line emission. The He II λ1640 emission is almost undetectable, especially in correspondence with the rest frame. SDSS J082936.30+080140.6, along with other sources with high Al III/He II λ1640 or Si IV/He II λ1640 ratios, may indicate selective enhancement of aluminum or silicon (see also Section 5.7).

4.1.3. BLUE Intensity Ratios

Similar considerations apply to the blue intensity ratios. We see systematic trends in Figure 8 that imply consistency of the ratios for most sources, although the uncertainties are larger, especially for C IV/He II λ1640. The ratio C IV/(Si IV + O IV]) values are systematically higher than for the BC, while the C IV/He II λ1640 is slightly higher (median BLUE 5.8 vs. median BC 4.38). The ratio (Si IV + O IV])/He II λ1640 is much lower than for the BC (median BLUE 2.09 vs. median BC 6.27). The difference might be in part explained by the difficulty of deblending Si IV from O IV], and by the frequent occurrence of absorptions affecting the blue side of the blend. Both factors may conspire to depress BLUE. The bottom panels of Figure 8 are again helpful to identify sources for which intensity ratios deviate significantly from the rest of the sample. SDSS J102606.67+011459.0 shows a strong enhancement of C IV/He II λ1640 and Si IV + O IV], confirming the trend seen in its BC.

4.1.4. Correlation between Diagnostic Ratios

Figure 9 shows a matrix of correlation coefficients for all diagnostic ratios that we considered in this work. The 2σ confidence level of significance for the Spearman's rank correlation coefficient for 13 objects is achieved at $\rho \approx 0.54$. The highest degree of correlation is found between the ratios C IV/He II λ1640 and C IV/Si IV (0.87) and between C IV/He II λ1640 and Si IV/He II λ1640 (0.81). A milder degree of correlation is found between Al III/He II λ1640 and C IV/He II λ1640 (0.23) and Si IV/He II λ1640 (0.44). These results imply that Si IV and C IV are likely affected in a related way by a

Table 3
Measurements in the C IV Spectral Region

SDSS JCODE	C IV W	C IV BC FWHM	C IV BC Flux	C IV BLUE Flux	He II BC Flux	He II BLUE Flux
(1)	(2)	(3)	(4)	(5)	(6)	(7)
J010657.94−085500.1	18.6	5530	6.35 ± 1.04	13.46 ± 0.13	1.79 ± 0.46	1.93 ± 0.65
J082936.30+080140.6	15.5	3710 ± 670	1.83 ± 0.4	11.86 ± 0.03	0.8 ± 0.11	1.72 ± 0.69
J084525.84+072222.3	16.8	3760	5.04 ± 0.68	11.11 ± 0.21	1.06 ± 0.15	1.87 ± 0.81
J084719.12+094323.4	17.6	5520	11.53 ± 0.53	13.24 ± 0.07	2.14 ± 0.61	2.1 ± 1.19
J085856.00+015219.4	22.8	5460	9.84 ± 0.82	11.39 ± 0.09	0.65 ± 0.32	1.28 ± 0.48
J092641.41+013506.6	25.5	5550	7.79 ± 1.98	7.08 ± 0.08	1.94 ± 0.33	1.47 ± 0.39
J094637.83−012411.5	23.6	3670	15.63 ± 0.6	5.89 ± 0.09	1.87 ± 0.39	1.76 ± 0.7
J102421.32+024520.2	20.1	5640	6.74 ± 0.45	10.9 ± 0.08	1.9 ± 0.19	2.19 ± 1.07
J102606.67+011459.0	17.3	3700 ± 650	6.92 ± 1.22	12.23 ± 0.05	0.82 ± 0.34	1.15 ± 0.32
J114557.84+080029.0	18.4	3500 ± 700	6.84 ± 0.3	12.57 ± 0.03	2.01 ± 0.5	2.26 ± 1.02
J150959.16+074450.1	16.8	3530 ± 690	4.19 ± 0.84	9.73 ± 0.22	2.21 ± 0.14	1.48 ± 0.74
J151929.45+072328.7	19.4	3470 ± 590	5.47 ± 0.41	12.04 ± 0.16	1.52 ± 0.09	2.14 ± 0.24
J211651.48+044123.7	19.1	4750	13.04 ± 0.68	3.01 ± 0.24	0.99 ± 0.03	1.77 ± 0.69

Note. Column (1): SDSS name. Column (2): rest-frame equivalent width of the total C IV emission, i.e., C IV BLUE+BC, in Å. Column (3): FWHM of the C IV line in km s^{-1}. Columns (4) and (5): fluxes of the C IV BC and BLUE line. Columns (6) and (7): fluxes of the BC and BLUE components for the He II λ1640 line. All fluxes are in units of 10^{-14} erg s^{-1} cm^{-2}.

Table 4
Measurements in the λ1400 Region

SDSS JCODE	Si IV+O IV] BC FWHM	Si IV+O IV] BC Flux	Si IV+O IV] BLUE Flux
(1)	(2)	(3)	(4)
J010657.94−085500.1	5070	9.23 ± 1.4	6.24 ± 0.24
J082936.30+080140.6	5560	4.39 ± 0.81	7.3 ± 0.06
J084525.84+072222.3	5060	10.52 ± 0.58	2.69 ± 0.24
J084719.12+094323.4	5550	13.69 ± 0.86	3.79 ± 0.19
J085856.00+015219.4	6960	7.34 ± 0.69	8.55 ± 0.05
J092641.41+013506.6	5540	14.89 ± 0.45	4.05 ± 0.32
J094637.83−012411.5	4030	18.09 ± 0.7	3.29 ± 0.31
J102421.32+024520.2	5530	8.77 ± 0.64	4.06 ± 0.09
J102606.67+011459.0	5300	10.16 ± 0.57	4.01 ± 0.33
J114557.84+080029.0	3760	12.19 ± 1.22	5.71 ± 0.08
J150959.16+074450.1	3650	9.97 ± 0.75	5.86 ± 0.12
J151929.45+072328.7	3670	9.32 ± 1.05	4.48 ± 0.31
J211651.48+044123.7	4770	11.02 ± 0.77	0.81 ± 0.03

Note. Column (1): SDSS name. Column (2): FWHM of the Si IV line in km s^{-1}. Columns (3) and (4): fluxes of the BCs and the blue component line in units of 10^{-14} $ergs^{-1}$ cm^{-2}.

single parameter. The main parameter is expected to be T_e, and hence Z (Section 3.5.1). The Al III (normalized to the He II λ1640 flux) line shows much lower values of the correlation coefficient. The Al III line has a different dependence on U, n_H, and optical depth variations. The prominence of C III] with respect to Si III] decreases with Si IV/He II λ1640 BLUE, C IV/He II λ1640, and Si IV/He II λ1640 BLUE and increases with C IV/Si IV + O IV]. Apparently the C III]/Si III] ratio is strongly affected by an increase in metallicity and more in general by ratios that are indicative of "extremeness" in our sample. For BLUE, the two main independent Z estimators are correlated ($\rho \approx 0.68$).

4.2. Analysis of Z Distributions: Global Inferences on Sample

4.2.1. Fixed (U, n_H)

We propagated the diagnostic intensity ratios measured on the BC and BLUE components with their lower and upper uncertainties following the relation between ratios and Z in Figure 2, for the fixed physical conditions assumed in the low- and high-ionization region. The results are reported in Tables 6 and 7 for the BC and for the blueshifted component, respectively. The last row reports the median values of the individual sources' Z estimates with the sample SIQR. The distributions are shown in Figures 10 and 11, along with a graphical presentation of each source and its associated uncertainties.

Tables 6 and 7 permit us to quantify the systematic differences that are apparent in Figures 10 and 11. The agreement between the various estimators is good on average (the medians scatter around $\log Z \approx 1$ by less than 0.2 dex). However, there are systematic differences between the Z obtained from the various diagnostic ratios. Si IV and Al III over He II λ1640 apparently overestimate the Z by a factor of 2 with respect to C IV/He II λ1640. The out-of-scale values of C IV/Si IV and C IV/Al III may suggest that metallicity scaling according to solar proportion may not be strictly correct (Section 5.6). In the case of BLUE, several estimates

Table 5
Intensity Ratios for the BC and BLUE Line Components

SDSS JCODE	Al III/Si III] (BC)	C III]/Si III] (BC)	C IV/Si IV (BC)	C IV/He II λ1640 (BC)	Si IV/He II λ1640 (BC)	C IV/Al III (BC)	Al III/He II λ1640 (BC)	C IV/He II λ1640 (BLUE)	C IV/Si IV + O IV] (BLUE)	Si IV+ O IV]/ He II λ1640 (BLUE)
(1)	(2)	(3)	(4)	(5)	(6)	(7)	(8)	(9)	(10)	(11)
J010657.94−085500.1	0.75 ± 0.11	0.4 ± 0.05	0.69 ± 0.15	3.55 ± 1.09	5.16 ± 1.55	1.17 ± 0.21	3.02 ± 0.81	6.98 ± 3	2.16 ± 0.58	3.24 ± 1.1
J082936.30+080140.6	1.53 ± 0.23	0.49 ± 0.08	0.42 ± 0.12	2.29 ± 0.6	5.48 ± 1.26	0.25 ± 0.06	9.28 ± 1.39	6.89 ± 3.75	1.62 ± 0.6	4.24 ± 1.69
J084525.84+072222.3	1.93 ± 0.17	1.36 ± 0.17	0.48 ± 0.07	4.76 ± 0.92	9.95 ± 1.48	0.83 ± 0.13	5.71 ± 0.93	5.93 ± 3.07	4.13 ± 1.23	1.43 ± 0.63
J084719.12+094323.4	1.65 ± 0.22	0.82 ± 0.12	0.84 ± 0.07	5.38 ± 1.55	6.39 ± 1.86	1.25 ± 0.07	4.31 ± 1.23	6.29 ± 4.74	3.5 ± 1.75	1.8 ± 1.02
J085856.00+015219.4	1.04 ± 0.16	0.91 ± 0.12	1.34 ± 0.17	15.25 ± 7.63	11.38 ± 5.71	2.15 ± 0.25	7.08 ± 3.54	8.87 ± 5.01	1.33 ± 0.57	6.66 ± 2.47
J092641.41+013506.6	0.88 ± 0.16	1.19 ± 0.21	0.52 ± 0.13	4.03 ± 1.23	7.69 ± 1.31	1.62 ± 0.42	2.49 ± 0.45	4.83 ± 1.92	1.75 ± 0.53	2.76 ± 0.77
J094637.83−012411.5	0.7 ± 0.1	1.25 ± 0.17	0.86 ± 0.05	8.34 ± 1.74	9.66 ± 2.02	4.41 ± 0.35	1.89 ± 0.41	3.35 ± 1.99	1.79 ± 0.8	1.87 ± 0.77
J102421.32+024520.2	1.2 ± 0.11	0.65 ± 0.06	0.77 ± 0.08	3.55 ± 0.43	4.61 ± 0.58	1.1 ± 0.09	3.23 ± 0.37	4.97 ± 3.09	2.68 ± 1.04	1.85 ± 0.9
J102606.67+011459.0	2.12 ± 0.2	0.5 ± 0.1	0.68 ± 0.13	8.48 ± 3.83	12.46 ± 5.23	0.9 ± 0.16	9.45 ± 3.96	10.6 ± 4.21	3.05 ± 0.9	3.47 ± 1.01
J114557.84+080029.0	1.39 ± 0.19	0.94 ± 0.18	0.56 ± 0.06	3.41 ± 0.87	6.07 ± 1.64	0.78 ± 0.05	4.36 ± 1.11	5.56 ± 3.76	2.2 ± 1.11	2.53 ± 1.14
J150959.16+074450.1	0.85 ± 0.16	1 ± 0.18	0.42 ± 0.09	1.9 ± 0.4	4.51 ± 0.44	0.65 ± 0.14	2.92 ± 0.3	6.58 ± 4.49	1.66 ± 0.77	3.96 ± 1.98
J151929.45+072328.7	1.03 ± 0.18	0.78 ± 0.15	0.59 ± 0.08	3.61 ± 0.35	6.14 ± 0.79	0.74 ± 0.08	4.86 ± 0.45	5.62 ± 1.66	2.69 ± 0.76	2.09 ± 0.28
J211651.48+044123.7	0.79 ± 0.13	0.99 ± 0.13	1.18 ± 0.1	13.12 ± 0.78	11.08 ± 0.84	3.1 ± 0.34	4.23 ± 0.42	1.7 ± 0.73	3.71 ± 0.67	0.46 ± 0.18
Median	1.04 ± 0.34	0.91 ± 0.17	0.68 ± 0.16	4.03 ± 2.395	6.39 ± 2.23	1.10 ± 0.42	4.31 ± 1.35	5.93 ± 0.96	2.2 ± 0.65	2.53 ± 0.81

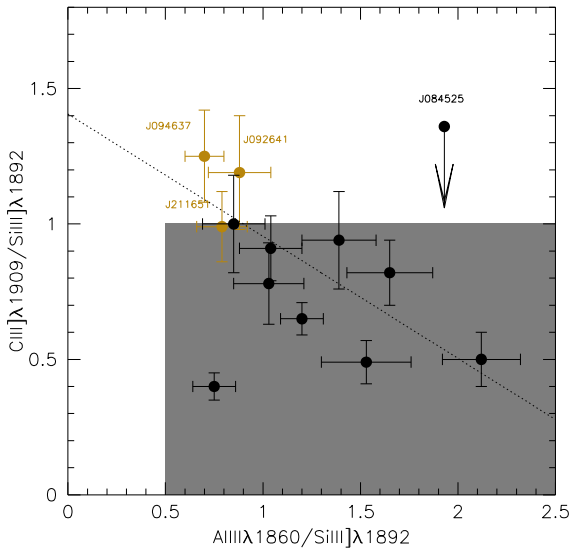

Figure 6. Relation between intensity ratios Al III λ1860/Si III] λ1892 and C III] λ1909/Si III] λ1892. The gray area corresponds to the parameter space occupied by the xA sources. Borderline sources are in orange color.

from C IV/He II λ1640 strongly deviate from the ones obtained with the other ratios, due to the nonmonotonic behavior of the relation between Z and C IV/He II λ1640, right in the range of metallicity that is expected. Figure 17 shows that the nonmonotonic behavior as a function of Z occurs for $-1 \lesssim \log U \lesssim 0$, assuming $\log n_{\rm H} = 9$.

The median values of all three ratios consistently suggest high metallicity with a firm lower limit $Z \approx 5$, and in the range $10\ Z_{\odot} \lesssim Z \lesssim 100\ Z_{\odot}$, with typical values between 20 and 50 $Z_{\odot}$. There is apparently a systematic difference between BC and BLUE, in the sense that Z derived from the BC is systematically higher than Z from BLUE. The difference is small in the case of C IV/He II λ1640 but is significant in the case of (Si IV + O IV])/He II λ1640, where Z from BLUE are a factor of 10 lower. We have stressed earlier that there are often absorptions affecting the BLUE of Si IV + O IV]/He II λ1640. Absorptions and the blending with C II λ1332 and Si IV BC lines make it difficult to properly define the continuum underlying the λ1400 blend at negative radial velocities. We think that the Si IV + O IV] BLUE intensity estimate is more of a lower limit. Another explanation might be related to the assumption of a constant density and U for all sources. While there are observational constraints supporting this condition for the BC (Panda et al. 2018, 2019, 2020b), there are no strong clues to the BLUE properties, save a high-ionization degree.

4.3. Z for Individual Sources for Fixed U, n_H

Table 8 reports the Z estimates for the BC, BLUE, and a combination of BC and BLUE for each individual object. The values reported are the median values of the individual objects' estimates from the different ratios. Here the Z value for each object is computed by vetting the ratios according to concordance. If the discordance is not due to a physical origin, but rather to instrumental problems (e.g., contamination by absorption lines, nonlinear dependence on Z of some ratios), a proper strategy is to use estimators such as the median that eliminate discordant values even for small sample sizes ($n \geqslant 3$). Measuring medians and SIQR is an efficient way to deal with the measurements of large samples of objects. All estimates $\log Z \lesssim 0$ were excluded, as either the product of heavy absorptions (Si IV + O IV])/He II λ1640) or the product of difficulties in relating the ratio (C IV/He II λ1640) to Z; apart from J211651.48+044123.7, the upper uncertainty of the negative estimates is so large that Z is actually unconstrained. The difference between BLUE and BC is even more evident: the median (last row) indicates a factor of $\approx$6 difference between BLUE and BC. The BC suggests a median $Z \approx 60\ Z_{\odot}$, while the BLUE $Z \approx 10\ Z_{\odot}$. The assumption that the wind and disk component have the same Z in each object is a reasonable one, with the caveats mentioned in Section 5.6. Therefore, the two estimates, for BLUE and BC, could be considered two independent estimators of Z. If the two estimates are combined for each individual object, $10\ Z_{\odot} \lesssim Z \lesssim 100\ Z_{\odot}$, with a median value of $Z \approx 20\ Z_{\odot}$.

There is a good agreement between the Z median estimates from the BC and BLUE of C IV, $\log Z \approx 1.27$ versus $\log Z \approx 1.13$, respectively (Tables 6 and 7). Ignoring Si IV +O IV] and Al III, the $Z \approx 20\ Z_{\odot}$ value derived for the C IV BC is not affected by a possible enhancement of [Si/C] and [Al/C] with respect to the solar values. If the carbon abundance is used as a reference, the BC Z estimate from Al III and Si IV could point toward a selective enhancement of Si and Al with respect to C.

The disagreement between BLUE and BC Z estimates rests on the blueshifted component of Si IV + O IV]. The disagreement between the Z estimates from ratios involving Si IV +O IV] BC and BLUE might be explained if one considers that the measurement of the Si IV+O IV] BLUE is most problematic and the Si IV+O IV] intensity might be systematically underestimated.

4.4. Estimates of Z Relaxing the Constraints on U and n_H

We computed the χ^2 in the following form, to identify the value of the metallicity for median values of the diagnostic ratios and for the diagnostic ratios of individual objects relaxing the assumption of fixed density and ionization parameters. For each object k, and for each component c, we can write

$$\chi^2_{\rm kc}(n_{\rm H}, U, Z) = \sum_{\rm i} w_{\rm ci} \left(\frac{R_{\rm kci} - R_{\rm kci,mod}(n_{\rm H}, U, Z)}{\delta R_{\rm kci}} \right)^2, \quad (8)$$

where the summation is done over the available diagnostic ratios, and the χ^2 is computed with respect to the results of the CLOUDY simulations as a function of U, $n_{\rm H}$, and Z (subscript "mod"). Weights $w_{\rm ci} = 1$ were assigned to C IV/He II λ1640, Si IV/He II λ1640, and Al III/He II λ1640; $w_{\rm ci} = 0$ or 0.5 was assigned to C IV/Al III and C IV/Si IV. For BLUE, the three diagnostic ratios were all assigned $w_{\rm ci} = 1$. The Z estimates for the BC are based on the three ratios involving He II λ1640 normalization.

To gain a global, bird's-eye view of the Z dependence on the physical parameters, Figure 12 shows the 3D space U, $n_{\rm H}$, Z. Each point in this space corresponds to an element of the grid of CLOUDY in the parameter space and is consistent with the minimum χ^2 within the uncertainties at 1σ confidence level. The case shown in the panels of Figure 12 is the one with the median values of the sample objects.

The distribution of the data points is constrained in a relatively narrow range of U, $n_{\rm H}$, Z, at very high density, low ionization, and high metallicity. Within the limit in U, $n_{\rm H}$, the

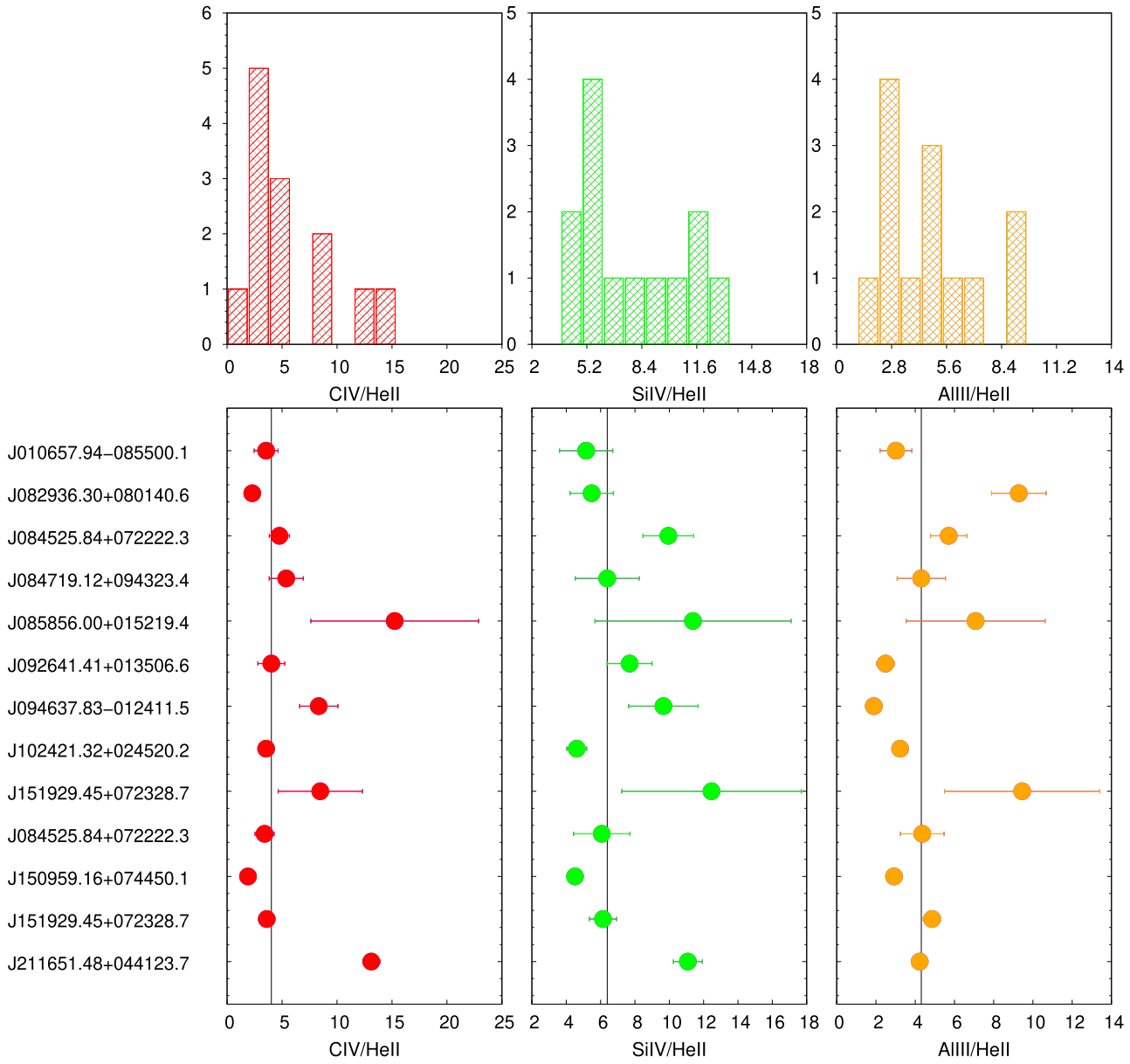

Figure 7. Distribution of diagnostic intensity ratios based on the BC (top) for C IV/He II λ1640 (red), Si IV/He II λ1640 (green), and Al III/He II λ1640 (orange). The bottom panels show results and associated uncertainties for individual sources with the same color-coding as histograms. The vertical black line in the bottom panels represents the median value of sources measurements.

distribution of Z is flat and thin, around $Z \sim 50$–$100\ Z_{\odot}$. This implies that, for a change of the U and $n_{\rm H}$ within the limits allowed by the data, the estimate of Z is stable and independent of U and $n_{\rm H}$. Table 8 reports the individual Z estimates and the SIQR for the sources in the sample (the last row is the median).

The allowed parameter space volume for BLUE is by far less constrained. The right panel of Figure 12 shows the parameter space for the Z estimates from the three BLUE intensity ratios. The condition on the χ^2 distribution is the same as used for the BC, namely, that the data points all satisfy the condition $\chi^2 \leqslant \chi^2_{\rm min} + 1$. A similar shape is obtained if we consider the condition that all three ratios agree with the ones predicted by the model within 1σ. The spread in ionization and density is very large, although the concentration of data points is higher in the case of low $n_{\rm H}$ (log $n_{\rm H} \sim 8$–9 [cm^{-3}]) and high ionization (log $U \sim 0$). At any rate the spread of the data points indicates that solutions at low ionization and high density are also possible. The results for individual sources tend to disfavor this scenario for the wide majority of the objects, but the properties of the gas emitting the BLUE component are less constrained than the ones of the gas emitting the BC. What is missing for BLUE is especially a firm diagnostic of density that in the case of BC is provided mainly by the ratio Al III/He II λ1640. Results on Z are, however, as stable as for the BC, even if the dispersion is larger, and suggest values in the range $10\ Z_{\odot} \lesssim Z \lesssim 50\ Z_{\odot}$.

Summing up, all meaningful estimators converge toward high Z values, definitely supersolar, with $Z \gtrsim 10\ Z_{\odot}$. Ratios C IV/Si IV significantly less than <1 are predicted in the parameter space. Si IV/He II λ1640 seems to give the largest estimates of Z. Also, the high Al III/C IV requires high values of Z. A conclusion has to be tentative, considering the possible

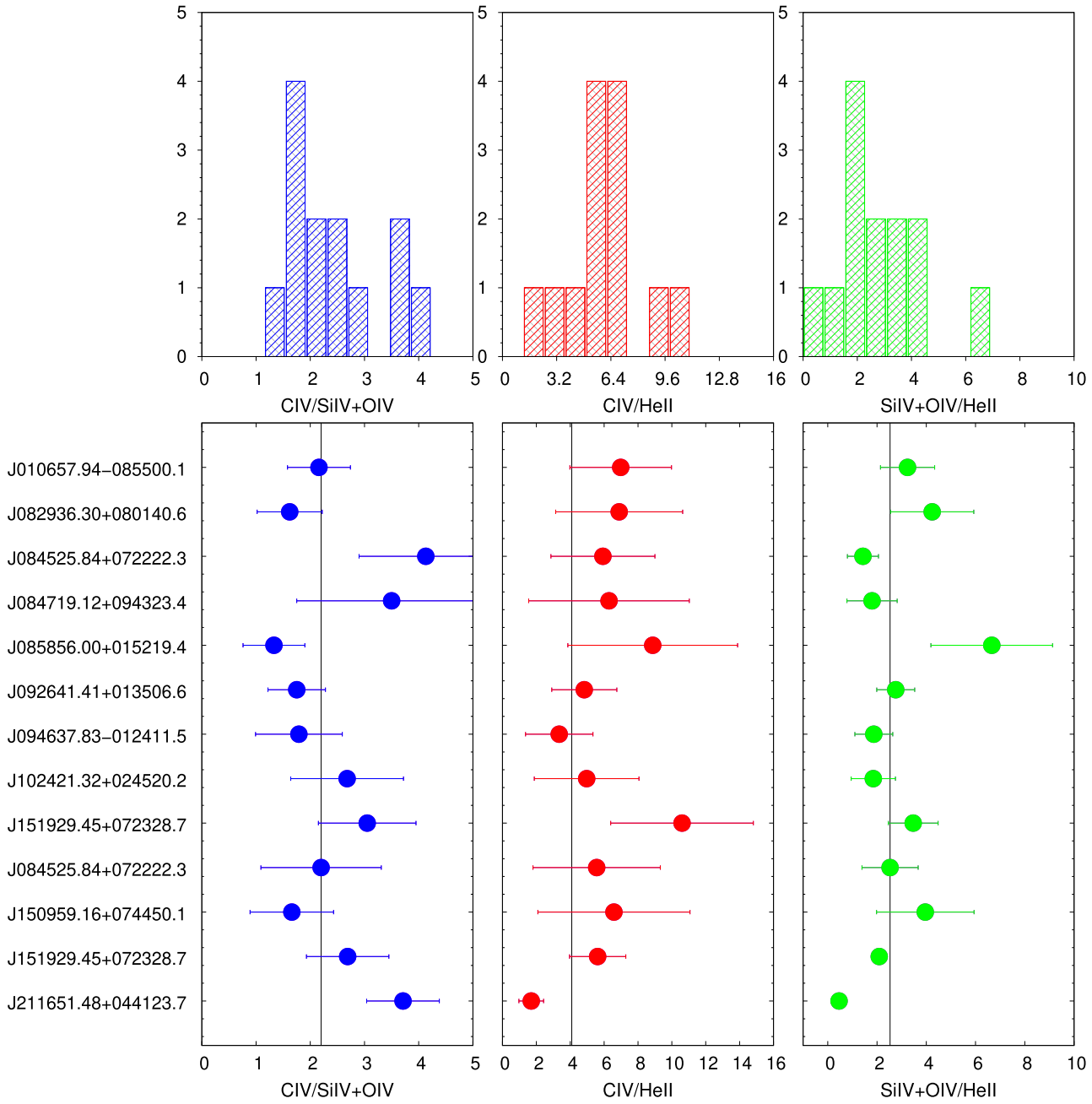

Figure 8. Distribution of diagnostic intensity ratios based on the BLUE components (top) for C IV/[S II] λλ6731, 6717 + O IV] (blue), C IV/He II λ1640 (red), and Si IV + O IV]/He II λ1640 (green). The bottom panels show results and associated uncertainties for individual sources with the same color-coding as histograms, as in the previous figure. The vertical black line represents the median value of ratio measurements.

systematic errors affecting the estimates of the C IV and Si IV intensities: for C IV, the BC in the most extreme cases is often buried under an overwhelming BLUE; a fit is not providing a reliable estimate of the BC (by far the fainter component) but provides a reliable BLUE intensity; for Si IV we may overestimate the intensity due to "cancellation" of the BLUE by absorptions. This said, the present data are consistent with the possibility of a selective enhancement of Al and Si, as already considered by Negrete et al. (2012). This issue will be briefly discussed in Section 5.

At any rate, the absence of correlation between BLUE and BC parameters (Figure 9), the difference in the diagnostic ratios and differences in inferred Z, and the results for individual sources described below justify the approach followed in the paper to maintain a separation between BLUE and BC. The meaning of possible systematic differences between the BC and BLUE is further discussed in Section 5.

4.4.1. Individual Sources

BC.—The best $n_{\rm H}$, U, and Z for each object have been obtained by minimizing the χ^2 as defined in Equation (8), and they are reported in Table 9. The $\chi^2_{\rm min}$ values are listed in the second column of Table 9. At the side of each value there is the uncertainty range for each parameter defined from volume in

Table 6
Metallicity ($\log Z$) of the BC Assuming Fixed U, $n_{\rm H}$

SDSS JCODE	C IV/He II λ1640	Si IV/He II λ1640	Al III/He II λ1640
J010657.94−085500.1	$1.16^{+0.26}_{-0.33}$	$1.85^{+0.20}_{-0.20}$	$1.7^{+0.16}_{-0.15}$
J085856.00+015219.4	$2.22^{+0.36}_{-0.35}$	$2.41^{+0.59}_{-0.36}$	$2.2^{+0.31}_{-0.29}$
J082936.30+080140.6	$0.63^{+0.36}_{-0.65}$	$1.89^{+0.16}_{-0.15}$	$2.36^{+0.10}_{-0.09}$
J084525.84+072222.3	$1.41^{+0.14}_{-0.16}$	$2.31^{+0.11}_{-0.11}$	$2.07^{+0.10}_{-0.09}$
J084719.12+094323.4	$1.50^{+0.20}_{-0.23}$	$1.99^{+0.21}_{-0.19}$	$1.91^{+0.17}_{-0.17}$
J092641.41+013506.6	$1.27^{+0.24}_{-0.29}$	$2.12^{+0.12}_{-0.12}$	$1.59^{+0.11}_{-0.10}$
J094637.83−012411.5	$1.80^{+0.15}_{-0.14}$	$2.29^{+0.16}_{-0.15}$	$1.44^{+0.12}_{-0.13}$
J102421.32+024520.2	$1.16^{+0.11}_{-0.12}$	$1.77^{+0.09}_{-0.08}$	$1.74^{+0.07}_{-0.06}$
J102606.67+011459.0	$1.82^{+0.30}_{-0.32}$	$2.49^{+0.51}_{-0.32}$	$2.38^{+0.27}_{-0.26}$
J114557.84+080029.0	$1.12^{+0.22}_{-0.27}$	$1.96^{+0.19}_{-0.18}$	$1.92^{+0.15}_{-0.15}$
J150959.16+074450.1	$0.19^{+0.49}_{-0.47}$	$1.76^{+0.06}_{-0.07}$	$1.69^{+0.05}_{-0.06}$
J151929.45+072328.7	$1.18^{+0.08}_{-0.09}$	$1.97^{+0.08}_{-0.09}$	$1.98^{+0.05}_{-0.05}$
J211651.48+044123.7	$2.11^{+0.04}_{-0.04}$	$2.39^{+0.06}_{-0.06}$	$1.9^{+0.06}_{-0.06}$
Median	1.27 ± 0.32	1.99 ± 0.21	1.91 ± 0.18

Note. Column (1): SDSS identification. Columns (2), (3), and (4): metallicity values for C IV/He II λ1640, Si IV + O IV]/He II λ1640, and Al III/He II λ1640 with uncertainties.

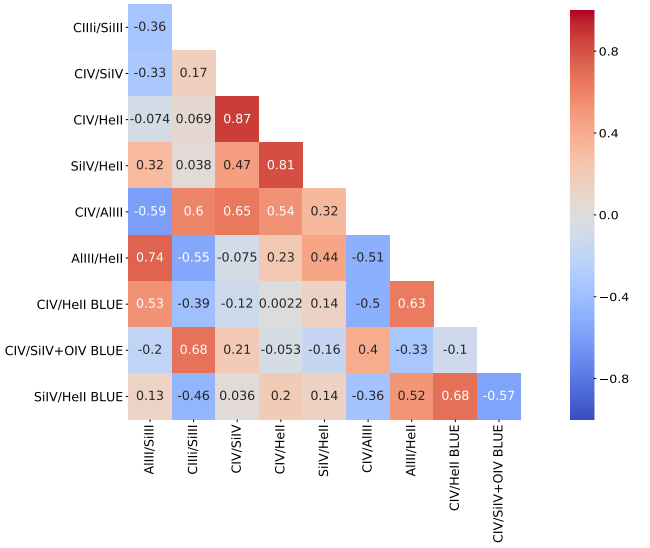

Figure 9. Correlation matrix between diagnostic ratios in BC and BLUE. The numbers in each square show the Spearman rank correlation coefficient. Red colors indicate a positive correlation; blue colors indicate a negative correlation.

the parameter space satisfying the condition $\chi^2 \approx \chi^2_{\rm min} + 1$.[11] In other words, the choice of the best physical conditions was obtained by minimizing the sum of the deviations between the model predictions and the observer diagnostic ratios. The last two rows list the minimum χ^2 values for the median (with the SIQR of the sample from Table 5) and for the median of the values reported for individual sources in Table 9. The obtained values of Z cover the range $5\ Z_\odot \lesssim Z \lesssim 100\ Z_\odot$, with 9 out of 13 sources with $50\ Z_\odot \lesssim Z \lesssim 100\ Z_\odot$, and medians of intensity ratios yielding $Z \sim 50\ Z_\odot$. There is some spread in the ionization parameter values, $-4 \lesssim U \lesssim -1$, but in most cases U indicates low or very low ionization level. The hydrogen density is very high: in only a few cases $\log n_{\rm H} \sim 10$–11, and in several cases $n_{\rm H}$ reaches 10^{14} cm^{-3}. The median values from the ratios are $\log U = -2.25$, $\log n_{\rm H} = 13.75$ (with a range 12.5–14), therefore validating the original assumption of $\log U = -2.5$, $\log n_{\rm H} = 12$ for a fixed physical condition. The results for individual sources confirm the scenario of Figure 12 for the wide majority of the sample sources. The higher $n_{\rm H}$ values are consistent with recent inferences for the low-ionization BLR derived from Temple et al. (2020), based on the Fe III UV emission, which is especially prominent in the UV spectra of xA quasars (Martínez-Aldama et al. 2018a). It is interesting to note that two of the borderline objects (Al III/Si III] ≈ 0.5, C III]/Si III] ≈ 1) show higher values of the ionization parameter ($\log U \approx -1.0$ to -1.5).

Large ($\gg$1) values of $\chi^2_{\rm min}$ are associated with cases in which the BC components of Al III and/or of Si IV are strong with respect to the BC of C IV, and are further increased by small uncertainty ranges (which are more likely to occur if a line is strong). Intensity ratios C IV/Al III $\lesssim 1$ and C IV/Si IV $\lesssim 1$ are reproduced by photoionization simulations in conditions of very low ionization. The ratio C IV/Al III tends to decrease with increasing Z, although the trend is shallow at the lower ionization levels appropriate for the BC emission (Appendix B). However, high values of the Al III and Si IV + O IV] over He II ratios induced by overabundances could bias the U and lower its values.

BLUE.—The inferences are less clear from BLUE (Table 10, organized like Table 9). In most cases, the permitted volume in the 3D parameter space for individual sources covers a broad range in U and $n_{\rm H}$ as for the median (Figure 12). Figure 12 shows that there is a strip of χ^2 values statistically consistent with the minimum χ^2 that crosses the full domain of the parameter space. Along this strip of permitted values $n_{\rm H}$ and U are linearly dependent, with $\log U \approx -0.5 \cdot n_{\rm H} + 4$ for the median composite ratios. In most sources the U value implies a high degree of ionization, $-1 \lesssim \log U \lesssim 0$, but in three cases (e.g., SDSS J150959.16+074450.1) there is apparently a

[11] This approach follows a standard procedure (Bevington & Robinson 2003, p. 209) for the determination of the confidence intervals, and we see in the matrix $\chi^2(Z, U, n_{\rm H})$ a well-defined global minimum around which the χ^2 increases systematically.

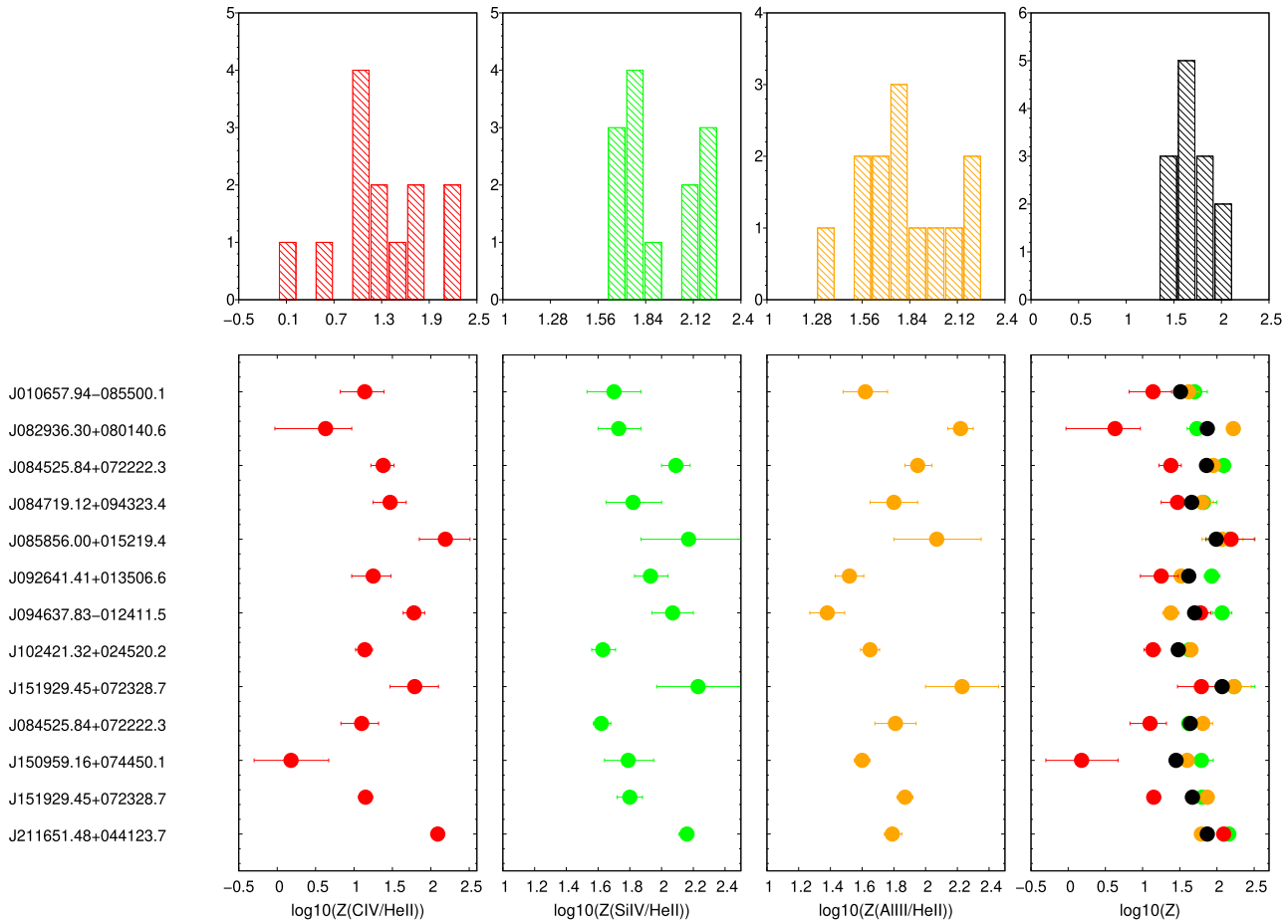

Figure 10. Top panels: distribution of metallicity measurements for the BC obtained from ratios C IV/He II λ1640 (red), Si IV/He II λ1640 (green), and Al III/He II λ1640 (orange), and the mean metallicity obtained from all ratios (black). Bottom panels: results and associated uncertainties for individual sources with the same color-coding as histograms. The last panel contains all metallicity measurements and the mean of them for each object.

Table 7
Metallicity ($\log Z$) of BLUE Assuming Fixed U, $n_{\rm H}$

SDSS JCODE	Si IV + O IV]/He II λ1640	C IV/Si IV + O IV]	C IV/He II λ1640
J010657.94−085500.1	$1.00^{+0.12}_{-0.16}$	$0.88^{+0.14}_{-0.12}$	$1.34^{+0.34}_{-1.99}$
J085856.00+015219.4	$1.26^{+0.20}_{-0.13}$	$1.12^{+0.23}_{-0.21}$	$1.55^{+0.35}_{-2.05}$
J082936.30+080140.6	$1.10^{+0.14}_{-0.16}$	$1.03^{+0.16}_{-0.19}$	$1.33^{+0.41}_{-2.14}$
J084525.84+072222.3	$0.62^{+0.20}_{-0.19}$	$0.63^{+0.09}_{-0.09}$	$1.13^{+0.50}_{-2.07}$
J084719.12+094323.4	$0.72^{+0.27}_{-0.24}$	$0.68^{+0.21}_{-0.15}$	$1.22^{+0.59}_{-2.32}$
J092641.41+013506.6	$0.93^{+0.11}_{-0.14}$	$0.99^{+0.14}_{-0.16}$	$-0.56^{+1.93}_{-0.46}$
J094637.83−012411.5	$0.74^{+0.20}_{-0.18}$	$0.98^{+0.20}_{-0.22}$	$-0.99^{+2.16}_{-1.06}$
J102421.32+024520.2	$0.73^{+0.24}_{-0.20}$	$0.78^{+0.19}_{-0.14}$	$-0.52^{+2.10}_{-0.65}$
J102606.67+011459.0	$1.02^{+0.11}_{-0.12}$	$0.73^{+0.12}_{-0.10}$	$1.67^{+0.24}_{-0.31}$
J114557.84+080029.0	$0.89^{+0.19}_{-0.22}$	$0.87^{+0.25}_{-0.20}$	$0.99^{+0.70}_{-2.12}$
J150959.16+074450.1	$1.07^{+0.18}_{-0.21}$	$1.01^{+0.22}_{-0.23}$	$1.28^{+0.52}_{-2.28}$
J151929.45+072328.7	$0.79^{+0.07}_{-0.06}$	$0.78^{+0.13}_{-0.11}$	$1.02^{+0.40}_{-0.59}$
J211651.48+044123.7	$-0.57^{+0.81}_{-0.43}$	$0.66^{+0.06}_{-0.05}$	$-1.46^{+0.27}_{-0.23}$
Medians	0.89 ± 0.15	0.87 ± 0.13	1.13 ± 0.92

Note. Column (1): SDSS identification. Columns (2), (3), and (4): metallicity values for Si IV + O IV]/He II λ1640, C IV/Si IV + O IV], and C IV/He II λ1640 with uncertainties.

low-ionization solution with U comparable to that of the low-ionization BLR. The medians are $\log n_{\rm H} \sim 7.75$, $\log U \sim -0.5$, close to the values that we assumed for the fixed (U, $n_{\rm H}$) approach. The results on metallicity suggest in most cases $Z \gtrsim 20\ Z_{\odot}$. However, within 1 SIQR from the minimum χ^2, Z values up to 30 are also possible.

Z values from BLUE are systematically lower than those from the BC. The medians differ by a factor of 2. However, a

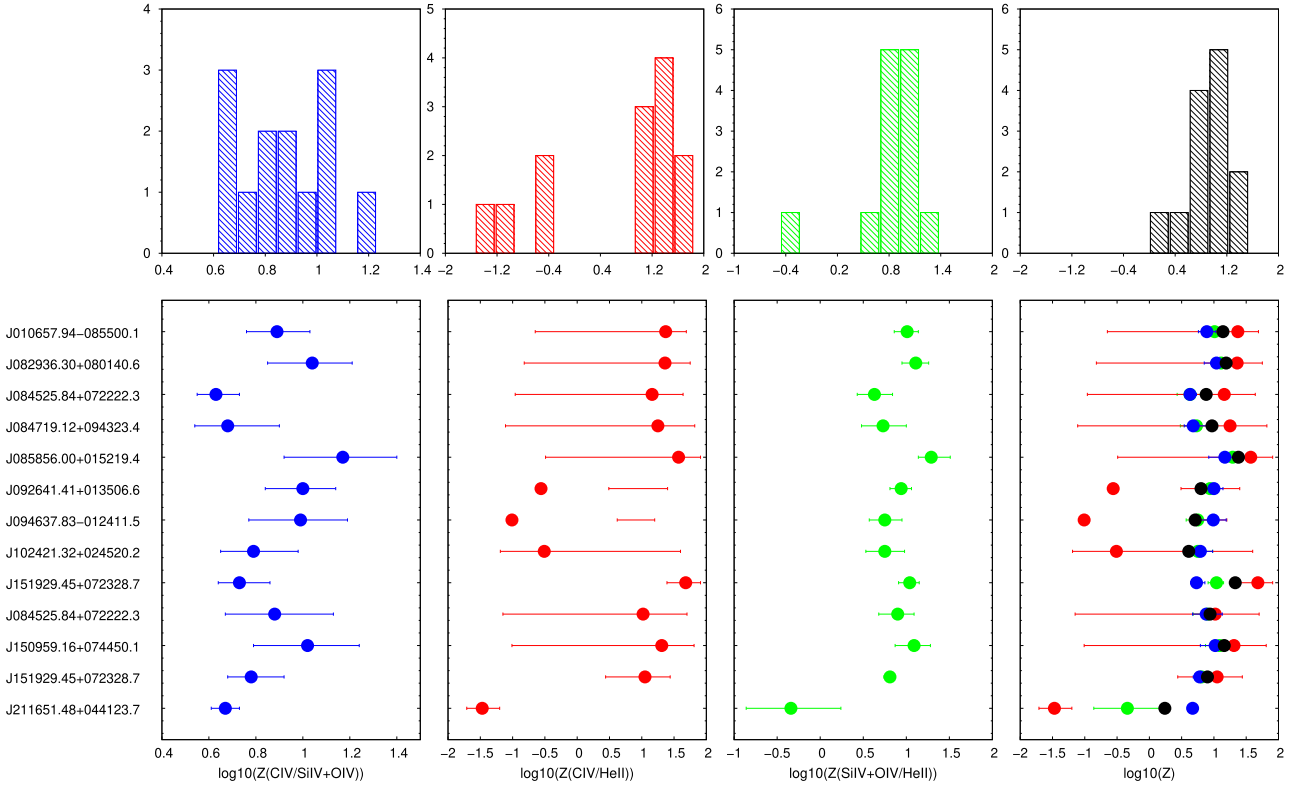

Figure 11. Top panels: distribution of metallicity measurements for blue component obtained from ratios C IV/Si IV + O IV] (blue), C IV/He II λ1640 (red), and Si IV + O IV]/He II λ1640 (green), and the mean metallicity obtained from all ratios (black). Bottom panels: results and associated uncertainties for individual sources with the same color-coding as histograms. The last panel contains all metallicity measurements and the mean of them for each object.

Table 8
Metallicity ($\log Z$) of Individual Quasars Assuming Fixed U, $n_{\rm H}$

SDSS JCODE	BC	BLUE	Combined
J010657.94−085500.1	1.70 ± 0.34	1.00 ± 0.23	1.34 ± 0.35
J082936.30+080140.6	1.89 ± 0.86	1.10 ± 0.15	1.33 ± 0.43
J084525.84+072222.3	2.07 ± 0.45	0.63 ± 0.25	1.41 ± 0.72
J084719.12+094323.4	1.91 ± 0.25	0.72 ± 0.27	1.50 ± 0.60
J085856.00+015219.4	2.22 ± 0.11	1.26 ± 0.21	2.20 ± 0.48
J092641.41+013506.6	1.59 ± 0.42	0.93 ± 0.77	1.27 ± 0.33
J094637.83−012411.5	1.80 ± 0.42	0.74 ± 0.99	1.44 ± 0.53
J102421.32+024520.2	1.74 ± 0.30	0.73 ± 0.65	1.16 ± 0.51
J102606.67+011459.0	2.38 ± 0.33	1.02 ± 0.47	1.82 ± 0.68
J114557.84+080029.0	1.92 ± 0.42	0.89 ± 0.06	1.12 ± 0.52
J150959.16+074450.1	1.69 ± 0.78	1.07 ± 0.14	1.28 ± 0.34
J151929.45+072328.7	1.97 ± 0.40	0.79 ± 0.12	1.18 ± 0.59
J211651.48+044123.7[a]	2.11 ± 0.24	$0.66 \pm \cdots$	2.11 ± 0.34
Median	1.91 ± 0.16	0.89 ± 0.12	1.34 ± 0.11

Notes. Column (1): SDSS identification. Columns (2), (3), and (4): metallicity medians for BC, BLUE, and a combination of the two, with uncertainties. Column (5): number of ratios used for the BLUE estimates. No uncertainty is reported for BLUE of SDSS J211651.48+044123.7 since only one ratio was used.
[a] Si IV and C IV affected by absorptions on the blue wings.

Welch t-test (Welch 1947) fails to detect a significant difference between the average values of the metallicity for the two components: $t \approx 0.86$ for 5 degrees of freedom (computed using the Welch-Satterthwaite equation) implies a significance of just 80%. Three cases in which the disagreement is large, more than a factor of 5, namely, J084525.84+072222.3, J084719.12+094323.4, and J102606.67+011459.0, are apparently not strongly affected by absorption lines, but the constraints from Tables 10 and 9 are poor, implying that also for BLUE the Z could be much higher. Therefore, we cannot substantiate any claim of a systematic difference between BLUE and BC Z estimates.

The Z, U, $n_{\rm H}$ parameter space occupation of xA quasars.— In summary, the low-ionization BLR of xA sources seems to be consistently characterized by low ionization, extremely high density, and very high metallicity, under the assumption that Z scales with the solar chemical composition. Diagnostics on BLUE is less constraining, and measurements are more difficult. The zero-order results are, however, consistent again with high metallicity $Z \gtrsim 5\ Z_{\odot}$.

The 3D distribution in Figure 12 indicates that, although there might be a large range of uncertainty in the U and $n_{\rm H}$ especially for BLUE, the Z values tend to remain constrained within a narrow strip around a well-defined Z, parallel to the U, $n_{\rm H}$ plane. In other words, Z estimates should be stable, as they are not strongly dependent on the assumed physical parameters.

Comparing the individual Z estimates for fixed and free $n_{\rm H}$ and U (Cols. (2) of Tables 6 and 9) for the BC, the agreement is good, with a median difference of 0.22 and an SIQR of 0.15, with the fixed $n_{\rm H}$ and U being therefore a factor of ≈1.65 higher than the one derived assuming a free $n_{\rm H}$ and U. Two sources (J151929.45+072328.7 and J114557.84+080029.0) show a large disagreement, in the sense that the Z values leaving U and $n_{\rm H}$ free are much lower. These Z estimates are, however, highly uncertain, with a shallow χ^2 distribution around the minimum especially for J151929.45+072328.7. For

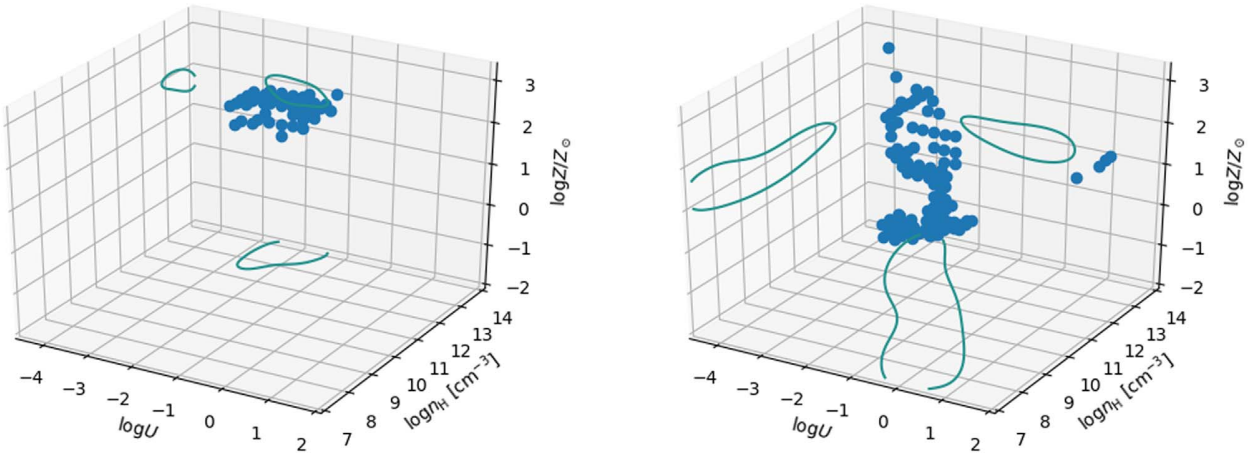

Figure 12. Parameter space n_H, U, Z. Left: data points in 3D space are elements in the grid of the parameter space selected for not being different from χ^2_{min} by more than $\delta\chi^2 \approx 1$, computed from the emission-line ratios measured for the BC and referring to the median values in Table 5. Right: same as the left panel, but for the BLUE component, also including the condition that the data points are in agreement with the three diagnostic ratios within the SIQR of the median estimate from Table 5. The individual contour line was smoothed with a Gaussian kernel.

Table 9
Z, U, n_H of Individual Sources and Median Derived from the BC

SDSS JCODE (1)	χ^2_{min} (2)	$\log Z$ ($Z_\odot$) (3)	$\delta \log Z$ ($Z_\odot$) (4)	$\log U$ (5)	$\delta \log U$ (6)	$\log n_H$ (7)	$\delta \log n_H$
J010657.94−085500.1	2.6894	1.7	0.7–1.7	−2.00	−2.75 to −1.25	13.50	12.00–14.00
J082936.30+080140.6	6.6414	1.3	0.7–2.7	−4.00	−4.00 to −3.50	14.00	12.75–14.00
J084525.84+072222.3	13.700	1.7	1.0–3.0	−1.75	−3.75 to −0.25	14.00	12.00–14.00
J084719.12+094323.4	1.7004	1.7	1.0–2.0	−2.25	−2.50 to −1.50	13.75	12.50–14.00
J085856.00+015219.4	0.0012	2.0	1.7–2.7	−2.25	−3.00 to −1.75	12.50	12.00–14.00
J092641.41+013506.6	1.7982	1.7	1.7–2.0	−1.50	−1.75 to −1.00	14.00	13.50–14.00
J094637.83−012411.5	0.3253	1.7	1.7–2.3	−1.00	−1.25 to −0.75	12.25	11.75–14.00
J102421.32+024520.2	15.819	1.7	1.3–2.0	−2.25	−3.00 to −1.50	13.50	12.75–14.00
J102606.67+011459.0	1.5020	2.0	1.7–2.3	−1.75	−2.50 to −0.75	14.00	12.50–14.00
J114557.84+080029.0	6.6174	0.7	0.7–2.0	−3.75	−3.75 to −1.25	14.00	12.25–14.00
J150959.16+074450.1	45.287	1.3	0.5–2.0	−1.75	−0.50 to −3.50	13.75	12.25–14.00
J151929.45+072328.7	29.220	0.7	0.3–3.0	−3.75	−4.00 to −2.75	14.00	11.00–14.00
J211651.48+044123.7	1.4476	2.0	1.7–2.0	−2.00	−2.00 to −0.75	12.25	10.75–12.25
$\mu_{\frac{1}{2}}$(Ratios)	1.9914	1.7	0.7–2.0	−2.25	−2.75 to −1.25	13.75	12.50–14.00
$\mu_{\frac{1}{2}}$(Objects)	⋯	1.7	1.5–1.9	−2.00	−2.25 to −1.75	13.75	13.50–14.00

Table 10
Z, U, n_H of Individual Sources and Median Derived from BLUE

SDSS JCODE (1)	χ^2_{min} (2)	$\log Z$ ($Z_\odot$) (3)	$\delta \log Z$ ($Z_\odot$) (4)	$\log U$ (5)	$\delta \log U$ (6)	$\log n_H$ (7)	$\delta \log n_H$
J010657.94−085500.1	0.00985	1.70	0.70–1.7	0.75	−1.5–0.75	7.75	7.50–9.75
J082936.30+080140.6	0.01506	1.30	1.00–1.70	−0.25	−2.0 to −0.00	8.00	7.75–12.25
J084525.84+072222.3	0.00143	1.0	0.00–2.30	−1.50	−2.50 to −1.25	7.25	7.00–11.25
J084719.12+094323.4	0.00097	1.00	0.00–3.00	−2.24	−2.50–0.75	8.75	7.50–11.50
J085856.00+015219.4	0.00305	1.70	1.0–2.00	0.50	−1.75–0.50	8.25	7.00–11.75
J102606.67+011459.0	0.00111	0.70	0.70–3.00	−1.00	−2.50 to −0.5	9.25	8.25–11.25
J114557.84+080029.0	0.00164	1.30	0.30–1.70	−2.50	−2.50–0.25	11.50	7.25–12.50
J150959.16+074450.1	0.00288	1.30	0.30–2.00	−2.00	−2.75–0.75	11.75	7.00–13.75
J151929.45+072328.7	0.00032	0.30	0.30–1.30	−0.50	−0.75–0.25	10.00	7.75–10.25
$\mu_{\frac{1}{2}}$(Ratios)	0.07336	1.30	1.0–1.30	−0.50	−0.50 to −0.50	7.75	7.75–8.00
$\mu_{\frac{1}{2}}$(Objects)	⋯	1.30	1.15–1.45	−1.00	−0.125 to −1.875	8.75	7.75–9.75

this object the maximum metallicity covered by the simulations $Z = 1000\ Z_{\odot}$ is still consistent within the uncertainties.

5. Discussion

5.1. A Method to Estimate Z

The determination of the metal content of the broad-line-emitting region of xA quasars was made possible by the following procedure:

1. The estimation of an accurate redshift. Even if all lines are affected by significant blueshifts that reduce the values of measured redshift, in the absence of information from the Hβ spectral range the Al III and the λ1900 blend can be used as proxies of proper redshift estimators. The blueshifts are the smallest in the intermediate-ionization lines at λ1900 (A. del Olmo et al. 2021, in preparation).
2. The separation of the BC and BLUE, for C IV and the λ1400 blend. The line width of the individual components of the Al III doublet can be used as a template BC. The component BLUE is defined as the excess emission on the blue side of the BC.
3. A first estimate of metallicity can be obtained from the assumption that the low-ionization BLR associated with the BC and wind/outflow component associated with BLUE can be described by similar physical conditions in different objects. Several diagnostic ratios can be associated with the intensity ratios predicted by an array of photoionization simulations, namely,
   (a) for the BC: Al III/He II λ1640, C IV/He II λ1640, Si IV/He II λ1640, assuming $(\log U, \log n_{\rm H}) = (-2.5, 12)$ or $(\log U, \log n_{\rm H}) = (-2.5, 13)$;
   (b) for the BLUE: C IV/He II λ1640, Si IV + O IV]/He II λ1640, C IV/Si IV + O IV] assuming $(\log U, \log n_{\rm H}) = (0, 9)$.
4. Estimates can be refined for individual sources relaxing the constant $(\log U, \log n_{\rm H})$ assumptions. Tight constraints can be obtained for the BC. The BLUE is more problematic, because of both observational difficulties and the absence of unambiguous diagnostics.

Our method relies on ratios involving He II λ1640 that have not been much considered in previous literature. In addition, we have considered fixed SED, turbulence (equal to 0), and column density in the simulations ($N_{\rm c} = 10^{23}$) as fixed. The role of turbulence is further discussed in Section 5.5 and is found to be not relevant, unlike in the case of Fe II emission in the optical spectral range, where effects of self- and Lyα-fluorescence are important (e.g., Verner et al. 1999; Panda et al. 2018), while the $N_{\rm c}$ effect is most likely negligible.

Extension of the method to the full Population A is a likely possibility, since we do not expect a very strong effect of the SED on the metallicity estimate, as long as the SED has a prominent big blue bump, as seems to be case for Population A. The role of SED is likely important if the method has to be extended to sources of Population B along the main sequence. At least two SED cases should be considered, if the aim is to apply the method presented in this paper to a large sample of quasars.

Intensity ratios involving He II λ1640 are difficult to measure in the xA spectra but may be more accessible for Population B spectra. Ferland et al. (2020) have shown significant differences in the SED as a function of $L/L_{\rm Edd}$, with a much flatter SED at low $L/L_{\rm Edd}$. The extension to Population B would therefore require a new dedicated array of simulations.

5.2. Accretion Parameters of Sample Sources

The bolometric luminosity has been computed assuming a flat ΛCDM cosmological model with $\Omega_{\Lambda} = 0.7$, $\Omega_m = 0.3$, and $H_0 = 70\ {\rm km\ s^{-1}\ Mpc^{-1}}$. Following Marziani & Sulentic (2014), we decided to use Al III as a virial broadening estimator for computing the $M_{\rm BH}$. Our estimates adopt two different scaling laws: the scaling laws of Vestergaard & Peterson (2006) for C IV, and a second, unpublished one based on Al III (A. del Olmo et al. 2021, in preparation). Eddington ratios have been obtained using the Eddington luminosity $L_{\rm Edd} \approx 1.3 \times 10^{38} (M_{\rm BH}/M_{\odot})\ {\rm erg\ s^{-1}}$. The luminosity range of the sample is very limited, less than a factor of 3, $46.8 \lesssim \log L \lesssim 47.3$, in line with the requirement of similar redshift and high flux values. Correspondingly, the $M_{\rm BH}$ and the Eddington ratio are constrained in the range $8.8 \lesssim \log M_{\rm BH} \lesssim 9.5$ and $-0.55 \lesssim \log L/L_{\rm Edd} \lesssim 0.18$, respectively. The $M_{\rm BH}$ sample dispersion is small, with $\log M_{\rm BH} \sim 9.4 \pm 0.2\ [M_{\odot}]$. The scatter in $M_{\rm BH}$ and $L/L_{\rm Edd}$ is reduced to $\approx$0.1 dex if we exclude one object with the lowest $M_{\rm BH}$ and highest $L/L_{\rm Edd}$. Applying a small correction (10%) to the FWHM to account for an excess broadening in Al III due to nonvirial motions will decrease the $M_{\rm BH}$ by 0.1 dex (as found by Negrete et al. 2018 for Hβ) and increase $L/L_{\rm Edd}$ correspondingly. If this correction is applied, the median $L/L_{\rm Edd}$ is $\approx$0.6. Using the C IV BC FWHM as a virial broadening estimator further decreases the $M_{\rm BH}$ median estimate by 0.1 dex. The accretion parameters are consistent with extreme quasars of Population A at high mass and luminosity; they are mainly at the low-$L/L_{\rm Edd}$ end of sample 3 (based on $M_{\rm BH}$ estimates from Al III) of Marziani & Sulentic (2014). The small dispersion in physical properties of the present sample (0.2 dex) focuses the analysis on properties that may differ for fixed accretion parameters, and fixed ratio of radiation and gravitation forces, perhaps related to different enrichment histories.

5.2.1. Correlation between Diagnostic Ratios and AGN Physical Properties

Considering the small dispersion in $M_{\rm BH}$, $L/L_{\rm Edd}$, and bolometric luminosity, it is hardly surprising that none of the ratios utilized in this paper are significantly correlated with the accretion parameter. The highest degree of correlation is seen between $L/L_{\rm Edd}$ and C IV/Al III, but still below the minimum ρ needed for a statistically significant correlation.

In Figure 13 we present the correlation between metallicity and diagnostic ratios, along with log of bolometric luminosity, log of black hole mass, and log of Eddington ratio, for BC and BLUE. The strongest correlations between $Z_{\rm BC}$ and intensity ratios are with Si IV/He II λ1640 (0.75) and Al III/He II λ1640 (0.77). For $Z_{\rm BLUE}$, Si IV/He II λ1640 (BLUE components) correlates strongly (0.99). $Z_{\rm BLUE}$ correlates with physical parameters, whereas $Z_{\rm BC}$ rather anticorrelates with them, but not at a statistically significant level. Considering the limited range in luminosity and $M_{\rm BH}$ and the small sample size, these trends should be confirmed.

The metallicity values we derive are very high among quasars analyzed with similar techniques (e.g., Nagao et al. 2006b; Shin et al. 2013; Sulentic et al. 2014): as mentioned, typical values for high-z quasars are around 5 $Z_{\odot}$. This value

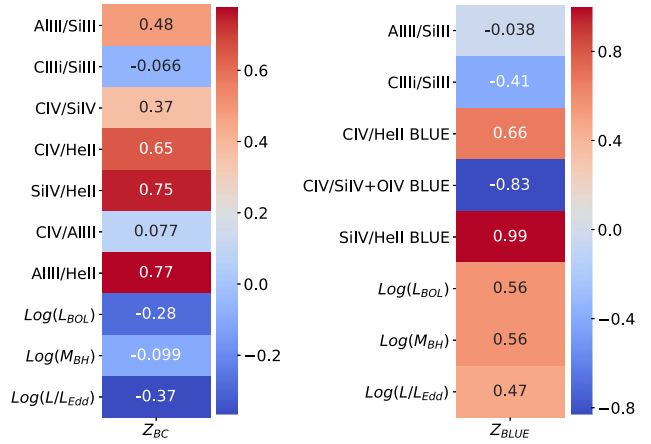

Figure 13. Left panel: correlation matrix between Z computed for the BC and BC diagnostic ratios assuming fixed $n_{\rm H}$ and U along with log of bolometric luminosity, log of black hole mass, and log of Eddington ratio. Right panel: same as the left panel, but for the BLUE component. The numbers in each square show the Spearman rank correlation coefficient. The color hue is proportional to the correlation, from dark blue (strong negative correlation) to red (strong positive correlation).

could be taken as a reference over a broad range of redshift, and also for the sample considered in the present paper, as there is no evidence of metallicity evolution in the BLR up to $z \approx 7.5$ (e.g., Nagao et al. 2006b; Juarez et al. 2009; Xu et al. 2012; Onoue et al. 2020). This is in line with the results of Negrete et al. (2012), who found very similar intensity ratios for the prototypical NLSy1 and xA source I Zw 1, of relatively low luminosity at low z, and a luminous xA object at redshift $z \approx 3.23$. Even if these authors did not derive Z from their data, the I Zw 1 intensity ratios reported in their paper indicate very high metallicity, consistent with the values derived for the present sample.

More than inferences on the global enhancement of Z in the host galaxies, the absence of evolution points toward a circumnuclear source of metal enrichment, ultimately associated with a starburst (e.g., Collin & Zahn 1999a; Xu et al. 2012).

A detailed comparison with previous work on the dependence of Z on accretion parameters is hampered by two difficulties: (1) Before comparing the intensity ratios of this paper, we should consider that other authors do not distinguish between BLUE and BC when computing the ratios. This has the unfortunate implication that in some cases, such as Al III/C IV, the ratio is taken between lines emitted predominantly in different regions (virialized and wind), presumably in very different physical conditions. Not distinguishing between BC and BLUE yields C IV/Al III $\sim 10 \gg 1$. (2) Methods of $M_{\rm BH}$ estimate differ. For example, Matsuoka et al. (2011) use the Vestergaard & Peterson (2006) scaling laws without any correction to the line width of C IV. This might easily imply overestimates of the $M_{\rm BH}$ by factors of 5–10 (Sulentic et al. 2007). The analysis by Shemmer et al. (2004) instead used Hβ from optical and IR observations to compute $M_{\rm BH}$ and to examine the dependence of metallicity on accretion parameters. These authors found the strongest dependence on Eddington ratio (with respect to luminosity and mass) over 6 orders of magnitude in luminosity, suggesting that luminosity and black hole mass are less relevant (as also found, e.g., by Shin et al. 2013).

5.3. A Posteriori Analysis of N V Strength

As was stressed in several works (e.g., Wang et al. 2012a; Sulentic et al. 2014), the intensity of the N V line is difficult to estimate owing to blending with Lyα and strongly affected by absorption. We model Lyα and N V using the same criteria as in Si IV modeling. However, in this work, we give only a qualitative judgment of N V strength for our sample, because of large uncertainties due to the effect mentioned above. For sources in the highest metallicity range obtained from ratios from BC, the N V BC intensity is slightly higher than or comparable to Lyα BC. Blue components dominate both lines. We notice also significantly higher intensity of the blue component in comparison to the broad one in Si IV and C IV blends. An example of source of this type is shown in the upper half of Figure 14. On the contrary, sources with the lowest metallicities obtained from BC intensity ratios show the Lyα BC intensity higher than in N V, and the BC is stronger than BLUE. We see the same behavior of strong BC in the Si IV and C IV ranges. An example of sources of this type is shown in the lower half of Figure 14. Shin et al. (2013) compared Si IV + O IV] and N V fluxes and found strong, significant correlation between them ($\rho = 0.75$). The N V over He II λ1640 or Hβ should be a strong tracer of Z, as it is sensitive to secondary Z production and hence proportional to Z^2 (Hamann & Ferland 1999). Therefore, we conclude that the N V emission is extremely strong and consistent with very high metal content. A much more thorough investigation of the quasar absorption/emission system is needed to include N V as a Z estimator. This is deferred to further work.

5.4. Role of Column Density

The column density assumed in the present paper is log $N_{\rm c} = 23$ [cm^{-2}]. With this value the emitting clouds in the low-ionization conditions remain optically thick to the Lyman continuum for most of the geometrical depth of the cloud. Even if the value log$N_{\rm c} = 23$ may appear as a lower limit for the low-ionization BLR, as higher values are required to explain low-ionization emission such as Ca II and Fe II (Panda 2020; Panda et al. 2020a), the emission of the intermediate- and high-ionized region is confined within the fully ionized part of the line-emitting gas, whose extension is already much less than the geometrical depth of the gas slab for log$N_{\rm c} = 23$. Therefore, we expect no or a negligible effect from an increase in the column density for the low-ionization part of the BLR.

For BLUE, the situation is radically different, and we have no actual strong constraints on column density. Most emission may come from a clumpy outflow (Matthews 2016 and references therein), and therefore assuming a constant $N_{\rm c}$ may not be appropriate. Considering the poor constraint that we are able to obtain, we leave the issue to an eventual investigation.

5.5. Role of Turbulence

The results presented in this work refer to the case in which there is no significant microturbulence included in the CLOUDY computations. Figure 15 shows that at low ionization the effect is relatively modest, and that in the high-ionization case appropriate for BLUE the effect is very modest. Less obvious is the behavior at low ionization for $R_{\rm Fe\ II}$: it shows an increase for $t = 10$ km s^{-1}, but then it has a surprising drop at a larger value of the microturbulence. While the increase can be explained by an increase of the transitions for which fluorescence is possible,

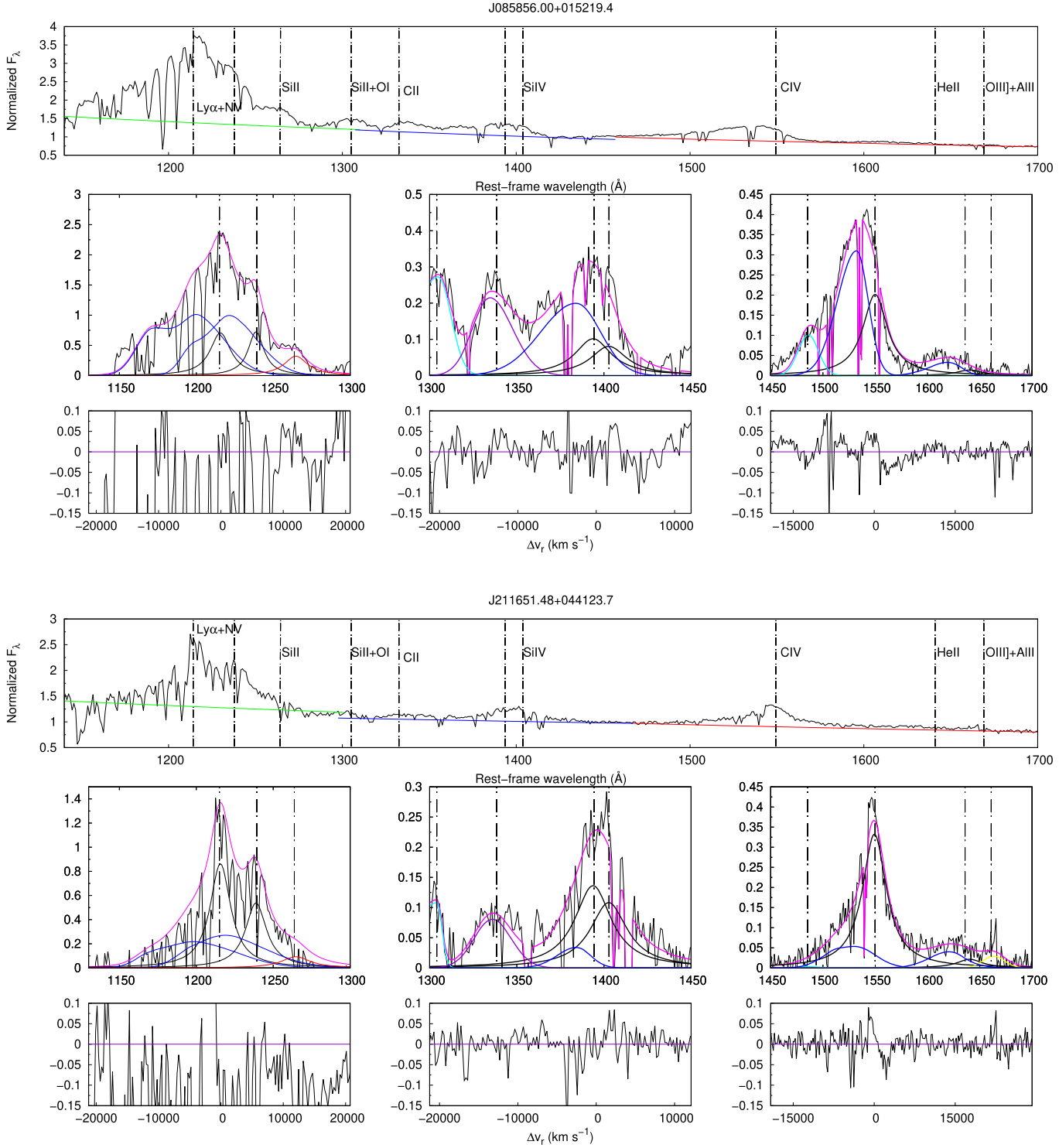

Figure 14. Analysis of sources showing the Lyα + N V blend. Top: calibrated rest-frame spectrum of SDSS J085856.00+015219.4, before continuum subtraction. Global or local continuum is specified by a solid colored line, while the black line marks rest-framed data. Dotted–dashed vertical lines correspond to the rest-frame wavelength of each emission line. Bottom: multicomponent fits after continuum subtraction for the Lα λ1216, Si IV λ1397, and C IV λ1549 spectral ranges. The solid black line marks the BC at rest frame associated with Lyα λ 1216, N V λ1240, Si IV λ1397, and C IV λ1549. The blue one marks the blueshifted component associated with each emission. The magenta line corresponds to the fit to the whole spectrum. In the bottom left panel, the red line corresponds to Si II λ1265. In the middle bottom panel, the light-blue line marks the contribution of the O I + Si II λ1304 blend, while the violet line corresponds to the C II λ1335 emission line. In the C IV λ1549 region, N IV] λ1486 is represented by a light-blue line, while the gold one corresponds to the O III] λ1663 + Al II λ1670 blend. Lower panels correspond to the residuals, in radial velocity units km s^{-1} and in Å. Bottom: same as in the previous panels, but for SDSS J211651.48+044123.7.

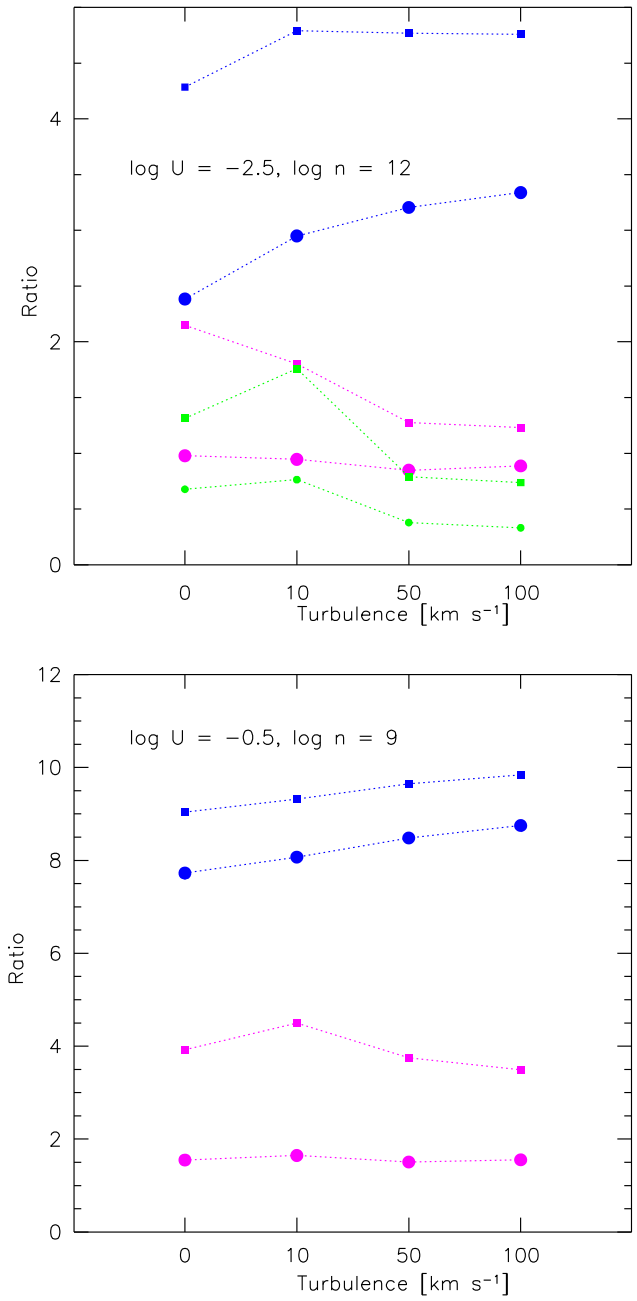

Figure 15. Effects of turbulence on diagnostic line ratios, for C IV/He II λ1640 (blue) and Si IV/He II λ1640 (magenta), considering 5 (circles) and 20 $Z_{\odot}$ (squares), according to CLOUDY 13.05 computations. The top panel assumes the low-ionization conditions appropriate for BC emission, the bottom one for BLUE. In the top panel the green lines trace the same trends for the Fe II blend at λ4570 over Hβ ratio, i.e., $R_{\rm Fe\ II}$.

the decrease is not of obvious interpretation. It has been, however, confirmed by the independent set of simulations of Panda et al. (2018, 2019).

5.6. Metal Segregation?

Metals are expected to be preferentially accelerated by resonance scattering (e.g., Proga 2007b; Risaliti & Elvis 2010). In principle, for a sufficiently large photon flux, the acceleration of metals by radiation pressure might become larger than the Coulomb friction, therefore causing a decoupling of the metals with respect to their parent plasma (Baskin & Laor 2012). This possibility has been explored in the context of the BALs, and broad absorption and emission components are expected to be related (Elvis 2000; Xu et al. 2020). The ionization parameter values are, however, several orders of magnitudes higher than the ones derived for the BLUE emission component. In addition, our Z estimates for the BLUE suggest, if anything, values lower than or equal to those for the BC, whose Z might be related more to the original chemical composition of the gas in the accretion material. However, we ascribe the systematic differences between BC and BLUE as uncertainties in the method and measurement, so that Z from BLUE and BC should be considered intrinsically equal.

Considering that the most metal-rich stars, galaxies, and molecular clouds in the universe do not exceed $Z \approx 5\ Z_{\odot}$ (Maiolino & Mannucci 2019), circumnuclear star formation is needed for the chemical enrichment of the BLR gas (e.g., Collin & Zahn 1999a, 1999b; Wang et al. 2011, 2012b). Star formation may occur in the self-gravitating, outer part of the disk. An alternative possibility is that a massive star could be formed inside the disk by accretion of disk gas (Cantiello et al. 2020).

5.7. Abundance Pollution?

An implication of the scenarios involving circumnuclear or even nuclear star formation is that there could be an alteration of the relative abundance of elements with respect to the standard solar composition (Anders & Grevesse 1989; Grevesse & Sauval 1998). Support for this hypothesis is provided by the extreme C IV/Si IV and C IV/Al III that may hint at a selective enhancement of Al with respect to C. As suggested by Negrete et al. (2012), core-collapse supernovæ with very massive progenitors could be at the origin of a selective enhancement. Supernovae with progenitors of masses between 15 and 40 $M_{\odot}$ have selective enhancement in their yields of Al and Si by factors of ≈100 and 10 relative to hydrogen with respect to solar (Chieffi & Limongi 2013). Since carbon is also increased by a factor of ∼10 with respect to solar, the [Al/C] is expected to be a factor of ∼10 larger than the solar value in supernova ejecta. The case for silicon is less clear, as the enhancement is of the same order of magnitude as the one expected for carbon. Pollution of gas by supernovæ may therefore lead to an estimate of the Z higher than the actual one, if solar relative abundances are assumed. This possibility will be explored in an eventual work (K. Garnica et al. 2021, in preparation).

5.8. Implications for Quasar Structure Evolution

Metallicity and the outflow prominence of quasars were found to be highly correlated (Wang et al. 2012a; Shin et al. 2017). The implication of these results is that xA sources, which show the highest blueshifts (Sulentic et al. 2017; Martinez-Aldama et al. 2018a, 2018b; Vietri et al. 2018), should also be the most metal-rich. The xA sources should be at the top of the Z outflow parameter correlation of Wang et al. (2012a), if $Z \gtrsim 10\ Z_{\odot}$.

There is evidence of a metallicity correlation between the BLR and NLR (Du et al. 2014), as expected if the outflows on spatial scales of kiloparsecs are originating in a disk wind. Zamanov et al. (2002) derived very small spatial scales at low

luminosity. This provides additional support to the idea that xA sources, which at low z phenomenologically appear as Fe II-strong NLSy1s, are relatively young sources. Their low [O III] λ5007 equivalent width implied young age more than orientation effects (Risaliti et al. 2011; Bisogni et al. 2017). The $z \approx 2$ quasars of the present sample are radiating at relatively high $L/L_{\rm Edd}$, although there are no examples of the extremes of xA sources showing blueshifted emission in Al III as prominent as the one of C IV (e.g., Martínez-Aldama et al. 2017). There is no evidence of heavy obscuration. They are certainly out of the obscured early evolution stage in which the accreting black hole is enveloped by gas and dust (see the sketch in D'Onofrio & Marziani 2018). The W C IV distribution covers the upper half of the one of Martínez-Aldama et al. (2018a). There are no weak-lined quasars following Diamond-Stanic et al. (2009). The xA sources of the present sample may have reached a sort of stable equilibrium between gravitation and radiation forces made perhaps possible by the development by an optically thick, geometrically thick accretion disk, and by its anisotropic radiation properties (e.g., Abramowicz et al. 1988; Szuszkiewicz et al. 1996; Sądowski et al. 2014).

The median value of the peak displacement of the BLUE component is $\approx$3500 km s^{-1}, and the centroid at half-maximum is shifted by 5000 km s^{-1}. The extreme blueshifts in the metal lines imply outflows that may not remain bound to the potential well of the black hole and of the inner bulge of the host galaxies (e.g., Marziani et al. 2016b and references therein). The high metal content of the outflows, estimated by the present work to be in the range of 10–50 $Z_{\odot}$, implies that these sources are likely to be a major source of metal enrichment of the interstellar gas of the host galaxy and of the intergalactic medium. Using a standard estimate for the mass outflow rate $\dot{M}$ (Marziani et al. 2016b), $\dot{M} \approx 15 L_{\rm C\,IV,45} v_{5000} r_{1\,\rm pc}^{-1} n_9^{-1}\, M_{\odot}\ {\rm yr}^{-1}$, we obtain an outflow rate of $\dot{M} \approx 20\, M_{\odot}\ {\rm yr}^{-1}$, assuming median values for the sources of our sample: median outflow velocity from the peak of BLUE ≈ -3500 km s^{-1}, a median luminosity of the C IV BLUE (corrected because of Galactic extinction) of 4.2×10^{44} erg s^{-1}, a median radius 5.9×10^{17} cm from the Kaspi et al. (2007) radius−luminosity correlation for C IV, and $n_9 = 1$. For a duty cycle of $\sim 10^8$ yr, the expelled mass of heavily enriched gas could be $\sim 10^9\, M_{\odot}$.

6. Conclusion

The sources at the extreme end of Population A along the main sequence are defined by the prominence of their Fe II emission and, precisely, by the selection criterion $R_{\rm Fe\,II} \gtrsim 1$ (Marziani & Sulentic 2014; Du et al. 2016a). Their properties as a class are scarcely known. Even if there has been a long history of studies focused on Fe II-strong sources since Lipari et al. (1993) and Graham et al. (1996), their relevance to galactic and large-scale structure evolution is being reconsidered anew with the help of the quasar main sequence. This paper adds to other aspects that were considered by previous investigations (e.g., the very powerful outflows, the disjoint low- and high-ionization emitting regions, first suggested by Collin-Souffrin et al. 1988), a quantitative analysis of the chemical composition of xA sources. The main aspects of the present investigations can be summarized as follows:

1. We distinguish between two emission-line components most likely originating from emitting in widely different physical conditions: a virialized low-ionization BLR, and a high-ionization region associated with a very strong blueshifted excess in the C IV emission line. This is the conditio sine qua non for meaningful Z estimates.
2. The physical conditions in the low and high regions were confirmed to be very different, with the low ionization (U, $n_{\rm H}$) $\approx$ (−2.75, 12.5–14) and the high ionization (U, $n_{\rm H}$) $\approx$ (−0.5, 8). The high-ionization region parameters are, however, poorly constrained.
3. Using intensity ratios between the strongest metal lines and He II λ1640 emission at λ1640, we derive metallicity values in the range $10\ Z_{\odot} \lesssim Z \lesssim 50\ Z_{\odot}$, with most likely values around several tens of the solar metallicity. Incidentally, we note that the low equivalent width is consistent with the high Z of the emitting regions.
4. We find evidence of overabundance of Al with respect to C. This result points toward possible pollution of the broad-line-emitting gas chemical composition by supernova ejecta.

xA quasars are perhaps the only quasars whose ejection are able to overcome the potential well of the black hole and of the host galaxy. Applying the method to large samples of quasars would permit us to constrain the metal enrichment processes on a galactic scale.

The present analysis relied heavily on the He II λ1640 line, which is of low equivalent width and with a flat, very broad profile. Therefore, a more precise analysis would require spectra of moderate dispersion but of higher S/N. A large part of the scatter and/or systematic difference for various Z estimators is related to the difficulty in isolating faint and broad emission in relatively noisy spectra.

M.S. acknowledges the support of the Erasmus+ program of the European Union and would like to express very great appreciation to Istituto Nazionale di Astrofisica (INAF) Osservatorio Astronomico di Padova, University of Padova, and Astronomical Observatory of the University of Warsaw for enabling her to complete an internship. The project was partially supported by the Polish Funding Agency National Science Centre project 2017/26/A/ST9/00756 (MAESTRO 9) and MNiSW grant DIR/WK/2018/12. P.M. acknowledges the Hypatia of Alexandria visiting grant SO-IAA (SEV-2017-0709) through the Center of Excellence Severo Ochoa and is deeply indebted to Drs. J. Perea and A. del Olmo for the generous allocation of computing resources and for a stay at IAA. A.d.O. acknowledges financial support from the Spanish grants MCI PID2019-106027GB-C41 and the State Agency for Research of the Spanish MCIU through the "Center of Excellence Severo Ochoa" award for the Instituto de Astrofísica de Andalucía (SEV-2017-0709).

Funding for the Sloan Digital Sky Survey (SDSS) has been provided by the Alfred P. Sloan Foundation, the Participating Institutions, the National Aeronautics and Space Administration, the National Science Foundation, the U.S. Department of Energy, the Japanese Monbukagakusho, and the Max Planck Society. The SDSS website is http://www.sdss.org/.

The SDSS is managed by the Astrophysical Research Consortium (ARC) for the Participating Institutions. The Participating Institutions are the University of Chicago, Fermilab, the Institute for Advanced Study, the Japan Participation Group, Johns Hopkins University, Los Alamos National Laboratory, the Max-Planck-Institute for Astronomy

(MPIA), the Max-Planck-Institute for Astrophysics (MPA), New Mexico State University, University of Pittsburgh, Princeton University, the United States Naval Observatory, and the University of Washington.

Appendix A
Rest-frame Spectra and Fits

The spectral analysis of the 13 objects of our sample is shown in Figure 16.

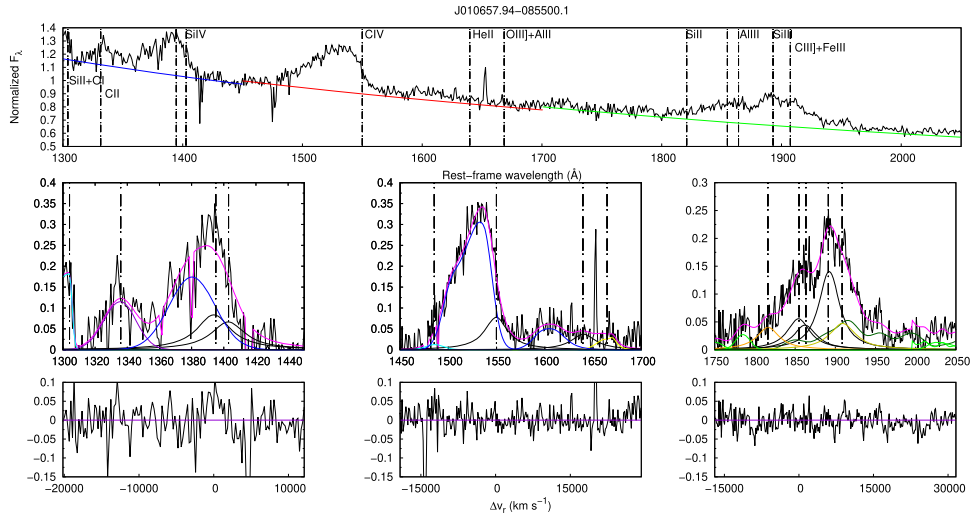

Figure 16. (a) Top panels: calibrated rest-frame spectrum of SDSS J010657.94−085500.1 before continuum subtraction. Global or local continuum is specified by a solid colored line, while the black line marks rest-framed data. Dotted–dashed vertical lines correspond to the rest-frame wavelength of each emission line. Bottom: multicomponent fits after continuum subtraction for the Si IV λ1397, C IV λ1549, and λ1900 blend spectral ranges. The solid black line marks the BC at rest frame associated with Si IV λ1397, C IV λ1549, and Al III λ1860; the blue one marks the blueshifted component associated with each emission. The magenta line corresponds to the fit to the whole spectrum. In the bottom left panel, the light-blue line marks the contribution of the O I + S II λ1304 blend, while the violet line corresponds to the C II λ1335 emission line. In the C IV λ1549 region, N IV] λ1486 is represented by a light-blue line, while the gold one corresponds to the O III] λ1663 + Al II λ1670 blend. In the λ1900 blend range, Fe III and Fe II contributions are marked by dark- and light-green lines, respectively. Violet lines mark the N III] λ1750 line, the orange one corresponds to the S III λ1816 line, and the gold one corresponds to the C III] λ1909 line. Lower panels correspond to the residuals, in radial velocity units km s^{-1} and in Å. (b) Same as the previous panel, but for SDSS J082936.30+080140.6, SDSS J084525.84+072222.3, and SDSS J084719.12 +094323.4. (c) Same as the previous panel, but for SDSS J085856.00+015219.4, SDSS J092641.41+013506.6, and SDSS J094637.83−012411.5. (d) Same as previous panel, but for SDSS J102421.32+024520.2, SDSS J102606.67+011459.0, and SDSS J114557.84+080029.0. (e) Same as the previous panel, but for SDSS J150959.16+074450.1, SDSS J151929.45+072328.7, and SDSS J211651.48+044123.7.

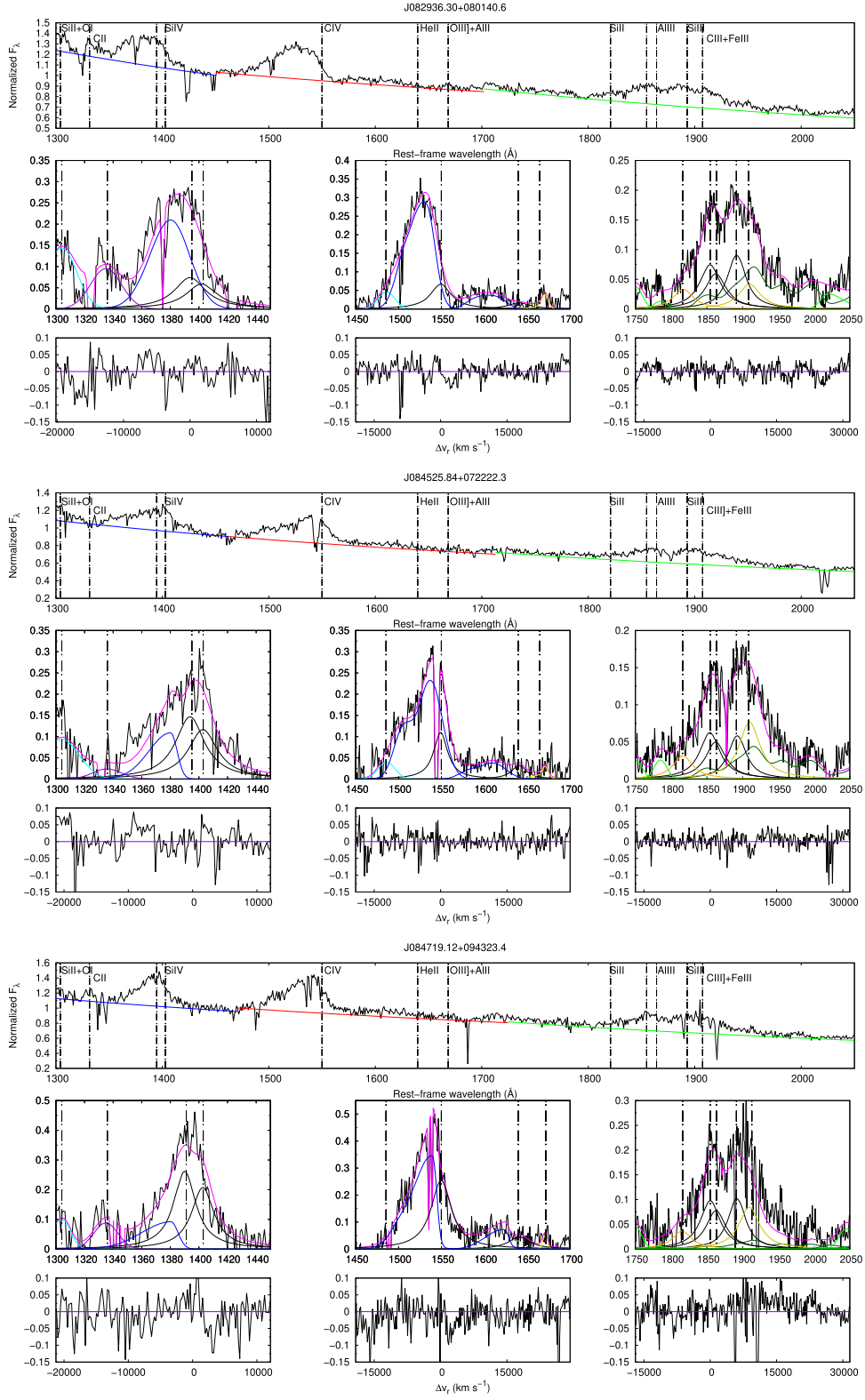

Figure 16. (Continued.)

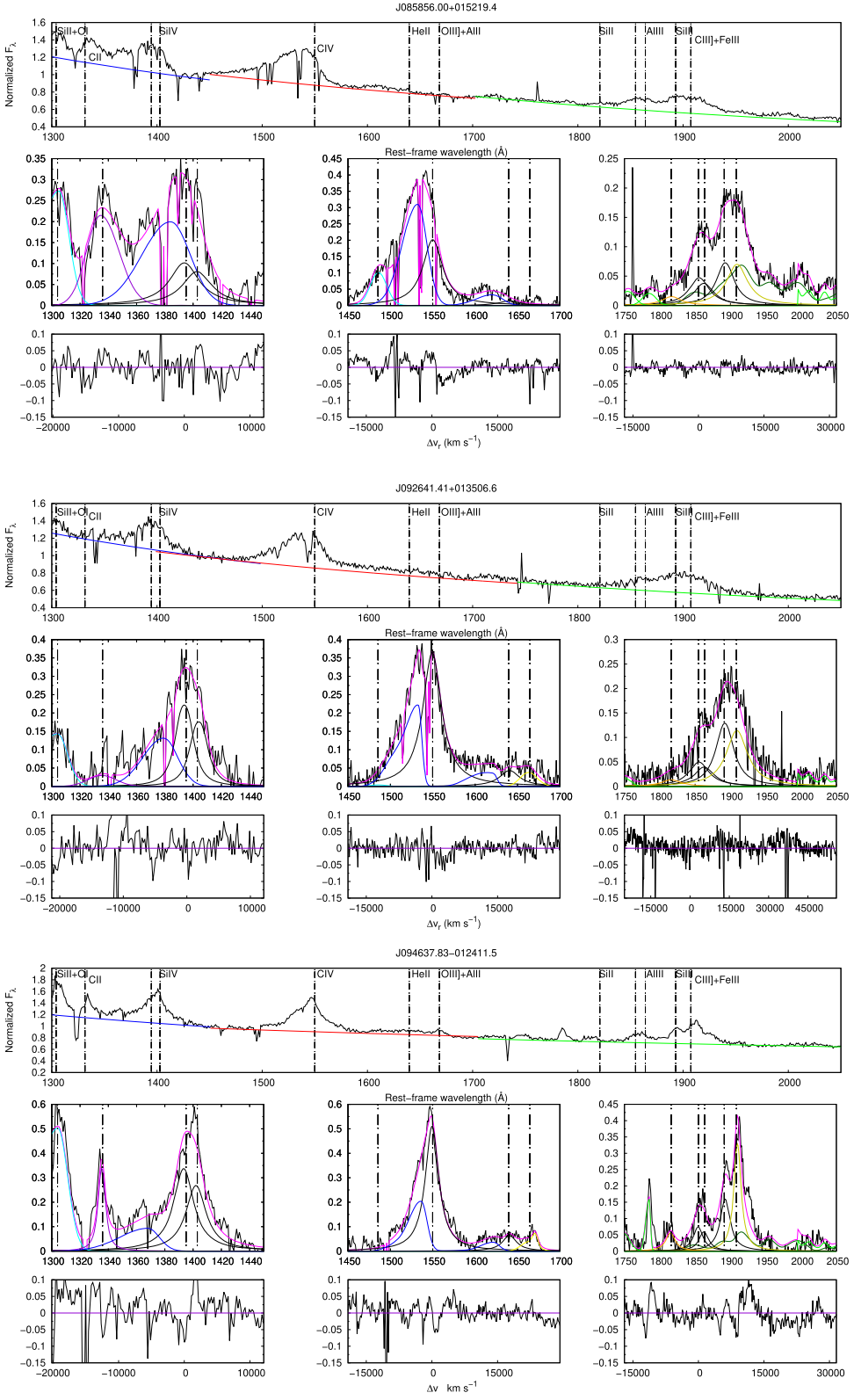

Figure 16. (Continued.)

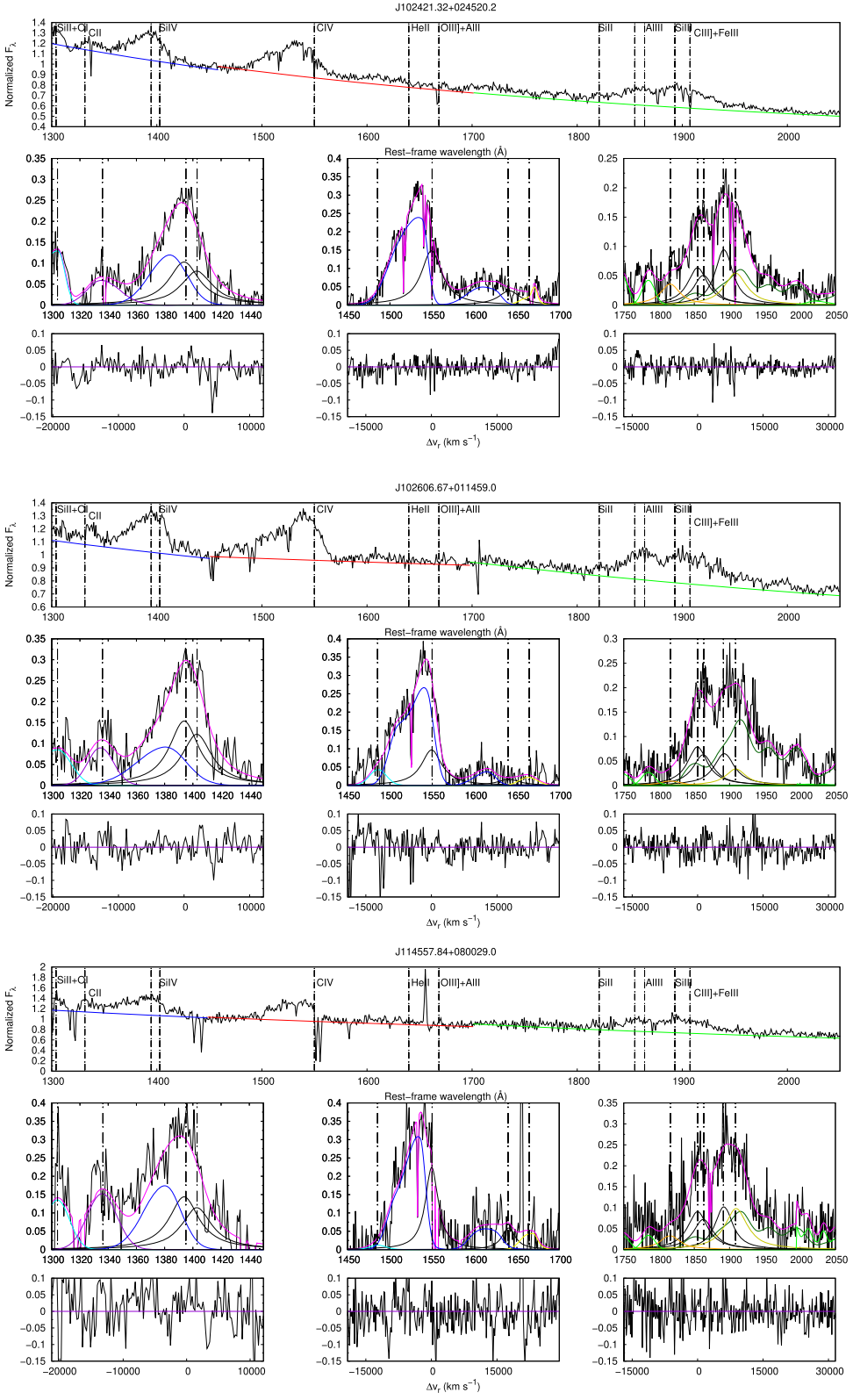

Figure 16. (Continued.)

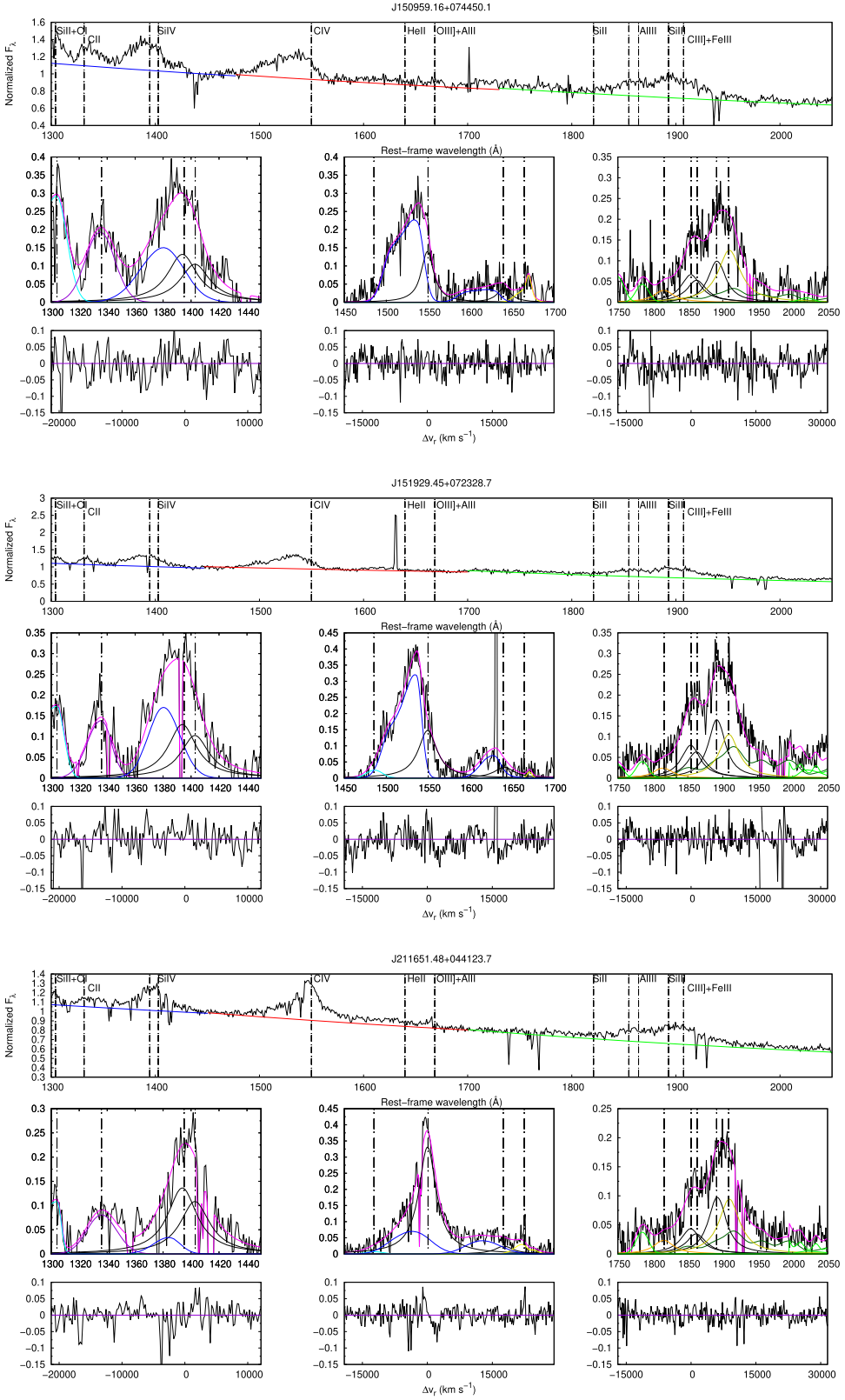

Figure 16. (Continued.)

Appendix B
Diagnostic Intensity Ratios in the Plane (U, $n_{\rm H}$) as a Function of Metallicity

The results of the arrays of simulations as a function of $n_{\rm H}$, U, and Z are shown in Figures 17 and 18, for $N_{\rm c} = 10^{23}$. The SED shape is the same for all simulations (table_agn), which corresponds to the SED of Mathews & Ferland (1987). No turbulence was assumed.

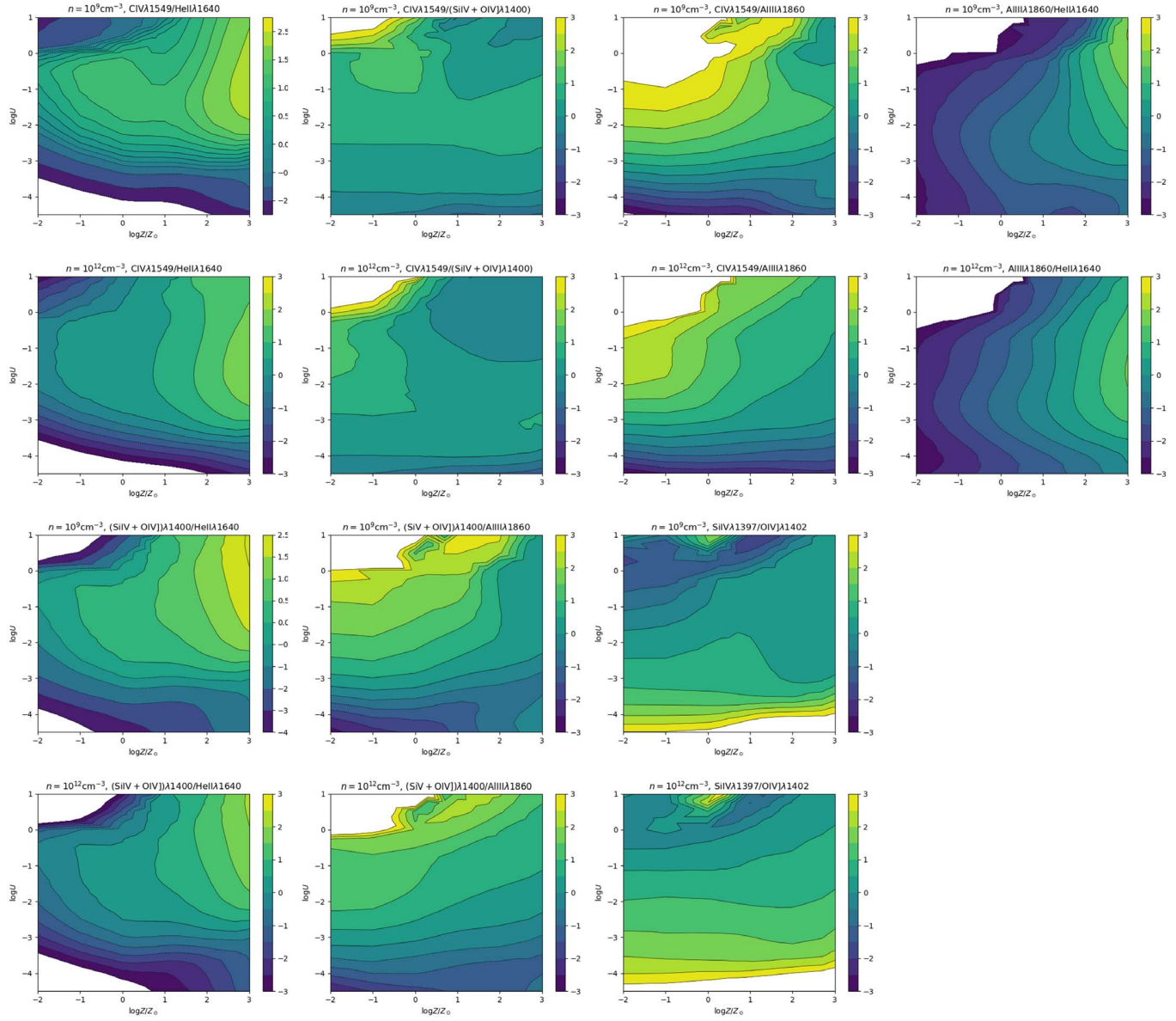

Figure 17. Isophotal contour in the $\log U$–$\log Z$ plane of seven diagnostic line intensity ratios, computed assuming column density $N_{\rm c} = 10^{23}$ cm^{-2}. Top rows, from left to right: logarithm of C IV/He II, C IV/(Si IV + O IV]), C IV/Al III, Al III/He II λ1640. Bottom rows, from left to right: logarithm of (Si IV + O IV])/He II, (Si IV + O IV])/Al III, Si IV/O IV]. The contour plots are shown for $n_{\rm H} = 10^9$ cm^{-3} (top) and $n_{\rm H} = 10^{12}$ cm^{-3} (bottom) for each diagnostic ratio.

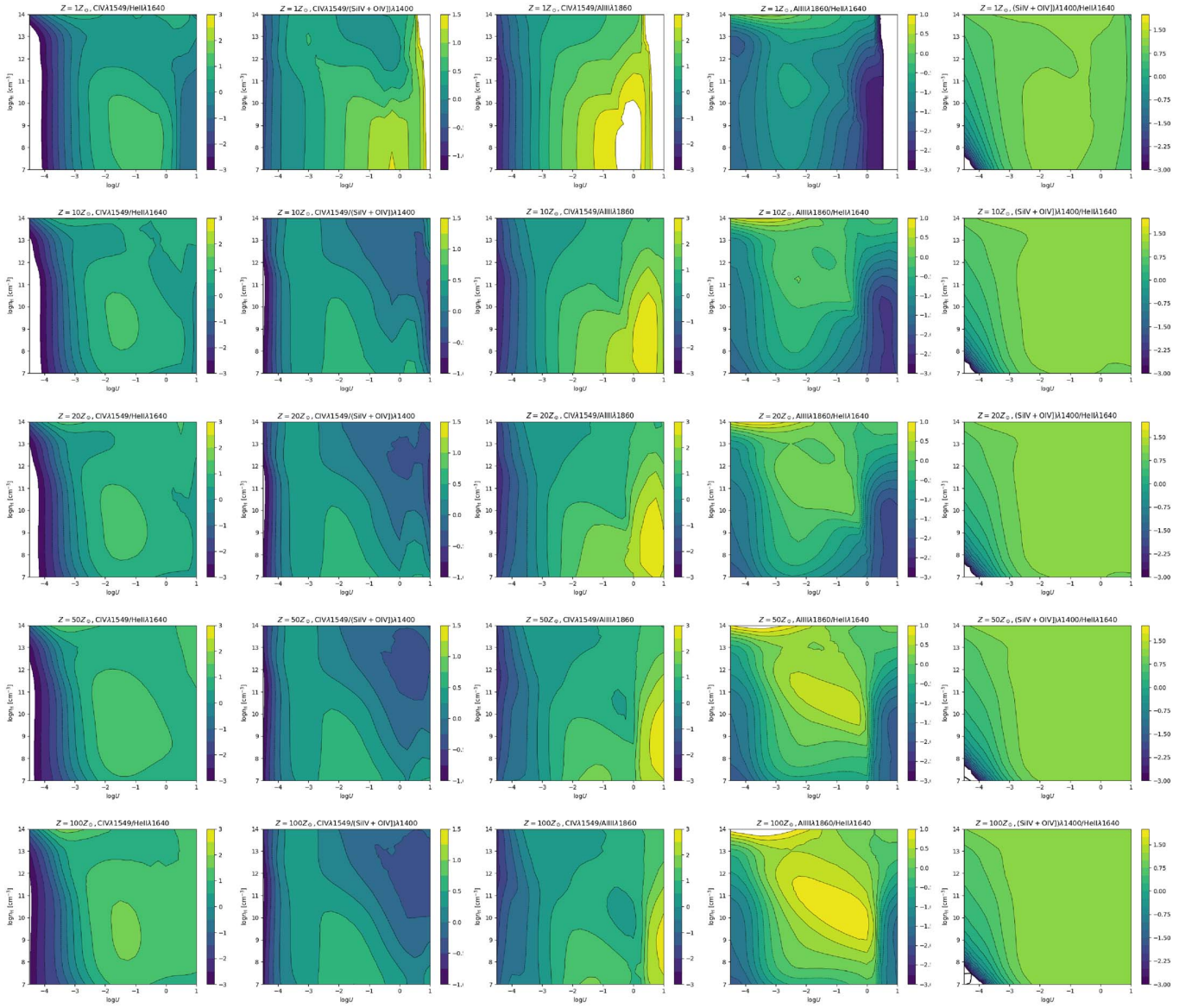

Figure 18. Isophotal contour in the $\log U$–$\log\ n_{\rm H}$ for line intensity ratios (from left to right) C IV/He II, C IV/(Si IV + O IV]), C IV/Al III, Al III/He II λ1640, (Si IV + O IV])/He II λ1640) as a function of metallicity (from top to bottom: $Z = 1$, 10, 20, 50, 100 $Z_{\odot}$), for column density $N_{\rm c} = 10^{23}$ cm^{-2}.

ORCID iDs

Marzena Śniegowska https://orcid.org/0000-0003-2656-6726
Paola Marziani https://orcid.org/0000-0002-6058-4912
Bożena Czerny https://orcid.org/0000-0001-5848-4333
Swayamtrupta Panda https://orcid.org/0000-0002-5854-7426
Mary Loli Martínez-Aldama https://orcid.org/0000-0002-7843-7689
Ascensión del Olmo https://orcid.org/0000-0003-2055-9816
Mauro D'Onofrio https://orcid.org/0000-0001-6441-9044

References

Abramowicz, M. A., Czerny, B., Lasota, J. P., & Szuszkiewicz, E. 1988, ApJ, 332, 646
Adelman-McCarthy, J. K., Agüeros, M. A., Allam, S. S., et al. 2008, ApJS, 175, 297
Adhikari, T. P., Różańska, A., Czerny, B., Hryniewicz, K., & Ferland, G. J. 2016, ApJ, 831, 68
Anders, E., & Grevesse, N. 1989, Geochim. Cosmochim. Acta, 53, 197
Baldwin, J. A., Hamann, F., Korista, K. T., et al. 2003, ApJ, 583, 649
Bañados, E., Venemans, B. P., Decarli, R., et al. 2016, ApJS, 227, 11
Baskin, A., & Laor, A. 2012, MNRAS, 426, 1144
Becker, R. H., White, R. L., & Helfand, D. J. 1995, ApJ, 450, 559
Bevington, P. R., & Robinson, D. K. 2003, Data Reduction and Error Analysis for the Physical Sciences (Boston, MA: McGraw-Hill)
Bisogni, S., di Serego Alighieri, S., Goldoni, P., et al. 2017, A&A, 603, A1
Boroson, T. A., & Green, R. F. 1992, ApJS, 80, 109
Brotherton, M. S., Wills, B. J., Francis, P. J., & Steidel, C. C. 1994, ApJ, 430, 495
Brühweiler, F., & Verner, E. 2008, ApJ, 675, 83
Cantiello, M., Jermyn, A. S., & Lin, D. N. C. 2020, arXiv:2009.03936
Chieffi, A., & Limongi, M. 2013, ApJ, 764, 21
Coatman, L., Hewett, P. C., Banerji, M., & Richards, G. T. 2016, MNRAS, 461, 647
Collin, S., & Zahn, J.-P. 1999a, A&A, 344, 433
Collin, S., & Zahn, J.-P. 1999b, Ap&SS, 265, 501
Collin-Souffrin, S., Dyson, J. E., McDowell, J. C., & Perry, J. J. 1988, MNRAS, 232, 539
Collin-Souffrin, S., & Lasota, J.-P. 1988, PASP, 100, 1041
Corbin, M. R., & Boroson, T. A. 1996, ApJS, 107, 69

D' Agostini, G. 2003, Bayesian Reasoning in Data Analysis—A Critical Introduction (Singapore: World Scientific)
Davidson, K., & Netzer, H. 1979, RvMP, 51, 715
Diamond-Stanic, A. M., Fan, X., Brandt, W. N., et al. 2009, ApJ, 699, 782
Dietrich, M., Hamann, F., Shields, J. C., et al. 2003, ApJ, 589, 722
D'Onofrio, M., & Marziani, P. 2018, FrASS, 5, 31
Du, P., Lu, K.-X., Hu, C., et al. 2016a, ApJ, 820, 27
Du, P., Wang, J.-M., Hu, C., et al. 2014, MNRAS, 438, 2828
Du, P., Wang, J.-M., Hu, C., et al. 2016b, ApJL, 818, L14
Elvis, M. 2000, ApJ, 545, 63
Feibelman, W. A., & Aller, L. H. 1987, ApJ, 319, 407
Ferland, G. J., Chatzikos, M., Guzmán, F., et al. 2017, RMxAA, 53, 385
Ferland, G. J., Done, C., Jin, C., Landt, H., & Ward, M. J. 2020, MNRAS, 494, 5917
Ferland, G. J., Hu, C., Wang, J., et al. 2009, ApJL, 707, L82
Ferland, G. J., Porter, R. L., van Hoof, P. A. M., et al. 2013, RMxAA, 49, 137
Gaskell, C. M. 2000, NewAR, 44, 563
Graham, M. J., Clowes, R. G., & Campusano, L. E. 1996, MNRAS, 279, 1349
Grevesse, N., & Sauval, A. J. 1998, SSRv, 85, 161
Hamann, F., & Ferland, G. 1992, ApJL, 391, L53
Hamann, F., & Ferland, G. 1999, ARA&A, 37, 487
Hamann, F., Korista, K. T., Ferland, G. J., Warner, C., & Baldwin, J. 2002, ApJ, 564, 592
Hartig, G. F., & Baldwin, J. A. 1986, ApJ, 302, 64
Izotov, Y. I., & Thuan, T. X. 1999, ApJ, 511, 639
Juarez, Y., Maiolino, R., Mujica, R., et al. 2009, A&A, 494, L25
Kaspi, S., Brandt, W. N., Maoz, D., et al. 2007, ApJ, 659, 997
Keenan, F. P., Ahmed, S., Brage, T., et al. 2002, MNRAS, 337, 901
Kovačević-Dojčinović, J., & Popović, L. Č. 2015, ApJS, 221, 35
Kriss, G. 1994, in ASP Conf. Ser. 61, Astronomical Data Analysis Software and Systems III, ed. D. R. Crabtree, R. J. Hanisch, & J. Barnes (San Francisco, CA: ASP), 437
Kuraszkiewicz, J., Wilkes, B. J., Schmidt, G., et al. 2009, ApJ, 692, 1180
Leighly, K. M., & Moore, J. R. 2004, ApJ, 611, 107
Lipari, S., Terlevich, R., & Macchetto, F. 1993, ApJ, 406, 451
Maiolino, R., & Mannucci, F. 2019, A&ARv, 27, 3
Martínez-Aldama, M. L., Del Olmo, A., Marziani, P., et al. 2017, FrASS, 4, 29
Martínez-Aldama, M. L., del Olmo, A., Marziani, P., et al. 2018a, A&A, 618, A179
Martínez-Aldama, M. L., Del Olmo, A., Marziani, P., et al. 2018b, FrASS, 4, 65
Marziani, P., del Olmo, A., Perea, J., D'Onofrio, M., & Panda, S. 2020, Atoms, 8, 94
Marziani, P., Dultzin, D., Sulentic, J. W., et al. 2018, FrASS, 5, 6
Marziani, P., Martínez Carballo, M. A., Sulentic, J. W., et al. 2016a, Ap&SS, 361, 29
Marziani, P., & Sulentic, J. W. 2014, MNRAS, 442, 1211
Marziani, P., Sulentic, J. W., Dultzin-Hacyan, D., Calvani, M., & Moles, M. 1996, ApJS, 104, 37
Marziani, P., Sulentic, J. W., Negrete, C. A., et al. 2010, MNRAS, 409, 1033
Marziani, P., Sulentic, J. W., Stirpe, G. M., et al. 2016b, Ap&SS, 361, 3
Marziani, P., Sulentic, J. W., Stirpe, G. M., Zamfir, S., & Calvani, M. 2009, A&A, 495, 83
Mathews, W. G., & Ferland, G. J. 1987, ApJ, 323, 456
Mathur, S. 2000, MNRAS, 314, L17
Matsuoka, K., Nagao, T., Marconi, A., Maiolino, R., & Taniguchi, Y. 2011, A&A, 527, A100
Matsuoka, Y., Oyabu, S., Tsuzuki, Y., & Kawara, K. 2007, ApJ, 663, 781
Matthews, J. H. 2016, PhD thesis, Univ. Southampton
Mejía-Restrepo, J. E., Trakhtenbrot, B., Lira, P., Netzer, H., & Capellupo, D. M. 2016, MNRAS, 460, 187
Murray, N., & Chiang, J. 1997, ApJ, 474, 91
Murray, N., Chiang, J., Grossman, S. A., & Voit, G. M. 1995, ApJ, 451, 498
Nagao, T., Maiolino, R., & Marconi, A. 2006a, A&A, 447, 863
Nagao, T., Marconi, A., & Maiolino, R. 2006b, A&A, 447, 157
Nardini, E., Lusso, E., Risaliti, G., et al. 2019, A&A, 632, A109
Negrete, A., Dultzin, D., Marziani, P., & Sulentic, J. 2012, ApJ, 757, 62
Negrete, C. A., Dultzin, D., Marziani, P., et al. 2018, A&A, 620, A118
Negrete, C. A., Dultzin, D., Marziani, P., & Sulentic, J. 2010, arXiv:1011.4248
Negrete, C. A., Dultzin, D., Marziani, P., & Sulentic, J. W. 2014, ApJ, 794, 95
Netzer, H., & Marziani, P. 2010, ApJ, 724, 318
Onoue, M., Bañados, E., Mazzucchelli, C., et al. 2020, ApJ, 898, 105
Osmer, P. S., & Smith, M. G. 1976, ApJ, 210, 267
Osterbrock, D. E., & Ferland, G. J. 2006, Astrophysics of Gaseous Nebulae and Active Galactic Nuclei (Mill Valley, CA: Univ. Science Books)
Osterbrock, D. E., & Pogge, R. W. 1985, ApJ, 297, 166
Panda, S. 2020, arXiv:2004.13113
Panda, S., Czerny, B., Adhikari, T. P., et al. 2018, ApJ, 866, 115
Panda, S., Martínez-Aldama, M. L., Marinello, M., et al. 2020a, ApJ, 902, 76
Panda, S., Marziani, P., & Czerny, B. 2019, ApJ, 882, 79
Panda, S., Marziani, P., & Czerny, B. 2020b, CoSka, 50, 293
Pâris, I., Petitjean, P., Ross, N. P., et al. 2017, A&A, 597, A79
Peimbert, A., Peimbert, M., & Luridiana, V. 2001, RMxAC, 10, 148
Peimbert, M. 2008, arXiv:0811.2980
Peterson, B. M., & Wandel, A. 1999, ApJL, 521, L95
Plotkin, R. M., Shemmer, O., Trakhtenbrot, B., et al. 2015, ApJ, 805, 123
Popović, L. Č., Mediavilla, E. G., Kubičela, A., & Jovanović, P. 2002, A&A, 390, 473
Proga, D. 2007a, ApJ, 661, 693
Proga, D. 2007b, in ASP Conf. Ser. 373, The Central Engine of Active Galactic Nuclei, ed. L. C. Ho & J.-W. Wang (San Francisco, CA: ASP), 267
Punsly, B., Marziani, P., Bennert, V. N., Nagai, H., & Gurwell, M. A. 2018, ApJ, 869, 143
Richards, G. T., Kruczek, N. E., Gallagher, S. C., et al. 2011, AJ, 141, 167
Richards, G. T., Lacy, M., Storrie-Lombardi, L. J., et al. 2006, ApJS, 166, 470
Risaliti, G., & Elvis, M. 2010, A&A, 516, A89
Risaliti, G., Salvati, M., & Marconi, A. 2011, MNRAS, 411, 2223
Sądowski, A., Narayan, R., McKinney, J. C., & Tchekhovskoy, A. 2014, MNRAS, 439, 503
Schneider, D. P., Richards, G. T., Hall, P. B., et al. 2010, AJ, 139, 2360
Shemmer, O., & Netzer, H. 2002, ApJL, 567, L19
Shemmer, O., Netzer, H., Maiolino, R., et al. 2004, ApJ, 614, 547
Shen, Y. 2016, ApJ, 817, 55
Shen, Y., & Ho, L. C. 2014, Natur, 513, 210
Shen, Y., Richards, G. T., Strauss, M. A., et al. 2011, ApJS, 194, 45
Shields, G. A. 1976, ApJ, 204, 330
Shin, J., Nagao, T., & Woo, J.-H. 2017, ApJ, 835, 24
Shin, J., Woo, J.-H., Nagao, T., & Kim, S. C. 2013, ApJ, 763, 58
Sulentic, J. W., Bachev, R., Marziani, P., Negrete, C. A., & Dultzin, D. 2007, ApJ, 666, 757
Sulentic, J. W., del Olmo, A., Marziani, P., et al. 2017, A&A, 608, A122
Sulentic, J. W., Marziani, P., del Olmo, A., et al. 2014, A&A, 570, A96
Sulentic, J. W., Marziani, P., & Dultzin-Hacyan, D. 2000a, ARA&A, 38, 521
Sulentic, J. W., Marziani, P., Dultzin-Hacyan, D., Calvani, M., & Moles, M. 1995, ApJL, 445, L85
Sulentic, J. W., Marziani, P., Zamanov, R., et al. 2002, ApJL, 566, L71
Sulentic, J. W., Repetto, P., Stirpe, G. M., et al. 2006, A&A, 456, 929
Sulentic, J. W., Zwitter, T., Marziani, P., & Dultzin-Hacyan, D. 2000b, ApJL, 536, L5
Szuszkiewicz, E., Malkan, M. A., & Abramowicz, M. A. 1996, ApJ, 458, 474
Temple, M. J., Ferland, G. J., Rankine, A. L., et al. 2020, MNRAS, 496, 2565
Vanden Berk, D. E., Richards, G. T., Bauer, A., et al. 2001, AJ, 122, 549
Verner, E. M., Verner, D. A., Korista, K. T., et al. 1999, ApJS, 120, 101
Véron-Cetty, M.-P., Véron, P., & Gonçalves, A. C. 2001, A&A, 372, 730
Vestergaard, M., & Peterson, B. M. 2006, ApJ, 641, 689
Vestergaard, M., & Wilkes, B. J. 2001, ApJS, 134, 1
Vietri, G., Piconcelli, E., Bischetti, M., et al. 2018, A&A, 617, A81
Vila-Costas, M. B., & Edmunds, M. G. 1993, MNRAS, 265, 199
Wang, H., Zhou, H., Yuan, W., & Wang, T. 2012a, ApJL, 751, L23
Wang, J.-M., Du, P., Baldwin, J. A., et al. 2012b, ApJ, 746, 137
Wang, J.-M., Du, P., Li, Y.-R., et al. 2014, ApJL, 792, L13
Wang, J.-M., Du, P., Valls-Gabaud, D., Hu, C., & Netzer, H. 2013, PhRvL, 110, 081301
Wang, J.-M., Ge, J.-Q., Hu, C., et al. 2011, ApJ, 739, 3
Warner, C., Hamann, F., & Dietrich, M. 2004, ApJ, 608, 136
Welch, B. L. 1947, Biometrika, 34, 28
Wildy, C., Czerny, B., & Panda, S. 2019, A&A, 632, A41
Wills, D., & Netzer, H. 1979, ApJ, 233, 1
Xu, D., Komossa, S., Zhou, H., et al. 2012, AJ, 143, 83
Xu, X., Zakamska, N. L., Arav, N., Miller, T., & Benn, C. 2020, MNRAS, 495, 305
Zamanov, R., Marziani, P., Sulentic, J. W., et al. 2002, ApJL, 576, L9
Zheng, W. 1988, ApL&C, 27, 275
Zhou, H., Wang, T., Yuan, W., et al. 2006, ApJS, 166, 128

Part IV

Summary and forthcoming work

Chapter 5

Summary and forthcoming work

5.1 Summary

The aim of the collection of works in this thesis was the investigation of the variability of AGN in different timescales. Recently discovered AGN variability patterns in the form of QPE and CL phenomena are inconsistent with the expectations of the standard accretion disk. Observed variations are too fast in comparison with the disk viscous timescales. I focused on the theoretical model of the radiation pressure instability operating in the accretion disk to check if such a model, with some modifications, can account for the fast variations. In Paper I, I proposed that sources radiating at a relatively low Eddington ratio have an instability zone that is not large. I also postulated that an inner disk is replaced with the ADAF flow. In such a picture, the instability zone is reduced to a radially very narrow zone, and a simple toy model indicated that in such a case, the narrow radial range reduces the outburst timescales from hundreds of years to years, thus opening a possibility to model CL AGN. However, in Paper II, the disk instability was modeled using a much more advanced 1-D numerical model, which properly accounted for the radial propagation of the developing instability. The timescales were not as short as in Paper I, so we introduced an important modification of the model. We allowed for the modification of the disk vertical structure by the large-scale magnetic field, which, if strong, actually could even stabilize the disk. Even more importantly, we introduced a small outer disk radius of 100 R_{schw} corresponding to an assumption that the disk formed in the TDE event. These two modifications shortened the outbursts again compared to the expectations of the standard radiation pressure instability models (of the order of $10^4 - 10^5$ yr). New timescales again were appropriate for CL AGN.

Since the radiation pressure instability, if not taking place in TDE powered source, usually operates at longer timescales, causing the subsequent rise and fall of the luminosity, we would not expect that hosts of high Eddington ratio sources are in any way different from low Eddington hosts. However, the observations of the Fe II content by many authors hinted at clearly different metal content in the BLR in the two classes. Thus in Paper III, I performed metallicity measurements in a sample of very high Eddington sources with good UV data where there are numerous emission lines that offer much better plasma diagnostics than Fe II. We confirmed that highly supersolar metal content is characteristic for the high Eddington ratio sources. The excess of aluminium over carbon suggests the supernova enrichment.

This last result may question the presence of the radiation pressure instability in AGN since the

low and high states expected from such a mechanism should not differ in metal content. The starburst phenomenon should last longer than $10^4 - 10^5$ yr, expected from radiation pressure instability. On the other hand, observations of the host ionization extension suggest that, indeed, a single activity episode lasts $\sim 10^5$ yr, and a quasar evolution consists of a thousand of such episodes. We can reconcile repeated on/off state and systematically higher metal content in high states either with different outer boundary conditions in a fraction of sources (systematically higher mean accretion rate and lower large scale magnetic field), which allows them to reach temporarily very high Eddington rates. In contrast, other sources, even at the peak of luminosity, are not as bright, and the starburst processes in the outer disk proceed less vigorously. This is a fascinating topic for future studies.

5.2 Forthcoming work

5.2.1 Effect of the inner ADAF, coronal flows, the magnetic field and the outer disk radius on timescales in radiation pressure dominated accretion disks

In Paper II, we presented only a few models calculated for the black hole mass $10^7 M_\odot$. In the subsequent paper (Śniegowska et al., 2022b), we introduced a new effect - the effect of the large-scale magnetic field on the disk vertical structure - and we performed computations of a large grid of models, exploring the role of the parameters in much more detail. We explored the case of a microquasar ($10 M_\odot$as a reference, and also the case $10^5 M_\odot$ as appropriate for QPE sources like GSN 069. I show that the role of the inner ADAF is not as important as I expected based on the Paper I toy model, but the role of the magnetic field is important, although its effect on the timescale is not simple. I expected a monotonic shortening of the period, but this was seen only for a microquasar. In contrast, for larger masses, the shortening of the period with the rise of the magnetic field is only seen when the magnetic field is strong, approaching the stage when the disk becomes fully stabilized. I confirm the critical role of the disk outer radius, so only small disks can oscillate in timescales appropriate for CL AGN or QPE.

Our computations confirm that the radiation pressure instability model can account for heartbeat states in microquasars. Rapid variability detected in IMBH in the form of Quasi-Periodic Ejection can be consistent with the model but only if combined with TDE phenomenon. Yearly repeating variability in Changing Look AGN also requires, in our model, a small outer radius either due to the recent TDE or due to the presence of the gap in the disk related to the presence of a secondary black hole.

5.2.2 Spectropolarimetry and spectral decomposition of high-accreting Narrow Line Seyfert 1

In Śniegowska et al. (2022c), I kept exploring the strongly accreting Active Galactic Nuclei using a different method. Strongly accreting sources are known as problematic in terms of their mass determination. Using the virial relation (dependent on the distribution of the broad line region and the viewing angle to the source), we obtain relatively small black hole masses, possibly to small due to a small viewing angle.

The spectropolarimetry technique helps in probing the geometry of this line-emitting gas and allows us to estimate the viewing angle of the source. The viewing angle is estimated by comparing the spectrum viewed under natural light and in polarized light. We focused on three NLSy1 - Mrk

1044, SDSS J080101.41+184840.7, and IRAS 04416+1215 and used spectropolarimetric data from the European Southern Observatory's Very Large Telescope. In this project, we aimed to take into account the correction for the angle of view of objects when calculating the mass of objects and model the geometry of these objects. We recovered relatively low polarization fractions of 0.2-0.5% for the three sources. We estimate the viewing angles for the three sources from an almost face-on (IRAS 04416+1215), an intermediate (SDSS J080101.41+184840.7), to a highly inclined (Mrk 1044) orientation. We confirmed the high accreting nature for all three sources.

We also modelled the Stokes parameters of those sources and inferred the properties of the scattering media - located in the equatorial and polar regions, and simulated the spectra observed both in natural light and in polarized light using the polarization radiative transfer code STOKES (Goosmann & Gaskell, 2007; Marin & Goosmann, 2014).

Bibliography

Abdurro'uf, Accetta, K., Aerts, C., Silva Aguirre, V., Ahumada, R., Ajgaonkar, N., Filiz Ak, N., Alam, S., Allende Prieto, C., Almeida, A., Anders, F., Anderson, S. F., Andrews, B. H., Anguiano, B., Aquino-Ortíz, E., Aragón-Salamanca, A., Argudo-Fernández, M., Ata, M., Aubert, M., ... Zhu, K. (2022). The Seventeenth Data Release of the Sloan Digital Sky Surveys: Complete Release of MaNGA, MaStar, and APOGEE-2 Data. ApJS, *259*(2), Article 35, 35. https://doi.org/10.3847/1538-4365/ac4414

Abramowicz, M. A., Czerny, B., Lasota, J. P., & Szuszkiewicz, E. (1988). Slim accretion disks. ApJ, *332*, 646–658. https://doi.org/10.1086/166683

Aird, J., Coil, A. L., Georgakakis, A., Nandra, K., Barro, G., & Pérez-González, P. G. (2015). The evolution of the X-ray luminosity functions of unabsorbed and absorbed AGNs out to z∼ 5. MNRAS, *451*(2), 1892–1927. https://doi.org/10.1093/mnras/stv1062

Akiyama, K., Alberdi, A., Alef, W., Algaba, J. C., Anantua, R., Asada, K., Azulay, R., Bach, U., Baczko, A.-K., Ball, D., Baloković, M., Barrett, J., Bauböck, M., Benson, B. A., Bintley, D., Blackburn, L., Blundell, R., Bouman, K. L., Bower, G. C., ... Zeballos, M. (2022). First Sagittarius A* Event Horizon Telescope Results. I. The Shadow of the Supermassive Black Hole in the Center of the Milky Way. ApJ, *930*(2), Article L12, L12. https://doi.org/10.3847/2041-8213/ac6674

Alloin, D., Pelat, D., Phillips, M. M., Fosbury, R. A. E., & Freeman, K. (1986). Recurrent outbursts in the broad-line region of NGC 1566. ApJ, *308*, 23–35. https://doi.org/10.1086/164475

Antonucci, R. R. J., & Miller, J. S. (1985). Spectropolarimetry and the nature of NGC 1068. ApJ, *297*, 621–632. https://doi.org/10.1086/163559

Antonucci, R. (1993). Unified models for active galactic nuclei and quasars. ARA&A, *31*, 473–521. https://doi.org/10.1146/annurev.aa.31.090193.002353

Arcodia, R., Merloni, A., Nandra, K., Buchner, J., Salvato, M., Pasham, D., Remillard, R., Comparat, J., Lamer, G., Ponti, G., Malyali, A., Wolf, J., Arzoumanian, Z., Bogensberger, D., Buckley, D. A. H., Gendreau, K., Gromadzki, M., Kara, E., Krumpe, M., ... Schwope, A. (2021). X-ray quasi-periodic eruptions from two previously quiescent galaxies. Nature, *592*(7856), 704–707. https://doi.org/10.1038/s41586-021-03394-6

Bañados, E., Venemans, B. P., Mazzucchelli, C., Farina, E. P., Walter, F., Wang, F., Decarli, R., Stern, D., Fan, X., Davies, F. B., Hennawi, J. F., Simcoe, R. A., Turner, M. L., Rix, H.-W., Yang, J., Kelson, D. D., Rudie, G. C., & Winters, J. M. (2018). An 800-million-solar-mass black hole in a significantly neutral Universe at a redshift of 7.5. Nature, *553*(7689), 473–476. https://doi.org/10.1038/nature25180

Balbus, S. A., & Hawley, J. F. (1991). A Powerful Local Shear Instability in Weakly Magnetized Disks. I. Linear Analysis. ApJ, *376*, 214. https://doi.org/10.1086/170270

Barai, P. (2020). Investigating central massive black hole feedback in galaxies using cosmological hydrodynamical simulations. *Boletin de la Asociacion Argentina de Astronomia La Plata Argentina*, *61C*, 16–18.

Bartos, I., Kocsis, B., Haiman, Z., & Márka, S. (2017). Rapid and Bright Stellar-mass Binary Black Hole Mergers in Active Galactic Nuclei. ApJ, *835*(2), Article 165, 165. https://doi.org/10.3847/1538-4357/835/2/165

Beckmann, V., & Shrader, C. The AGN phenomenon: open issues. *Proceedings of "an integral view of the high-energy sky (the first 10 years)" - 9th integral workshop and celebration of the 10th anniversary of the launch (integral 2012). 15-19 october 2012. bibliotheque nationale de france.* 2012, January, 69, 69. arXiv: 1302.1397 [astro-ph.HE].

Bellm, E. C., Kulkarni, S. R., Graham, M. J., Dekany, R., Smith, R. M., Riddle, R., Masci, F. J., Helou, G., Prince, T. A., Adams, S. M., Barbarino, C., Barlow, T., Bauer, J., Beck, R., Belicki, J., Biswas, R., Blagorodnova, N., Bodewits, D., Bolin, B., ... Zolkower, J. (2019). The Zwicky Transient Facility: System Overview, Performance, and First Results. PASP, *131*(995), 018002. https://doi.org/10.1088/1538-3873/aaecbe

Bentz, M. C., Denney, K. D., Grier, C. J., Barth, A. J., Peterson, B. M., Vestergaard, M., Bennert, V. N., Canalizo, G., De Rosa, G., Filippenko, A. V., Gates, E. L., Greene, J. E., Li, W., Malkan, M. A., Pogge, R. W., Stern, D., Treu, T., & Woo, J.-H. (2013). The Low-luminosity End of the Radius-Luminosity Relationship for Active Galactic Nuclei. ApJ, *767*(2), Article 149, 149. https://doi.org/10.1088/0004-637X/767/2/149

Bentz, M. C., Peterson, B. M., Pogge, R. W., & Vestergaard, M. (2009). The Black Hole Mass-Bulge Luminosity Relationship for Active Galactic Nuclei From Reverberation Mapping and Hubble Space Telescope Imaging. ApJ, *694*(2), L166–L170. https://doi.org/10.1088/0004-637X/694/2/L166

Bianchi, S., Guainazzi, M., Matt, G., Chiaberge, M., Iwasawa, K., Fiore, F., & Maiolino, R. (2005). A search for changing-look AGN in the Grossan catalog. A&A, *442*(1), 185–194. https://doi.org/10.1051/0004-6361:20053389

Bianchi, S., Maiolino, R., & Risaliti, G. (2012). AGN Obscuration and the Unified Model. *Advances in Astronomy*, *2012*, Article 782030, 782030. https://doi.org/10.1155/2012/782030

Boroson, T. A., & Green, R. F. (1992). The emission-line properties of low-redshift quasi-stellar objects. *ApJS*, *80*, 109–135. https://doi.org/10.1086/191661

Bouwens, R. J., Illingworth, G. D., Oesch, P. A., Labbé, I., Trenti, M., van Dokkum, P., Franx, M., Stiavelli, M., Carollo, C. M., Magee, D., & Gonzalez, V. (2011). Ultraviolet Luminosity Functions from 132 z ˜7 and z ˜8 Lyman-break Galaxies in the Ultra-deep HUDF09 and Wide-area Early Release Science WFC3/IR Observations. ApJ, *737*(2), Article 90, 90. https://doi.org/10.1088/0004-637X/737/2/90

Bouwens, R. J., Illingworth, G. D., Oesch, P. A., Trenti, M., Labbé, I., Bradley, L., Carollo, M., van Dokkum, P. G., Gonzalez, V., Holwerda, B., Franx, M., Spitler, L., Smit, R., & Magee, D. (2015). UV Luminosity Functions at Redshifts z $\sim$ 4 to z $\sim$ 10: 10,000 Galaxies from HST Legacy Fields. ApJ, *803*(1), Article 34, 34. https://doi.org/10.1088/0004-637X/803/1/34

Brandt, W. N., Mathur, S., & Elvis, M. (1997). A comparison of the hard ASCA spectral slopes of broad- and narrow-line Seyfert 1 galaxies. MNRAS, *285*(3), L25–L30. https://doi.org/10.1093/mnras/285.3.L25

Brotherton, M. S., Wills, B. J., Steidel, C. C., & Sargent, W. L. W. (1994). Statistics of QSO Broad Emission-Line Profiles. II. The C IV lambda 1549, C iii] lambda 1909, and MG II lambda 2798 Lines. ApJ, *423*, 131. https://doi.org/10.1086/173794

Cantiello, M., Jermyn, A. S., & Lin, D. N. C. (2021). Stellar Evolution in AGN Disks. ApJ, *910*(2), Article 94, 94. https://doi.org/10.3847/1538-4357/abdf4f

Cao, X. (2010). On the Disappearance of the Broad-line Region in Low-luminosity Active Galactic Nuclei: The Role of the Outflows from Advection Dominated Accretion Flows. ApJ, *724*(2), 855–860. https://doi.org/10.1088/0004-637X/724/2/855

Chakraborty, J., Kara, E., Masterson, M., Giustini, M., Miniutti, G., & Saxton, R. (2021). Possible X-Ray Quasi-periodic Eruptions in a Tidal Disruption Event Candidate. ApJ, *921*(2), Article L40, L40. https://doi.org/10.3847/2041-8213/ac313b

Chan, C.-H., Piran, T., Krolik, J. H., & Saban, D. (2019). Tidal Disruption Events in Active Galactic Nuclei. ApJ, *881*(2), Article 113, 113. https://doi.org/10.3847/1538-4357/ab2b40

Charisi, M., Bartos, I., Haiman, Z., Price-Whelan, A. M., Graham, M. J., Bellm, E. C., Laher, R. R., & Márka, S. (2016). A population of short-period variable quasars from PTF as supermassive black hole binary candidates. MNRAS, *463*(2), 2145–2171. https://doi.org/10.1093/mnras/stw1838

Collin, S., & Zahn, J. P. (2008). Star formation in accretion discs: from the Galactic center to active galactic nuclei. A&A, *477*(2), 419–435. https://doi.org/10.1051/0004-6361:20078191

Collin, S., & Zahn, J.-P. (1999). Star formation and evolution in accretion disks around massive black holes. A&A, *344*, 433–449.

Combes, F. Fueling the AGN (I. Aretxaga, D. Kunth, & R. Mújica, Eds.). In *Advanced lectures on the starburst-agn* (I. Aretxaga, D. Kunth, & R. Mújica, Eds.). Ed. by Aretxaga, I., Kunth, D., & Mújica, R. 2001, January, 223. https://doi.org/10.1142/9789812811318_0006. arXiv: astro-ph/0010570 [astro-ph].

Crain, R. A., Schaye, J., Bower, R. G., Furlong, M., Schaller, M., Theuns, T., Dalla Vecchia, C., Frenk, C. S., McCarthy, I. G., Helly, J. C., Jenkins, A., Rosas-Guevara, Y. M., White, S. D. M., & Trayford, J. W. (2015). The EAGLE simulations of galaxy formation: calibration of subgrid physics and model variations. MNRAS, *450*(2), 1937–1961. https://doi.org/10.1093/mnras/stv725

Czerny, B., & Nikolajuk, M. (2010). Mass of black holes: . The state of the art. Mem. Soc. Astron. Italiana, *81*, 281.

Czerny, B., Różańska, A., & Kuraszkiewicz, J. (2004). Constraints for the accretion disk evaporation rate in AGN from the existence of the Broad Line Region. A&A, *428*, 39–49. https://doi.org/10.1051/0004-6361:20040487

Czerny, B., & Elvis, M. (1987). Constraints on Quasar Accretion Disks from the Optical/Ultraviolet/Soft X-Ray Big Bump. ApJ, *321*, 305. https://doi.org/10.1086/165630

Czerny, B., Siemiginowska, A., Janiuk, A., Nikiel-Wroczyński, B., & Stawarz, Ł. (2009). Accretion Disk Model of Short-Timescale Intermittent Activity in Young Radio Sources. ApJ, *698*(1), 840–851. https://doi.org/10.1088/0004-637X/698/1/840

Dexter, J., & Begelman, M. C. (2019). Extreme AGN variability: evidence of magnetically elevated accretion? MNRAS, *483*(1), L17–L21. https://doi.org/10.1093/mnrasl/sly213

Di Gesu, L., Costantini, E., Ebrero, J., Mehdipour, M., Kaastra, J. S., Ursini, F., Petrucci, P. O., Cappi, M., Kriss, G. A., Bianchi, S., Brand uardi-Raymont, G., De Marco, B., De Rosa, A., Kaspi, S., Paltani, S., Pinto, C., Ponti, G., Steenbrugge, K. C., & Whewell, M. (2015). Anatomy of the AGN in NGC 5548. IV. The short-term variability of the outflows. A&A, *579*, Article A42, A42. https://doi.org/10.1051/0004-6361/201525934

Ding, N., Gu, Q., Tang, Y., Ge, X., Guo, X., Xu, X., Chen, Y., Geng, X., & Liu, J. (2021). In-depth investigation of the physical origin of the soft X-ray excess in PG 1448+273. A&A, *650*, Article A183, A183. https://doi.org/10.1051/0004-6361/202140848

Done, C., Davis, S. W., Jin, C., Blaes, O., & Ward, M. (2012). Intrinsic disc emission and the soft X-ray excess in active galactic nuclei. MNRAS, *420*(3), 1848–1860. https://doi.org/10.1111/j.1365-2966.2011.19779.x

Du, P., Wang, J.-M., Hu, C., Valls-Gabaud, D., Baldwin, J. A., Ge, J.-Q., & Xue, S.-J. (2014). Outflows from active galactic nuclei: the BLR-NLR metallicity correlation. MNRAS, *438*(4), 2828–2838. https://doi.org/10.1093/mnras/stt2386

Eckert, D., Gaspari, M., Gastaldello, F., Le Brun, A. M. C., & O'Sullivan, E. (2021). Feedback from Active Galactic Nuclei in Galaxy Groups. *Universe*, *7*(5), 142. https://doi.org/10.3390/universe7050142

Elitzur, M., & Ho, L. C. (2009). On the Disappearance of the Broad-Line Region in Low-Luminosity Active Galactic Nuclei. ApJ, *701*(2), L91–L94. https://doi.org/10.1088/0004-637X/701/2/L91

Event Horizon Telescope Collaboration, Akiyama, K., Alberdi, A., Alef, W., Asada, K., Azulay, R., Baczko, A.-K., Ball, D., Baloković, M., Barrett, J., Bintley, D., Blackburn, L., Boland, W., Bouman, K. L., Bower, G. C., Bremer, M., Brinkerink, C. D., Brissenden, R., Britzen, S., ... Ziurys, L. (2019). First M87 Event Horizon Telescope Results. I. The Shadow of the Supermassive Black Hole. ApJ, *875*(1), Article L1, L1. https://doi.org/10.3847/2041-8213/ab0ec7

Farrell, S. A., Webb, N. A., Barret, D., Godet, O., & Rodrigues, J. M. (2009). An intermediate-mass black hole of over 500 solar masses in the galaxy ESO243-49. Nature, *460*(7251), 73–75. https://doi.org/10.1038/nature08083

Fath, E. A. (1909). The spectra of some spiral nebulae and globular star clusters. *Lick Observatory Bulletin*, *149*, 71–77. https://doi.org/10.5479/ADS/bib/1909LicOB.5.71F

Ferland, G. J., Chatzikos, M., Guzmán, F., Lykins, M. L., van Hoof, P. A. M., Williams, R. J. R., Abel, N. P., Badnell, N. R., Keenan, F. P., Porter, R. L., & Stancil, P. C. (2017). The 2017 Release Cloudy. Rev. Mexicana Astron. Astrofis., *53*, 385–438.

Ferrarese, L., & Merritt, D. (2000). A Fundamental Relation between Supermassive Black Holes and Their Host Galaxies. ApJ, *539*(1), L9–L12. https://doi.org/10.1086/312838

Fiore, F., Feruglio, C., Shankar, F., Bischetti, M., Bongiorno, A., Brusa, M., Carniani, S., Cicone, C., Duras, F., Lamastra, A., Mainieri, V., Marconi, A., Menci, N., Maiolino, R., Piconcelli, E., Vietri, G., & Zappacosta, L. (2017). AGN wind scaling relations and the co-evolution of black holes and galaxies. A&A, *601*, Article A143, A143. https://doi.org/10.1051/0004-6361/201629478

Foord, A., Liu, X., Gültekin, K., Whitley, K., Shi, F., & Chen, Y.-C. (2022). Investigating the Accretion Nature of Binary Supermassive Black Hole Candidate SDSS J025214.67-002813.7. ApJ, *927*(1), Article 3, 3. https://doi.org/10.3847/1538-4357/ac4af1

Frank, J., King, A., & Raine, D. J. (2002). *Accretion Power in Astrophysics: Third Edition.*

Fritz, J., Franceschini, A., & Hatziminaoglou, E. (2006). Revisiting the infrared spectra of active galactic nuclei with a new torus emission model. MNRAS, *366*(3), 767–786. https://doi.org/10.1111/j.1365-2966.2006.09866.x

Gaia Collaboration, Prusti, T., de Bruijne, J. H. J., Brown, A. G. A., Vallenari, A., Babusiaux, C., Bailer-Jones, C. A. L., Bastian, U., Biermann, M., Evans, D. W., Eyer, L., Jansen, F., Jordi, C., Klioner, S. A., Lammers, U., Lindegren, L., Luri, X., Mignard, F., Milligan, D. J., ... Zschocke, S. (2016). The Gaia mission. A&A, *595*, Article A1, A1. https://doi.org/10.1051/0004-6361/201629272

Gardner, J. P., Mather, J. C., Clampin, M., Doyon, R., Greenhouse, M. A., Hammel, H. B., Hutchings, J. B., Jakobsen, P., Lilly, S. J., Long, K. S., Lunine, J. I., McCaughrean, M. J., Mountain, M., Nella, J., Rieke, G. H., Rieke, M. J., Rix, H.-W., Smith, E. P., Sonneborn, G., ... Wright, G. S. (2006). The James Webb Space Telescope. Space Sci. Rev., *123*(4), 485–606. https://doi.org/10.1007/s11214-006-8315-7

Gaskell, M., Thakur, N., Tian, B., & Saravanan, A. (2022). Fe II emission in active galactic nuclei. *Astronomische Nachrichten*, *343*(1-2), Article e210112, e210112. https://doi.org/10.1002/asna.20210112

Giallongo, E., Trevese, D., & Vagnetti, F. (1991). Optical Variability of Quasars: Statistics and Cosmological Properties. ApJ, *377*, 345. https://doi.org/10.1086/170365

Gierliński, M., & Done, C. (2004). Is the soft excess in active galactic nuclei real? MNRAS, *349*(1), L7–L11. https://doi.org/10.1111/j.1365-2966.2004.07687.x

Gierlinski, M., Middleton, M., Ward, M., & Done, C. (2008). A ~1-hour X-ray periodicity in an active galaxy RE J1034+396. *arXiv e-prints*, Article arXiv:0807.1899, arXiv:0807.1899.

Giustini, M., Miniutti, G., & Saxton, R. D. (2020). X-ray quasi-periodic eruptions from the galactic nucleus of RX J1301.9+2747. A&A, *636*, Article L2, L2. https://doi.org/10.1051/0004-6361/202037610

González Delgado, R. M., Heckman, T., Leitherer, C., Meurer, G., Krolik, J., Wilson, A. S., Kinney, A., & Koratkar, A. (1998). Ultraviolet-Optical Observations of the Seyfert 2 Galaxies NGC 7130, NGC 5135, and IC 3639: Implications for the Starburst-Active Galactic Nucleus Connection. ApJ, *505*(1), 174–198. https://doi.org/10.1086/306154

Goosmann, R. W., & Gaskell, C. M. (2007). Modeling optical and UV polarization of AGNs. I. Imprints of individual scattering regions. A&A, *465*(1), 129–145. https://doi.org/10.1051/0004-6361:20053555

Graham, M. J., Ross, N. P., Stern, D., Drake, A. J., McKernan, B., Ford, K. E. S., Djorgovski, S. G., Mahabal, A. A., Glikman, E., Larson, S., & Christensen, E. (2020). Understanding extreme quasar optical variability with CRTS - II. Changing-state quasars. MNRAS, *491*(4), 4925–4948. https://doi.org/10.1093/mnras/stz3244

Green, P. J., Pulgarin-Duque, L., Anderson, S. F., MacLeod, C. L., Eracleous, M., Ruan, J. J., Runnoe, J., Graham, M., Roulston, B. R., Schneider, D. P., Ahlf, A., Bizyaev, D., Brownstein, J. R., Joesephone del Casal, S., Dodd, S. A., Hoover, D., Matt, C., Merloni, A., Pan, K., ... Ridder, M. (2022). The Time Domain Spectroscopic Survey: Changing-Look Quasar Candidates from Multi-Epoch Spectroscopy in SDSS-IV. *arXiv e-prints*, Article arXiv:2201.09123, arXiv:2201.09123.

Gruppioni, C., Calura, F., Pozzi, F., Delvecchio, I., Berta, S., De Lucia, G., Fontanot, F., Franceschini, A., Marchetti, L., Menci, N., Monaco, P., & Vaccari, M. (2015). Star formation in Herschel's Monsters versus semi-analytic models. MNRAS, *451*(4), 3419–3426. https://doi.org/10.1093/mnras/stv1204

Grzędzielski, M., Janiuk, A., Czerny, B., & Wu, Q. (2017). Modified viscosity in accretion disks. Application to Galactic black hole binaries, intermediate mass black holes, and active galactic nuclei. A&A, *603*, Article A110, A110. https://doi.org/10.1051/0004-6361/201629672

Guo, D.-F., Hu, S.-M., Tao, J., Yin, H.-X., Chen, X., & Pan, H.-J. (2014). Optical Monitoring of the Seyfert Galaxy NGC 4151 and Possible Periodicities in the Historical Light Curve. *arXiv e-prints*, Article arXiv:1405.4636, arXiv:1405.4636.

Haardt, F., & Maraschi, L. (1993). X-Ray Spectra from Two-Phase Accretion Disks. ApJ, *413*, 507. https://doi.org/10.1086/173020

Hamann, F., & Ferland, G. (1999). Elemental Abundances in Quasistellar Objects: Star Formation and Galactic Nuclear Evolution at High Redshifts. ARA&A, *37*, 487–531. https://doi.org/10.1146/annurev.astro.37.1.487

Hamann, F., Korista, K. T., Ferland, G. J., Warner, C., & Baldwin, J. (2002). Metallicities and Abundance Ratios from Quasar Broad Emission Lines. ApJ, *564*(2), 592–603. https://doi.org/10.1086/324289

Harrison, C. (2014, September). *Observational constraints on the influence of active galactic nuclei on the evolution of galaxies* (Doctoral dissertation). Durham University, UK.

Hawkins, M. R. S. (2007). Timescale of variation and the size of the accretion disc in active galactic nuclei. A&A, *462*(2), 581–589. https://doi.org/10.1051/0004-6361:20066283

Hickox, R. C., Mullaney, J. R., Alexander, D. M., Chen, C.-T. J., Civano, F. M., Goulding, A. D., & Hainline, K. N. (2014). Black Hole Variability and the Star Formation-Active Galactic Nucleus Connection: Do All Star-forming Galaxies Host an Active Galactic Nucleus? ApJ, *782*(1), Article 9, 9. https://doi.org/10.1088/0004-637X/782/1/9

Ho, L. C., & Kim, M. (2014). The Black Hole Mass Scale of Classical and Pseudo Bulges in Active Galaxies. ApJ, *789*(1), Article 17, 17. https://doi.org/10.1088/0004-637X/789/1/17

Hönig, S. F., Kishimoto, M., Tristram, K. R. W., Prieto, M. A., Gandhi, P., Asmus, D., Antonucci, R., Burtscher, L., Duschl, W. J., & Weigelt, G. (2013). Dust in the Polar Region as a Major Contributor to the Infrared Emission of Active Galactic Nuclei. ApJ, *771*(2), Article 87, 87. https://doi.org/10.1088/0004-637X/771/2/87

Hönig, S. F. (2019). Redefining the Torus: A Unifying View of AGNs in the Infrared and Submillimeter. ApJ, *884*(2), Article 171, 171. https://doi.org/10.3847/1538-4357/ab4591

Hu, C.-P., Chou, Y., Yang, T.-C., & Su, Y.-H. (2014). Tracking the Evolution of Quasi-periodic Oscillation in RE J1034+396 Using the Hilbert-Huang Transform. ApJ, *788*(1), Article 31, 31. https://doi.org/10.1088/0004-637X/788/1/31

Husemann, B., Singha, M., Scharwächter, J., McElroy, R., Neumann, J., Smirnova-Pinchukova, I., Urrutia, T., Baum, S. A., Bennert, V. N., Combes, F., Croom, S. M., Davis, T. A., Fournier, Y., Galkin, A., Gaspari, M., Enke, H., Krumpe, M., O'Dea, C. P., Pérez-Torres, M., ... Walcher, C. J. (2022). The Close AGN Reference Survey (CARS). IFU survey data and the BH mass dependence of long-term AGN variability. A&A, *659*, Article A124, A124. https://doi.org/10.1051/0004-6361/202141312

Ichimaru, S. (1977). Bimodal behavior of accretion disks: theory and application to Cygnus X-1 transitions. ApJ, *214*, 840–855. https://doi.org/10.1086/155314

Ingram, A., Done, C., & Fragile, P. C. (2009). Low-frequency quasi-periodic oscillations spectra and Lense-Thirring precession. MNRAS, *397*(1), L101–L105. https://doi.org/10.1111/j.1745-3933.2009.00693.x

Ingram, A., Motta, S. E., Aigrain, S., & Karastergiou, A. (2021). A self-lensing binary massive black hole interpretation of quasi-periodic eruptions. MNRAS, *503*(2), 1703–1716. https://doi.org/10.1093/mnras/stab609

Ivezić, Ž., Kahn, S. M., Tyson, J. A., Abel, B., Acosta, E., Allsman, R., Alonso, D., AlSayyad, Y., Anderson, S. F., Andrew, J., Angel, J. R. P., Angeli, G. Z., Ansari, R., Antilogus, P., Araujo, C., Armstrong, R., Arndt, K. T., Astier, P., Aubourg, É., … Zhan, H. (2019). LSST: From Science Drivers to Reference Design and Anticipated Data Products. ApJ, *873*(2), Article 111, 111. https://doi.org/10.3847/1538-4357/ab042c

Janiuk, A. GLADIS: GLobal Accretion Disk Instability Simulation. *Multifrequency behaviour of high energy cosmic sources - xiii. 3-8 june 2019. palermo*. 2020, December, 48, 48. arXiv: 1911.05357 [astro-ph.HE].

Janiuk, A., & Czerny, B. (2011). On different types of instabilities in black hole accretion discs: implications for X-ray binaries and active galactic nuclei. MNRAS, *414*(3), 2186–2194. https://doi.org/10.1111/j.1365-2966.2011.18544.x

Jermyn, A. S., Dittmann, A. J., Cantiello, M., & Perna, R. (2021). Stellar Evolution in the Disks of Active Galactic Nuclei Produces Rapidly Rotating Massive Stars. ApJ, *914*(2), Article 105, 105. https://doi.org/10.3847/1538-4357/abfb67

Kauffmann, G., Heckman, T. M., Tremonti, C., Brinchmann, J., Charlot, S., White, S. D. M., Ridgway, S. E., Brinkmann, J., Fukugita, M., Hall, P. B., Ivezić, Richards, G. T., & Schneider, D. P. (2003). The host galaxies of active galactic nuclei. *Monthly Notices of the Royal Astronomical Society*, *346*(4), 1055–1077. https://doi.org/10.1111/j.1365-2966.2003.07154.x

Keenan, M., Meyer, E. T., Georganopoulos, M., Reddy, K., & French, O. J. (2021). The relativistic jet dichotomy and the end of the blazar sequence. MNRAS, *505*(4), 4726–4745. https://doi.org/10.1093/mnras/stab1182

Kelly, B. C., Bechtold, J., & Siemiginowska, A. (2009). Are the Variations in Quasar Optical Flux Driven by Thermal Fluctuations? ApJ, *698*(1), 895–910. https://doi.org/10.1088/0004-637X/698/1/895

Kerr, R. P. (1963). Gravitational Field of a Spinning Mass as an Example of Algebraically Special Metrics. Phys. Rev. Lett., *11*(5), 237–238. https://doi.org/10.1103/PhysRevLett.11.237

King, A. (2020). GSN 069 - A tidal disruption near miss. MNRAS, *493*(1), L120–L123. https://doi.org/10.1093/mnrasl/slaa020

King, A., & Nixon, C. (2015). AGN flickering and chaotic accretion. MNRAS, *453*(1), L46–L47. https://doi.org/10.1093/mnrasl/slv098

Kokubo, M., & Minezaki, T. (2020). Rapid luminosity decline and subsequent reformation of the innermost dust distribution in the changing-look AGN Mrk 590. MNRAS, *491*(4), 4615–4633. https://doi.org/10.1093/mnras/stz3397

Kollmeier, J. A., Zasowski, G., Rix, H.-W., Johns, M., Anderson, S. F., Drory, N., Johnson, J. A., Pogge, R. W., Bird, J. C., Blanc, G. A., Brownstein, J. R., Crane, J. D., De Lee, N. M., Klaene,

M. A., Kreckel, K., MacDonald, N., Merloni, A., Ness, M. K., O'Brien, T., ... van Saders, J. L. (2017). SDSS-V: Pioneering Panoptic Spectroscopy. *arXiv e-prints*, Article arXiv:1711.03234, arXiv:1711.03234.

Kormendy, J., & Ho, L. C. (2013). Coevolution (Or Not) of Supermassive Black Holes and Host Galaxies. ARA&A, *51*(1), 511–653. https://doi.org/10.1146/annurev-astro-082708-101811

Kozlowski, S. (2016). Revisiting Stochastic Variability of AGNs with Structure Functions. ApJ, *826*(2), Article 118, 118. https://doi.org/10.3847/0004-637X/826/2/118

Krishnan, S., Markowitz, A. G., Schwarzenberg-Czerny, A., & Middleton, M. J. (2021). Detection of periodic signals in AGN red noise light curves: empirical tests on the Auto-Correlation Function and Phase Dispersion Minimization. MNRAS, *508*(3), 3975–3994. https://doi.org/10.1093/mnras/stab2839

Kriss, G. A., De Rosa, G., Ely, J., Peterson, B. M., Kaastra, J., Mehdipour, M., Ferland, G. J., Dehghanian, M., Mathur, S., Edelson, R., Korista, K. T., Arav, N., Barth, A. J., Bentz, M. C., Brandt, W. N., Crenshaw, D. M., Dalla Bontà, E., Denney, K. D., Done, C., ... Zu, Y. (2019). Space Telescope and Optical Reverberation Mapping Project. VIII. Time Variability of Emission and Absorption in NGC 5548 Based on Modeling the Ultraviolet Spectrum. ApJ, *881*(2), Article 153, 153. https://doi.org/10.3847/1538-4357/ab3049

Kubota, A., & Done, C. (2018). A physical model of the broad-band continuum of AGN and its implications for the UV/X relation and optical variability. MNRAS, *480*(1), 1247–1262. https://doi.org/10.1093/mnras/sty1890

Laha, S., Meyer, E., Roychowdhury, A., Becerra González, J., Acosta-Pulido, J. A., Thapa, A., Ghosh, R., Behar, E., Gallo, L. C., Kriss, G. A., Panessa, F., Bianchi, S., La Franca, F., Scepi, N., Begelman, M. C., Longinotti, A. L., Lusso, E., Oates, S., Nicholl, M., & Cenko, S. B. (2022). A radio, optical, UV and X-ray view of the enigmatic changing look Active Galactic Nucleus 1ES˜1927+654 from its pre- to post-flare states. *arXiv e-prints*, Article arXiv:2203.07446, arXiv:2203.07446.

LaMassa, S. M., Cales, S., Moran, E. C., Myers, A. D., Richards, G. T., Eracleous, M., Heckman, T. M., Gallo, L., & Urry, C. M. (2015). The Discovery of the First "Changing Look" Quasar: New Insights Into the Physics and Phenomenology of Active Galactic Nucleus. ApJ, *800*(2), Article 144, 144. https://doi.org/10.1088/0004-637X/800/2/144

Laor, A., Fiore, F., Elvis, M., Wilkes, B. J., & McDowell, J. C. (1997). The Soft X-Ray Properties of a Complete Sample of Optically Selected Quasars. II. Final Results. ApJ, *477*(1), 93–113. https://doi.org/10.1086/303696

Laor, A., & Netzer, H. (1989). Massive thin accretion discs. - I. Calculated spectra. MNRAS, *238*, 897–916. https://doi.org/10.1093/mnras/238.3.897

Leftley, J. H., Tristram, K. R. W., Hönig, S. F., Kishimoto, M., Asmus, D., & Gandhi, P. (2018). New Evidence for the Dusty Wind Model: Polar Dust and a Hot Core in the Type-1 Seyfert ESO 323-G77. ApJ, *862*(1), Article 17, 17. https://doi.org/10.3847/1538-4357/aac8e5

Levenson, N. A., Weaver, K. A., Heckman, T. M., Awaki, H., & Terashima, Y. (2005). Deconstructing NGC 7130. ApJ, *618*(1), 167–177. https://doi.org/10.1086/425913

Lin, D. N. C. Star/Disk Interaction in the Nuclei of Active Galaxies (B. M. Peterson, F.-Z. Cheng, & A. S. Wilson, Eds.). In *Iau colloq. 159: Emission lines in active galaxies: New methods and techniques* (B. M. Peterson, F.-Z. Cheng, & A. S. Wilson, Eds.). Ed. by Peterson, B. M.,

Cheng, F.-Z., & Wilson, A. S. *113*. Astronomical Society of the Pacific Conference Series. 1997, 64.

Lira, P., Kishimoto, M., Goosmann, R. W., Campos, R., Axon, D., Elvis, M., Lawrence, A., Peterson, B. M., & Robinson, A. (2021). Spectropolarimetry of NGC 3783 and Mrk 509: Evidence for powerful nuclear winds in Seyfert 1 Galaxies. MNRAS, *507*(1), 579–593. https://doi.org/10.1093/mnras/stab1751

Liska, M. T. P., Musoke, G., Tchekhovskoy, A., Porth, O., & Beloborodov, A. M. (2022). Formation of Magnetically Truncated Accretion Disks in 3D Radiation-Transport Two-Temperature GRMHD Simulations. *arXiv e-prints*, Article arXiv:2201.03526, arXiv:2201.03526.

López-Navas, E., Martínez-Aldama, M. L., Bernal, S., Sánchez-Sáez, P., Arévalo, P., Graham, M. J., Hernández-García, L., Lira, P., & Rojas Lobos, P. A. (2022). Confirming new changing-look AGNs discovered through optical variability using a random forest-based light-curve classifier. MNRAS, *513*(1), L57–L62. https://doi.org/10.1093/mnrasl/slac033

MacLeod, C. L., Green, P. J., Anderson, S. F., Bruce, A., Eracleous, M., Graham, M., Homan, D., Lawrence, A., LeBleu, A., Ross, N. P., Ruan, J. J., Runnoe, J., Stern, D., Burgett, W., Chambers, K. C., Kaiser, N., Magnier, E., & Metcalfe, N. (2019). Changing-look Quasar Candidates: First Results from Follow-up Spectroscopy of Highly Optically Variable Quasars. ApJ, *874*(1), Article 8, 8. https://doi.org/10.3847/1538-4357/ab05e2

Madau, P., & Dickinson, M. (2014). Cosmic Star-Formation History. ARA&A, *52*, 415–486. https://doi.org/10.1146/annurev-astro-081811-125615

Madau, P., Pozzetti, L., & Dickinson, M. (1998). The Star Formation History of Field Galaxies. ApJ, *498*(1), 106–116. https://doi.org/10.1086/305523

Magorrian, J., Tremaine, S., Richstone, D., Bender, R., Bower, G., Dressler, A., Faber, S. M., Gebhardt, K., Green, R., Grillmair, C., Kormendy, J., & Lauer, T. (1998). The Demography of Massive Dark Objects in Galaxy Centers. AJ, *115*(6), 2285–2305. https://doi.org/10.1086/300353

Maiolino, R., & Mannucci, F. (2019). De re metallica: the cosmic chemical evolution of galaxies. A&A Rev., *27*(1), Article 3, 3. https://doi.org/10.1007/s00159-018-0112-2

Marin, F., & Goosmann, R. W. 2004 – 2014: Ten years of radiative transfer with STOKES (J. Ballet, F. Martins, F. Bournaud, R. Monier, & C. Reylé, Eds.). In *Sf2a-2014: Proceedings of the annual meeting of the french society of astronomy and astrophysics* (J. Ballet, F. Martins, F. Bournaud, R. Monier, & C. Reylé, Eds.). Ed. by Ballet, J., Martins, F., Bournaud, F., Monier, R., & Reylé, C. 2014, December, 103–108. arXiv: 1409.7278 [astro-ph.GA].

Martínez-Aldama, M. L., del Olmo, A., Marziani, P., Sulentic, J. W., Negrete, C. A., Dultzin, D., D'Onofrio, M., & Perea, J. (2018). Extreme quasars at high redshift. A&A, *618*, Article A179, A179. https://doi.org/10.1051/0004-6361/201833541

Martínez-Aldama, M. L., Del Olmo, A., Marziani, P., Sulentic, J. W., Negrete, C. A., Dultzin, D., Perea, J., & D'Onofrio, M. (2018). Highly accreting quasars at high redshift. *Frontiers in Astronomy and Space Sciences*, *4*, 65. https://doi.org/10.3389/fspas.2017.00065

Marziani, P., del Olmo, A., Perea, J., D'Onofrio, M., & Panda, S. (2020). Broad UV Emission Lines in Type-1 Active Galactic Nuclei: A Note on Spectral Diagnostics and the Excitation Mechanism. *Atoms*, *8*(4), 94. https://doi.org/10.3390/atoms8040094

Masoura, V. A., Mountrichas, G., Georgantopoulos, I., & Plionis, M. (2021). Relation between AGN type and host galaxy properties. A&A, *646*, Article A167, A167. https://doi.org/10.1051/0004-6361/202039238

Mathews, W. G., & Ferland, G. J. (1987). What Heats the Hot Phase in Active Nuclei? ApJ, *323*, 456. https://doi.org/10.1086/165843

Matt, G., Perola, G. C., & Piro, L. (1991). The iron line and high energy bump as X-ray signatures of cold matter in Seyfert 1 galaxies. A&A, *247*, 25.

Matt, G., Guainazzi, M., & Maiolino, R. (2003). Changing look: from Compton-thick to Compton-thin, or the rebirth of fossil active galactic nuclei. MNRAS, *342*(2), 422–426. https://doi.org/10.1046/j.1365-8711.2003.06539.x

Mazzucchelli, C., Bañados, E., Venemans, B. P., Decarli, R., Farina, E. P., Walter, F., Eilers, A. C., Rix, H. W., Simcoe, R., Stern, D., Fan, X., Schlafly, E., De Rosa, G., Hennawi, J., Chambers, K. C., Greiner, J., Burgett, W., Draper, P. W., Kaiser, N., ... Wainscoat, R. J. (2017). Physical Properties of 15 Quasars at z $\gtrsim$ 6.5. ApJ, *849*(2), Article 91, 91. https://doi.org/10.3847/1538-4357/aa9185

McHardy, I. M., Koerding, E., Knigge, C., Uttley, P., & Fender, R. P. (2006). Active galactic nuclei as scaled-up Galactic black holes. Nature, *444*(7120), 730–732. https://doi.org/10.1038/nature05389

Mejía-Restrepo, J. E., Lira, P., Netzer, H., Trakhtenbrot, B., & Capellupo, D. M. (2018). The effect of nuclear gas distribution on the mass determination of supermassive black holes. *Nature Astronomy*, *2*, 63–68. https://doi.org/10.1038/s41550-017-0305-z

Merloni, A., Dwelly, T., Salvato, M., Georgakakis, A., Greiner, J., Krumpe, M., Nandra, K., Ponti, G., & Rau, A. (2015). A tidal disruption flare in a massive galaxy? Implications for the fuelling mechanisms of nuclear black holes. MNRAS, *452*(1), 69–87. https://doi.org/10.1093/mnras/stv1095

Miniutti, G., Saxton, R. D., Giustini, M., Alexand er, K. D., Fender, R. P., Heywood, I., Monageng, I., Coriat, M., Tzioumis, A. K., Read, A. M., Knigge, C., Gandhi, P., Pretorius, M. L., & Agís-González, B. (2019). Nine-hour X-ray quasi-periodic eruptions from a low-mass black hole galactic nucleus. Nature, *573*(7774), 381–384. https://doi.org/10.1038/s41586-019-1556-x

Mirabel, I. F. Microquasars: Summary and Outlook (T. Belloni, Ed.). In: In *Lecture notes in physics, berlin springer verlag* (T. Belloni, Ed.). Ed. by Belloni, T. Vol. 794. 2010, p. 1. https://doi.org/10.1007/978-3-540-76937-8_1.

Mushotzky, R. F., Done, C., & Pounds, K. A. (1993). X-ray spectra and time variability of active galactic nuclei. ARA&A, *31*, 717–717. https://doi.org/10.1146/annurev.aa.31.090193.003441

Narayan, R., & Yi, I. (1994). Advection-dominated Accretion: A Self-similar Solution. ApJ, *428*, L13. https://doi.org/10.1086/187381

Negrete, A., Dultzin, D., Marziani, P., & Sulentic, J. (2012). BLR Physical Conditions in Extreme Population A Quasars: a Method to Estimate Central Black Hole Mass at High Redshift. *ApJ*, *757*, 62.

Nenkova, M., Sirocky, M. M., Ivezić, Ž., & Elitzur, M. (2008). AGN Dusty Tori. I. Handling of Clumpy Media. ApJ, *685*(1), 147–159. https://doi.org/10.1086/590482

Netzer, H. (2019). Bolometric correction factors for active galactic nuclei. MNRAS, *488*(4), 5185–5191. https://doi.org/10.1093/mnras/stz2016

Netzer, H. (2015). Revisiting the Unified Model of Active Galactic Nuclei. ARA&A, *53*, 365–408. https://doi.org/10.1146/annurev-astro-082214-122302

Noda, H., & Done, C. (2018). Explaining changing-look AGN with state transition triggered by rapid mass accretion rate drop. MNRAS, *480*, 3898–3906. https://doi.org/10.1093/mnras/sty2032

Novikov, I. D., & Thorne, K. S. Astrophysics of black holes. *Black holes (les astres occlus)*. 1973, January, 343–450.

Oknyansky, V. L., Winkler, H., Tsygankov, S. S., Lipunov, V. M., Gorbovskoy, E. S., van Wyk, F., Buckley, D. A. H., & Tyurina, N. V. (2019). New changing look case in NGC 1566. MNRAS, *483*, 558–564. https://doi.org/10.1093/mnras/sty3133

Osterbrock, D. E. (1981). Seyfert galaxies with weak broad H alpha emission lines. ApJ, *249*, 462–470. https://doi.org/10.1086/159306

Osterbrock, D. E., & Pogge, R. W. (1985). The spectra of narrow-line Seyfert 1 galaxies. ApJ, *297*, 166–176. https://doi.org/10.1086/163513

Osterbrock, D. E., & Ferland, G. J. (2006). *Astrophysics of gaseous nebulae and active galactic nuclei*.

Paczyński, B., & Wiita, P. J. (1980). Thick Accretion Disks and Supercritical Luminosities. A&A, *88*, 23.

Padovani, P., Alexander, D. M., Assef, R. J., De Marco, B., Giommi, P., Hickox, R. C., Richards, G. T., Smolčić, V., Hatziminaoglou, E., Mainieri, V., & Salvato, M. (2017). Active galactic nuclei: what's in a name? A&A Rev., *25*(1), Article 2, 2. https://doi.org/10.1007/s00159-017-0102-9

Pan, X., Li, S.-L., Cao, X., Miniutti, G., & Gu, M. (2022). A Disk Instability Model for the Quasi-periodic Eruptions of GSN 069. ApJ, *928*(2), Article L18, L18. https://doi.org/10.3847/2041-8213/ac5faf

Panda, S., Czerny, B., Adhikari, T. P., Hryniewicz, K., Wildy, C., Kuraszkiewicz, J., & Śniegowska, M. (2018). Modeling of the Quasar Main Sequence in the Optical Plane. ApJ, *866*(2), Article 115, 115. https://doi.org/10.3847/1538-4357/aae209

Panda, S., Czerny, B., & Wildy, C. (2017). The physical driver of the optical Eigenvector 1 in Quasar Main Sequence. *Frontiers in Astronomy and Space Sciences*, *4*, Article 33, 33. https://doi.org/10.3389/fspas.2017.00033

Parker, M. L., Komossa, S., Kollatschny, W., Walton, D. J., Schartel, N., Santos-Lleó, M., Harrison, F. A., Fabian, A. C., Zetzl, M., Grupe, D., Rodríguez-Pascual, P. M., & Vasudevan, R. V. (2016). The detection and X-ray view of the changing look AGN HE 1136-2304. MNRAS, *461*(2), 1927–1936. https://doi.org/10.1093/mnras/stw1449

Parker, M. L., Schartel, N., Grupe, D., Komossa, S., Harrison, F., Kollatschny, W., Mikula, R., Santos-Lleó, M., & Tomás, L. (2019). X-ray spectra reveal the reawakening of the repeat changing-look AGN NGC 1566. MNRAS, *483*, L88–L92. https://doi.org/10.1093/mnrasl/sly224

Petrucci, P. O., Gronkiewicz, D., Rozanska, A., Belmont, R., Bianchi, S., Czerny, B., Matt, G., Malzac, J., Middei, R., De Rosa, A., Ursini, F., & Cappi, M. (2020). Radiation spectra of warm and optically thick coronae in AGNs. A&A, *634*, Article A85, A85. https://doi.org/10.1051/0004-6361/201937011

Pons, E., & Watson, M. G. (2016). A new sample of X-ray selected narrow emission-line galaxies. II. Looking for True Seyfert 2. A&A, *594*, Article A72, A72. https://doi.org/10.1051/0004-6361/201629194

Raj, A., & Nixon, C. J. (2021). Disk Tearing: Implications for Black Hole Accretion and AGN Variability. ApJ, *909*(1), Article 82, 82. https://doi.org/10.3847/1538-4357/abdc25

Rees, M. J. (1984). Black Hole Models for Active Galactic Nuclei. ARA&A, *22*, 471–506. https://doi.org/10.1146/annurev.aa.22.090184.002351

Reines, A. E., & Volonteri, M. (2015). Relations between Central Black Hole Mass and Total Galaxy Stellar Mass in the Local Universe. ApJ, *813*(2), Article 82, 82. https://doi.org/10.1088/0004-637X/813/2/82

Ricci, C., Loewenstein, M., Kara, E., Remillard, R., Trakhtenbrot, B., Arcavi, I., Gendreau, K. C., Arzoumanian, Z., Fabian, A. C., Li, R., Ho, L. C., MacLeod, C. L., Cackett, E., Altamirano, D., Gandhi, P., Kosec, P., Pasham, D., Steiner, J., & Chan, C. H. (2021). The 450 Day X-Ray Monitoring of the Changing-look AGN 1ES 1927+654. ApJS, *255*(1), Article 7, 7. https://doi.org/10.3847/1538-4365/abe94b

Richards, G. T., Lacy, M., Storrie-Lombardi, L. J., Hall, P. B., Gallagher, S. C., Hines, D. C., Fan, X., Papovich, C., Vanden Berk, D. E., Trammell, G. B., Schneider, D. P., Vestergaard, M., York, D. G., Jester, S., Anderson, S. F., Budavári, T., & Szalay, A. S. (2006). Spectral Energy Distributions and Multiwavelength Selection of Type 1 Quasars. ApJS, *166*(2), 470–497. https://doi.org/10.1086/506525

Ripperda, B., Liska, M., Chatterjee, K., Musoke, G., Philippov, A. A., Markoff, S. B., Tchekhovskoy, A., & Younsi, Z. (2022). Black Hole Flares: Ejection of Accreted Magnetic Flux through 3D Plasmoid-mediated Reconnection. ApJ, *924*(2), Article L32, L32. https://doi.org/10.3847/2041-8213/ac46a1

Rosario, D. J., Trakhtenbrot, B., Lutz, D., Netzer, H., Trump, J. R., Silverman, J. D., Schramm, M., Lusso, E., Berta, S., Bongiorno, A., Brusa, M., Förster-Schreiber, N. M., Genzel, R., Lilly, S., Magnelli, B., Mainieri, V., Maiolino, R., Merloni, A., Mignoli, M., ... Zamorani, G. (2013). The mean star-forming properties of QSO host galaxies. A&A, *560*, Article A72, A72. https://doi.org/10.1051/0004-6361/201322196

Ross, N. P., Ford, K. E. S., Graham, M., McKernan, B., Stern, D., Meisner, A. M., Assef, R. J., Dey, A., Drake, A. J., Jun, H. D., & Lang, D. (2018). A new physical interpretation of optical and infrared variability in quasars. MNRAS, *480*, 4468–4479. https://doi.org/10.1093/mnras/sty2002

Różańska, A., Malzac, J., Belmont, R., Czerny, B., & Petrucci, P. O. (2015). Warm and optically thick dissipative coronae above accretion disks. A&A, *580*, Article A77, A77. https://doi.org/10.1051/0004-6361/201526288

Ruan, J. J., Anderson, S. F., Cales, S. L., Eracleous, M., Green, P. J., Morganson, E., Runnoe, J. C., Shen, Y., Wilkinson, T. D., Blanton, M. R., Dwelly, T., Georgakakis, A., Greene, J. E., LaMassa, S. M., Merloni, A., & Schneider, D. P. (2016). Toward an Understanding of Changing-look Quasars: An Archival Spectroscopic Search in SDSS. ApJ, *826*, Article 188, 188. https://doi.org/10.3847/0004-637X/826/2/188

Ruan, J. J., Anderson, S. F., Dexter, J., & Agol, E. (2014). Evidence for Large Temperature Fluctuations in Quasar Accretion Disks from Spectral Variability. ApJ, *783*(2), Article 105, 105. https://doi.org/10.1088/0004-637X/783/2/105

Ruthven Ward, S., Harrison, C., Costa, T., & Mainieri, V. (2022). Cosmological simulations predict that AGN preferentially live in gas-rich, star-forming galaxies despite effective feedback. *arXiv e-prints*, Article arXiv:2204.13712, arXiv:2204.13712.

Santini, P., Fontana, A., Grazian, A., Salimbeni, S., Fiore, F., Fontanot, F., Boutsia, K., Castellano, M., Cristiani, S., de Santis, C., Gallozzi, S., Giallongo, E., Menci, N., Nonino, M., Paris, D., Pentericci, L., & Vanzella, E. (2009). Star formation and mass assembly in high redshift galaxies. A&A, *504*(3), 751–767. https://doi.org/10.1051/0004-6361/200811434

Scepi, N., Begelman, M. C., & Dexter, J. (2021). Magnetic flux inversion in a peculiar changing look AGN. MNRAS, *502*(1), L50–L54. https://doi.org/10.1093/mnrasl/slab002

Schawinski, K., Koss, M., Berney, S., & Sartori, L. F. (2015). Active galactic nuclei flicker: an observational estimate of the duration of black hole growth phases of $\sim 10^5$ yr. MNRAS, *451*(3), 2517–2523. https://doi.org/10.1093/mnras/stv1136

Schaye, J., Crain, R. A., Bower, R. G., Furlong, M., Schaller, M., Theuns, T., Dalla Vecchia, C., Frenk, C. S., McCarthy, I. G., Helly, J. C., Jenkins, A., Rosas-Guevara, Y. M., White, S. D. M., Baes, M., Booth, C. M., Camps, P., Navarro, J. F., Qu, Y., Rahmati, A., ... Trayford, J. (2015). The EAGLE project: simulating the evolution and assembly of galaxies and their environments. MNRAS, *446*(1), 521–554. https://doi.org/10.1093/mnras/stu2058

Schmidt, M. (1963). 3C 273 : A Star-Like Object with Large Red-Shift. Nature, *197*(4872), 1040. https://doi.org/10.1038/1971040a0

Schutte, Z., Reines, A. E., & Greene, J. E. (2019). The Black Hole-Bulge Mass Relation Including Dwarf Galaxies Hosting Active Galactic Nuclei. ApJ, *887*(2), Article 245, 245. https://doi.org/10.3847/1538-4357/ab35dd

Schwarzschild, K. (1916). On the Gravitational Field of a Mass Point According to Einstein's Theory. *Abh. Konigl. Preuss. Akad. Wissenschaften Jahre 1906,92, Berlin,1907*, *1916*, 189–196.

Seyfert, C. K. (1943). Nuclear Emission in Spiral Nebulae. ApJ, *97*, 28. https://doi.org/10.1086/144488

Shakura, N. I., & Sunyaev, R. A. (1973). Reprint of 1973A&A....24..337S. Black holes in binary systems. Observational appearance. A&A, *500*, 33–51.

Shankar, F., Crocce, M., Miralda-Escudé, J., Fosalba, P., & Weinberg, D. H. (2010). On the Radiative Efficiencies, Eddington Ratios, and Duty Cycles of Luminous High-redshift Quasars. ApJ, *718*(1), 231–250. https://doi.org/10.1088/0004-637X/718/1/231

Shen, Y., & Ho, L. C. (2014). The diversity of quasars unified by accretion and orientation. *Nature*, *513*, 210–213. https://doi.org/10.1038/nature13712

Shields, G. A. (1978). Thermal continuum from accretion disks in quasars. Nature, *272*(5655), 706–708. https://doi.org/10.1038/272706a0

Shin, J., Woo, J.-H., Nagao, T., & Kim, S. C. (2013). The Chemical Properties of Low-redshift QSOs. ApJ, *763*, Article 58, 58. https://doi.org/10.1088/0004-637X/763/1/58

Shin, J., Nagao, T., & Woo, J.-H. (2017). Outflow and Metallicity in the Broad-Line Region of Low-Redshift Active Galactic Nuclei. ApJ, *835*(1), Article 24, 24. https://doi.org/10.3847/1538-4357/835/1/24

Siemiginowska, A., & Czerny, B. (1989). Observational constraints on viscosity in AGN accretion discs. MNRAS, *239*, 289–295. https://doi.org/10.1093/mnras/239.1.289

Siemiginowska, A., & Elvis, M. (1997). Deriving the Quasar Luminosity Function from Accretion-Disk Instabilities. ApJ, *482*(1), L9–L12. https://doi.org/10.1086/310673

Sikora, M. (2009). Radio bimodality: Spin, accretion mode, or both? *Astronomische Nachrichten*, *330*(2), 291. https://doi.org/10.1002/asna.200811178

Slipher, V. M. (1917). The spectrum and velocity of the nebula N.G.C. 1068 (M 77). *Lowell Observatory Bulletin*, *3*, 59–62.

Sniegowska, M., Czerny, B., Bon, E., & Bon, N. (2020). Possible mechanism for multiple changing-look phenomena in active galactic nuclei. A&A, *641*, Article A167, A167. https://doi.org/10.1051/0004-6361/202038575

Śniegowska, M., Grzedzielski, M., Czerny, B., & Janiuk, A. (2022a). Modeling changing-look active galactic nuclei phenomenon in 1D using accretion disk instabilities. *Astronomische Nachrichten*, *343*(1-2), Article e210065, e210065. https://doi.org/10.1002/asna.20210065

Śniegowska, M., Grzędzielski, M., Czerny, B., & Janiuk, A. (2022b). Modified models of radiation pressure instability in application to 10, 10^5, and 10^7 $M_\odot$ accreting black holes. *arXiv e-prints*, Article arXiv:2204.10067, arXiv:2204.10067.

Śniegowska, M., Marziani, P., Czerny, B., Panda, S., Martínez-Aldama, M. L., del Olmo, A., & D'Onofrio, M. (2021). High Metal Content of Highly Accreting Quasars. ApJ, *910*(2), Article 115, 115. https://doi.org/10.3847/1538-4357/abe1c8

Śniegowska, M., Panda, S., Czerny, B., Savić, Đ., Martínez-Aldama, M. L., Marziani, P., Wang, J.-M., Du, P., & Popović, L. Č. (2022c). Spectropolarimetry and spectral decomposition of high-accreting Narrow Line Seyfert 1 galaxies. *arXiv e-prints*, Article arXiv:2202.13839, arXiv:2202.13839.

Stalevski, M., Fritz, J., Baes, M., Nakos, T., & Popović, L. Č. (2012). 3D radiative transfer modelling of the dusty tori around active galactic nuclei as a clumpy two-phase medium. MNRAS, *420*(4), 2756–2772. https://doi.org/10.1111/j.1365-2966.2011.19775.x

Stone, Z., Shen, Y., Burke, C. J., Chen, Y.-C., Yang, Q., Liu, X., Gruendl, R. A., Adamów, M., Andrade-Oliveira, F., Annis, J., Bacon, D., Bertin, E., Bocquet, S., Brooks, D., Burke, D. L., Carnero Rosell, A., Carrasco Kind, M., Carretero, J., da Costa, L. N., ... To, C. (2022). Optical Variability of Quasars with 20-Year Photometric Light Curves. MNRAS. https://doi.org/10.1093/mnras/stac1259

Suková, P., Zajaček, M., Witzany, V., & Karas, V. (2021). Stellar Transits across a Magnetized Accretion Torus as a Mechanism for Plasmoid Ejection. ApJ, *917*(1), Article 43, 43. https://doi.org/10.3847/1538-4357/ac05c6

Sulentic, J. W., del Olmo, A., Marziani, P., Martínez-Carballo, M. A., D'Onofrio, M., Dultzin, D., Perea, J., Martínez-Aldama, M. L., Negrete, C. A., Stirpe, G. M., & Zamfir, S. (2017). What does CIVλ1549 tell us about the physical driver of the Eigenvector quasar sequence? A&A, *608*, Article A122, A122. https://doi.org/10.1051/0004-6361/201630309

Sulentic, J. W., Zwitter, T., Marziani, P., & Dultzin-Hacyan, D. (2000). Eigenvector 1: An Optimal Correlation Space for Active Galactic Nuclei. *ApJl*, *536*, L5–L9. https://doi.org/10.1086/312717

Sun, W.-H., & Malkan, M. A. (1989). Fitting Improved Accretion Disk Models to the Multiwavelength Continua of Quasars and Active Galactic Nuclei. ApJ, *346*, 68. https://doi.org/10.1086/167986

Thompson, T. A., Quataert, E., & Murray, N. (2005). Radiation Pressure-supported Starburst Disks and Active Galactic Nucleus Fueling. ApJ, *630*(1), 167–185. https://doi.org/10.1086/431923

Tohline, J. E., & Osterbrock, D. E. (1976). Variation of the spectrum of the Seyfert galaxy NGC 7603. ApJ, *210*, L117–L120. https://doi.org/10.1086/182317

Trakhtenbrot, B., Arcavi, I., MacLeod, C. L., Ricci, C., Kara, E., Graham, M. L., Stern, D., Harrison, F. A., Burke, J., Hiramatsu, D., Hosseinzadeh, G., Howell, D. A., Smartt, S. J., Rest, A., Prieto, J. L., Shappee, B. J., Holoien, T. W. S., Bersier, D., Filippenko, A. V., ... Loewenstein, M.

(2019). 1ES 1927+654: An AGN Caught Changing Look on a Timescale of Months. ApJ, *883*(1), Article 94, 94. https://doi.org/10.3847/1538-4357/ab39e4

Trakhtenbrot, B., Lira, P., Netzer, H., Cicone, C., Maiolino, R., & Shemmer, O. (2017). ALMA Observations Show Major Mergers Among the Host Galaxies of Fast-growing, High-redshift Supermassive Black Holes. ApJ, *836*(1), Article 8, 8. https://doi.org/10.3847/1538-4357/836/1/8

Urry, C. M., & Padovani. (1995). Unified Schemes for Radio-Loud Active Galactic Nuclei. PASP, *107*, 803. https://doi.org/10.1086/133630

Vietri, G., Piconcelli, E., Bischetti, M., Duras, F., Martocchia, S., Bongiorno, A., Marconi, A., Zappacosta, L., Bisogni, S., Bruni, G., Brusa, M., Comastri, A., Cresci, G., Feruglio, C., Giallongo, E., La Franca, F., Mainieri, V., Mannucci, F., Ricci, F., ... Fiore, F. (2018). The WISSH quasars project. IV. Broad line region versus kiloparsec-scale winds. A&A, *617*, Article A81, A81. https://doi.org/10.1051/0004-6361/201732335

Wang, F., Yang, J., Fan, X., Hennawi, J. F., Barth, A. J., Banados, E., Bian, F., Boutsia, K., Connor, T., Davies, F. B., Decarli, R., Eilers, A.-C., Farina, E. P., Green, R., Jiang, L., Li, J.-T., Mazzucchelli, C., Nanni, R., Schindler, J.-T., ... Yue, M. (2021). A Luminous Quasar at Redshift 7.642. ApJ, *907*(1), Article L1, L1. https://doi.org/10.3847/2041-8213/abd8c6

Wang, H., Zhou, H., Yuan, W., & Wang, T. (2012). Metallicity and Quasar Outflows. ApJ, *751*, Article L23, L23. https://doi.org/10.1088/2041-8205/751/2/L23

Wang, J.-M., & Bon, E. (2020). Changing-look active galactic nuclei: close binaries of supermassive black holes in action. A&A, *643*, Article L9, L9. https://doi.org/10.1051/0004-6361/202039368

Wang, J.-M., Chen, Y.-M., & Zhang, F. (2006). Cosmological Evolution of the Duty Cycle of Quasars. ApJ, *647*(1), L17–L20. https://doi.org/10.1086/507271

Wu, X.-B., Chen, Z.-Y., Jia, Z.-D., Zuo, W.-W., Zhao, Y.-H., Luo, A. L., Bai, Z.-R., Chen, J.-J., Zhang, H.-T., Yan, H.-L., Ren, J.-J., Sun, S.-W., Wu, H., Zhang, Y., Li, Y.-P., Lu, Q.-S., Wang, Y., Ni, J.-J., Wang, H., ... Shen, S.-Y. (2010). A very bright (i = 16.44) quasar in the 'redshift desert' discovered by the Guoshoujing Telescope (LAMOST). *Research in Astronomy and Astrophysics*, *10*(8), 737–744. https://doi.org/10.1088/1674-4527/10/8/003

Xian, J., Zhang, F., Dou, L., He, J., & Shu, X. (2021). X-Ray Quasi-periodic Eruptions Driven by Star-Disk Collisions: Application to GSN069 and Probing the Spin of Massive Black Holes. ApJ, *921*(2), Article L32, L32. https://doi.org/10.3847/2041-8213/ac31aa

Yan, H., Li, H., Wang, S., Zong, W., Yuan, H., Xiang, M., Huang, Y., Xie, J., Dong, S., Yuan, H., Bi, S., Chu, Y., Cui, X., Deng, L., Fu, J., Han, Z., Hou, J., Li, G., Liu, C., ... Zhao, Y. (2022). Overview of the LAMOST survey in the first decade. *The Innovation*, *3*, Article 100224, 100224. https://doi.org/10.1016/j.xinn.2022.100224

Yang, Q., Wu, X.-B., Fan, X., Jiang, L., McGreer, I., Shangguan, J., Yao, S., Wang, B., Joshi, R., Green, R., Wang, F., Feng, X., Fu, Y., Yang, J., & Liu, Y. (2018). Discovery of 21 New Changing-look AGNs in the Northern Sky. ApJ, *862*, Article 109, 109. https://doi.org/10.3847/1538-4357/aaca3a

Yao, S., Yang, X., Gu, M., An, T., Yang, J., Ho, L. C., Liu, X., Wang, R., Wu, X.-B., & Yuan, W. (2021). Detection of a parsec-scale jet in a radio-quiet narrow-line Seyfert 1 galaxy with highly accreting supermassive black hole. MNRAS, *508*(1), 1305–1313. https://doi.org/10.1093/mnras/stab2651

York, D. G., Adelman, J., Anderson, J., John E., Anderson, S. F., Annis, J., Bahcall, N. A., Bakken, J. A., Barkhouser, R., Bastian, S., Berman, E., Boroski, W. N., Bracker, S., Briegel, C., Briggs, J. W., Brinkmann, J., Brunner, R., Burles, S., Carey, L., Carr, M. A., ... SDSS Collaboration. (2000). The Sloan Digital Sky Survey: Technical Summary. AJ, *120*(3), 1579–1587. https://doi.org/10.1086/301513

Yuan, W., Zhou, H. Y., Komossa, S., Dong, X. B., Wang, T. G., Lu, H. L., & Bai, J. M. (2008). A Population of Radio-Loud Narrow-Line Seyfert 1 Galaxies with Blazar-Like Properties? ApJ, *685*(2), 801–827. https://doi.org/10.1086/591046

Zajaček, M., Tursunov, A., Eckart, A., & Britzen, S. (2018). On the charge of the Galactic centre black hole. MNRAS, *480*(4), 4408–4423. https://doi.org/10.1093/mnras/sty2182

Zhou, H., Wang, T., Yuan, W., Shan, H., Komossa, S., Lu, H., Liu, Y., Xu, D., Bai, J. M., & Jiang, D. R. (2007). A Narrow-Line Seyfert 1-Blazar Composite Nucleus in 2MASX J0324+3410. ApJ, *658*(1), L13–L16. https://doi.org/10.1086/513604

Appendix: statements of contribution

Center for Theoretical Physics
of the Polish Academy of Sciences
Centrum Fizyki Teoretycznej Polskiej Akademii Nauk

Warsaw, 10 May 2022

Prof. Bożena Czerny
Centrum Fizyki Teoretyczej PAN
Al. Lotników 32/46
02-668 Warsaw, Poland
tel. +48 22 847 09 20
email: bcz@cft.edu.pl

Information about the co-authorship of the paper

As a co-author of the paper by Sniegowska et al. Titled "Possible mechanism for multiple changing-look phenomena in active galactic nuclei" published in Astronomy & Astrophysics in 2020, (Volume 641, id.A167, pp.), I contributed to this paper by helping with convergence of the computer program and helped with final editing of this paper. I contributed about 10% to the total effort of this paper. I confirm that Ms. Sniegowska contributed in 80% to the total effort by modelling the lightcurves and writing the manuscript.

B Czerny

Bożena Czerny

ASTRONOMICAL OBSERVATORY
VOLGINA 7, 11060 BELGRADE, SERBIA
PHONE: ++ 381 11 3088-062, 3088-073, 2404-513
PHONE/FAX: ++ 381 11 2419-553

Astronomical Observatory

Volgina 7, 11060 Belgrade, Serbia

Edi Bon

ebon@aob.rs

May 9. 2022.

As a co-author of the paper by Sniegowska et al. Titled “Possible mechanism for multiple changing-look phenomena in active galactic nuclei” published in Astronomy & Astrophysics in 2020, (Volume 641, id.A167, pp.), I contributed to this paper with construction of observational light curves from long term spectral monitoring campaigns of NGC5548 and NGC4151 and helped with the editing of this paper. I contributed about 5% to the total effort of this paper. I confirm that Ms. Sniegowska contributed in 80% to the total effort by modeling the lightcurves and writing the manuscript.

Dr. Edi Bon
Associate Research Professor
Astronomical Observatory, Belgrade, Serbia

ASTRONOMICAL OBSERVATORY
VOLGINA 7, 11060 BELGRADE, SERBIA
PHONE: ++ 381 11 3088-062, 3088-073, 2404-513
PHONE/FAX: ++ 381 11 2419-553

Astronomical Observatory

Volgina 7, 11060 Belgrade, Serbia

Nataša Bon
nbon@aob.rs

May 9. 2022.

As a co-author of the paper by Sniegowska et al. Titled “Possible mechanism for multiple changing-look phenomena in active galactic nuclei” published in Astronomy & Astrophysics in 2020, (Volume 641, id.A167, pp.), I contributed to this paper with construction of observational light curves from long term spectral monitoring campaigns of NGC5548 and NGC4151 and helped with the editing of this paper. I contributed about 5% to the total effort of this paper. I confirm that Ms. Sniegowska contributed in 80% to the total effort by modeling the lightcurves and writing the manuscript.

Dr. Nataša Bon

Associate Research Professor
Astronomical Observatory
Belgrade, Serbia

Center for Theoretical Physics Polish Academy of Sciences
Al. Lotników 32/46, 02-668 Warsaw, Poland

Mikołaj Grzędzielski

Elbląska 57/21, 01-737 Warszawa, Poland

16th May 2022

As a co-author of the paper by Sniegowska et al. Titled "Modeling changing-look active galactic nuclei phenomenon in 1D using accretion disk instabilities" published in Astronomische Nachrichten in 2022, (Volume 343, Issue 1-2, article id. e210065), I contributed to this paper by the help in the modyfing the software and helped with the editing of this paper. I contributed about 5% to the total effort of this paper. I confirm that Ms. Sniegowska contributed in 80% to the total effort by modelling the lightcurves and writing the manuscript.

Mikołaj Grzędzielski

Mikołaj Grzędzielski
Center for Theoretical Physics Polish Academy of Sciences

Center for Theoretical Physics of the Polish Academy of Sciences

Centrum Fizyki Teoretycznej Polskiej Akademii Nauk

Warsaw, 10 May 2022

Prof. Bożena Czerny
Centrum Fizyki Teoretyczej PAN
Al. Lotników 32/46
02-668 Warsaw, Poland
tel. +48 22 847 09 20
email: bcz@cft.edu.pl

Information about the co-authorship of the paper

As the co-author of the publication by Sniegowska et al. Titled "Modeling changing-look active galactic nuclei phenomenon in 1D using accretion disk instabilities" published in Astronomische Nachrichten in 2022, (Volume 343, Issue 1-2, article id. e210065), I contributed to this paper by helping to set the model scenario as outlined in Fig. 1 and with final rounding the discussion. I contributed about 10% to the total effort of this paper. I confirm that Ms. Sniegowska contribution was about 80% to the total effort by modelling the lightcurves and writing the manuscript.

B Czerny

Bożena Czerny

Center for Theoretical Physics PAS Al. Lotników 32/46, 02-668 Warsaw,
Phone: (+48 22) 847 09 20, Fax: (+48 22) 843 13 69
Email: cft@cft.edu.pl; www.cft.edu.pl

prof. dr hab. Agnieszka Janiuk agnes@cft.edu.pl

Warsaw, 23.05.2022

As a co-author of the paper by Sniegowska et al. Titled “Modeling changing-look active galactic nuclei phenomenon in 1D using accretion disk instabilities” published in Astronomische Nachrichten in 2022, (Volume 343, Issue 1-2, article id. e210065), I contributed to this paper by providing numerical code GLADIS, used for the accretion disk instability simulations, and training on this code usage. I also helped with the editing of the paper. I contributed about **5%** to the total effort of this paper. I confirm that Ms. Sniegowska contributed in 80% to the total effort by modelling the lightcurves and writing the manuscript.

Agnieszka Janiuk
Digitally signed by Agnieszka Janiuk
Date: 2022.05.23 13:48:18 +02'00'

Agnieszka Janiuk
Center for Theoretical Physics,
Polish Academy of Sciences

ISTITUTO NAZIONALE DI ASTROFISICA
NATIONAL INSTITUTE FOR ASTROPHYSICS

OSSERVATORIO ASTRONOMICO DI PADOVA

May 6, 2022

To whom it may concern

As a co-author of the paper by Sniegowska et al. Titled “High Metal Content of Highly Accreting Quasars” published in The Astrophysical Journal in 2021 (Volume 910, Issue 2, id.115, pp.), I contributed to this paper by 5% and helped with the editing of this paper. I contributed about 5% to the total effort of this paper. I confirm that Ms. Sniegowska contributed in 70% to the total effort by modelling the spectra, comparison of data to CLOUDY models and writing the manuscript.

Paola Marziani

Paola Marziani, Mg. Ph., Ph. D.
National Institute for Astrophysics (INAF)
Osservatorio Astronomico di Padova
Vicolo dell’Osservatorio 5
IT35122 Padova (Italy)
e-mail: paola.marziani@inaf.it
Tel. +39.049.8293415

Center for Theoretical Physics of the Polish Academy of Sciences

Centrum Fizyki Teoretycznej Polskiej Akademii Nauk

Warsaw, 10 May 2022

Prof. Bożena Czerny
Centrum Fizyki Teoretyczej PAN
Al. Lotników 32/46
02-668 Warsaw, Poland
tel. +48 22 847 09 20
email: bcz@cft.edu.pl

Information about the co-authorship of the paper

As the co-author of the publication by Sniegowska et al. Titled "High Metal Content of Highly Accreting Quasars" published in The Astrophysical Journal in 2021 (Volume 910, Issue 2, id.115, pp.), I contributed to this paper by helping to design the efficient method of parameter fitting and helped with the editing the final version of this paper. I contributed about 5% to the total effort of this paper. I confirm that Ms. Sniegowska contributed in 70% to the total effort by modelling the spectra, comparison of data to CLOUDY models and writing the manuscript.

Bożena Czerny

Center for Theoretical Physics
Polish Academy of Sciences
Aleja Lotników 32/46, 02-668 Warsaw
Tel. (+48 22) 847 09 20, Fax/Tel: (+48 22) 843 13 69
E-mail: cft@cft.edu.pl, NIP: 525-000-92-81, REGON: 000844815

Dr. Swayamtrupta Panda
Email: panda@cft.edu.pl
Date: 07-May-2022

As a co-author of the paper by Sniegowska et al. Titled "High Metal Content of Highly Accreting Quasars" published in The Astrophysical Journal in 2021 (Volume 910, Issue 2, id.115, pp.), I contributed to this paper by assisting with the CLOUDY simulations, theoretical interpretation of the results and helped with the editing of this paper. I contributed about 5% to the total effort of this paper. I confirm that Ms. Sniegowska contributed in 70% to the total effort by modelling the spectra, comparison of data to CLOUDY models and writing the manuscript.

Swayamtrupta Panda

Swayamtrupta Panda, Ph.D.
Center for Theoretical Physics, Polish Academy of Sciences, Warsaw, Poland

DEPARTAMENTO DE ASTRONOMÍA

UNIVERSIDAD DE CHILE

CAMINO DEL OBSERVATORIO 1515, LAS CONDES, SANTIAGO, CHILE

DR. MARY LOLI MARTÍNEZ ALDAMA MAY 6, 2022

As a co-author of the paper by Sniegowska et al. Titled “High Metal Content of Highly Accreting Quasars” published in The Astrophysical Journal in 2021 (Volume 910, Issue 2, id.115, pp.), I contributed to this paper by checking the data reduction and helped with the editing of this paper. I contributed about 5% to the total effort of this paper. I confirm that Ms. Sniegowska contributed in 70% to the total effort by modelling the spectra, comparison of data to CLOUDY models and writing the manuscript.

DR. MARY LOLI MARTINEZ ALDAMA
DEPARTAMENTO DE ASTRONOMÍA
UNIVERSIDAD DE CHILE

MINISTERIO DE CIENCIA E INNOVACIÓN

CSIC
CONSEJO SUPERIOR DE INVESTIGACIONES CIENTÍFICAS

IAA INSTITUTO DE ASTROFÍSICA DE ANDALUCÍA

EXCELENCIA SEVERO OCHOA

11 May 2022

Dr. Ascensión del Olmo Orozco
Instituto de Astrofísica de Andalucía, IAA-CSIC
Glrta. de la Astronomía s/n
18008 Granada, Spain

As a co-author of the paper by Sniegowska et al. Titled “High Metal Content of Highly Accreting Quasars” published in The Astrophysical Journal in 2021 (Volume 910, Issue 2, id.115, pp.), I contributed to this paper by the analysis of the results of the fitting of the broad emission lines, the metallicity diagnostic ratios as well as in the general discussion of the results, and helped with the editing of this paper. I contributed about 5% to the total effort of this paper. I confirm that Ms. Sniegowska contributed in 70% to the total effort by modelling the spectra, comparison of data to CLOUDY models and writing the manuscript.

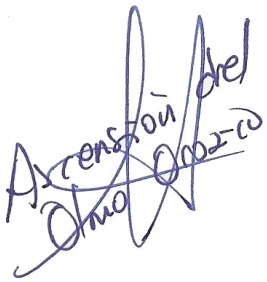

Dr. Ascensión del Olmo Orozco
Científica Titular CSIC, Senior Astronomer
Extragalactic Astronomy Department, IAA
e-mail: chony@iaa.es

UNIVERSITY OF PADUA

VICOLO OSSERVATORIO 3, I35122 PADOVA (ITALY)

D'ONOFRIO MAURO

Dep. of Physics & Astronomy
G.GALILEI
May 13, 2022

As a co-author of the paper by Sniegowska et al. Titled "High Metal Content of Highly Accreting Quasars" published in The Astrophysical Journal in 2021 (Volume 910, Issue 2, id.115, pp.), I contributed to this paper by reading and commenting it and helped with the editing of this paper. I contributed about 5% to the total effort of this paper. I confirm that Ms. Sniegowska contributed in 70% to the total effort by modelling the spectra, comparison of data to CLOUDY models and writing the manuscript.

Prof. Mauro D'Onofrio
Dep. of Physis & Astronomy G. Galilei
University of Padua
Vicolo Osservatorio 3